Neural Plasticity

Stress-Induced Glial Changes in Neurological Disorders 2021

Lead Guest Editor: Fushun Wang
Guest Editors: Fang Pan, Alexei Verkhratsky, and Jason H. Huang

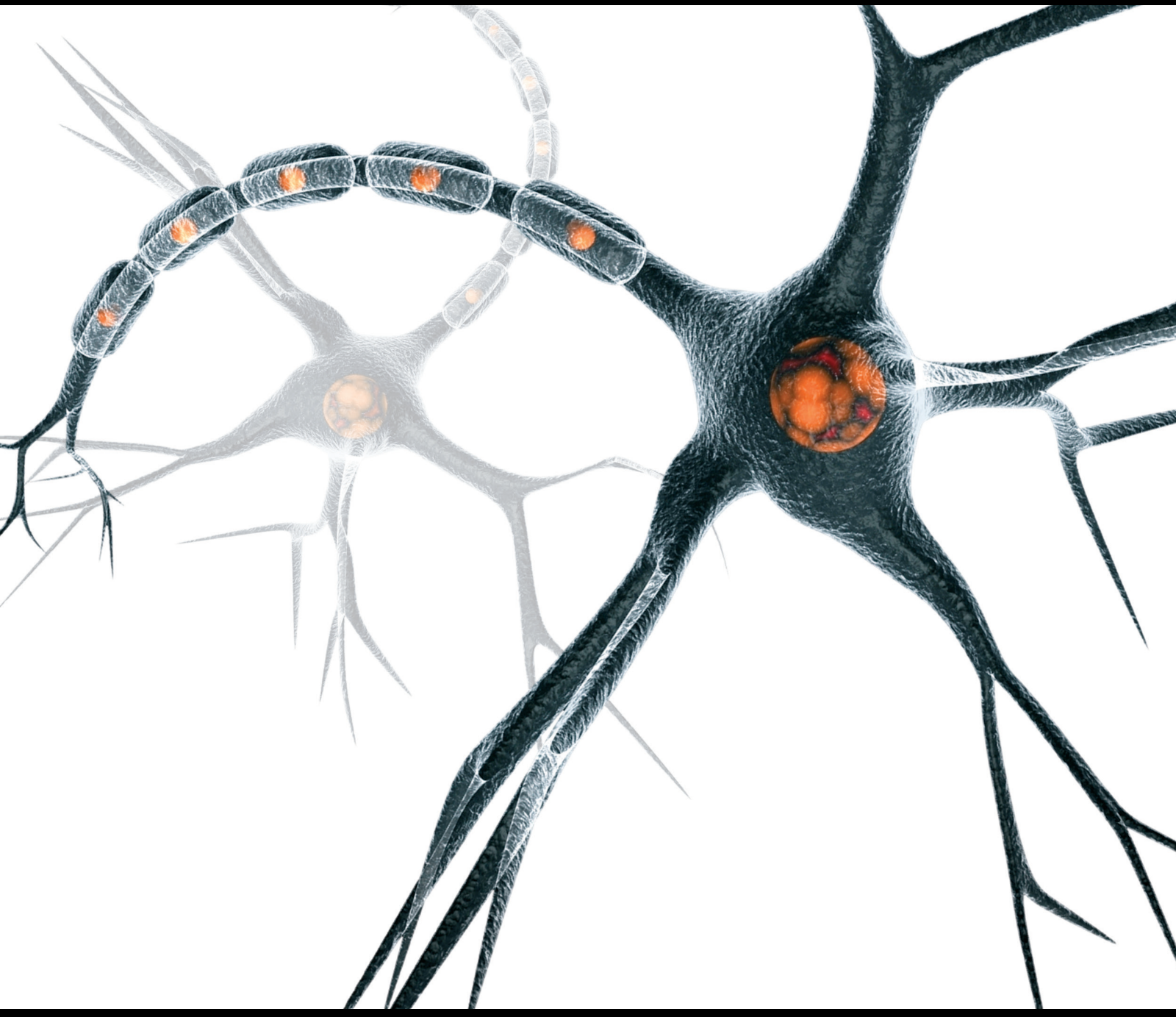

Stress-Induced Glial Changes in Neurological Disorders 2021

Neural Plasticity

Stress-Induced Glial Changes in Neurological Disorders 2021

Lead Guest Editor: Fushun Wang
Guest Editors: Fang Pan, Alexei Verkhratsky, and Jason H. Huang

Contents

Hindawi
Neural Plasticity
Volume 2024, Article ID 9780493, 1 page
https://doi.org/10.1155/2024/9780493

Retraction

Retracted: Molecular Basis of GABA Hypofunction in Adolescent Schizophrenia-Like Animals

Neural Plasticity

Received 23 January 2024; Accepted 23 January 2024; Published 24 January 2024

This article has been retracted by Hindawi following an investigation undertaken by the publisher [1]. This investigation has uncovered evidence of one or more of the following indicators of systematic manipulation of the publication process:

(1) Discrepancies in scope
(2) Discrepancies in the description of the research reported
(3) Discrepancies between the availability of data and the research described
(4) Inappropriate citations
(5) Incoherent, meaningless and/or irrelevant content included in the article
(6) Manipulated or compromised peer review

The presence of these indicators undermines our confidence in the integrity of the article's content and we cannot, therefore, vouch for its reliability. Please note that this notice is intended solely to alert readers that the content of this article is unreliable. We have not investigated whether authors were aware of or involved in the systematic manipulation of the publication process.

Wiley and Hindawi regrets that the usual quality checks did not identify these issues before publication and have since put additional measures in place to safeguard research integrity.

We wish to credit our own Research Integrity and Research Publishing teams and anonymous and named external researchers and research integrity experts for contributing to this investigation.

The corresponding author, as the representative of all authors, has been given the opportunity to register their agreement or disagreement to this retraction. We have kept a record of any response received.

References

[1] X. Wang, Y. Hu, W. Liu et al., "Molecular Basis of GABA Hypofunction in Adolescent Schizophrenia-Like Animals," *Neural Plasticity*, vol. 2021, Article ID 9983438, 15 pages, 2021.

Hindawi
Neural Plasticity
Volume 2023, Article ID 9867463, 1 page
https://doi.org/10.1155/2023/9867463

Retraction

Retracted: Sports Augmented Cognitive Benefits: An fMRI Study of Executive Function with Go/NoGo Task

Neural Plasticity

Received 19 December 2023; Accepted 19 December 2023; Published 20 December 2023

This article has been retracted by Hindawi following an investigation undertaken by the publisher [1]. This investigation has uncovered evidence of one or more of the following indicators of systematic manipulation of the publication process:

(1) Discrepancies in scope
(2) Discrepancies in the description of the research reported
(3) Discrepancies between the availability of data and the research described
(4) Inappropriate citations
(5) Incoherent, meaningless and/or irrelevant content included in the article
(6) Manipulated or compromised peer review

The presence of these indicators undermines our confidence in the integrity of the article's content and we cannot, therefore, vouch for its reliability. Please note that this notice is intended solely to alert readers that the content of this article is unreliable. We have not investigated whether authors were aware of or involved in the systematic manipulation of the publication process.

In addition, our investigation has also shown that one or more of the following human-subject reporting requirements has not been met in this article: ethical approval by an Institutional Review Board (IRB) committee or equivalent, patient/participant consent to participate, and/or agreement to publish patient/participant details (where relevant).

Wiley and Hindawi regrets that the usual quality checks did not identify these issues before publication and have since put additional measures in place to safeguard research integrity.

We wish to credit our own Research Integrity and Research Publishing teams and anonymous and named external researchers and research integrity experts for contributing to this investigation.

The corresponding author, as the representative of all authors, has been given the opportunity to register their agreement or disagreement to this retraction. We have kept a record of any response received.

References

[1] Q. Ding, L. Huang, J. Chen et al., "Sports Augmented Cognitive Benefits: An fMRI Study of Executive Function with Go/NoGo Task," *Neural Plasticity*, vol. 2021, Article ID 7476717, 6 pages, 2021.

Hindawi
Neural Plasticity
Volume 2023, Article ID 9857506, 1 page
https://doi.org/10.1155/2023/9857506

Retraction

Retracted: Three Mediating Pathways of Anxiety and Security in the Relationship between Coping Style and Disordered Eating Behaviors among Chinese Female College Students

Neural Plasticity

Received 29 August 2023; Accepted 29 August 2023; Published 30 August 2023

This article has been retracted by Hindawi following an investigation undertaken by the publisher [1]. This investigation has uncovered evidence of one or more of the following indicators of systematic manipulation of the publication process:

(1) Discrepancies in scope
(2) Discrepancies in the description of the research reported
(3) Discrepancies between the availability of data and the research described
(4) Inappropriate citations
(5) Incoherent, meaningless and/or irrelevant content included in the article
(6) Peer-review manipulation

The presence of these indicators undermines our confidence in the integrity of the article's content and we cannot, therefore, vouch for its reliability. Please note that this notice is intended solely to alert readers that the content of this article is unreliable. We have not investigated whether authors were aware of or involved in the systematic manipulation of the publication process.

In addition, our investigation has also shown that one or more of the following human-subject reporting requirements has not been met in this article: ethical approval by an Institutional Review Board (IRB) committee or equivalent, patient/participant consent to participate, and/or agreement to publish patient/participant details (where relevant).

Wiley and Hindawi regrets that the usual quality checks did not identify these issues before publication and have since put additional measures in place to safeguard research integrity.

We wish to credit our own Research Integrity and Research Publishing teams and anonymous and named external researchers and research integrity experts for contributing to this investigation.

The corresponding author, as the representative of all authors, has been given the opportunity to register their agreement or disagreement to this retraction. We have kept a record of any response received.

References

[1] W. Han, Z. Zheng, and N. Zhang, "Three Mediating Pathways of Anxiety and Security in the Relationship between Coping Style and Disordered Eating Behaviors among Chinese Female College Students," *Neural Plasticity*, vol. 2021, Article ID 7506754, 6 pages, 2021.

Hindawi
Neural Plasticity
Volume 2023, Article ID 9795436, 1 page
https://doi.org/10.1155/2023/9795436

Retraction

Retracted: Sustained Auditory Attentional Load Decreases Audiovisual Integration in Older and Younger Adults

Neural Plasticity

Received 29 August 2023; Accepted 29 August 2023; Published 30 August 2023

This article has been retracted by Hindawi following an investigation undertaken by the publisher [1]. This investigation has uncovered evidence of one or more of the following indicators of systematic manipulation of the publication process:

(1) Discrepancies in scope
(2) Discrepancies in the description of the research reported
(3) Discrepancies between the availability of data and the research described
(4) Inappropriate citations
(5) Incoherent, meaningless and/or irrelevant content included in the article
(6) Peer-review manipulation

The presence of these indicators undermines our confidence in the integrity of the article's content and we cannot, therefore, vouch for its reliability. Please note that this notice is intended solely to alert readers that the content of this article is unreliable. We have not investigated whether authors were aware of or involved in the systematic manipulation of the publication process.

Wiley and Hindawi regrets that the usual quality checks did not identify these issues before publication and have since put additional measures in place to safeguard research integrity.

We wish to credit our own Research Integrity and Research Publishing teams and anonymous and named external researchers and research integrity experts for contributing to this investigation.

The corresponding author, as the representative of all authors, has been given the opportunity to register their agreement or disagreement to this retraction. We have kept a record of any response received.

References

[1] Y. Ren, Y. Hou, J. Huang et al., "Sustained Auditory Attentional Load Decreases Audiovisual Integration in Older and Younger Adults," *Neural Plasticity*, vol. 2021, Article ID 4516133, 10 pages, 2021.

Hindawi
Neural Plasticity
Volume 2023, Article ID 9867463, 1 page
https://doi.org/10.1155/2023/9867463

Retraction

Retracted: Sports Augmented Cognitive Benefits: An fMRI Study of Executive Function with Go/NoGo Task

Neural Plasticity

Received 19 December 2023; Accepted 19 December 2023; Published 20 December 2023

This article has been retracted by Hindawi following an investigation undertaken by the publisher [1]. This investigation has uncovered evidence of one or more of the following indicators of systematic manipulation of the publication process:

(1) Discrepancies in scope
(2) Discrepancies in the description of the research reported
(3) Discrepancies between the availability of data and the research described
(4) Inappropriate citations
(5) Incoherent, meaningless and/or irrelevant content included in the article
(6) Manipulated or compromised peer review

The presence of these indicators undermines our confidence in the integrity of the article's content and we cannot, therefore, vouch for its reliability. Please note that this notice is intended solely to alert readers that the content of this article is unreliable. We have not investigated whether authors were aware of or involved in the systematic manipulation of the publication process.

In addition, our investigation has also shown that one or more of the following human-subject reporting requirements has not been met in this article: ethical approval by an Institutional Review Board (IRB) committee or equivalent, patient/participant consent to participate, and/or agreement to publish patient/participant details (where relevant).

Wiley and Hindawi regrets that the usual quality checks did not identify these issues before publication and have since put additional measures in place to safeguard research integrity.

We wish to credit our own Research Integrity and Research Publishing teams and anonymous and named external researchers and research integrity experts for contributing to this investigation.

The corresponding author, as the representative of all authors, has been given the opportunity to register their agreement or disagreement to this retraction. We have kept a record of any response received.

References

[1] Q. Ding, L. Huang, J. Chen et al., "Sports Augmented Cognitive Benefits: An fMRI Study of Executive Function with Go/NoGo Task," *Neural Plasticity*, vol. 2021, Article ID 7476717, 6 pages, 2021.

Hindawi
Neural Plasticity
Volume 2021, Article ID 7476717, 6 pages
https://doi.org/10.1155/2021/7476717

Research Article

Sports Augmented Cognitive Benefits: An fMRI Study of Executive Function with Go/NoGo Task

Qingguo Ding,[1] Lina Huang,[1] Jie Chen,[2] Farzaneh Dehghani,[1,2,3] Juan Du,[4] Yingli Li,[4] Qin Li,[1] Hongqiang Zhang,[1] Zhen Qian,[1] Wenbin Shen,[1] Xiaowei Yin,[1] and Pei Liang[1,2,5]

[1]*Imaging Department, Changshu No. 2 People's Hospital (The Clinical Medical College Affiliated to Xuzhou Medical University), Changshu, China*
[2]*Department of Psychology, Faculty of Education, Hubei University, Wuhan, China*
[3]*Department of Psychiatry, Research Center of Addiction and Behavioral Sciences, Shahid Sadoughi University of Medical Sciences, Yazd, Iran*
[4]*The School of Education, Soochow University, Soochow, China*
[5]*Brain and Cognition Research Center, Faculty of Education, Hubei University, Wuhan, China*

Correspondence should be addressed to Pei Liang; liangpei0108@126.com

Received 20 August 2021; Revised 15 November 2021; Accepted 25 November 2021; Published 7 December 2021

Academic Editor: Fushun Wang

Exercise is believed to have significant cognitive benefits. Although an array of experimental paradigms have been employed to test the cognitive effects on exercising individuals, the mechanism as to how exercise induces cognitive benefits in the brain remains unclear. This study explores the effect of dynamic neural network processing with the classic Go/NoGo task with regular exercisers. We used functional magnetic resonance imaging to analyze the brain activation of areas involved in executive function, especially inhibitory control. Nineteen regular joggers and twenty-one subjects as a control group performed the task, and their brain imaging data were analyzed. The results showed that at the attentive visual period, the frontal and parietal areas, including the prefrontal cortex, putamen, thalamus, lingual, fusiform, and caudate, were significantly enhanced in positive activities than the control group. On the other hand, in the following inhibitory control processing period, almost the same areas of the brains of the exercise group have shown stronger negative activation in comparison to the control group. Such dynamic temporal response patterns indicate that sports augment cognitive benefits; i.e., regular jogging increases the brain's visual attention and inhibitory control capacities.

1. Introduction

Exercise is getting increasingly popular, and it has become one of the significant designators to indicate one's social status. Different studies have evidenced that exercise can shape the brain structure and lead to cognitive benefits. Variant cognitive task paradigms have been applied to explore the relationship between exercise and the brain's cognitive function, such as executive function [1], attention [2], and memory [3]. The elderly subjects with higher aerobic exercise have the greater gray matter capacity of the prefrontal cortex and larger gray matter volume, such as the dorsolateral prefrontal cortex (DLPFC) [4]. They improved attention and memory and performed better in the Stroop and Spatial Working Memory (SPWM) tasks. Exercise training can increase the individual's exercise adaptability and improve cognitive performance, especially in perception speed and executive control [5]. Independent of ages, a similar performance effect has been observed in the adult population for the enhanced inhibition control and the reevaluation of cognitive ability [6].

How is the processing of exercise shaping the brain? It is essential and urgent to understand the etiology of the brain mechanism involved in the exercise-induced neural process of functional cognitive benefits. The cue reactivity and inhibitory control are the critical processes involved in developing

and maintaining motion ability and capacity. Traditionally, the Go/NoGo (GNG) task has been used as a tool to observe the inhibition function in the brain network processing by comparing the Go and the NoGo conditions. For instance, an electrophysiological (EEG) study showed that elite athletes performed GNG tasks better than the table tennis college students [7]. The authors observed a pronounced "NoGo effect" of the larger N2 and P3 components with the athletes, indicating a more substantial inhibitory function [7]. Although the EEG data has a very rough spatial resolution, the electrodes recorded from the frontal-central and central-top areas have shown stronger athletes' responses than those of the college students, under the conditions of Go and No Go. Similarly, the GNG [8] and Stroop Color Word (SCW) tasks [9] both elicit the negative amplitudes of N200 and N450 with a frontal/frontocentral distribution and in the anterior cingulate cortex [10, 11]. A positive-going amplitude of P300, peaks at parietal/centroparietal regions, was observed [12, 13]. The magnitude of P300 is suggested to be proportional to the allocation of attentional resources to evaluate task-relevant stimuli [14]. The task-relevant stimuli may activate the shared set of the neural network, including attention, inhibitory control, and other cognitive-related function. The exerciser could perceive task cues and evoke better attentive behavior. They perform the task better, especially with the inhibitory behavior such as the NoGo task. However, the brain mechanism of exercise above-mentioned was mostly discovered with EEG recordings. The complex neural networks involved with enhanced cue reactivity and response inhibition remain unclear. Hence, it is urgent to look exactly into the complex neural networks of the particular cognitive benefits. Functional magnetic resonance imaging (fMRI) can help to locate the brain activities in detail. Therefore, in this study, we aim to observe the neural response patterns of habituated exercisers with fMRI. In doing so, the effect on dynamic neural network processing with the classic GNG task with regular exercisers will be analyzed. The results will also be compared with the previous literature.

In order to delineate the mechanism of exercise-induced visual cue responses and inhibitory responses, we hypothesized the following: (1) visual cue responses would be enhanced. In other words, the exercise group would demonstrate increased cue reactivity in mesolimbic dopamine regions in the presence of cues; (2) inhibitory systems would be enhanced. There would be stronger negative responses of prefrontal neural activity during response inhibition compared to controls. In the end, by testing our hypothesis with the observed neural correlates, we could compare the results with other exercise behavioral studies and discuss the validity of exercise shaping cognitive benefits.

2. Methods and Materials

2.1. Participants. The free volunteers were selected through a social media advertisement, precisely on WeChat, which lasted for about three months in Changshu, China. The participants of the exercise group were mainly members of the local running clubs in Changshu. The total number of subjects in the exercise group was 19, including 13 males and 6 females (average age: 45.42 ± 3.50 years). As a control group, 21 nonathletic enthusiasts were recruited, including 10 males and 11 females (average age: 46.10 ± 5.16 years). No significant difference was observed in the gender (chi-square, $p = 0.184$), age, and education years (t-test, both $p > 0.05$) among the subjects of the exercise group and the control group. All subjects reported normal or corrected vision and no history of mental disorder problems.

Table 1: Exercise data and EAI scores of the excessive exercise and the control groups.

	Exercise group	Control group	t	df	p
Times per week	4.14 ± 1.01	1.31 ± 1.09	10.02	53	≤0.001
Hours per time	1.22 ± 0.47	0.63 ± 0.57	4.25	53	≤0.001
Total exercise time	5.11 ± 2.84	1.14 ± 1.13	6.66	53	≤0.001

All the volunteers had regular office sedentary work, and none of them was a full-time or part-time athlete. We selected the participant as the exercise group (1) if she/he had participated in a marathon at least once a month, (2) if she/he had jogging at least three times a week, and (3) if each of their jogging sessions lasted more than one hour. The frequencies, the total exercise time per week, and the control groups are compared and listed in Table 1. After comparing the columns of Table 1, it can be seen that the frequencies and the total exercise time per week of the exercise group are significantly higher than those of the control group.

All the subjects were well informed about the procedures of this study and before the experiment were made to sign the written consent. The study was approved by the Ethics Committee (IEC) of the No. 2 People's Hospital of Changshu (license number 2018-68), according to the Ethics Guidelines.

2.2. Tasks. After the participants were recruited and selected, they were scheduled to be scanned for the GNG tasks. The participants executed the traditional GNG task with an event-related design. The stimuli contained 26 black capital alphabets on the white background of the display. On display, the stimuli are divided into two groups: X group with 20% frequency and non-X group with 80% frequency. Each trial began with a fixation (+) on display for 750 ms, followed by an alphabet presented for 250 ms. Then, the black screen lasted for 1000 ms. During the presentation of the black screen, the participants were requested to identify the alphabet and press the button with the right hand if the alphabet was non-X (the Go trial) or not respond at all, if it was X (the No Go trial). The block consisted of 120 trials, and after 1 min break, the block was to be repeated once more. The whole run lasted around 9 min.

2.3. MRI Data Acquisition. Structural and functional MRI data were collected using the GE Discovery MR750W 3.0 T scanning system, housed in the Imaging Department of No. 2 People's Hospital of Changshu. The scanner was with the 8-channel head coil. During the scanning process, the

participants were quietly lying on the back in the magnetic resonance examination bed, fixing the head inside the head coil with foam padding, and wearing earplugs to reduce machine noise. The participants watched the visual stimuli through a reflector mirror mounted on the head coil. Through the mirror, the visual stimuli were reflected from the projector screen, placed outside the gate of the MRI. For structural imaging, high-resolution T1-weighted scans were acquired. The 3D T1 BRAVO_SPM volume sequence was applied with TR = 8.5 ms, TE = 3.2 ms, flip angle = 12°, FOV = 24 cm, 256 × 256 matrix size, and 1 mm slice thickness. The MR sequence for T2-weighted functional imaging was acquired using TR = 2000 ms, TE = 30 ms, flip angle = 90 °, scan resolution of 64 × 64, 33 slices, intervals of 0.2 mm with slice thickness = 3.6 mm, FOV = 24 cm, and voxel size = 3.75 × 3.75 × 3.75 mm^3. The first 2 scans were discarded to allow for the BOLD signal to stabilize.

2.4. fMRI Data Analysis. Preprocessing and statistical analysis of fMRI data were performed using SPM12 (Wellcome Department of Imaging Neuroscience, University College London, UK, http://www.fil.ion.ucl.ac.uk/spm), implemented in MATLAB R2013b (MathWorks, Inc., Natick, MA). The preprocessing included head motion correction, spatial normalization, and spatial smoothing with a 6 mm full-width at half-maximum Gaussian kernel. The coregistered functional and anatomical images were registered to Montreal Neurological Institute (MNI) space, with a resolution of 3 × 3 × 3 mm^3. The sequences with head movement range exceeding 3 mm or rotation that exceeded 3 degrees were removed.

After the preprocessing was completed in a first-order analysis, the evoked hemodynamic responses under three conditions were modeled for each subject, using box-car functions to convolve with canonical HRF (hemodynamic response function) to construct a general linear model (GLM). The nuisance regressor consisted of the six head motion parameters and a constant regressor for each run. The contrast responses were divided into two-time windows at the individual subject level: the visual stimuli lasting 250 ms and the following 1000 ms after visual stimuli disappeared. The analysis was performed: No Go condition vs. baseline condition, Go condition vs. baseline condition, and No Go condition vs. Go condition (intergroup comparisons). A second-order group-level random-effect analysis was then implemented across the maps, using the permutation-based nonparametric method [15] to run 5000 permutations in the DPABI software [16]. We had initially set a primary voxel-level threshold at $p < 0.05$ and a minimum extent of 30 voxels in order to form activation clusters. Brain activation was anatomically labeled according to revised atlas AAL2 [17], which was rendered using the bspmview toolbox (10.5281/zenodo.168074).

3. Results

The results have shown that, compared with the control group, the exercisers' brain activation of the frontal and center parietal lobes has been positively enhanced during attentive visual perception (Figure 1, Table 2). In the following time, almost the same brain areas of the exercisers responded stronger in negative inhibition control than the control group (Figure 2, Table 3).

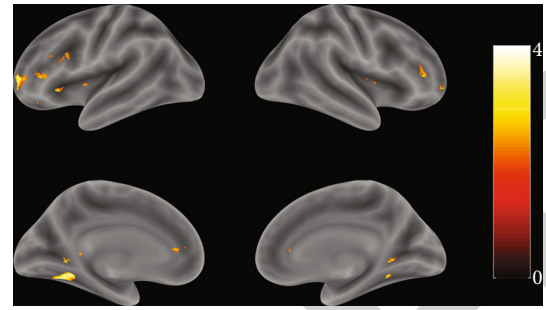

Figure 1: Full view of the brain response differences between the exercise and control groups with visual stimuli (t-value map). The color bar on the right side indicates the brain activity level.

Table 2: The contrast responses to visual stimuli between exercise and control groups.

Labels	Clusters	t	MNI		
			x	y	z
Putamen_L	63	2.85	-33	0	3
Putamen_R	96	2.84	27	15	-3
Thalamus_L	668	3.38	0	-27	3
Lingual_L	668	3.14	-24	-48	-3
Fusiform_L	668	3.11	-30	-58	-6
Lingual_R	80	2.57	24	-45	-3
Thalamus_R	65	2.02	9	0	21
PFC_L	660	3.03	-27	45	3
PFC_R	660	2.28	33	36	0
Caudate_L	660	3.27	0	0	9
Caudate_R	660	2.49	24	27	3
PFC_R	36	2.03	-54	21	27

Regions were automatically labeled using the Anatomy Toolbox atlas.x,y, and$z$ = Montreal Neurological Institute (MNI) coordinate in the left-right, anterior-posterior, and inferior-superior dimensions, respectively. Results were filtered with a cluster-forming threshold of$p < 0.05$and a cluster-wise minimum cluster size of$k \geq 30$.

4. Discussion

This study surveyed the neurophysiological responses of the frequent jogging group using classic GNG paradigms. The exercise group has shown more robust activation of areas like the putamen, thalamus, lingual, fusiform, PFC, and caudate within the perceptive stage than the control group, whereas during the next inhibitory control stage, most of the areas mentioned above of the exercise group have shown augmented inhibitory response compared to the control group. The enhanced responses involved not only activation but also deactivation. Such effects of the temporal dynamic neural network patterns might closely relate to specific functional plasticity shaped by the regular exercise. The two cognitive benefits of increased attention capacity and inhibitory control are focused on being discussed below.

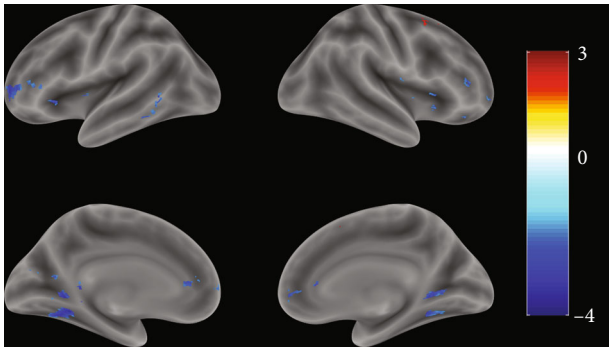

Figure 2: Full view of the brain response differences between the exercise and control groups after visual stimuli (t-value map). The color bar on the right side indicates the brain activity level.

Table 3: The contrast responses with inhibitory control between exercise and control groups.

Labels	Clusters	t	MNI		
			x	y	z
Frontal_Sup_R	30	2.40	15	15	51
Temporal_Mid_L	31	-2.32	-60	-54	3
Thalamus_L	2472	-2.54	-6	-15	0
Thalamus_R	2472	-2.52	10	-6	9
Putamen_L	2472	-2.72	-30	6	-6
Putamen_R	2472	-2.92	27	15	-3
Caudate_L	2472	-2.36	-7	9	4
Caudate_R	2472	-2.92	15	34	9
Lingual_L	2472	-3.52	-24	-48	-3
Lingual_R	2472	-2.75	27	-48	-2
PFC_L	2472	-3.02	-27	45	3
PFC_R	2472	-3.06	6	51	1
Cingulum_Ant_L	2472	-2.18	-5	40	8
Cingulum_Ant_R	2472	-2.03	4	42	8

Region labeling and data filtering were the same as in Table 2.

A recent meta-analysis study has demonstrated that physical exercise training leads to changes in functional activation patterns primarily located in the precuneus and associated with frontoparietal, dorsal attention, and default mode networks [18]. Notably, the long-term exercisers have reshaped regions connected with frontoparietal and dorsal attention networks. Our observation is consistent with the previous results. The increased responses of the visual cue-induced reactivity of the exercise group (Table 3) involved mainly the functional networks such as visual information processing (fusiform, lingual gyrus), motivation, and expectation (prefrontal regions). The lateral temporal lobe, including the middle temporal gyrus, has been suggested to consist of the visual association cortex [19]. The visual association cortex has been recently shown to play a role in forming associative memories [20]. Hence, consistent with previous studies of exercise, brain, attention, learning, and memory areas have been reported for cue reactivity, and associative learning plays a significant role in motion maintenance. The enhanced fMRI BOLD response in the functional areas' dopaminergic neuron activity in regions of the frontal cortex (FC) is postulated to be involved in conditioning for reward expectancy from sensory cues [21, 22].

Additionally, PFC, connecting neuroanatomically with limbic structures, is believed to be more responsible for reward expectancy's emotional and motivational features [23]. As expected, the enhanced activation of PFC in our study suggested that the exercise group is more sensitive and attentive with visual stimuli, and consequently, the motivational networks are overexcited. PFC is considered engaged with memory and reward expectancy by evaluating and integrating sensory input and affective information [24–26], leading to goal-directed action [27]. Hence, our observation supported the hypothesis that the enhanced activation of PFC indicates that the exercise subjects were more sensitive and attentive to the visual stimuli.

During the following inhibition control process (NoGo > Go), the exercise group showed significant deactivation in the left and right thalamus, putamen, caudate, lingual, PFC, and anterior cingulum (Table 3). Almost the same brain areas, which have been involved in overexcitation (more positive) at the perception stage (receiving the visual image), have been switched to more substantial inhibitory control (more negative) for the following decisive process (Go or No Go). Such activity may imply stronger activity of the brain for inhibitory control in the exercise group. Previous literature has shown that inhibitory control is a crucial component common to executive functions [28]. On one side, the development of inhibitory control with the children has a massive impact on their academic achievement [29, 30] and mental health [31]. On the other side, poor inhibitory control predicts risky addictive behaviors. For example, a study of the Internet gaming disorder group has shown more impulsivity and lower activity of the right Secondary Motor Area (SMA)/pre-SMA compared to the control group [32]. Combining both the aspects of the salience of gambling-related cues and response inhibition, using the GNG task, van Holst et al. [33] showed lower activation of the dorsolateral and anterior cingulate cortex during neural inhibition in individuals with gambling disorder. Ding et al. [34] observed both enhanced and reduced responses in different brain areas with the NoGo task. The subjects with Internet game addiction exhibited hyperactivity during No Go trials in the left superior medial frontal gyrus, right anterior cingulate cortex, right superior/middle frontal gyrus, left inferior parietal lobule, and left precentral gyrus, as well as the left precuneus and left cuneus. Meanwhile, several brain regions exhibited decreased activity, including in the bilateral middle temporal gyrus, bilateral inferior temporal gyrus, and right superior parietal lobule. This hypeactivation might be an impairment in turning off the default mode during No Go trials. Based on the inhibitory control impairment of addictive behavior, some literature has reported that exercise can be effective for addiction treatment [35]. Thus, it is essential to understand the details of the temporal neural dynamic patterns involved in the inhibitory control process, indicating the mechanism of neuroplasticity shaped by exercises.

Although this study was to explore the exercise-brain mechanism with fMRI, there are some limitations. Some more specific experiment paradigms, like selective attention with exercise-related images, may help further to analyze the task-specific attention, reward, and task-related cognitive benefits. In the future, a detailed analysis of the GNG behavior data could be looked at, such as correct and incorrect response ratios and the corresponding brain activities. The stimuli can be replaced with sports pictures instead of classic GNG alphabets. Such modification of experiments can help to observe more specific task-related responses. Moreover, the participants of the exercise are recruited from the jogging club. It could be extended to adopt many other exercisers such as football players and basketball players. The average age of the participants in this study was around the fifties. It would be better to categorize young (below 35, the cognitive function not affected with age) or elders (above 60, the cognitive function most probably affected with age) to extend the understanding of the cognitive development benefits with different age groups.

5. Conclusion

To conclude, the present GNG study has supported our hypothesis and indicated that the temporal dynamic neural network activities, including the increased positive activation and stronger inhibitory control located in the frontal and parietal lobes, exhibit the cognitive benefits of regular joggers.

Data Availability

The fMRI data used to support the findings of this study are available from the corresponding author upon request.

Disclosure

The authors declare that the results of the study are presented clearly, honestly, and without fabrication, falsification, or inappropriate data manipulation.

Conflicts of Interest

The authors declare no conflicts of interest.

Authors' Contributions

QD, YL, and PL designed the experiment. QD, JD, LH, QL, HZ, ZQ, WS, and XY performed the experiments and analyzed the data together with PL. FD, JC, and PL wrote the manuscript. All authors approved the final paper.

Acknowledgments

This work has been supported by the National Key R&D Program of China (2021YFF0306500), National Natural Science Foundation of China (61703058), Guidance Project of Suzhou Municipal Science and Technology Bureau (SYSD2018014), and Project of Changshu Science and Technology Bureau (CS201807).

References

[1] S. J. Colcombe, A. F. Kramer, E. McAuley, K. I. Erickson, and P. Scalf, "Neurocognitive aging and cardiovascular Fitness: Recent Findings and Future Directions," *Journal of Molecular Neuroscience*, vol. 24, no. 1, pp. 009–014, 2004.

[2] H. L. Hawkins, A. F. Kramer, and D. Capaldi, "Aging, exercise, and attention," *Psychology and Aging*, vol. 7, no. 4, pp. 643–653, 1992.

[3] K. I. Erickson, D. L. Miller, and K. A. Roecklein, "The aging hippocampus: interactions between exercise, depression, and BDNF," *The Neuroscientist*, vol. 18, no. 1, pp. 82–97, 2012.

[4] A. M. Weinstein, M. W. Voss, R. S. Prakash et al., "The association between aerobic fitness and executive function is mediated by prefrontal cortex volume," *Brain, Behavior, and Immunity*, vol. 26, no. 5, pp. 811–819, 2012.

[5] M. W. Voss, "Chapter 9- the chronic exercise–cognition interaction: fMRI research," in *Exercise-Cognition Interaction*, T. McMorris, Ed., pp. 187–209, Academic Press, San Diego, 2016.

[6] G. E. Giles, J. A. Cantelon, M. D. Eddy et al., "Habitual exercise is associated with cognitive control and cognitive reappraisal success," *Experimental Brain Research*, vol. 235, no. 12, pp. 3785–3797, 2017.

[7] X. Libin, "Event-related potentials analysis on table tennis athletes' perceptually judging service types in the "Go/NoGo" task," *Journal of Tianjin University of Sport*, vol. 34, no. 3, pp. 250–255, 2019.

[8] S. Enriquez-Geppert, C. Konrad, C. Pantev, and R. J. Huster, "Conflict and inhibition differentially affect the N200/P300 complex in a combined Go/NoGo and stop-signal task," *NeuroImage*, vol. 51, no. 2, pp. 877–887, 2010.

[9] S. Hanslmayr, B. Pastötter, K. H. Bäuml, S. Gruber, M. Wimber, and W. Klimesch, "The electrophysiological dynamics of interference during the Stroop task," *Journal of Cognitive Neuroscience*, vol. 20, no. 2, pp. 215–225, 2008.

[10] M. J. Larson, P. E. Clayson, and A. Clawson, "Making sense of all the conflict: a theoretical review and critique of conflict-related ERPs," *International Journal of Psychophysiology*, vol. 93, no. 3, pp. 283–297, 2014.

[11] J. R. Folstein and C. Van Petten, "Influence of cognitive control and mismatch on the N2 component of the ERP: a review," *Psychophysiology*, vol. 45, no. 1, pp. 152–170, 2008.

[12] L. Pires, J. Leitão, C. Guerrini, and M. R. Simões, "Event-related brain potentials in the study of inhibition: cognitive control, source localization and age-related modulations," *Neuropsychology Review*, vol. 24, no. 4, pp. 461–490, 2014.

[13] T. Riggins and L. S. Scott, "P300 development from infancy to adolescence," *Psychophysiology*, vol. 57, no. 7, article e13346, 2020.

[14] J. Polich, "Updating P300: an integrative theory of P3a and P3b," *Clinical Neurophysiology*, vol. 118, no. 10, pp. 2128–2148, 2007.

[15] T. E. Nichols and A. P. Holmes, "Nonparametric permutation tests for functional neuroimaging: a primer with examples," *Human Brain Mapping*, vol. 15, no. 1, pp. 1–25, 2002.

[16] C. G. Yan, X. D. Wang, X. N. Zuo, and Y. F. Zang, "DPABI: data processing & analysis for (resting-state) brain imaging," *Neuroinformatics*, vol. 14, no. 3, pp. 339–351, 2016.

[17] E. T. Rolls, M. Joliot, and N. Tzourio-Mazoyer, "Implementation of a new parcellation of the orbitofrontal cortex in the

Hindawi
Neural Plasticity
Volume 2021, Article ID 4762027, 10 pages
https://doi.org/10.1155/2021/4762027

Research Article

Levodopa Challenge Test Predicts STN-DBS Outcomes in Various Parkinson's Disease Motor Subtypes: A More Accurate Judgment

Zijian Zheng,[1,2] Zixiao Yin,[1,3] Bohan Zhang,[1,4] Houyou Fan,[1,3] Dan Liu,[1] Yuancheng Zhou,[1,2] Jian Duan,[1] Dongwei Zhou,[1] Xi Wu,[5] and Guohui Lu[1]

[1]*Department of Neurosurgery, The First Affiliated Hospital of Nanchang University, Nanchang, Jiangxi, China*
[2]*The First Clinical Medical College of Nanchang University, Nanchang, Jiangxi, China*
[3]*Department of Neurosurgery, Beijing Tiantan Hospital, Capital Medical University, Beijing, China*
[4]*Department of Neurology, Qilu Hospital, Shandong University, Jinan, Shandong, China*
[5]*Department of Neurosurgery, Changhai Hospital of the Second Military Medical University of Chinese PLA, Shanghai, China*

Correspondence should be addressed to Xi Wu; wuxi_smmu@sina.com and Guohui Lu; guohui-lu@163.com

Received 29 June 2021; Revised 1 August 2021; Accepted 16 August 2021; Published 21 October 2021

Academic Editor: Fushun Wang

Background. The relationship between the levodopa challenge test (LDCT) and postoperative subthalamic nucleus-deep brain stimulation (STN-DBS) benefits is controversial in patients with Parkinson's disease (PD). We aim to evaluate the value of total levodopa response (TLR) and symptom levodopa response (SLR) in predicting postoperative improvement in different PD motor subtypes. *Methods*. Studies were split into a training set (147 patients) and a validation set (304 patients). We retrospectively collected data from 147 patients who received the Unified Parkinson's Disease Rating Scale- (UPDRS-) III and the Parkinson's Disease Questionnaire- (PDQ-) 39 evaluation. Patients were classified into tremor-dominant (TD), akinetic-rigid-dominant (AR), and mixed (MX) groups. Clinically important difference (CID) was employed to dichotomize DBS effects. For patients in each subtype group from the training set, we used the correlation and receiver operator characteristic (ROC) curve analyses to explore the strength of their relations. Areas under the curve (AUCs) were calculated and compared through the DeLong test. Results developed from the training set were applied into the validation set to predict postoperative improvement in different PD motor subtypes. *Results*. In the validation cohort, TLR significantly correlated with postoperative motor ($p < 0.001$) and quality of life (QOL) ($p < 0.001$) improvement in the MX group. The AUC between TLR and UPDRS-III (TU) is 0.800. The AUC between TLR and PDQ-39 (TP) is 0.770. An associated criterion in both TU and TP is around 50%. In the AR group, strong correlation was only found in SLR and PDQ-39 (SP) ($p < 0.001$). And the AUC of SP is significantly larger than that in TLR and PDQ-39 (TP) ($p = 0.034$). An associated criterion in SP is around 37%. No significant correlation was found in the TD group. *Conclusions*. We provide a more accurate judgment for LDCT. TLR strongly correlated with postoperative UPDRS-III and PDQ-39 improvement in MX patients. A TLR > 50% may indicate a higher possibility of clinically meaningful benefits from STN-DBS comparing to medication only. SLR can well predict QOL improvement in AR patients. Similarly, a SLR > 37% may indicate a higher possibility of clinically significant benefits from STN-DBS. LDCT provides limited information for TD patients.

1. Introduction

Parkinson's disease (PD) is a neurodegenerative disease with two main therapies of levodopa and deep brain stimulation (DBS). Typically, an acute levodopa challenge test (LDCT) is conducted before DBS surgery to screen potential beneficiaries. Levodopa response (LR) assessed by the Unified Parkinson's Disease Rating Scale- (UPDRS-) III has been regarded as the best outcome predictor for postoperative response to DBS [1]. The relation between the preoperative LR and postoperative DBS benefits has long been disputed [2]. Some authors found that the preoperative LR is a key predictor for outcomes of bilateral STN-DBS for advanced PD [3, 4], while others indicated that the significant

correlations are only the result of statistical methods and primary assumptions [5]. There are reports that patients who do not have a 30%-or-greater LR do obtain satisfactory improvements after DBS surgery [6, 7]. The mismatch between levodopa and DBS responses can be more commonly observed in single-symptom-dominated (SSD) patients, such as tremor-dominated patients or rigidity-dominated patients [8]. For those patients, the effect of levodopa on the total UPDRS score can be less informative than that on particular symptoms [9]. The LR toward particular symptoms calculated by UPDRS subitems, which we termed as "symptom levodopa response (SLR)" to distinguish from total levodopa response (TLR), might better predict STN-DBS efficiency in a certain group of patients. We employed both the receiver operating characteristic (ROC) curve analysis and correlation analysis to explore the predictive value of LDCT in different PD motor subtypes. In addition, since single-center outcomes may not be well generalized to a large population, we further validated our results in an external validation set to enhance the credibility of the findings.

2. Material and Methods

2.1. Patients. We reviewed the electronic medical records of all PD patients who received bilateral STN-DBS between June 1, 2015, and June 1, 2019, in the First Affiliated Hospital of Nanchang University. Patients with complete baseline and 3-month follow-up data were included. The diagnosis of PD was in accordance with the United Kingdom PD Society Brain Bank Diagnostic Criteria [10]. Sex, age, age at onset, disease duration, duration of motor fluctuations, and medication were recorded by inquiring the case history. Hoehn-Yahr stage, UPDRS, PDQ-39, Hamilton depression rating scale (HAMD), and Hamilton anxiety rating scale (HAMA) values were assessed for all included patients under the guidance of movement disorder specialists. The ethics committee of the First Affiliated Hospital of Nanchang University approved the study protocol, and all patients or their families provided written informed consent.

2.2. Subtype Classification. Two methods were commonly used to classify PD patients. Jankovic et al. [11] divided patients into tremor-dominant (TD), postural instability and gait difficulty, and intermediate motor subtypes, and Lewis [12] divided patients into TD, akinetic-rigid-dominant (AR), and mixed (MX) motor subtypes. We adopted Lewis' method and did not choose Jankovic's method because UPDRS-II was involved in Jankovic's classification process, which will cause problems to the calculation of SLR since UPDRS-II was not included in the LDCT. To divide the patients into various subtype groups, we calculated a tremor score (TS) and an akinetic-rigid score (ARS) for each patient in line with the methods previously reported. The TS was defined as the mean value of the sum of UPDRS items 20 and 21. The SLR of TS is calculated according to UPDRS items 20 and 21. The ARS was defined as the mean value of the sum of UPDRS items 18, 19, 22, and 27-31; therefore, the SLR of ARS is calculated according to UPDRS items 18, 19, 22, and 27-31. A patient was classified as TD if his or her TS/ARS ≥ 2. Conversely, a patient was classified as AR if his or her TS/ARS ≤ 0.5. The remaining patients, with a TS/ARS between 0.5 and 2, were classified as MX type. The classification was conducted based on the UPDRS off-medication score.

2.3. Patient Management and Follow-Up. After eliminating contraindications and signing the informed consent, all patients received LDCT and STN-DBS. Levodopa, compound levodopa, and other anti-Parkinson's drugs were stopped 12 hours before the test, and dopaminergic receptor agonists were stopped 72 hours before the test. Patients were administered 1.5 times the levodopa equivalent dose of the first dose they take every morning, and the test drug is standard compound levodopa. The electrode implantation was operated as follows. A stereotactic head frame was installed before CT scanning, and the CT imaging was fused with MRI to locate the STN. The surgical path was determined by a surgical planning workstation. Craniotomy was performed under local anesthesia, and the DBS devices (Medtronic 3387/3389 or PINS 1101) were implanted after target refinement by microelectrode recording and intraoperative test stimulation. Implantable pulse generators were then placed in the subclavicular position under general anesthesia. The DBS devices were programmed one month after the surgery. The patients accepted a postoperative programming with little difference. The stimulation effect was measured 3 months after surgery by the UPDRS-III and PDQ-39. The improvement of motor symptoms was calculated in both the on-medication/on-stimulation state and the off-medication/on-stimulation state. Regarding improvements of quality of life (QOL), we did not distinguish between on-medication and off-medication because the PDQ-39 reflects the QOL in the past month.

2.4. Dichotomize STN-DBS Effects. To better explore the predictive value of LDCT on patient's postoperative states, we divided patients into marked-improved ones and fair-improved ones. For motor improvement, we employed minimal clinically important difference (MICID) based on UPDRS-III to determine whether a patient got clinically meaningful improvement after surgery. MICID was established in approximately 6 points for detecting minimal, but clinically pertinent, improvement for UPDRS-III [13]. Since on-medications and on-stimulation can best represent the patient's postoperative state, an at-least-six-point difference in the comparison of baseline UPDRS-III on-medications and postoperative UPDRS-III on-medications and on-stimulation indicated the patient improved markedly. Since PDQ-39 scores reflect the overall QOL in both on- and off-medication states, the calculated score difference would overestimate the real improvement between preoperative-on-state and postoperative-on-state. Thus, we employed a stricter criterion for detecting clinically substantial changes. Moderate clinically important difference (MOCID) was established as approximately 3.5 points, around two times of MICID in PDQ-39 [14]. Patients reached an at-least-four-point difference in PDQ-39 after surgery was regarded as marked-improved patients.

2.5. External Validation Set. Results developed from the training set were validated in an external validation set for further evaluation. 304 PD patients who received the levodopa challenge test before STN-DBS in the Changhai Hospital Affiliated to Navy Medical University were included as a validation set. We viewed the baseline and the 3-month follow-up data of the PD patients who underwent STN-DBS surgery and employed the aforementioned method to divide these patients into TD, AR, and MX motor subtypes. Patients were divided into marked-improved ones and fair-improved ones in a similar way as described in the training set.

2.6. Statistical Analysis. Continuous data were presented as the mean ± SD. Comparison among the three groups was conducted by one-way ANOVA. Pairwise comparisons were conducted by the Bonferroni test. ROC curve was normally employed in the diagnosis test, but its application is not limited to diagnostic analysis. Authors have used it to explore the correlation between patient satisfactory and scale scores [15, 16]. ROC curve can better demonstrate the strength of correlation and visualize outcomes. In our study, we employed both ROC curve analysis and correlation analysis in the training set and the validation set. The areas under the curve (AUCs) show how well the classifier can distinguish marked-improved patients from fair-improved ones. Besides, the DeLong test made it possible to compare the strength of correlation. Pearson's correlation was employed to calculate the correlation coefficient. A scatter plot with a fit line and 95% CI was shown. The result of the ROC curve analysis was presented as AUC (95% CI). An AUC > 0.75 indicates the classifier provides clinically meaningful discriminative ability [17]. The Youden indexes and associated LDCT criteria were reported only in ROC curves with an AUC > 0.75. The DeLong tests were performed to compare different AUCs. A 2-tailed p value of 0.05 was considered statistically significant for the comparisons. All statistical procedures were performed using MedCalc version 15.2 (MedCalc, Ostend, Belgium) and SPSS version 24 (IBM, Chicago, IL).

3. Results

3.1. Baseline Characteristics and Patient Improvement. Data from the preoperative assessments and postoperative follow-ups in the training set are shown in Table 1. Of the preoperative indices, age at onset, duration of motor fluctuation, Hoehn-Yahr stage, UPDRS-III off scores, LR for akinetic-rigid score, LEDD, PDQ-39, and HAMA scores were significantly different between the three groups. For postoperative indices, the UPDRS-III and PDQ-39 scores assessed 3 months after the surgery were significantly different between the three groups. Overall, patients in the AR group have longer disease duration and worse baseline conditions. Fifty-eight patients reached MICID in comparing the baseline UPDRS-III on-medications and the postoperative UPDRS-III on-medications and on-stimulation. Seventy-six patients reached MOCID in comparing the baseline PDQ-39 on-medications and the postoperative PDQ-39 on-medications and on-stimulation. Related data from the preoperative assessments and postoperative follow-ups in the validation set are shown in Table 2.

3.2. The Relationship of LDCT and STN-DBS Benefits in the Training Set Patients. The ROC curves and scatter plots between preoperative LR and postoperative UPDRS-III and PDQ-39 improvement are shown in Figure 1. The AUC of LDCT in differentiating significant and insignificant motor beneficiaries is 0.769 according to UPDRS-III improvement. The AUC of LDCT in differentiating significant and insignificant QOL beneficiaries is 0.757 according to PDQ-39 improvement. The Youden indexes and their associated criteria are shown in the figure. Postoperative score changes of both UPDRS-III ($p = 0.015$) and PDQ-39 ($p < 0.001$) significantly correlate with preoperative levodopa response.

3.3. The Relationship of LDCT and STN-DBS Benefits in Different PD Subtypes. For the sake of clarity in the reporting, we used acronyms to represent the various classification and correlation combinations. TU represented the combination of TLR and UPDRS-III, and SP represented the combination of SLR and PDQ-39. Similarly, TP represented the combination of TLR and PDQ-39, and SU represented the combination of SLR and UPDRS-III.

3.3.1. Classification Performance of SLR and TLR. The ROC curves of different classification combinations are shown in Figure 2. No statistical difference was found between SLR and TLR in the TD group, while the AUC of SP is significantly larger than that of TP in the AR group ($p = 0.029$). In the MX group, the ROC of both TU (0.816) and TP (0.802) is above 0.8. The Youden indexes and associated LDCT criteria were reported if the AUC is above 0.75. For SP in the AR group, the Youden index is 0.75, and the associated criterion is 32%. For TU and TP in the MX group, the Youden index is 0.54 and 0.57, and the associated criterion is 50% and 53%.

3.3.2. Correlation Performance of SLR and TLR. The scatter plots of different correlation combinations are shown in Figure 2. SLR positively correlated with both UPDRS-III ($p = 0.035$) and PDQ-39 ($p < 0.001$) improvement in the AR group. TLR positively correlated with both UPDRS-III ($p < 0.001$) and PDQ-39 ($p < 0.001$) improvement in the MX group. We found no significant correlation in the TD group.

3.4. Evaluation in the Validation Set. ROC curves of different classification combinations are shown in Figure 3. In the MX group, the AUC of LDCT in TU is 0.800 with a Youden index of 0.52 and associated criterion of 48%. The AUC of LDCT in TP is 0.770 with a Youden index of 0.59 and associated criterion of 49%. In the AR group, the AUC of LDCT in SP is 0.844 with a Youden index of 0.66 and associated criterion of 37%.

Table 1: Comparison of baseline and postoperative indices among the three subtype groups in the training set.

	Total ($n = 147$)	TD ($n = 24$)	AR ($n = 46$)	MX ($n = 77$)	ANOVA*	TD vs. AR*	TD vs. MX*	AR vs. MX*
Sex (male/female)	87/60	10/14	29/17	48/29				
Reach MICID in UPDRS-III (n)	58 (39.5%)	11 (45.8%)	18 (39.1%)	29 (37.7%)				
Reach MOCID in PDQ-39 (n)	76 (51.7%)	10 (41.7%)	26 (56.5%)	40 (51.9%)				
Age at surgery (years)	62.3 ± 9.6	65.5 ± 6.8	59.9 ± 11.1	62.7 ± 9.1	0.053			
Age at onset (years)	52.8 ± 9.4	56.9 ± 6.5	49.9 ± 10.2	53.3 ± 9.3	**0.009**	**0.008**	0.295	0.131
DD (years)	9.5 ± 2.7	8.6 ± 1.6	10.0 ± 2.7	9.4 ± 2.8	0.106			
Duration of MF (years)	5.2 ± 2.8	3.7 ± 1.9	6.4 ± 2.8	5.1 ± 2.7	**<0.001**	**<0.001**	0.088	**0.030**
H-Y on	2.2 ± 0.8	1.8 ± 0.9	2.4 ± 0.9	2.1 ± 0.8	**0.007**	**0.005**	0.128	0.239
H-Y off	3.2 ± 1.1	2.7 ± 1.3	3.4 ± 0.9	3.2 ± 1.1	**0.049**	**0.043**	0.219	0.843
UPDRS-III on	17.8 ± 6.1	17.0 ± 5.8	19.4 ± 7.0	17.0 ± 5.5	0.102			
UPDRS-III off	37.9 ± 15.2	32.7 ± 12.4	42.3 ± 15.5	37.0 ± 15.2	**0.030**	0.381	1.000	0.126
LR for UPDRS-III (%)	49.4 ± 15.5	45.5 ± 13.1	51.7 ± 13.1	49.3 ± 15.6	0.230			
LR for tremor score (%)	77.1 ± 17.9	72.2 ± 13.2	74.9 ± 16.9	80.0 ± 19.4	0.107			
LR for akinetic-rigid score (%)	42.1 ± 18.7	25.1 ± 21.3	44.1 ± 18.6	46.3 ± 14.8	**<0.001**	**<0.001**	**<0.001**	1.000
LEDD	987 ± 306	915.6 ± 356.2	1089.7 ± 297.3	949.3 ± 283.4	**0.021**	0.068	1.000	**0.040**
PDQ-39	35.8 ± 11.6	28.3 ± 9.7	39.9 ± 11.9	35.7 ± 10.9	**<0.001**	**<0.001**	**0.014**	0.135
HAMD	12.7 ± 3.6	12.4 ± 2.9	13.3 ± 3.7	13.8 ± 2.6	0.150			
HAMA	11.9 ± 3.4	11.6 ± 2.9	13.4 ± 2.9	12.5 ± 2.6	**0.025**	**0.027**	0.527	0.187
Post UPDRS-III on	14.7 ± 6.8	12.5 ± 4.4	17.6 ± 8.2	13.7 ± 6.0	**0.002**	**0.007**	1.000	**0.006**
Post UPDRS-III off	19.9 ± 8.7	16.7 ± 5.7	23.4 ± 10.3	18.8 ± 7.8	**0.002**	**0.005**	0.813	**0.012**
Post PDQ-39	31.6 ± 9.8	24.8 ± 7.9	35.2 ± 10.1	31.6 ± 9.2	**<0.001**	**<0.001**	**0.006**	0.120

TD: tremor-dominated patients; AR: akinetic-rigid-dominated patients; MX: mixed patients; MICID: minimal clinically important difference; MOCID: moderate clinically important difference; DD: duration of diagnosis; MF: motor fluctuation; H-Y: Hoehn-Yahr stage; UPDRS: Unified Parkinson's Disease Rating Scale; LR: levodopa response; LEDD: levodopa equivalent doses; PDQ-39: Parkinson's Disease Questionnaire-39; HAMD: Hamilton depression scale; HAMA: Hamilton anxiety scale; Post: postoperative; Post UPDRS-III on: on-stimulation/on-medicine; Post UPDRS-III off: on-stimulation/off-medicine. *p value. Significant comparisons are highlighted in bold.

4. Discussion

This study discussed the value of LDCT in predicting STN-DBS benefits in different PD motor subtypes and evaluated the findings in an external validation set. We found that on-state improvement is predictable by TLR, especially in MX patients. SLR strongly correlated with postoperative QOL improvement in AR patients. LDCT showed no significant predictive value in TD patients.

We employed both the methods of Pearson's correlation and the ROC curve to explore the relationship between LDCT and STN-DBS benefits. Pearson's correlation focused on detecting the consistency of two continuous variables while this method can only detect linearly correlated relations and is highly vulnerable to outliers [18]. Laying emphasis on exploring the predictive effect of continuous variables on binary variables, ROC curve analysis can alleviate the influence of outliers and can also show the strength of relation between two variables. Dichotomizing outcome variable according to research objective can endow associated ROC curve with different clinical significance. The construction of ROC curve is based on the classifier's sensitivity and specificity, which are both incidence measures, the percent or ratio of those patients who exceed a cutoff compared to those that did not reach cutoff. Consequently, establishment of the cutoff is very important. In our study, clinically important difference (CID) was used to differentiate marked-improved patients and fair-improved patients. CID has been widely employed in large clinical trial to reflect clinically meaning change [19]. Only around 40% and 50% of samples reached CID in UPDRS-III and PDQ-39 in our study, respectively. This is quite different from the ratio of 70% obtained by Katz et al. [20]. Possible reasons could be that we calculated on-state improvement while they calculated off-state improvement. The comparison between baseline UPDRS-III on-medications and postoperative UPDRS-III on-medications and on-stimulation better shows patients' overall improvement over medical treatment alone. This comparison is more clinically relevant to patients since this reflects the state that the patient is most likely to be in. Off-state comparison would be more helpful when only the stimulation effect is of interest.

The LDCT is commonly regarded as an important referee for predicting DBS effects. It helps to the diagnosis of PD, and typically, DBS response is more robust for the levodopa-responsive symptoms [21]. In the literature,

Table 2: Comparison of baseline and postoperative indices among the three subtype groups in the validation set.

	Total ($n = 304$)	TD ($n = 80$)	AR ($n = 67$)	MX ($n = 157$)	ANOVA*	TD vs. AR*	TD vs. MX*	AR vs. MX*
Sex (male/female)	157/147	43/37	32/35	82/75				
Reach MICID in UPDRS-III (n)	145 (47.7%)	35 (43.8%)	45 (67.1%)	65 (41.4%)				
Reach MOCID in PDQ-39 (n)	76 (51.7%)	41 (41.7%)	32 (47.8%)	82 (52.2%)				
Age at surgery (years)	60.7 ± 7.6	63.5 ± 5.7	61.2 ± 10.7	60.8 ± 7.3	0.178			
Age at onset (years)	55.4 ± 6.4	52.9 ± 5.5	48.3 ± 7.2	50.3 ± 5.5	**0.003**	**<0.001**	0.178	0.232
DD (years)	8.5 ± 2.4	8.6 ± 1.8	9.1 ± 1.5	7.8 ± 3.4	0.235			
Duration of MF (years)	6.2 ± 2.1	3.5 ± 2.1	7.3 ± 3.1	4.3 ± 2.0	**<0.001**	**<0.001**	0.234	**0.015**
H-Y on	1.8 ± 1.0	2.3 ± 0.9	1.7 ± 1.0	3.5 ± 0.4	**0.012**	**0.123**	0.228	**0.022**
H-Y off	4.2 ± 1.1	3.3 ± 1.8	3.1 ± 1.1	3.3 ± 1.5	0.172	0.243	0.919	0.843
UPDRS-III on	19.3 ± 7.1	18.0 ± 4.8	17.4 ± 6.0	18..0 ± 5.7	0.202			
UPDRS-III off	36.6 ± 14.8	33.5 ± 11.3	41.3 ± 14.6	38.6 ± 17.3	**0.043**	0.381	1.000	0.126
LR for UPDRS-III (%)	50.2 ± 13.5	47.3 ± 12.8	51.3 ± 12.1	53.3 ± 13.8	0.371			
LR for tremor score (%)	75.2 ± 16.9	74.9 ± 11.8	75.4 ± 15.2	79.0 ± 20.1	0.207			
LR for akinetic-rigid score (%)	41.5 ± 17.7	24.9 ± 20.7	43.2 ± 16.6	45.4 ± 13.9	**<0.001**	**<0.001**	**<0.001**	0.945
LEDD	955 ± 321	873.3 ± 342.2	989.7 ± 286.3	903.3 ± 222.4	**0.015**	0.023	0.847	**0.030**
PDQ-39	34.7 ± 10.6	29.3 ± 7.7	37.5 ± 12.9	34.4 ± 8.9	**<0.001**	**<0.001**	**0.026**	0.365
HAMD	10.7 ± 3.6	11.4 ± 3.9	12.3 ± 3.3	12.8 ± 3.6	0.333			
HAMA	9.9 ± 2.7	10.3 ± 1.9	12.4 ± 1.9	11.5 ± 1.7	**0.013**	**0.019**	0.433	0.636
Post UPDRS-III on	13.5 ± 7.8	11.1 ± 5.4	16.6 ± 8.2	12.5 ± 5.0	**0.003**	**0.002**	0.936	**0.012**
Post UPDRS-III off	18.5 ± 7.7	14.7 ± 5.7	21.2 ± 9.3	16.3 ± 6.9	**0.002**	**<0.001**	0.623	**0.008**
Post PDQ-39	30.3 ± 8.9	25.2 ± 7.3	34.3 ± 8.1	28.9 ± 7.3	**<0.001**	**<0.001**	**0.023**	0.078

TD: tremor-dominated patients; AR: akinetic-rigid-dominated patients; MX: mixed patients; MICID: minimal clinically important difference; MOCID: moderate clinically important difference; DD: duration of diagnosis; MF: motor fluctuation; H-Y: Hoehn-Yahr stage; UPDRS: Unified Parkinson's Disease Rating Scale; LR: levodopa response; LEDD: levodopa equivalent doses; PDQ-39: Parkinson's Disease Questionnaire-39; HAMD: Hamilton depression scale; HAMA: Hamilton anxiety scale; Post: postoperative; Post UPDRS-III on: on-stimulation/on-medicine; Post UPDRS-III off: on-stimulation/off-medicine. *p value. Significant comparisons are highlighted in bold.

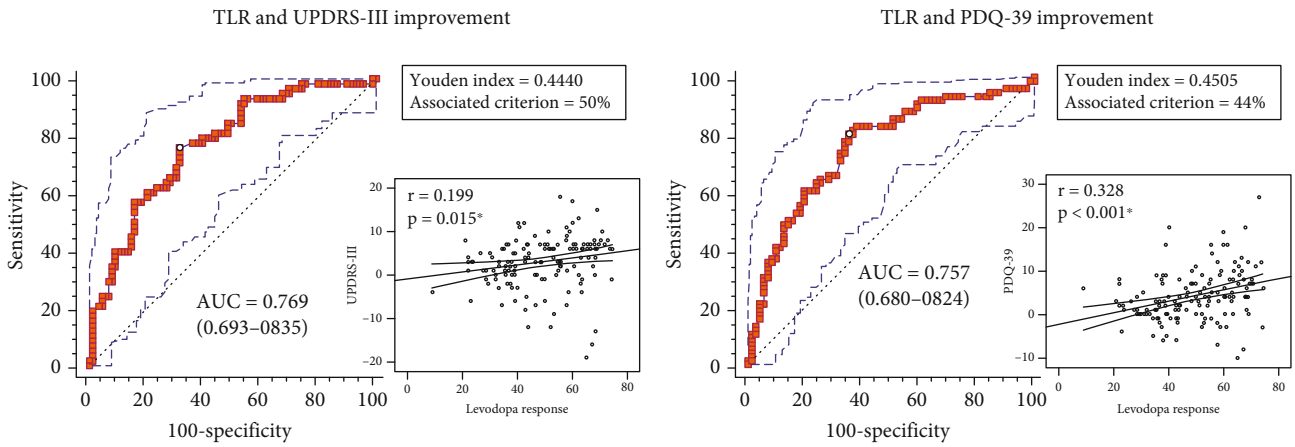

Figure 1: The receiver operating characteristic curves and scatter plots between TLR and postoperative STN-DBS benefits in the training set. (a) The combination of TLR and UPDRS-III improvement. (b) The combination of TLR and PDQ-39 improvement. Significant correlations are highlighted in bold and marked by ∗.

several publications argued that preoperative LR does not predict long-term STN-DBS outcomes, but there are also reports claiming the contrary [2, 4]. In our study, in both the analysis in the training set and the validation set, the ROC curve showed that the predictive ability of LDCT on STN-DBS effects was not very solid since the AUCs were just over 0.75, despite the significant correlation being observed. However, the predictive ability increased a lot in the MX

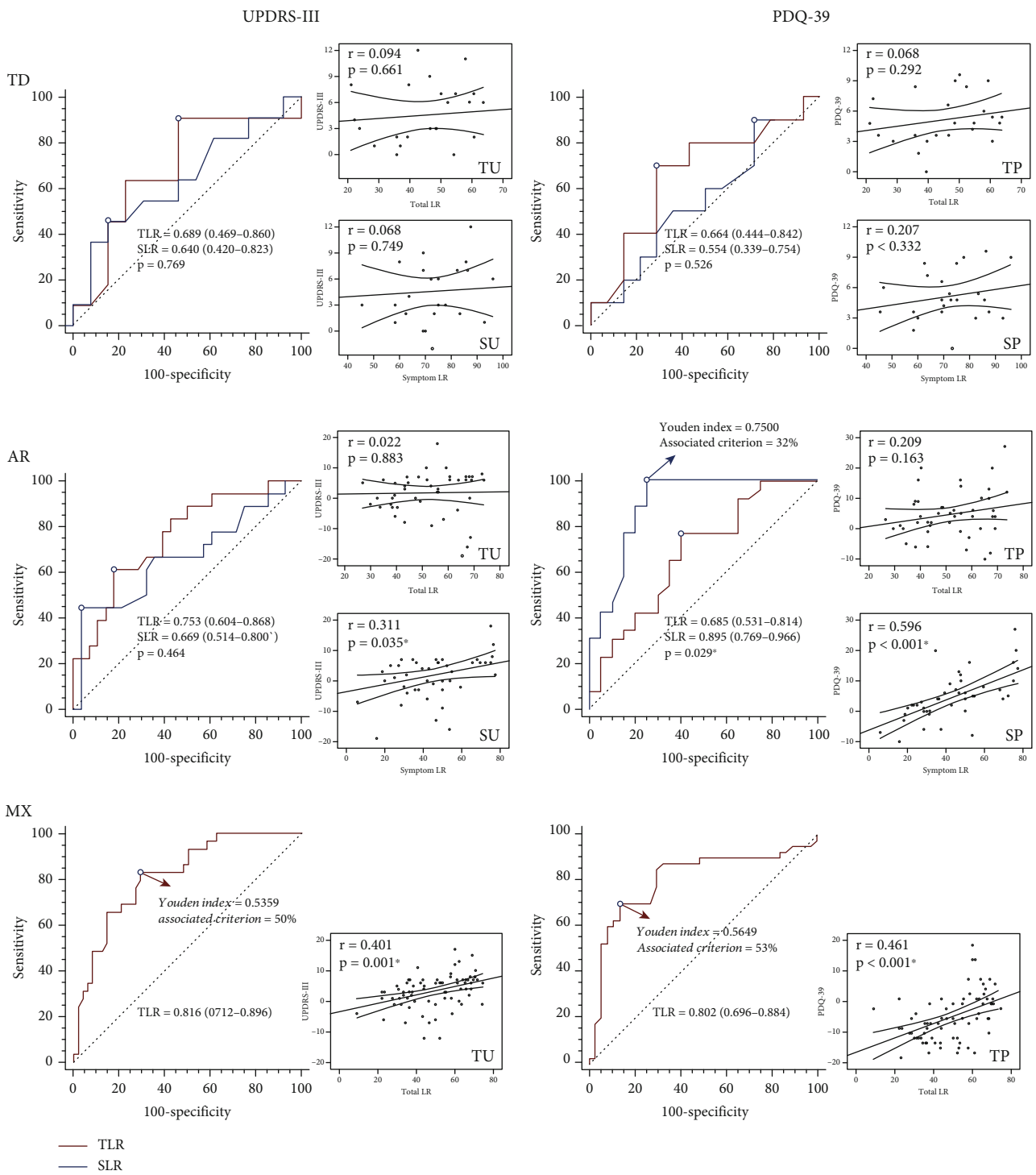

Figure 2: The receiver operating characteristic curves and scatter plots between TLR or SLR and postoperative STN-DBS benefits among the three PD motor subtypes in the training set. Significant correlations or comparisons are highlighted in bold and marked by ∗.

group both in the AUC and correlation coefficient r. The AUC of TLR in the MX group was the highest in all three subtypes. Possible reasons could be that the UPDRS-III score is more evenly distributed among all symptoms in the MX group. A uniform distribution could make the percent improvement of UPDRS-III in LDCT reflect the information of levodopa responsiveness more comprehensively. Instead, for SSD patients, the UPDRS-III score was mainly contributed by several subitems related to a certain symptom, while other less severe symptoms also have the same weight when calculating percentage improvement. This could result in that the calculated LR value does not match the real responsiveness to levodopa. Besides, MX patients have moderate baseline UPDRS scores, between that of TD

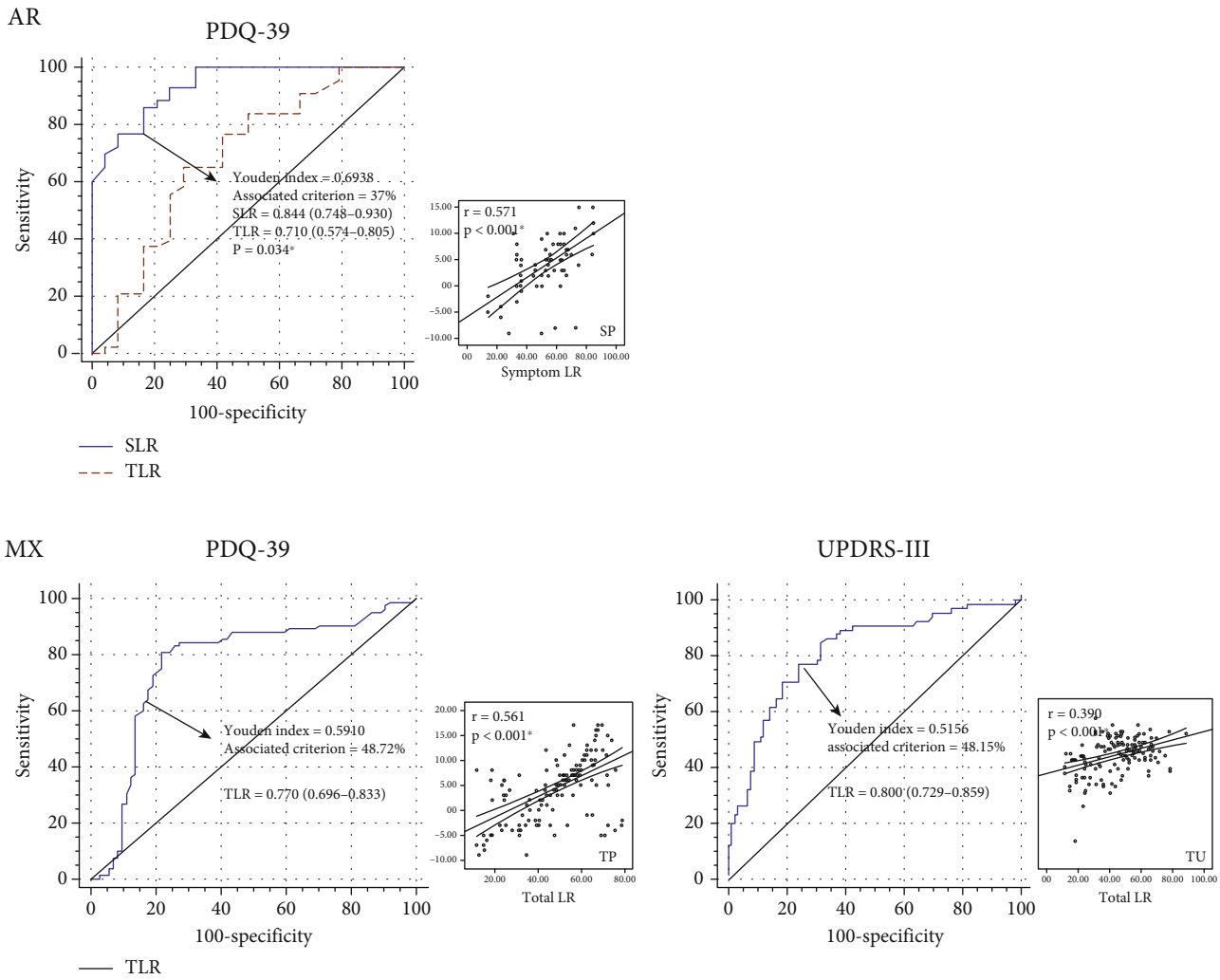

Figure 3: The receiver operating characteristic curves and scatter plots between TLR or SLR and postoperative STN-DBS benefits among the two PD motor subtypes in the validation cohort. Significant correlations or comparisons are highlighted in bold and marked by ∗.

and AR patients. An absence of outliers can also increase the accuracy of prediction. For MX patients, we further found that around 50% LR can predict STN-DBS effects. Approximately, patients with a LR > 50% are highly likely to gain clinically meaningful benefits from STN-DBS comparing to medication only. This is different from the widely accepted 30% LR. Thirty-percent LR is the clinically minimal motor improvement of UPDRS-III after taking a dopaminergic drug, which is aimed at assisting the diagnosis of PD through levodopa responsiveness [22]. However, many patients with LRs exceeding 30% do not get significant benefits from STN-DBS because this value was not originally established to predict DBS effects. In our study, 50% LR could well distinguish marked-improved patients and fair-improved patients only in the MX group. Interestingly, 50% is very close to the average postoperative UPDRS-III improvement reported by a large meta-analysis [23]. The strong correlation between LDCT and postoperative benefits in the MX group could possibly explain this.

As previously mentioned, for SSD patients, only one or two major symptoms are the source of most of their problems and are the target concerns they are most urgently willing to address. To better emphasize on the improvement of these dominated symptoms, we thus introduced the concept of SLR. However, we did not find any significant correlations between SLR or TLR and postoperative motor or QOL improvement in TD patients. The major reason could be that the responsiveness of severe tremor to levodopa therapy is not in accordance with that to the DBS therapy. In contrast, in the AR group, SLR showed strong correlation with PDQ-39 change. And the differentiating ability of SLR was significantly higher than TLR in judging QOL improvement. Regarding why QOL improvements are more predictable in the ARD group by SLR, we suspect the following reasons. First, patient expectation and satisfaction may play an important role here. Some patients may not receive significant benefit on total motor function, but addressing the problems of concern can greatly enhance their satisfaction and QOL score [7, 24]. SLR can accurately reflect improvements in major symptoms without being affected by the less-concerning items in UPDRS-III and thus can be more sensitive in judging a patient's possible QOL change [25].

Second, ARD symptoms, including gait disorder and postural instability, have long been reported as significant influencing factors upon QOL [26]. Gómez-Esteban et al. further indicated that rigidity had more impact on QOL than tremor [27]. The alleviation of annoying and dominant problem can undoubtedly increase patient's life quality. Besides, unlike tremor, which can be resistant to levodopa therapy, rigidity's responses toward levodopa and DBS are more consistent [28]. Third, the ARD patients in our study had the worst baseline conditions and PDQ-39 scores. And it is reported that patients with impaired preoperative QOL are more likely to have better postoperative QOL improvement [29]. For AR patients, we also found that patients with a SLR > 37% are more likely to gain clinically meaningful QOL benefits after STN-DBS. This will give us a reference in predicting postoperative QOL improvement even before the STN-DBS surgery.

Our study has several limitations. First, the data were retrospectively collected, and a relatively small sample size (only 24 patients in the TD group in the training set) could reduce statistical power. But it is generally harder to generate significant differences with a small sample size. Second, the follow-up period was short (3 months), leaving some long-term adverse events unrecognized including depression and progressive cognitive decline, which may also markedly affect QOL. Third, the data sources in our research only come from two single clinical centers, and it is necessary to carry out multicenter clinical research. Future studies should employ a prospective design, increase the sample size, and prolong the follow-up period to further strengthen the evidence, despite that an external verification was conducted in our study which will undoubtedly enhance the credibility of the findings.

5. Conclusion

We provide a more accurate judgment for LDCT. In a short follow-up period of three months, LDCT provides different information to the three PD motor subtypes receiving STN-DBS surgery. For MX patients, TLR is strongly correlated with postoperative motor and QOL improvement. A TLR > 50% may indicate a higher possibility of clinically meaningful benefits from STN-DBS. For AR patients, SLR can well predict postoperative QOL change. A SLR > 37% may indicate a higher possibility of clinically meaningful benefits from STN-DBS. Both TLR and SLR cannot provide valid predictive information for TD patients. These findings should be considered when screening PD-DBS candidates.

Abbreviations

PD: Parkinson's disease
STN-DBS: Subthalamic nucleus-deep brain stimulation
LDCT: Levodopa challenge test
LR: Levodopa response
TLR: Total levodopa response
SLR: Symptom levodopa response
SSD: Single-symptom-dominated
UPDRS: Unified Parkinson's Disease Rating Scale
PDQ-39: Parkinson's Disease Questionnaire-39
HAMD: Hamilton depression rating scale
HAMA: Hamilton anxiety rating scale
QOL: Quality of life
TS: Tremor score
ARS: Akinetic-rigid score
TD: Tremor-dominant
AR: Akinetic-rigid dominant
MX: Mixed
CID: Clinically important difference
MICID: Minimal clinically important difference
MOCID: Moderate clinically important difference
ROC: Receiver operating characteristic
AUC: Area under the curve
TU: TLR~UPDRS-III
TP: TLR~PDQ-39
SU: SLR~UPDRS-III
SP: SLR~PDQ-39.

Data Availability

The relevant valuable data are described in the manuscript.

Additional Points

Highlights. TLR and SLR can predict postoperative improvement in different PD motor subtypes. TLR correlated with postoperative motor and quality of life improvement in the MX group. A TLR > 50% may indicate a higher possibility of clinically meaningful benefits from STN-DBS in the MX group. SLR correlated with postoperative motor and quality of life improvement in AR patients. A SLR > 37% may indicate a higher possibility of clinically meaningful benefits from STN-DBS in AR patients.

Ethical Approval

We confirm that we have read the journal's position on issues involved in ethical publication and affirm that this report is consistent with those guidelines.

Disclosure

The funders were not involved either in the design of the study, collection, analysis and interpretation of the data, and writing of the report or in the decision to submit the article for publication. Every author had full access to all data of the study, and the corresponding author had final responsibility for the decision to submit the article for publication.

Conflicts of Interest

The authors report no conflict of interest concerning the materials or methods used in this study or the findings specified in this paper.

Authors' Contributions

Zijian Zheng, Zixiao Yin, Bohan Zhang, Houyou Fan, and Dan Liu are co-first authors.

Acknowledgments

Research reported in this publication was supported by the National Natural Science Foundation of China (CN) (82060649), the Key Project of Jiangxi Science Foundation (20202ACBL206005), the General Program of Natural Science Foundation of Jiangxi Province (20192BAB205042), and the Science and Technology Plan of Health and Family Planning Commission of Jiangxi Province (20195109) which provided the funds for the research project and participated in the supervision of the research. We would like to acknowledge Dr. Jill Ostrem, Dr. Danilo Romero, and their team in the Department of Neurology, University of California, San Francisco.

References

[1] R. Pahwa, S. B. Wilkinson, J. Overman, and K. E. Lyons, "Preoperative clinical predictors of response to bilateral subthalamic stimulation in patients with Parkinson's disease," *Stereotactic and Functional Neurosurgery*, vol. 83, no. 2-3, pp. 80–83, 2005.

[2] P. Piboolnurak, A. E. Lang, A. M. Lozano et al., "Levodopa response in long-term bilateral subthalamic stimulation for Parkinson's disease," *Movement Disorders*, vol. 22, no. 7, pp. 990–997, 2007.

[3] M. L. Welter, J. L. Houeto, S. Tezenas du Montcel et al., "Clinical predictive factors of subthalamic stimulation in Parkinson's disease," *Brain*, vol. 125, no. 3, pp. 575–583, 2002.

[4] G. Kleiner-Fisman, D. N. Fisman, E. Sime, J. A. Saint-Cyr, A. M. Lozano, and A. E. Lang, "Long-term follow up of bilateral deep brain stimulation of the subthalamic nucleus in patients with advanced Parkinson disease," *Journal of Neurosurgery*, vol. 99, no. 3, pp. 489–495, 2003.

[5] A. Zaidel, H. Bergman, Y. Ritov, and Z. I. Md, "Levodopa and subthalamic deep brain stimulation responses are not congruent," *Movement Disorders*, vol. 25, no. 14, pp. 2379–2386, 2010.

[6] A. Umemura, Y. Oka, K. Ohkita, T. Yamawaki, and K. Yamada, "Effect of subthalamic deep brain stimulation on postural abnormality in Parkinson disease," *Journal of Neurosurgery*, vol. 112, no. 6, pp. 1283–1288, 2010.

[7] T. Morishita, M. Rahman, K. D. Foote et al., "DBS candidates that fall short on a levodopa challenge test: alternative and important indications," *The Neurologist*, vol. 17, no. 5, pp. 263–268, 2011.

[8] M. C. Jiménez and F. J. G. Vingerhoets, "Tremor revisited: treatment of PD tremor," *Parkinsonism & Related Disorders*, vol. 18, pp. S93–S95, 2012.

[9] A. G. Machado, M. Deogaonkar, and S. Cooper, "Deep brain stimulation for movement disorders: patient selection and technical options," *Cleveland Clinic Journal of Medicine*, vol. 79, 7 suppl 2, pp. S19–S24, 2012.

[10] I. Litvan, K. P. Bhatia, D. J. Burn et al., "SIC task force appraisal of clinical diagnostic criteria for parkinsonian disorders," *Movement Disorders*, vol. 18, no. 5, pp. 467–486, 2003.

[11] J. Jankovic, M. McDermott, J. Carter et al., "Variable expression of Parkinson's disease: a base-line analysis of the DAT ATOP cohort," *Neurology*, vol. 40, no. 10, pp. 1529–1529, 1990.

[12] S. J. G. Lewis, T. Foltynie, A. D. Blackwell, T. W. Robbins, A. M. Owen, and R. A. Barker, "Heterogeneity of Parkinson's disease in the early clinical stages using a data driven approach," *Journal of Neurology, Neurosurgery & Psychiatry*, vol. 76, no. 3, pp. 343–348, 2005.

[13] R. A. Hauser, M. F. Gordon, Y. Mizuno et al., "Minimal clinically important difference in Parkinson's disease as assessed in pivotal trials of pramipexole extended release," *Parkinson's Disease*, vol. 2014, 8 pages, 2014.

[14] C. E. Clarke, A. Furmston, E. Morgan et al., "Pilot randomised controlled trial of occupational therapy to optimise independence in Parkinson's disease: the PD OT trial," *Journal of Neurology, Neurosurgery & Psychiatry*, vol. 80, no. 9, pp. 976–978, 2009.

[15] K. C. Chung and A. Haas, "Relationship between patient satisfaction and objective functional outcome after surgical treatment for distal radius fractures," *Journal of Hand Therapy*, vol. 22, no. 4, pp. 302–308, 2009.

[16] M. J. Shauver and K. C. Chung, "The minimal clinically important difference of the Michigan Hand Outcomes Questionnaire," *The Journal of Hand Surgery*, vol. 34, no. 3, pp. 509–514, 2009.

[17] J. Fan, S. Upadhye, and A. Worster, "Understanding receiver operating characteristic (ROC) curves," *CJEM*, vol. 8, no. 1, pp. 19-20, 2006.

[18] R. N. Forthofer and R. G. Lehnen, "*Rank Correlation Methods*," in *Public Program Analysis*, pp. 146–163, Springer US, Boston, MA, 1981.

[19] R. A. Hauser, P. Auinger, and on behalf of the Parkinson Study Group, "Determination of minimal clinically important change in early and advanced Parkinson's disease," *Movement Disorders*, vol. 26, no. 5, pp. 813–818, 2011.

[20] M. Katz, M. S. Luciano, K. Carlson et al., "Differential effects of deep brain stimulation target on motor subtypes in Parkinson's disease," *Annals of Neurology*, vol. 77, no. 4, pp. 710–719, 2015.

[21] P. D. Charles, N. van Blercom, P. Krack et al., "Predictors of effective bilateral subthalamic nucleus stimulation for PD," *Neurology*, vol. 59, no. 6, pp. 932–934, 2002.

[22] S. Schade, F. Sixel-Döring, J. Ebentheuer, X. Schulz, C. Trenkwalder, and B. Mollenhauer, "Acute levodopa challenge test in patients with de novo Parkinson's disease: data from the DeNoPa cohort," *Mov Disord Clin Pract*, vol. 4, no. 5, pp. 755–762, 2017.

[23] G. Kleiner-Fisman, J. Herzog, D. N. Fisman et al., "Subthalamic nucleus deep brain stimulation: summary and meta-analysis of outcomes," *Movement Disorders*, vol. 21, no. S14, pp. S290–S304, 2006.

[24] L. Almeida, W. Deeb, C. Spears et al., "Current practice and the future of deep brain stimulation therapy in Parkinson's disease," *Seminars in Neurology*, vol. 37, no. 2, pp. 205–214, 2017.

[25] S.-E. Soh, M. E. Morris, and J. L. McGinley, "Determinants of health-related quality of life in Parkinson's disease: A systematic review," *Parkinsonism & Related Disorders*, vol. 17, no. 1, pp. 1–9, 2011.

[26] J. C. Gómez-Esteban, J. J. Zarranz, E. Lezcano et al., "Influence of motor symptoms upon the quality of life of patients with

Parkinson's disease," *European Neurology*, vol. 57, no. 3, pp. 161–165, 2007.

[27] M. Behari, A. K. Srivastava, and R. M. Pandey, "Quality of life in patients with Parkinson's disease," *Parkinsonism & Related Disorders*, vol. 11, no. 4, pp. 221–226, 2005.

[28] J. M. Bronstein, M. Tagliati, R. L. Alterman, A. M. Lozano, J. Volkmann, A. Stefani et al., "Deep brain stimulation for Parkinson Disease," *Archives of Neurology*, vol. 68, no. 2, pp. 165–165, 2011.

[29] W. M. M. Schuepbach, L. Tonder, A. Schnitzler et al., "Quality of life predicts outcome of deep brain stimulation in early Parkinson disease," *Neurology*, vol. 92, no. 10, pp. e1109–e1120, 2019.

Hindawi
Neural Plasticity
Volume 2023, Article ID 9857506, 1 page
https://doi.org/10.1155/2023/9857506

Retraction

Retracted: Three Mediating Pathways of Anxiety and Security in the Relationship between Coping Style and Disordered Eating Behaviors among Chinese Female College Students

Neural Plasticity

Received 29 August 2023; Accepted 29 August 2023; Published 30 August 2023

This article has been retracted by Hindawi following an investigation undertaken by the publisher [1]. This investigation has uncovered evidence of one or more of the following indicators of systematic manipulation of the publication process:

(1) Discrepancies in scope
(2) Discrepancies in the description of the research reported
(3) Discrepancies between the availability of data and the research described
(4) Inappropriate citations
(5) Incoherent, meaningless and/or irrelevant content included in the article
(6) Peer-review manipulation

The presence of these indicators undermines our confidence in the integrity of the article's content and we cannot, therefore, vouch for its reliability. Please note that this notice is intended solely to alert readers that the content of this article is unreliable. We have not investigated whether authors were aware of or involved in the systematic manipulation of the publication process.

In addition, our investigation has also shown that one or more of the following human-subject reporting requirements has not been met in this article: ethical approval by an Institutional Review Board (IRB) committee or equivalent, patient/participant consent to participate, and/or agreement to publish patient/participant details (where relevant).

Wiley and Hindawi regrets that the usual quality checks did not identify these issues before publication and have since put additional measures in place to safeguard research integrity.

We wish to credit our own Research Integrity and Research Publishing teams and anonymous and named external researchers and research integrity experts for contributing to this investigation.

The corresponding author, as the representative of all authors, has been given the opportunity to register their agreement or disagreement to this retraction. We have kept a record of any response received.

References

[1] W. Han, Z. Zheng, and N. Zhang, "Three Mediating Pathways of Anxiety and Security in the Relationship between Coping Style and Disordered Eating Behaviors among Chinese Female College Students," *Neural Plasticity*, vol. 2021, Article ID 7506754, 6 pages, 2021.

Hindawi
Neural Plasticity
Volume 2021, Article ID 7506754, 6 pages
https://doi.org/10.1155/2021/7506754

Research Article

Three Mediating Pathways of Anxiety and Security in the Relationship between Coping Style and Disordered Eating Behaviors among Chinese Female College Students

Wenyue Han,[1] Zheng Zheng,[1] and Ning Zhang[2]

[1]*School of Medicine & Holistic Integrative Medicine, Nanjing University of Chinese Medicine, Nanjing, China 210023*
[2]*Nanjing Brain Hospital Affiliated to Nanjing Medical University, Nanjing, China 210029*

Correspondence should be addressed to Zheng Zheng; zzdoctor@126.com and Ning Zhang; zn6360@126.com

Received 28 July 2021; Accepted 31 August 2021; Published 21 September 2021

Academic Editor: Fang Pan

Background. According to previous studies, eating disorders and disordered eating behaviors are associated with coping style, anxiety, and sense of security. However, the specific mechanism between them has not been elucidated. The purpose of this study was to explore whether anxiety and sense of security play mediating roles in coping style and disordered eating behaviors among Chinese female college students. *Method.* Six hundred and ninety-one female college students (mean age = 19.36; SD = 1.06) completed the Simple Coping Style Questionnaire, the Eating Disorder Inventory, the Security Questionnaire, the Hospital Anxiety and Depression Scale, and a brief demographic survey. The percentage bootstrap method of deviation correction was conducted to determine the mediating effect of anxiety and sense of security on coping style and disordered eating behaviors. *Results.* Coping style had direct and indirect effects on disordered eating behaviors. Anxiety and sense of security were not only independent mediators in the relationship between coping style and disordered eating behaviors but also chain mediators. *Conclusions.* The results of the current study provide preliminary evidence that preventive interventions targeting anxiety and sense of security may be feasible for young women who develop disordered eating behaviors due to stress in their lives.

1. Introduction

Eating disorders are prevalent, severe psychiatric disorders and often emerge during college-age women [1, 2]. Ward and his colleagues found that the incidence of eating disorders peaked at age 21, with initial onset mostly before the age of 25 [3]. Before meeting an eating disorder diagnosis, these young women often exhibit varying degrees of disordered eating behaviors, including overeating and restricted eating [4].

It has been reported that eating disorders and disordered eating behaviors are related to coping style and anxiety. Coping style reflects an individual's attitude and behavior pattern when facing various events in life. Anxiety is the most common comorbid diagnose in eating disorders [5]. Studies have shown that negative coping style is remarkably correlated with bulimia [6] and high anxiety level [7]. In addition, if individuals adopt positive coping style, they will have lower anxiety level and healthier eating behaviors [8–10].

Other studies have examined the relationship between coping style, sense of security, and eating behaviors. Sense of security refers to the perception of potential psychological and physiological risks, as well as the individual's self-efficacy in risk management, which is generally manifested as interpersonal security and certainty of control [11]. Individuals with negative coping style tend to have lower sense of security and higher social anxiety [12]. Uncertainty caused by insecurity reduces people's ability to control themselves and leads to overeating [13]. Moreover, the negative coping style of individuals with low sense of security prevents them from acquiring necessary social skills, which leads to interpersonal stress and further disordered eating behaviors [14].

Based on these studies, coping style, anxiety, sense of security, and disordered eating behaviors are related. However, no study has studied all four variables simultaneously to explore the specific mechanism between them. Therefore, this study will verify the specific role of anxiety and sense of security in coping style and disordered eating behaviors and provide theoretical basis for early intervention of disordered eating behaviors and prevention of eating disorders. We hypothesized that coping style not only directly affects disorder eating behaviors but also indirectly influences disordered eating behaviors through the mediating role of anxiety and sense of security.

2. Methods

2.1. Participants. The study sample comprised 691 female college students in Eastern China. Demographic characteristics of the sample are summarized in Table 1.

2.2. Measures

2.2.1. Demographic Questionnaire. Participants completed a demographic questionnaire constructed to gather information about their age, hometown, and major.

2.2.2. Disordered Eating Behavior. The Eating Disorder Inventory (EDI) is a 64-item self-report inventory consisting of 8 subscales: (1) drive for thinness, (2) body dissatisfaction, (3) bulimia, (4) perfectionism, (5) interpersonal distrust, (6) mature fear, (7) interoceptive awareness, and (8) inefficiency. The questions are presented on a six-point Likert scale, with scores ranging from 0 to 5 for each disordered eating behavior. The 8 subscales are calculated by totaling the items on each respective scale, while the total EDI score is calculated by adding all items together. Higher total EDI scores indicate more severe disordered eating behaviors [15]. In the current study, internal consistency $\alpha = 0.903$.

2.2.3. Coping Style. The Simple Coping Style Questionnaire (SCSQ) contains 20 items which effectively reflect the individual's coping style in the context of Chinese culture. Items 1-12 belong to positive coping and 13-20 belong to negative coping. The score of each item is from 0 (never) to 3 (always). If the Z score difference between positive coping and negative coping is greater than 0, it is positive coping; if less than 0, it is negative coping [16]. In the present study, total questionnaire internal consistency $\alpha = 0.77$.

2.2.4. Sense of Security. The Security Questionnaire (SQ) consists of 16 items, including 2 subscales of interpersonal security (personal security experience in interpersonal communication) and certainty of control (personal life prediction, sense of certainty and control). Each subscale has 8 items, and the score of each item is from 1 (not consistent at all) to 5 (completely consistent). Higher total SQ scores indicate higher sense of security [11]. In the current study, internal consistency $\alpha = 0.89$.

2.2.5. Anxiety. The Hospital Anxiety and Depression Scale (HAD) is a 14-item self-rating scale that measures symptoms of anxiety and depression respectively. Each item is scored from 0 to 3. The overall score for depression or anxiety can be considered the severity of the symptoms. The anxiety subscale has 7 items, and higher total scores indicate higher level of anxiety [17]. The internal consistency of this study $\alpha = 0.81$.

Table 1: Demographic characteristics of study participants.

Characteristic	*N* or mean	% or SD	Range
Age (years)	19.36	1.06	18-22
Hometown			
Urban area	429	62.1%	
Rural area	262	37.9%	
Major			
Science and engineering	141	20.4%	
Medicine	273	39.5%	
Art	80	11.6%	
Liberal arts	197	28.5%	
Eating Disorder Inventory (EDI)			
Drive for thinness	4.49	4.54	0-21
Body dissatisfaction	10.65	6.45	0-27
Bulimia	1.97	2.87	0-21
Perfectionism	4.91	3.51	0-18
Interpersonal distrust	3.38	3.10	0-21
Mature fear	7.72	4.32	0-24
Interceptive awareness	4.21	4.34	0-27
Inefficiency	4.17	3.99	0-23
Total	41.50	20.69	4-139
Simple Coping Style Questionnaire (SCSQ)			
Positive coping style	350	50.65%	
Negative coping style	341	49.35%	
Security Questionnaire (SQ)			
Interpersonal security	27.33	5.35	8-40
Certainty of control	25.96	5.68	8-40
Total	53.29	10.30	16-80
Hospital Anxiety and Depression Scale (HADS)			
Anxiety	6.71	3.09	0-19

2.3. Procedures. Participants were recruited through psychological health classes. Assessments took place in class and were supervised by members of the research team. The survey lasted half an hour, and questionnaires were collected on the spot. The effective recovery rate of the questionnaires was 97.3%. The research was approved by the Human Research Ethics Committee of NJUCM. Study information was provided directly to participants and informed consent was obtained.

2.4. Statistical Analysis. Analyses were performed using SPSS22.0. All statistical tests were two-tailed, and the significance level was set at $p < 0.05$. Pearson's correlation was used to examine the correlations between coping style, disordered

eating behaviors, anxiety level, and sense of security. T-test was used to analyze the effects of coping style on anxiety, sense of security, and disordered eating behaviors. The mediation model was examined by PROCESS program developed by Preacher and Hayes [18], and the percentage bootstrap method of deviation correction was used to test the significance of mediating effect [19].

2.5. Common Method Biases. The Harman single-factor test was used to eliminate the common method deviation caused by the questionnaire survey. The results of factor analysis showed that the characteristic roots of 26 factors were greater than 1, and the explained variance percentage of the first common factor was 13.63% (less than 40%), indicating that there was no obvious method error.

3. Results

3.1. Correlations between Coping Style, Anxiety, Sense of Security, and Disordered Eating Behaviors. As shown in Table 2, coping style was negatively correlated with anxiety and disordered eating behaviors ($r = -0.418$, -0.318, $p < 0.001$) and was positively correlated with sense of security ($r = 0.510$, $p < 0.001$). Sense of security was negatively correlated with anxiety and disordered eating behaviors ($r = -0.551$, -0.414, $p < 0.001$). Anxiety was positively correlated with disordered eating behaviors ($r = 0.443$, $p < 0.001$).

3.2. Effects of Coping Style on Anxiety, Sense of Security, and Disordered Eating Behaviors. According to the score of SCSQ, the participants were divided into positive or negative coping style. As illustrated in Table 3, there were significant differences in disordered eating behaviors, sense of security, and anxiety between positive and negative coping styles ($t\,(1{,}689) = -6.36$, 11.33, -9.07; $p < 0.001$).

3.3. Mediating Effect Test. Table 4 revealed that coping style had a direct negative predictive effect on anxiety ($\beta = -0.310$, $p < 0.001$) and a direct positive predictive effect on sense of security ($\beta = 0.250$, $p < 0.001$). Anxiety had a direct negative predictive effect on sense of security ($\beta = -0.408$, $p < 0.001$). When coping style, anxiety, and sense of security predicted disordered eating behaviors simultaneously, coping style and sense of security had negative predictive effects ($\beta = -0.067$, -0.207; $p < 0.05$, 0.001), and anxiety had a positive predictive effect ($\beta = 0.290$, $p < 0.001$).

As shown in Table 5, analyses of total indirect effects indicated that anxiety and sense of security partially mediated the relationship between coping style and disordered eating behaviors (Effect = −0.168, SE = 0.020, 95% CI (-0.208, -0.131)). The mediating effect accounted for 71.8% of the total effect (Effect = −0.234, SE = 0.027, 95% CI (-0.287, -0.182)). In the meantime, when tested separately, three mediating paths were significant: coping style ⟶ anxiety ⟶ disordered eating behaviors (Effect = −0.090, SE = 0.020, 95% CI (-0.131, -0.053)), accounting for 38.5% of the total effect; coping style ⟶ sense of security ⟶ disordered eating behaviors (Effect = −0.052, SE = 0.160, 95% CI (-0.084, -0.022)), accounting for 22.2% of the total effect, and coping style ⟶ anxiety ⟶ sense of security ⟶ disordered eating behaviors (Effect = −0.026, SE = 0.087, 95% CI (-0.044, -0.010)), accounting for 11.1% of the total effect. The specific paths are presented in Figure 1.

Table 2: Correlations between coping style, anxiety, sense of security, and disordered eating behaviors.

	1	2	3	4
(1) Coping style	1			
(2) Anxiety	-0.418***	1		
(3) Sense of security	0.510***	-0.551***	1	
(4) Disordered eating behaviors	-0.318***	0.443***	-0.414***	1

***$p < 0.001$ (two-tailed), **$p < 0.01$ (two-tailed), and *$p < 0.05$ (two-tailed).

4. Discussion

The purpose of this study was to explore whether anxiety and sense of security play mediating roles in coping style and disordered eating behaviors among Chinese female college students. To the best of our knowledge, this is the first empirical study to evaluate these relationships in a sample of female women. Our study found that, first of all, coping style was negatively correlated with anxiety and disordered eating behaviors while positively correlated with sense of security. And there were significant differences in anxiety, sense of security, and disordered eating behaviors between positive coping style and negative coping style. These results correspond to previous research findings, which have indicated negative coping style could lead to more severe disordered eating behaviors [20], higher level of anxiety [21], and lower sense of security [22]. Next, when analyzing the mediating roles of anxiety and sense of security between coping style and disordered eating behaviors, we found an overall mediating role of 71.8%. These results revealed that coping style had both direct and indirect effects on disordered eating behaviors. Through further analysis, we found three indirect effect pathways. The first pathway was coping style ⟶ anxiety ⟶ disordered eating behaviors, which indicated that negative coping style could enhance anxiety level and further induced more serious disordered eating behaviors. The second pathway was coping style ⟶ sense of security ⟶ disordered eating behaviors, which showed that negative coping style could reduce the sense of security and led to the aggravation of eating problems. Similar findings have been observed in previous studies [23, 24]. The third pathway was coping style ⟶ anxiety ⟶ sense of security ⟶ disordered eating behaviors, which illustrated that anxiety and sense of security played a chain mediating role in the relationship between coping style and disordered eating behaviors. In other words, negative coping style enhanced anxiety level, high anxiety level reduced the sense of security, and further aggravated disordered eating behaviors. Kuipers and his colleagues have found that when the symptoms of eating disorders alleviated, patients' anxiety and sensitivity to others were reduced, and their ability to deal with new

Table 3: Effects of coping style on anxiety, sense of security, and disordered eating behaviors.

	Positive coping style ($n = 350$)	Negative coping style ($n = 341$)	t
Disordered eating behaviors	36.71 ± 18.27	46.48 ± 21.86	-6.36***
Sense of security	57.33 ± 8.76	49.16 ± 10.13	11.33***
Anxiety	5.72 ± 2.66	7.74 ± 3.17	-9.07***

***$p < 0.001$ (two-tailed), **$p < 0.01$ (two-tailed), and *$p < 0.05$ (two-tailed).

Table 4: Regression analysis between variables.

Regression equation		Global fit index			Significance of regression coefficient	
Outcome variable	Predictor variable	R	R^2	F	β	t
Anxiety	Coping style	0.418	0.175	145.642	-0.310	-12.068***
Sense of security	Coping style	0.631	0.399	228.112	0.250	10.409***
	Anxiety				-0.408	-12.598***
Disordered eating behaviors	Coping style	0.494	0.244	73.756	-0.067	-2.306*
	Anxiety				0.290	7.194***
	Security				-0.207	-4.835***

***$p < 0.001$ (two-tailed), **$p < 0.01$ (two-tailed), and *$p < 0.05$ (two-tailed).

Table 5: The mediating effect of anxiety and security between coping style and disordered eating behaviors.

	Effect value	Boot SE	Boot CI lower	Boot CI upper	Relative mediation effect
Total effect	-0.234	0.027	-0.287	-0.182	100%
Total indirect effect	-0.168	0.020	-0.208	-0.131	71.8%
Indirect path 1	-0.090	0.020	-0.131	-0.053	38.5%
Indirect path 2	-0.052	0.160	-0.084	-0.022	22.2%
Indirect path 3	-0.026	0.087	-0.044	-0.010	11.1%

Indirect path 1: coping style ⟶ anxiety ⟶ disordered eating behaviors; Indirect path 2: coping style ⟶ sense of security ⟶ disordered eating behaviors; Indirect path 3: coping style ⟶ anxiety ⟶ sense of security ⟶ disordered eating behaviors.

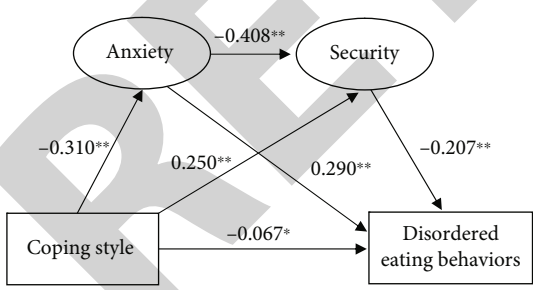

Figure 1: Model of mediating roles of anxiety and sense of security between coping style and disordered eating behaviors.

situations was enhanced [25], which well supports the existence of chain mediating role identified in our study.

Findings from the present study have clinical implications for psychologists who work with young women. The present study provides evidence that negative coping style leads to higher anxiety level, lower sense of security, and more severe disordered eating behaviors. These findings provide preliminary support for targeting anxiety and sense of security in preventative interventions, particularly for female youth that have the propensity to disordered eating behaviors in response to feelings of stressful daily life. In clinical interventions, while therapists could help clients with eating disorders or disordered eating behaviors by teaching them coping strategies, the improvement of coping skills requires long-term learning and practice. In contrast, the regulation of anxiety is flexible and diversified, such as progressive muscle relaxation, meditation, breathing exercises, and visualization [26]. Therefore, if therapists aim at anxiety, they might achieve ideal effect in reducing disordered eating behaviors in a short period of time. In addition, due to the existence of chain mediating role, reducing anxiety also helps to improve safety and further alleviate disordered eating behaviors.

There are several limitations to the present study. Considering the present sample was restricted to female college students in East China, the findings may have limited generality. Besides that, the cross-sectional nature of this study prevents us from inferring causation. Future longitudinal studies are necessary to examine what predictive roles

anxiety and sense of security play in mediating the relationship between negative coping style and disordered eating behaviors in female youth.

Data Availability

Data and questionnaires are available upon request, contact at zzdoctor@126.com.

Ethical Approval

Ethical approval of our study was given by the ethics committee of NJUCM.

Conflicts of Interest

The authors declare that they have no competing interests.

Acknowledgments

The study was supported by a grant of Jiangsu Province University Graduate Students' Innovation and Entrepreneurship Training Program (SJCX21_0658).

References

[1] U. Volpe, A. Tortorella, M. Manchia, A. M. Monteleone, U. Albert, and P. Monteleone, "Eating disorders: what age at onset?," *Psychiatry Research*, vol. 238, pp. 225–227, 2016.

[2] M. Galmiche, P. Dechelotte, G. Lambert, and M. P. Tavolacci, "Prevalence of eating disorders over the 2000-2018 period: a systematic literature review," *The American Journal of Clinical Nutrition*, vol. 109, no. 5, pp. 1402–1413, 2019.

[3] Z. J. Ward, P. Rodriguez, D. R. Wright, S. B. Austin, and M. W. Long, "Estimation of eating disorders prevalence by age and associations with mortality in a simulated nationally representative US cohort," *JAMA Network Open*, vol. 2, no. 10, article e1912925, 2019.

[4] L. Reba-Harrelson, A. von Holle, R. M. Hamer, R. Swann, M. L. Reyes, and C. M. Bulik, "Patterns and prevalence of disordered eating and weight control behaviors in women ages 25-45," *Eating and Weight Disorders*, vol. 14, no. 4, pp. 190–e198, 2009.

[5] N. T. Godart, F. Perdereau, Z. Rein et al., "Comorbidity studies of eating disorders and mood disorders. Critical review of the literature," *Journal of Affective Disorders*, vol. 97, no. 1-3, pp. 37–49, 2007.

[6] A. E. Lee-Winn, L. Townsend, S. P. Reinblatt, and T. Mendelson, "Associations of neuroticism-impulsivity and coping with binge eating in a nationally representative sample of adolescents in the United States," *Eating Behaviors*, vol. 22, pp. 133–140, 2016.

[7] A. Ribadier and I. Varescon, "Anxiety and depression in alcohol use disorder individuals: the role of personality and coping strategies," *Substance Use & Misuse*, vol. 54, no. 9, pp. 1475–1484, 2019.

[8] R. Trigueros, I. Mercader, J. J. González-Bernal et al., "The influence of the trainer's social behaviors on the resilience, anxiety, stress, depression and eating habits of athletes," *Nutrients*, vol. 12, no. 8, p. 2405, 2020.

[9] M. T. Allen and C. E. Myers, "A computer-based avatar task can differentiate avoidant and non-avoidant coping styles," *Anxiety, Stress, and Coping*, vol. 32, no. 5, pp. 477–483, 2019.

[10] K. E. Giel, A. Hermann-Werner, J. Mayer et al., "Eating disorder pathology in elite adolescent athletes," *The International Journal of Eating Disorders*, vol. 49, no. 6, pp. 553–562, 2016.

[11] C. Zhong and A. Lijuan, "Developing of security questionnaire and its reliability and validity," *Chinese Mental Health Journal*, vol. 18, no. 2, pp. 97–99, 2004.

[12] T. Yang, J. Liu, Y. Zhang et al., "Coping style predicts sense of security and mediates the relationship between autistic traits and social anxiety: moderation by a polymorphism of the FKBP5 gene," *Behavioural Brain Research*, vol. 404, p. 113142, 2021.

[13] T. J. Core, M. M. Price, J. L. Alquist, R. F. Baumeister, and D. M. Tice, "Life is uncertain, eat dessert first: uncertainty causes controlled and unemotional eaters to consume more sweets," *Appetite*, vol. 131, pp. 68–72, 2018.

[14] A. Faber, L. Dubé, and B. Knäuper, "Attachment and eating: a meta-analytic review of the relevance of attachment for unhealthy and healthy eating behaviors in the general population," *Appetite*, vol. 123, pp. 410–438, 2018.

[15] D. M. Garner, M. P. Olmstead, and J. Polivy, "Development and validation of a multidimensional eating disorder inventory for anorexia nervosa and bulimia," *The International Journal of Eating Disorders*, vol. 2, no. 2, pp. 15–34, 1983.

[16] X. Yaning, "Preliminary study on the reliability and validity of the Simplified Coping Style Questionnaire," *Chinese Journal of Clinical Psychology*, vol. 6, no. 2, pp. 114-115, 1998.

[17] A. S. Zigmond and R. P. Snaith, "The hospital anxiety and depression scale," *Acta Psychiatrica Scandinavica*, vol. 67, no. 6, pp. 361–370, 1983.

[18] K. J. Preacher and A. F. Hayes, "SPSS and SAS procedures for estimating indirect effects in simple mediation models," *Behavior Research Methods, Instruments, & Computers*, vol. 36, no. 4, pp. 717–731, 2004.

[19] A. F. Hayes, *Introduction to Mediation, Moderation, and Conditional Process Analysis: A Regression-Based Approach*, The Guilford Press, New York, NY, USA, 2012.

[20] C. M. M. Polhuis, L. Vaandrager, S. S. Soedamah-Muthu, and M. A. Koelen, "Salutogenic model of health to identify turning points and coping styles for eating practices in type 2 diabetes mellitus," *International Journal for Equity in Health*, vol. 19, no. 1, p. 80, 2020.

[21] S. C. Segerstrom and G. T. Smith, "Personality and coping: individual differences in responses to emotion," *Annual Review of Psychology*, vol. 70, no. 1, pp. 651–671, 2019.

[22] M. Movahed Abtahi and K. A. Kerns, "Attachment and emotion regulation in middle childhood: changes in affect and vagal tone during a social stress task," *Attachment & Human Development*, vol. 19, no. 3, pp. 221–242, 2017.

[23] C. E. Richardson, N. R. Magson, J. Fardouly et al., "Longitudinal associations between coping strategies and psychopathology in pre-adolescence," *Journal of Youth and Adolescence*, vol. 50, no. 6, pp. 1189–1204, 2021.

[24] C. Munro, L. Randell, and S. M. Lawrie, "An integrative bio-psycho-social theory of anorexia nervosa," *Clinical Psychology & Psychotherapy*, vol. 24, no. 1, pp. 1–21, 2017.

Hindawi
Neural Plasticity
Volume 2021, Article ID 5519330, 15 pages
https://doi.org/10.1155/2021/5519330

Research Article

Lycopene-Loaded Microemulsion Regulates Neurogenesis in Rats with Aβ-Induced Alzheimer's Disease Rats Based on the Wnt/β-catenin Pathway

Wen-jing Ning,[1,2,3] **Ren-jun Lv**,[4] **Ning Xu**,[5] **Xun-yao Hou**,[1,3,5] **Chao Shen**,[1,4,5] **Yun-liang Guo**,[1,3,5] **Zhong-yu Fan**,[5] **Na Cao**,[6] **and Xue-Ping Liu**[1,3,5]

[1]*Department of Geriatric Neurology, Shandong Provincial Hospital, Cheeloo College of Medicine, Shandong University, Jinan, Shandong 250012, China*
[2]*First People's Hospital of Jinan, Jinan, Shandong 250000, China*
[3]*Provincial Hospital Affiliated to Shandong First Medical University, Jinan, Shandong 250000, China*
[4]*Department of Respiratory Medicine, The First School of Clinical Medicine, Lanzhou University, Lanzhou 730000, China*
[5]*Shandong First Medical University&Shandong Academy of Medical Sciences, Jinan, Shandong 250000, China*
[6]*Jigang Hospital of Jinan, Jinan, Shandong 250000, China*

Correspondence should be addressed to Xue-Ping Liu; liuxueping1962@163.com

Received 25 February 2021; Revised 14 August 2021; Accepted 16 August 2021; Published 6 September 2021

Academic Editor: Fushun Wang

Objective. To investigate the effects of lycopene-loaded microemulsion (LME) on the cognitive function and neurogenesis in the dentate gyrus (DG) of the hippocampus and subventricular (SVZ) region of rats with amyloid β- (Aβ-) induced Alzheimer's disease (AD) and its mechanism based on the Wnt/β-catenin pathway. *Methods*. Healthy Wistar rats were divided into four groups: the blank control (CON), AD control, traditional lycopene (LOO), and LME groups. The CON and AD groups were fed with normal saline, while the LOO group was fed with traditional lycopene, and the LME group was fed with lycopene-loaded microemulsion. Behavioral tests were performed after three weeks of gastric administration. Immunofluorescence-labeled cells were used to observe the differentiation and maturation of new nerve cells in the DG of the hippocampus and SVZ region. qRT-PCR and Western blotting detected the expression of neurogenesis genes and Wnt/β-catenin pathway-related proteins, respectively. *Results*. On the Morris water maze test, LME rats had significantly shortened movement trajectory on the searching platform, reduced escape latency time, and increased residence time on the original platform quadrant. In addition, more LME rats crossed the platform when it was removed. Thus, LME can improve the spatial learning and memory of Aβ-induced AD rats. On qRT-PCR, LME significantly increased Reelin, Nestin, and Pax6 gene expressions, which regulate neurogenesis. Immunofluorescence showed that LME could significantly increase $BrdU^+$, Dcx^+, $BrdU^+/Neun^+$, $BrdU^+/Dcx^+$ cells in the DG and SVZ regions, thus promoting neurogenesis. LME also reduced the number of $Iba1^+$ and $Iba1^+/BrdU^+$ cells, thus reducing the neuroinflammatory response. On Western blot, LME upregulated the Wnt/β-catenin pathway by upregulating Wnt3a, β-catenin, Disheveled (Dvl), and p-GSK3β and downregulating p-β-catenin and GSK3β. *Conclusion*. LME attenuates cognitive impairment in Aβ-induced AD rats by promoting neurogenesis in the hippocampus and SVZ region through upregulating the Wnt/β-catenin pathway.

1. Introduction

Alzheimer's disease (AD) is a progressive degenerative disease of the central nervous system. It is one of the most common neurological diseases and often occurs in the elderly. The main clinical manifestations are progressive dementia, memory, and cognitive decline. The main pathological features are intracellular and extracellular amyloid β (Aβ)

deposition and formation of intracellular neuronal tangles, which trigger neurodegeneration and neuronal loss [1]. Adult mammalian brain neurogenesis occurs at the subventricular zone(SVZ) and the lower levels of the hippocampal dentate gyrus (DG). Under certain conditions, two areas with the neural stem cells (NSCs) have the ability of differentiation, proliferation, and migration. Since these new neurons can develop in multiple directions, these can replace lost nerve cells in situ. Thus, making full use of endogenous NSCs can provide new means for AD treatment [2]. However, autologous NSCs have a limited ability to proliferate in situ under spontaneous conditions, and the mechanism of the brain's responses to Aβ injury remains unclear. Thus, neuroscientists face the issue of determining how to activate the proliferation of endogenous NSCs to complete the repair process. The Wnt/β-catenin signaling pathway gets its name because of its initial Wnt protein. It is widely distributed in various tissues and has functions in embryonic neural development, such as nerve cell proliferation, differentiation, fate determination, apoptosis, axon guidance, and synaptic formation [3–5]. The Wnt pathway plays an important role in the development of the embryonic nervous system [5]. Lycopene, which is found in tomatoes and other red fruits, belongs to the carotenoid family. As an effective antioxidant and singlet oxygen quenching agent, lycopene has many physiologic roles such as antioxidative stress, anti-inflammatory, antiapoptosis, and antitumor effects and promoting neurogenesis and protecting the nervous system. Microemulsion is a stable thermodynamic system formed by mixing oil phase, surfactant, cosurfactant, and water with particle size < 100 μm. Studies have shown that microemulsions with a specific composition can improve the oral bioavailability of insoluble drugs and promote targeted brain transport, potentially improving neuroprotection and promoting neurogenesis [6, 7]. Lycopene-loaded microemulsion (LME) is prepared by the synthesis of lycopene and a nanoemulsion. Previous studies have shown that LME can significantly improve lycopene's oral absorption and bioavailability, reduce its elimination rate, and increase its retention time in blood circulation; it also has good brain targeting [6]. In this study, an Aβ-induced AD cognitive impairment model was established. Rats in each group were fed differently to observe behavior changes such as spatial learning ability and neurogenesis in the hippocampal DG and SVZ regions. The expression of the Wnt/β-catenin pathway-related proteins in hippocampal regions were also studied to explore the possible mechanism of LME on Aβ-induced AD model rats.

2. Materials and Methods

2.1. Reagents and Instruments. The main reagents and instruments included Aβ1-42 (Sigma, A9810, GER), lycopene (Shanxi Comsenz Biological Technology Co., Ltd.), mouse monoclonal antibody of BrdU (Sigma B5002, GER), rabbit monoclonal antibody of Dcx (Abcam, ab207175, UK), rabbit monoclonal antibodies Neun resistance (Abcam, ab177487, UK), rabbit monoclonal antibody of Iba1 (Abcam, ab178846, UK), β-actin antibody (Proteintech, PTG 20536-1-AP, China), Anti-Wnt3a antibody (Abcam, EPR21889, UK), DVL1 Polyclonal antibody (Proteintech, 27384-1-AP, China), GSK3β Polyclonal antibody (Proteintech, 22104-1-AP, China), Anti-beta Catenin antibody(Abcam ab32572, UK), Morris water maze, panoramic biopsy scanner, brain stereotaxic instrument, gel scan imaging, and image analysis system,

2.2. Preparation of Aβ Amyloid Protein. The samples were diluted to 1 mg/ml with sterile PBS solution and incubated at 37°C for 1 week to form polymerized Aβ for later use.

2.3. Preparation of Lycopene-Loaded Microemulsion and Traditional Lycopene. Polysorbate 80 and Transcutol Hp were prepared at a 2 : 1 ratio, then nitrogen-sealed, vortexed for 5 min, avoiding light, and then mixed at low speeds with a magnetic stirrer for 30 min. Then, we thoroughly incorporated the Smix formation with lycopene (463 μg/ml) into limonene. The mixture was gently shaken using a nitrogen inflator while blending to filter impurities. Next, the Smix was added; then, it was nitrogen-sealed, avoiding light. Afterward, it was placed in a 37°C warm bath and mixed at low speeds with a magnetic stirrer for 30 min. At the same time, syringes for the intravenous drip with a corresponding amount of deionized water (18°Ω) were nitrogen-sealed and mixed with a magnetic stirrer for 30 min at 4°C, avoiding light. After 1 day, the transparent crystal LME was available [6]. Traditional lycopene (LOO) was prepared by dissolving the same amount of lycopene in olive oil [6].

2.4. Establishment of AD Cognitive Impairment Model in Rats. After the rats were anesthetized by intraperitoneal injection of 2% pentobarbital, the cranial-top hair was shaved to expose the skin, and the rats were fixed on the stereotactic locator. The skin was cut open to expose the skull, and the left lateral ventricle was positioned as the injection target area according to the "stereotactic map of rat brain." With bregma point as the origin, the skull was drilled with a side opening of 1.3 mm and a back opening of 0.8 mm. A 4 mm microsyringe needle containing Aβ 10 μl (>10 min) was then injected slowly, and the needle core was withdrawn slowly after 5 min of needle retention. Afterward, the opening was sutured, and single cage feeding was performed after surgery until the rat was fully awake.

2.5. Animal and Intervention. An animal laboratory provided a total of 24 healthy male Wistar rats (Liaoning Changsheng Biotechnology Co., Ltd.) weighing 150–200 g. The rats were fed adaptively for 1 week. Then, the rats were completely randomly divided into 4 groups: (1) the blank control group (CON group), with no special treatment and nasal feeding with the same amount of normal saline; (2) the AD control group (AD group), injected with Aβ into the lateral ventricle and fed with the same volume of normal saline; (3) the LOO group, injected with Aβ into the lateral ventricle and fed with traditional lycopene; and (4) the LME group, injected with Aβ into the lateral ventricle and fed with LME. The LOO and LME groups were fed with the same amount of LOO and LME (calculated by the

content of lycopene, 4 mg/kg/day for each rat). Nasal feeding lasted for 3 weeks in a clean environment, with clean water and a proper diet.

2.6. Morris Water Maze Behavior Test. The spatial memory learning ability of rats was measured using the Morris water maze behavioral test. First, the localization cruise experiment was conducted. Here, the rats were immersed into the water from 4 different directions (north, south, east, and west) 4 times a day for 4 days, and the time to find the platform (escape incubation period) and swimming path were recorded within 2 min. If the rat did not find the platform within 2 min, the escape incubation period was recorded as 120 s, and the rats were guided to the platform and placed there for 15 s. The learning ability of the rats could be observed by training the rats to find the platform. On the fifth day of the test, the platform was removed, and two relatively distant entry points were selected for entry into the water. Herein, a space exploration experiment was conducted, which recorded the following variables: time to reach the platform quadrant, times the platform was crossed, and the percentage of time staying in each quadrant.

2.7. Sample Sampling. Intraperitoneal injection of 2% pentobarbital was given. Hemostatic forceps were placed, using rat leg pain avoidance reaction as the standard. The chest was cut open, exposing the heart; then, a syringe was used to pierce the rat cardiac apex. Throbbing occurred. The right auricle was cut, and physiological saline was given for heart perfusion until the liver of rats started to bleach. The liquid crystal stop was avoided until after infusion. The rat was beheaded, and the brain was frozen. The hippocampus was separated and frozen using liquid nitrogen, then later cryopreserved for standby at a −80°C refrigerator. The heart was given 4% paraformaldehyde perfusion; then, the hippocampus was harvested after sliced paraffin embedding ($d = 3$ μm) for immunofluorescence staining.

2.8. qRT-PCR Was Used to Detect Genes Related to Neurogenesis. The total RNA was isolated from the hippocampal tissues using TRIzol (Thermo, 15596026, USA) according to the manufacturer's instructions. A reverse transcription kit (Takara, RR047A, Japan) was used to reverse-transcribe RNA to cDNA. Next, qRT-PCR was performed using cDNA as a template on a Light Cycler system with FastStart DNA Master SYBR Green *I* (Roche, 03003230001, Germany). The primers used were as follows: 36B4, 5′-CACTGGTCTAGGACCC GAGAAG-3′ and 5′-GGTGCCTCTGGAGATTTTCG-3′; Pax6, 5ax6, TGCCTCAGCATGCAGAACAGTCAC-3′ and 5nd6, TGCCTCAGCATGCAGAACAGTCAC-3′; Reelin, 5′ -GCGTGCTGCTGGACTACTCT-3′ and 5′-GAAATCCAT CTCATGAAGCAAA-3′; and Nestin, 5estin, ATCCATCTC ATGAAGCAAA- and 5dtin, ATCCATCTCATGAAGC AAA-3.

The difference between the Ct values (ΔCt) of the gene of interest and the housekeeping gene was calculated for each experimental sample. Then, the difference in the ΔCt values between the experimental and control sample $\Delta\Delta$Ct was calculated. The fold-change in the expression of the gene of interest between the two samples was equal to $2^{-\Delta\Delta Ct}$.

2.9. Western Blotting to Detect the Expression of Wnt3a, β-Catenin, GSK3β, and p-GSK3β in the Hippocampus. The proteins were extracted according to the BCA extraction kit instructions, and the samples were loaded for denaturing discontinuous polyacrylamide gel electrophoresis (SDS-PAGE) then transferred to the PVDF membrane. The PVDF membrane was soaked in a blocking solution of 5% skimmed milk powder for washing. After washing, the PVDF membrane reacted with the corresponding primary antibody and then incubated overnight in a 4°C refrigerator and shaker. After rinsing the next day, the corresponding secondary antibody was added and incubated at room temperature for 1 hour. The newly configured chromographic solution was then for photographic preservation.

2.10. Tissue Fluorescence Staining to Detect Neurogenesis in the Hippocampus. Sections were routinely dewaxed, microwave antigens were repaired, and the 3% bovine serum was sealed for 30 minutes. Next, the corresponding primary antibodies of BrdU, Neun, Dcx, and Iba1 were added, and the sections were incubated overnight in a wet box at 4°C. The second antibody was added after PBS rinsing the next day, and the reaction was conducted at room temperature for 1 hour. The second antibody was decanted then rinsed with PBS. The nucleus was stained with DAPI, the slices were sealed, and then, the fluorescence section scanner was used to take photos. The corresponding color of positive cells was shown, and the colabeled cells were considered double-positive cells. The negative control was 3% BSA instead of the primary antibody.

2.11. Statistical Analysis. Data were expressed as mean ± SEM and standard deviation. One-way ANOVA was performed using the SPSS11.0 statistical software, followed by the Tukey-Kramer post hoc multiple comparison test. Test level $\alpha = 0.5$ and $p < 0.05$ indicated statistically significant difference.

3. Results

3.1. Behavioral Test of Rats (Figure 1). In the Morris water maze directional cruise experiment, the average escape latency time of rats in each group gradually shortened (Figures 1(d) and 1(e)), indicating that the ability to find the platform improved after learning and training. In 2 d, when comparing the AD and CON groups, the escape latency was significantly prolonged (Figures 1(d and 1(e)). The trajectory of rats was mostly marginal and random (Figure 1(a)), indicating that the modeling was successful. After removing the platform, the AD group had significantly shortened platform quadrant time than other groups (Figures 1(b) and 1(f)), suggesting the effects of learning and memory impairment. Compared with the LOO group, the escape latency of the LME group was significantly shorter (Figures 1(d and 1(e)), but both the LOO and LME groups were significantly shorter than the CON group. There was also no significant difference between the LME

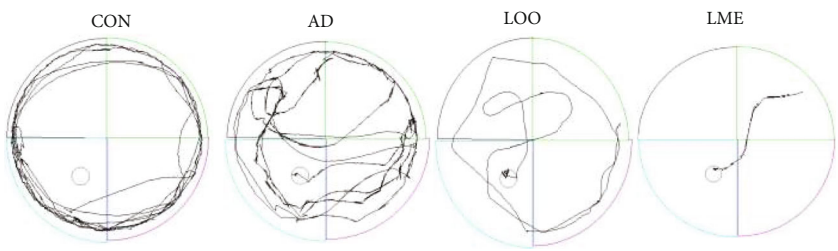

(a)

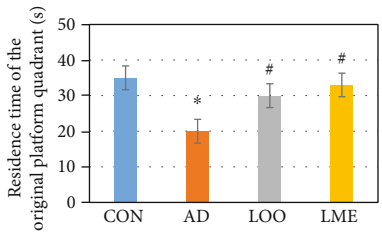

(b)

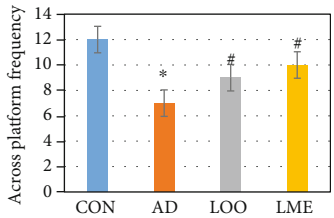

(c)

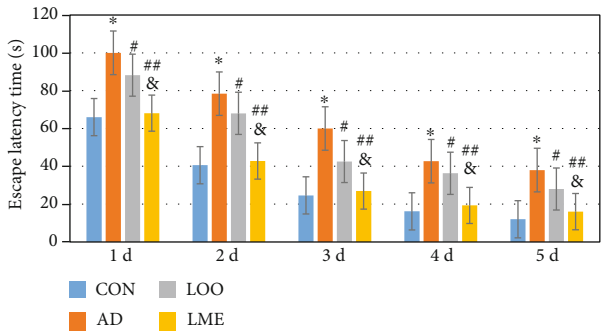

(d)

Escape latency time ($\bar{x}$±s, s)

Group \ Date	1 d	2 d	3 d	4 d	5 d
CON	66.0±12.0	40.6±11.2	24.6±9.2	16.2±7.8	12±5.3
AD	100.0±11.1*	78.4±12.3*	60.0±13.0*	42.7±11.2*	38.0±10.8*
LOO	88.2±10.2#	68.0±9.7#	42.5±8.4#	36.3±7.2#	28.0±6.8#
LME	68.1±10.7##,&	42.8±8.5##,&	26.9±7.8##,&	19.3±8.2##,&	16.2±6.1##,&

(e)

Percentage of residence time in each quadrant ($\bar{x}$±s, %)

Group \ Date	Morris' quadrants			
	I	II (platform)	III	IV
CON	20.82±6.23	41.21±5.21	19.62±4.29	19.35±6.02
AD	24.04±5.62	24.35±6.32*	25.46±4.82	26.15±7.32
LOO	22.16±7.52	36.08±7.86#	21.09±5.67	20.67±4.82
LME	21.08±4.71	40.48±5.58##	17.92±7.84	20.52±8.20

(f)

Figure 1: Effect of LME on spatial memory and learning ability in rats. (a) Trajectory map of rats. The trajectory of untrained rats was mainly marginal. The trained rats' path to find the platform gradually shortened. (b) Residence time of the original platform quadrant of the CON-, AD-, LOO-, and LME-treated rats. The AD group had a shorter time than the control group. This indicates that the AD model is successful. The LOO-treated rats had a longer time than the AD group, while compared with the AD group, the LME group had much longer time. (c) Across platform frequency of rats. The times of crossing the platform in LME group was close to that in the control group. This indicates that LME could effectively improve the spatial memory and learning ability in AD rats. (d, e) Escape latency time of four group rats. The AD group had longer than the CON group. The LOO and LME groups are significantly shorter than the AD group. Compared with the AD group, the LME group could make much shorter escape latency time. (f) Percentage of residence time of the platform quadrant. Values are expressed as mean ± SEM ($n = 6$ rats/group). $^{*}p < 0.05$ versus the control group. $^{\#}p < 0.05$ versus the AD group. $^{\#\#}p < 0.01$ versus the AD group. $^{\&}p < 0.05$ versus the LOO group.

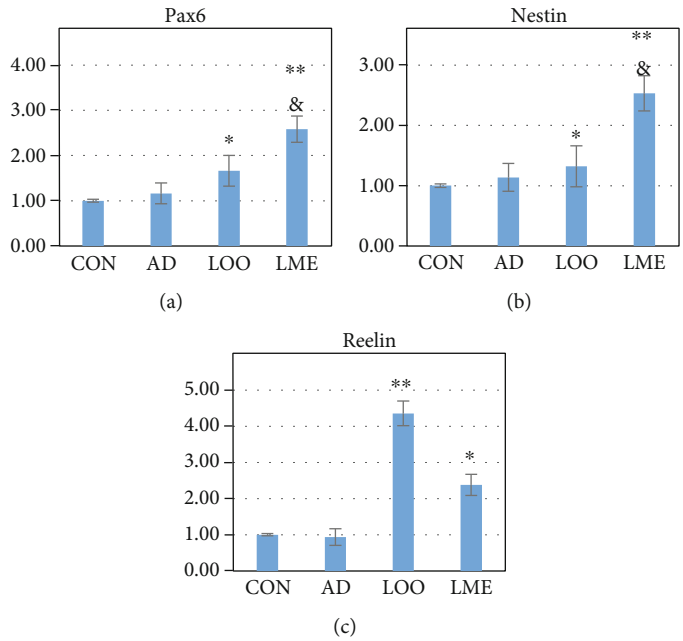

Figure 2: (a–c) Quantitative real-time PCR analysis was performed for relative mRNA expression of nestin (marker of NSC), Reelin (an extracellular matrix protein required for proper migration and differentiation of NSC), and Pax6 in the hippocampus and normalized to β-actin. Values are expressed as mean ± SEM ($n = 6$ rats/group). Compared with the control group, the expression of nestin, Reelin, and Pax6 of the AD has no obvious change ($p > 0.05$). Compared with the AD group, the expression of Pax6 and nestin in the LOO and LME groups is significantly increased. Compared with the LOO group, the expression of Pax6 and nestin is significantly increased. $^{*}p < 0.05$ versus the AD group. $^{**}p < 0.05$ versus the AD group. $^{\&}p < 0.05$ versus the LOO group.

and CON groups. These results indicate that LOO and LME can improve AD rats' spatial learning and memory ability, with a more significant improvement with LME (Figures 1(d and 1(e)).

3.2. Detection of Neural Proliferation-Related Genes on qRT-PCR (Figure 2). The CON and AD groups were not significantly different in detecting Pax6, Nestin, and Reelin. On the other hand, LOO increased the expression of these genes. Furthermore, the LME group had significantly increased expression of Pax6 and Nestin compared to the LOO group. Thus, LOO and LME had positive effects on Reelin, Nestin, and Pax6 expressions in the rat hippocampus, with LME having a more positive effect on the expression of these genes. Thus, LME likely regulates neurogenesis by increasing the expression of Pax6, Nestin, and Reelin genes.

3.3. Nerve Proliferation in the Hippocampus (Figure 3). In the SVZ region of the CON and AD groups, the number of $BrdU^{+}$ cells was very small. Similarly, a small amount of $BrdU^{+}$ cells was in the LOO group, but this number significantly increased in the LME group (Figures 3(a) and 3(c)). In the DG region, the Dcx^{+} cells were almost invisible in the CON group, while a small amount was found in the AD group (Figures 3(b) and 3(d)). Compared to the CON and AD groups, many $BrdU^{+}$, Dcx^{+}, and BrdU+/Dcx^{+} colabeled cells were observed in the LOO and LME groups (Figures 3(h) and 3(e)), with the latter having a significant increase than the former (Figures 3(h) and 3(g)). Compared to the CON and AD groups, a small amount of $BrdU^{+}$/-$Neun^{+}$ colabeled cells was observed in the LOO group, with a significantly higher number in the LME group compared to the LOO group (Figures 3(i) and 3(e)). Thus, lycopene could promote neurogenesis to a certain extent, while the effect of LME on neurogenesis was more significant.

A small number of $Iba1^{+}$ and $Iba1^{+}$/$BrdU^{+}$ colabeled cells were observed in the CON group, while many were observed in the AD group. However, compared with the AD group, these cells were significantly reduced in the LOO and LME groups, with a more obvious decrease in the LME group (Figures 3(j)–3(m)). Thus, LME can reduce the neuroinflammatory response.

3.4. Effect of Lycopene Nanoemulsion on the Protein Expression of Wnt Pathway in the Hippocampus Seen on Western Blot (Figure 4). Compared to the CON group, the protein expressions of Wnt3a, β-catenin, and Dvl in the AD group increased, while the protein expressions of P-β-catenin and GSK3β decreased. Compared to the AD control group, the LOO group had increased protein expressions of Wnt3a, β-catenin, and DVL and decreased protein expressions of p-β-catenin and GSK3β. In the LME group, the trend was more significant, and the differences were statistically significant. These results indicate that the proteins associated with the Wnt pathway changed in each group. Compared with the CON group, the other 3 groups showed elevations in active proteins (Wnt3a, β-catenin, and Dvl) and reductions in inhibitory proteins (P-β-catenin and GSK3β). Thus, it can be inferred that the Wnt pathway may be involved in the neurogenesis of Aβ-induced AD rats.

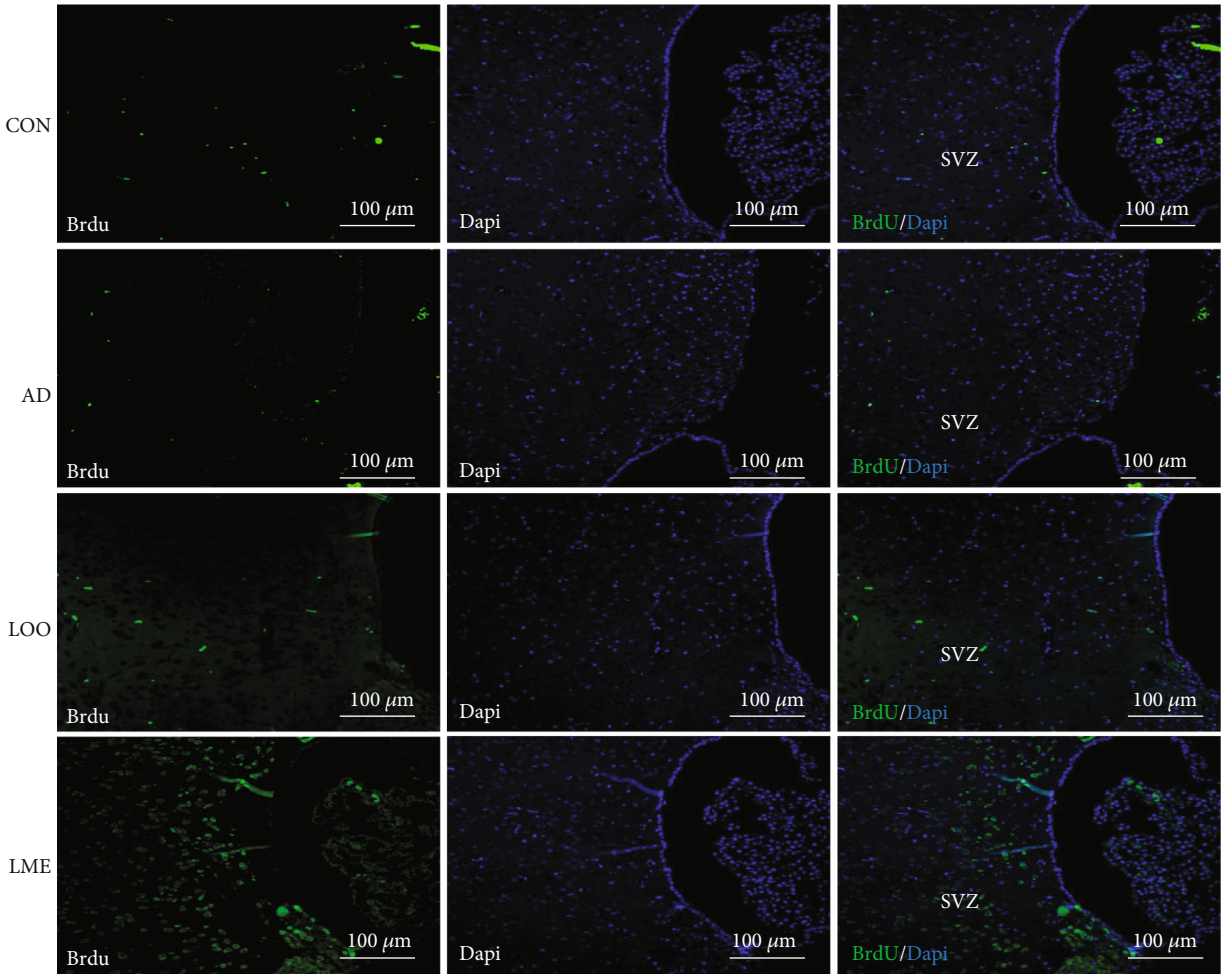

(a)

Figure 3: Continued.

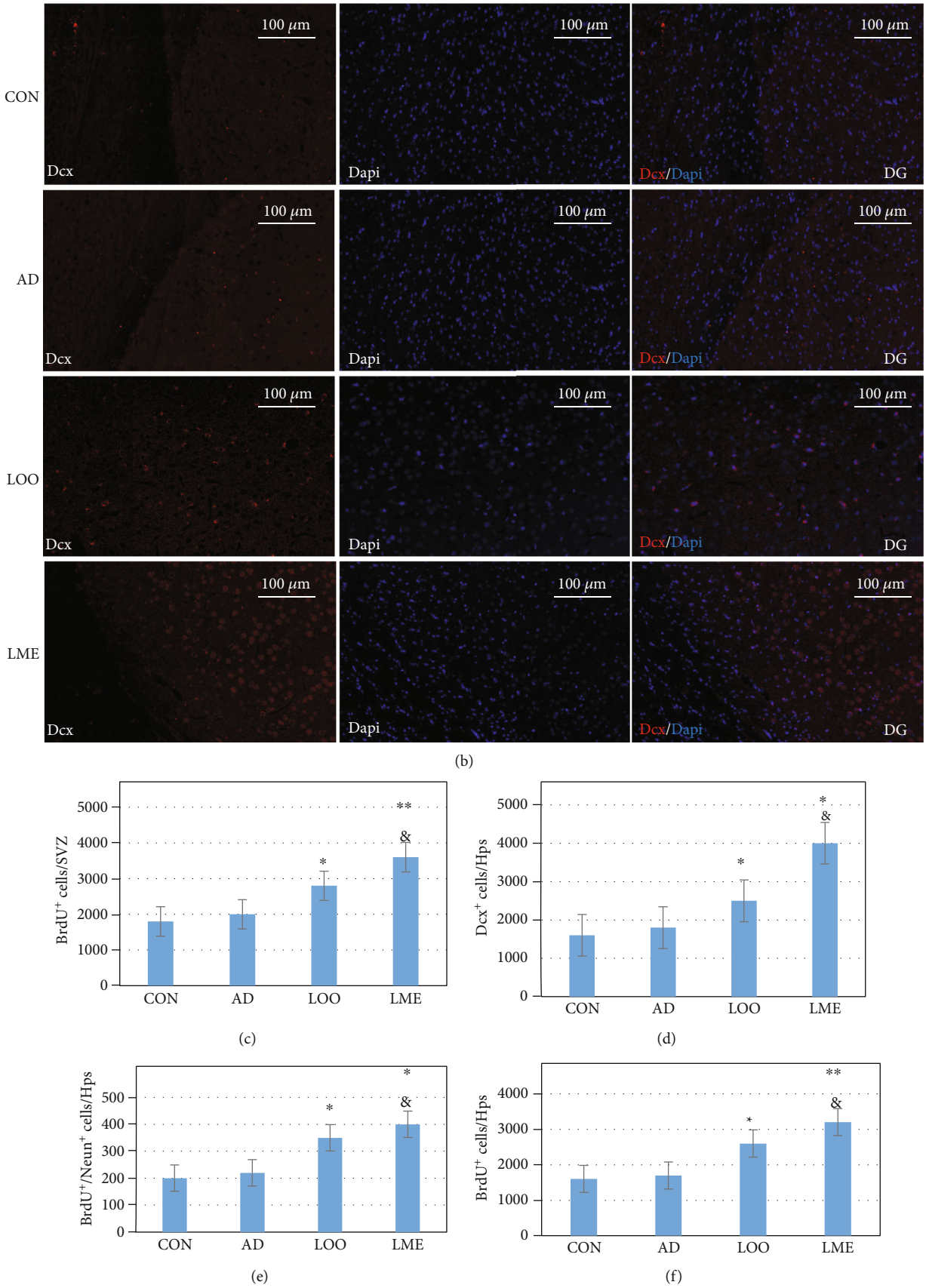

Figure 3: Continued.

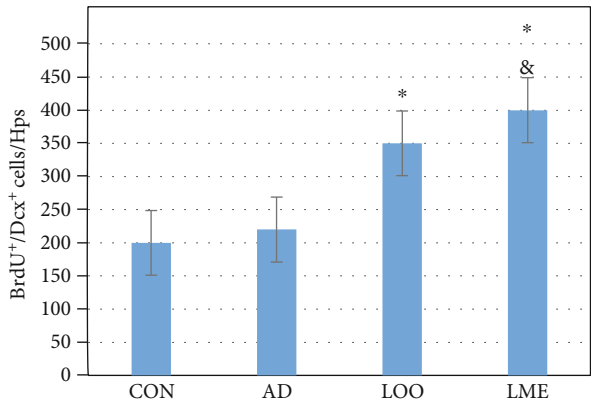

(g)

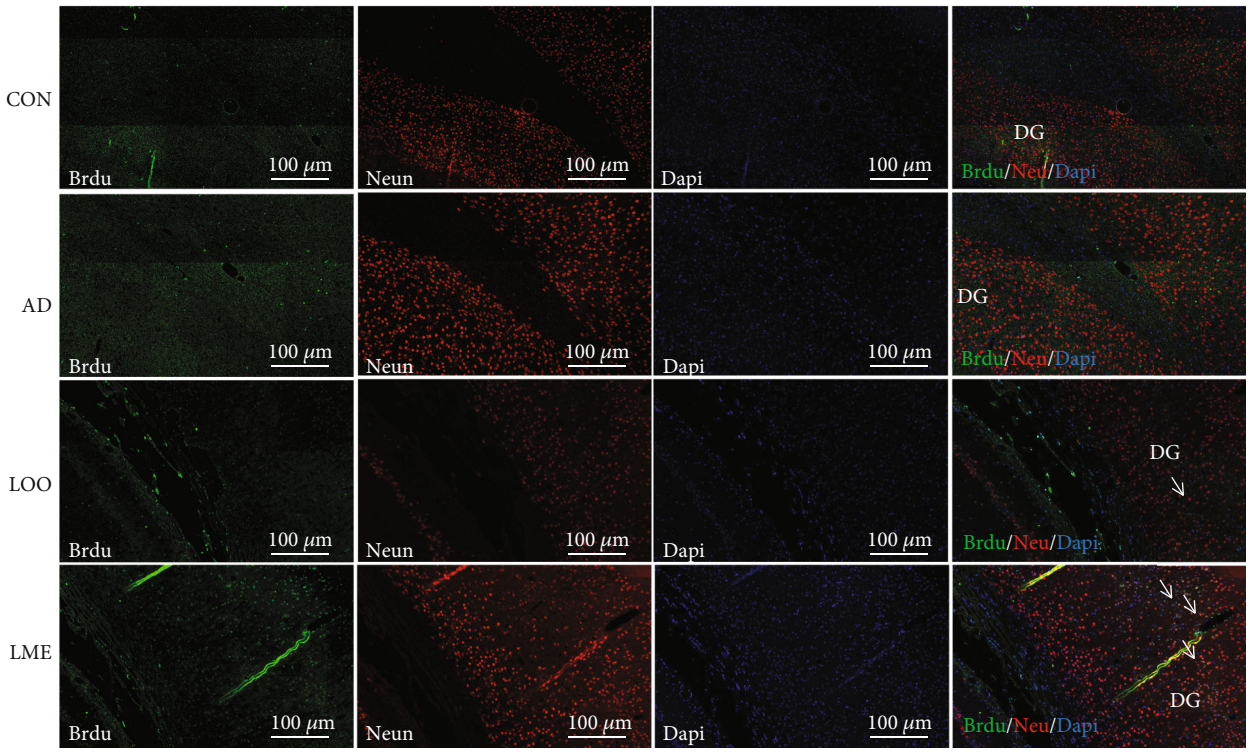

(h)

Figure 3: Continued.

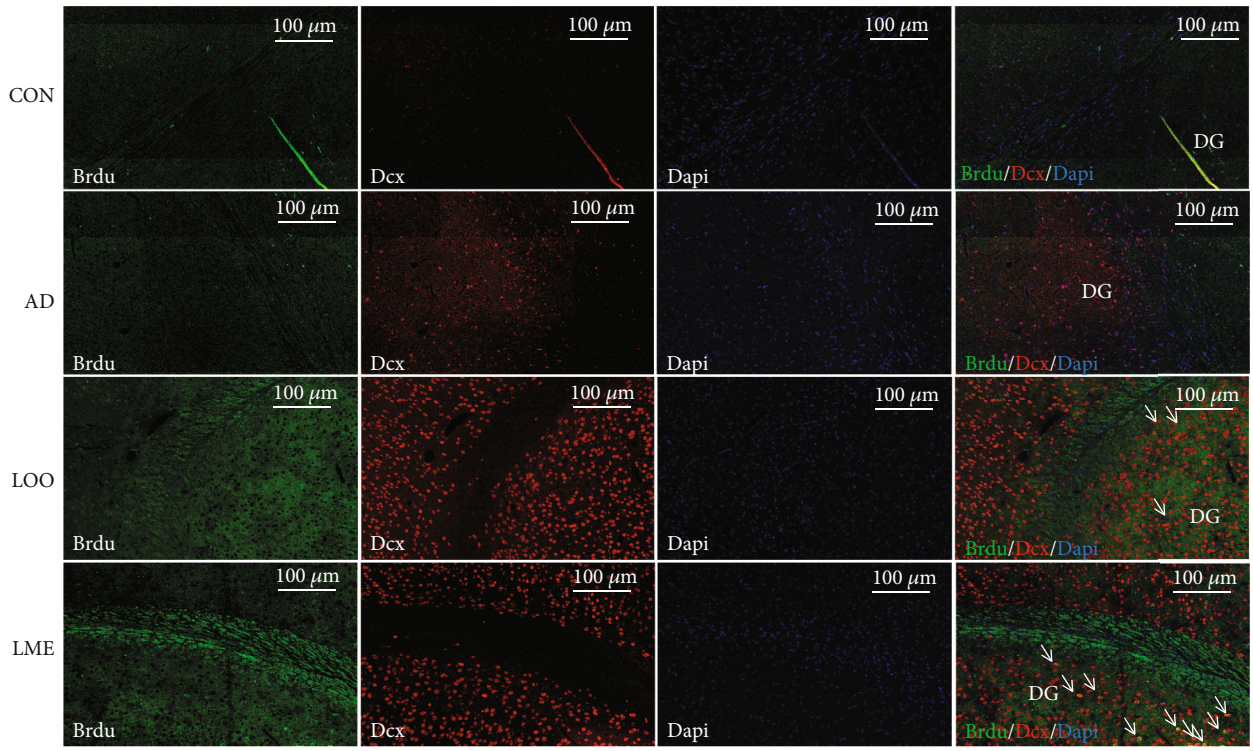

(i)

Figure 3: Continued.

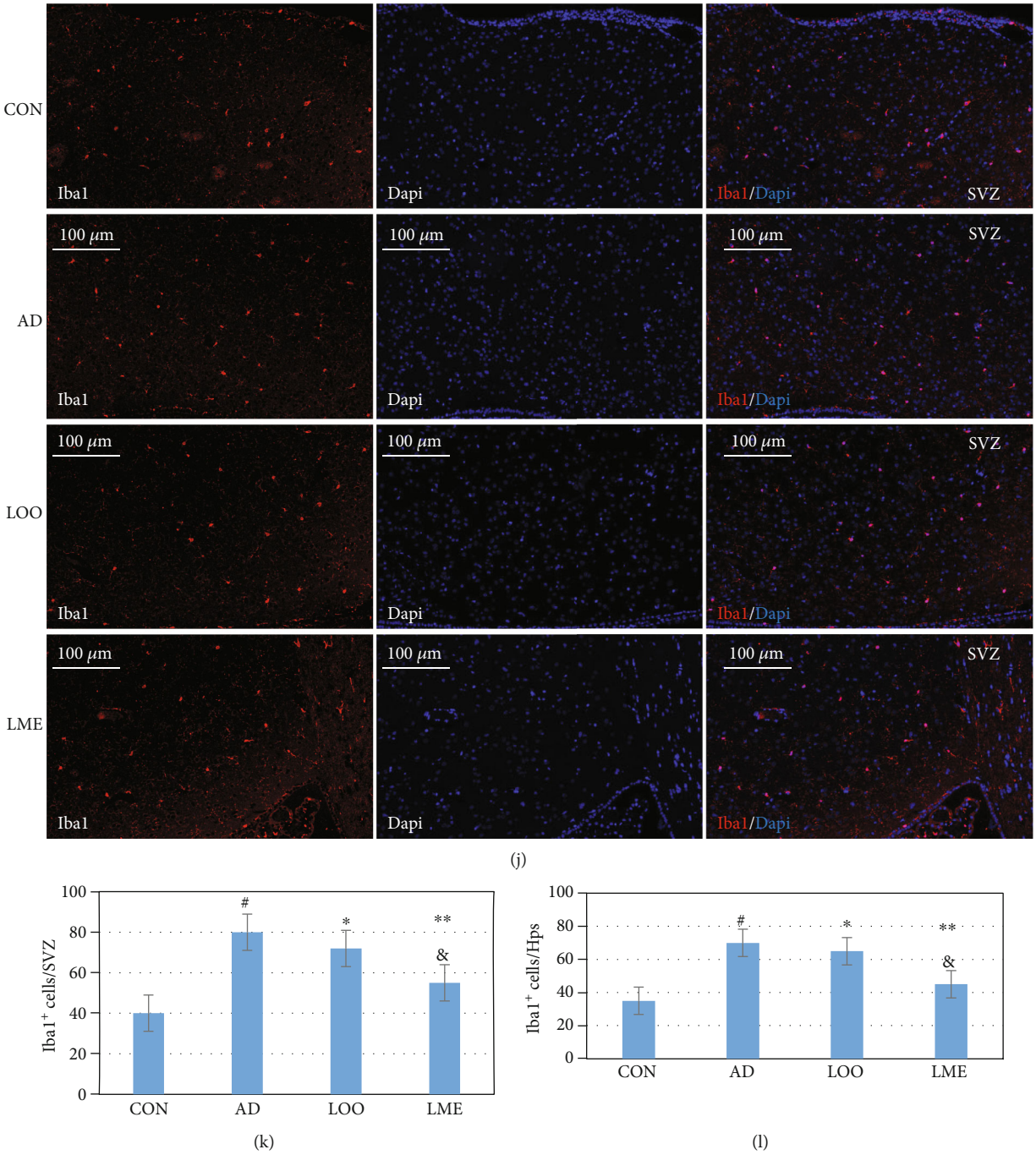

Figure 3: Continued.

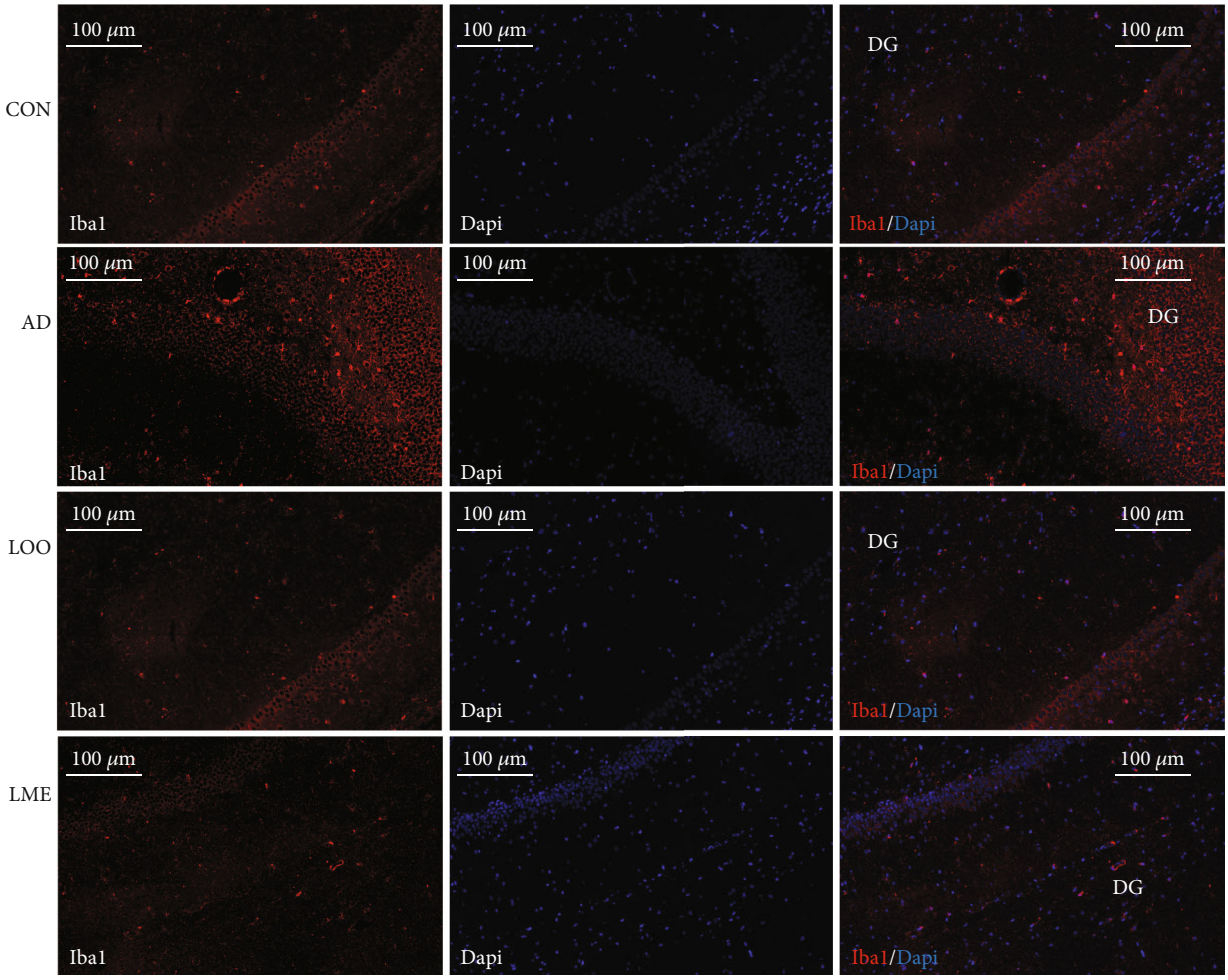

(m)

Figure 3: Continued.

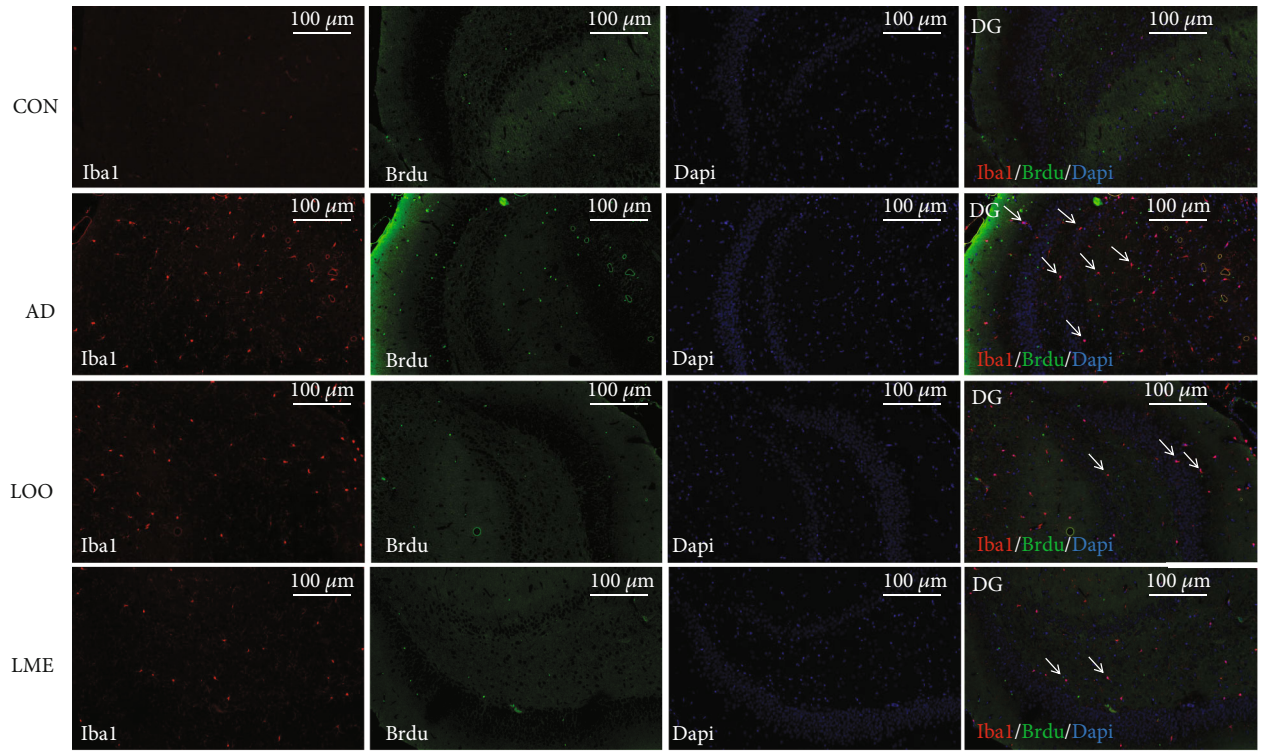

(n)

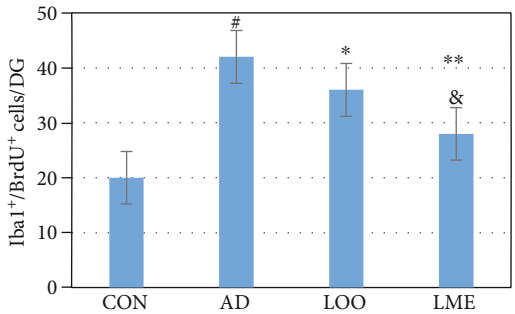

(o)

Figure 3: LOO and LME increase neuronal differentiation and adult neurogenesis in the hippocampus and SVZ of rats, especially LME. Dcx (red: marker for adult neurogenesis); BrdU (green; proliferating marker); NeuN (red; mature neuronal marker); Iba1(red; microglia marker).(a) Photomicrographs showing immunostaining of $BrdU^+$ cells in the region of SVZ. There were almost no $BrdU^+$ cells in the CON group. Scattered BrdU+ cells were found in the AD group, while the LOO group could see many $BrdU^+$ cells. A large number of $BrdU^+$ cells were observed in the LME group. LME significantly promoted neurogenesis in AD rats. (b) Photomicrographs showing immunostaining of Dcx^+ cells in the dentate gyrus region of the hippocampus. The number of Dcx^+ cells in the LOO group was higher than that in the CON and AD groups and in LME group was higher than that in the LOO group. (c, f) Quantification analysis suggested a significantly increased number of mature neurons with BrdU in the SVZ and dentate gyrus region of the hippocampus of LOO- and LME-treated rats, especially LME-treated rats. (d) Quantification analysis of Dcx^+ cells in the dentate gyrus region of the hippocampus. (h) Double immunofluorescence analysis of newly born neurons colabeled with Dcx and BrdU in the dentate gyrus region of the hippocampus of CON-, AD-, LOO-, and LME-treated rats. The LME group can see a lot of colabeled with Dcx and BrdU cells. Arrows indicate BrdU+ nuclei colabeled with Dcx. (i) The LOO group can see many $BrdU^+$ cells and colabeled with BrdU and Neun in the dentate gyrus region of the hippocampus; the LME group can see more $BrdU^+$ and $BrdU^+/Neun^+$ cells. LME promotes the differentiation of newborn neurons into mature neuronal. (e, g) Quantitative analysis in the hippocampal sections showed a significantly increased number of immature neurons colabeled with $BrdU^+/Dcx^+$ and $BrdU^+/Neun^+$, suggesting increased neuronal differentiation in LME-treated rats. (j, k, o) Photomicrographs showing immunostaining of $Iba1^+$ and $Iba1^+/BruU^+$ colabeled cells in the region of SVZ. (l–o) Immunostaining of $Iba1^+$ and $Iba1^+/BrdU^+$ colabeled cells in the dentate gyrus region of the hippocampus. (m, n) A small number of $Iba1^+$ and $Iba1^+/BruU^+$ cells in the CON group. Compared with the CON group, the number of $Iba1^+$ and $Iba1^+/BruU^+$ colabeled cells were significantly increased. Compared with the AD group, the number of positive cells of the LOO group was decreased. Compared with the LOO group, the number of positive cells of the LME group was even lower. Values are expressed as mean ± SEM ($n = 6$ rats/group). $^*p < 0.05$ versus the AD group. $^{**}p < 0.01$ versus the AD group. Scale bar = 100 μm. $^\#p < 0.05$ versus the CON group. $^\&p < 0.05$ versus the LOO group.

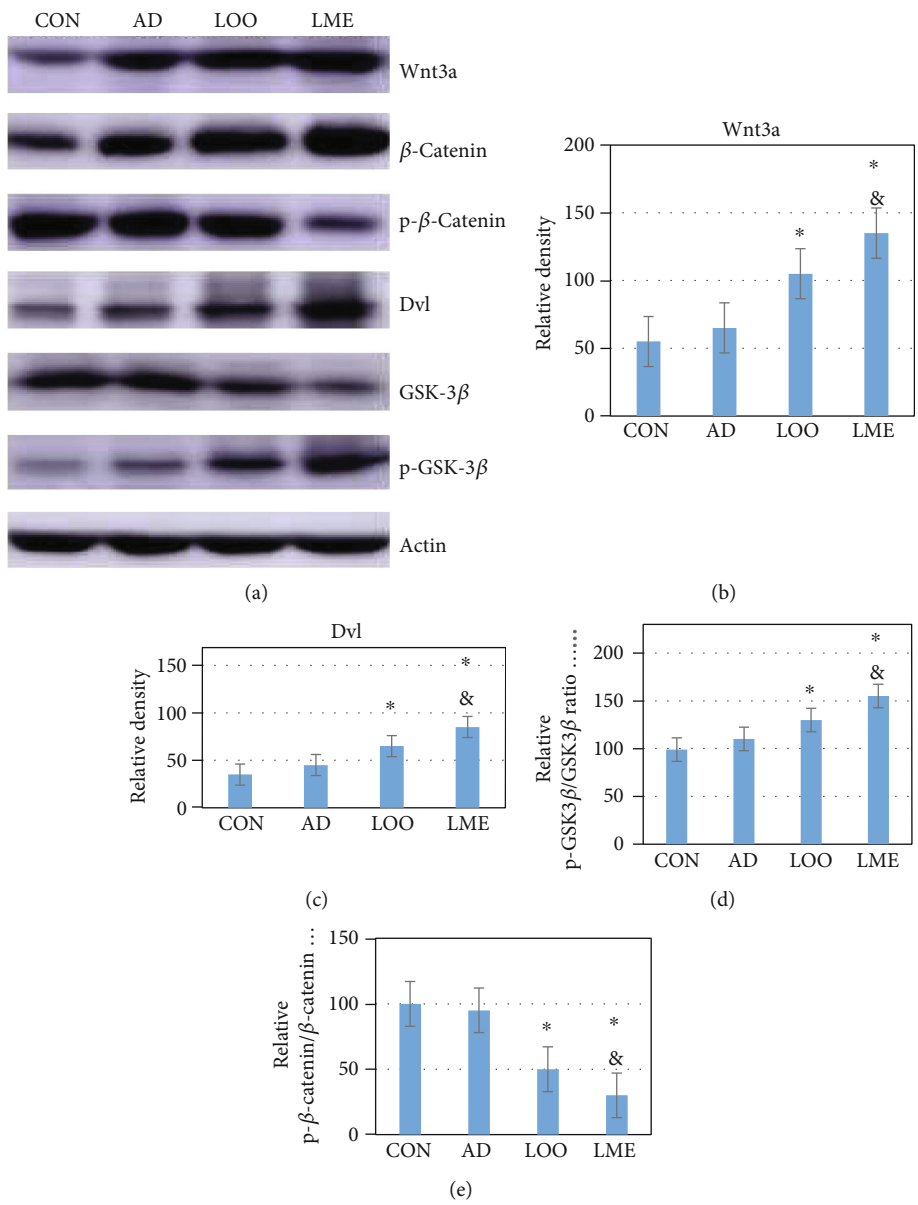

Figure 4: LME increases neurogenesis in the hippocampus through activation of the Wnt/β-catenin pathway. (a) Western blot analysis of Wnt3a, Disheveled, GSK-3β, p-GSK-3β, β-catenin, and p-β-catenin protein levels in the hippocampus. Values were normalized to β-actin. (b, c) Quantification of relative protein density after normalization with β-actin. (d, e) Ratio of p-GSK-3β/GSK-3β was significantly increased, and p-β-catenin/β-catenin significantly decreased in the LOO- and LME-treated rats. Representative blots showing two samples from each group. Mean ± SEM ($n = 6$ rats/group). $^{*}p < 0.05$ versus the AD group. $^{\&}p < 0.05$ versus the LOO group.

4. Discussion

The Morris water maze is an experimental method designed by the British psychologist Morris in 1981. It is used to study brain learning and memory mechanisms, and its application in AD research is very common [3]. The more classic Morris water maze test procedure mainly includes a positioning sea trial and space exploration test in two parts. In this study, the LOO group had shortened escape latency time and more frequently crossed the platform than the AD group. Furthermore, these variables were significantly different when comparing the LOO group with the LME group. Thus, LME could effectively improve the spatial learning and memory impairment of Aβ-induced AD rats.

Reelin is a secreted glycoprotein and extracellular matrix protein involved in brain development, synaptic plasticity, learning and memory, NSC proliferation, neurosphericity, and neuroblast migration [8, 9]. The absence of Reelin has a negative effect on the proliferation of NSC [8]. Reelin-mediated reduction in signal transduction is associated with the pathogenesis of various neurodegenerative diseases, including AD and other age-related diseases [9, 10]. Nestin-intermediate filament protein is necessary for NSC proliferation and self-renewal [11]. Pax6 is another gene that

is highly expressed in neural stem cells and plays an important role in neurogenesis [12, 13]. The high expression of Pax6 in the hippocampus is necessary for the generation and maintenance of neurogenesis [14, 15]. In our study, LOO and LME had positive effects on Reelin, Nestin, and Pax6 expressions in the hippocampus of rats, with the LME group demonstrating a more distinct expression level. Thus, LME likely promotes neurogenesis by increasing the expression of this gene.

BrdU, also known as 5′-′bromo-2′-deoxyuridine, is a thymidine analog, which competitively binds to DNA with endogenous thymidines. Studies have shown that once bound to DNA, BrdU persists and is gradually passed on to the next generation as cells divide. BrdU-labeled neurons can be detected days, weeks, months, or even years after the fixation of brain tissue with specific antibodies [16]. Typically, mice injected intraperitoneally with BrdU can pass the blood-brain barrier, which is the gold standard for research related to nerve cell regeneration. Simply put, BrdU markers can detect new cells in neurogenesis [17–19]. Dcx, also known as doublecortin, is widely expressed in migratory neurons and can also be observed early in neuronal development. It is a microtubule-related protein whose antibody can specifically mark the cytoplasm and processes of neural precursor cells. Dcx was detected on the 3rd day after injecting a virus with transcription factor Neuord1 in Parkinson's model mice [20] and in a MCAO model, Dcx can also be detected on the 7th day [20]. Studies have confirmed that Dcx is a reliable and specific marker reflecting the level of adult neurogenesis and its regulation. It has become a widely used marker in the analysis of adult neurogenesis [21, 22]. In our study, a large number of new $BrdU^+$, Dcx^+, and $BrdU^+$/-Dcx^+ cells were observed in the LME group, suggesting that LME significantly promotes neurogenesis.

Neuroinflammation is one of the major pathological changes in patients with AD, which can accelerate the deterioration of the disease. Aβ deposition can activate astrocytes and microglia, leading to the release of various proinflammatory factors and further promoting Aβ accumulation, neuronal degeneration, and dysfunction [23, 24]. Astrocytes and microglia were abundant in the brains of autopsied AD patients [25], and the same site was observed in Aβ1-42 injected rats [26]. Iba1, also known as Ionized calcium-binding adapter molecule 1, is a specific protein antibody of the microglia and macrophage. Iba1 is expressed in and increased during the activation of these cells. LME significantly reduced the number of $Iba1^+$ and $Iba1^+$/$BrdU^+$ cells in the DG and SVZ regions, suggesting that LME could significantly reduce the neuroinflammatory response.

Wnt is a type of protein that widely exists in the secretion of organism protein growth factor (either through the autocrine or paracrine route) and in the related receptors on the surface of the cell membrane. It activates the cell signaling pathways and regulates the corresponding target gene expression. It is important in the embryonic development of various kinds of cell proliferation, differentiation, migration, and apoptosis [27, 28]. The Wnt signaling pathway is mainly composed of the Wnt protein family of extracellular factors: frizzled (FZD) protein, Dvl protein, adenomatous polyposis coli gene products, GSK-3β, β-catenin, Axin, T-cytokine/-lymphoid enhancement factor (TCF/LEF), and other factors. The Wnt signaling pathway plays an important role in the development of the nervous system, which is closely related to neural tube development and ganglion formation. It can induce axon growth, dendrite formation, and protrusion and participate in the regulation of forebrain formation during the development of the central nervous system. The Wnt signaling pathways are divided into the classical Wnt/β-catenin signaling pathway and nonclassical signaling pathway according to different modes of action [29, 30]. In the classic Wnt/β-catenin signaling pathway, extracellular proteoglycan promotes Wnt signaling in the cytoplasm. The Wnt/β-catenin signaling pathway then activates the cytoplasmic Dvl protein through the FZD family. Studies have shown that the loss of Wnt3a leads to the loss of the entire hippocampus [31]. This defect may be caused by the changes of the Wnt/β-catenin pathway that interfere with NSC proliferation. This inhibits the activity of GSK-3β, which in turn inhibits the degradation of β-catenin, which continuously accumulates in the cytoplasm. Finally, the Wnt signal is transmitted into the cell to perform its corresponding function [30]. The Western blot analysis in our study proved that LME might regulate neurogenesis by activating the Wnt/β-catenin pathway to compensate for nerve loss caused by AD.

Studies have shown that lycopene-loaded microemulsion(LME) has excellent physical and chemical properties, higher oral bioavailability, and superior brain-targeting ability [8, 32]. These findings provide the basis for the application of oral brain-targeted drug delivery strategies. We further studied the promotion effect of lycopene-loaded microemulsion on cognition and neurogenesis in Aβ-induced Alzheimer's rats and the possible signaling pathway, This may providing a new idea for the treatment and research of Alzheimer's disease.

Data Availability

The data that support the findings of this study are available from the corresponding author upon reasonable request.

Conflicts of Interest

The authors declare that there is no potential conflict of interest.

Authors' Contributions

WJN, RJL, and XPL designed the study. WJN, RJL, and XN prepared the Aβ-induced AD model. GYL guide the preparation of LOO and LME. XYH and CS provided statistical support. NX, ZYF, and NC participated in PCR and other experimental operations. WJN and XPL drafted the manuscript. XPL supervised the study. All authors read, revised, and approved the final version of the manuscript.

Acknowledgments

The authors are grateful to all of the subjects for participating in this study.

References

[1] C. R. Jack, D. S. Knopman, W. J. Jagust et al., "Tracking pathophysiological processes in Alzheimer's disease: an updated hypothetical model of dynamic biomarkers," *Lancet Neurology*, vol. 12, no. 2, pp. 207–216, 2013.

[2] G. L. Ming and H. Song, "Adult neurogenesis in the mammalian brain: significant answers and significant questions," *Neuron*, vol. 70, no. 4, pp. 687–702, 2011.

[3] R. T. Moon, B. Bowerman, M. Boutros, and N. Perrimon, "The promise and perils of Wnt signaling through beta-catenin," *Science*, vol. 296, no. 5573, pp. 1644–1646, 2002.

[4] L. Jia, J. Piña-Crespo, and Y. Li, "Restoring Wnt/β-catenin signaling is a promising therapeutic strategy for Alzheimer's disease," *Molecular Brain*, vol. 12, no. 1, p. 104, 2019.

[5] K. Willert, J. D. Brown, E. Danenberg et al., "Wnt proteins are lipid-modified and can act as stem cell growth factors," *Nature*, vol. 423, no. 6938, pp. 448–452, 2003.

[6] R. Nusse, "Wnts and Hedgehogs: lipid-modified proteins and similarities in signaling mechanisms at the cell surface," *Development*, vol. 130, no. 22, pp. 5297–5305, 2003.

[7] Y. Guo, X. Mao, J. Zhang et al., "Oral delivery of lycopene-loaded microemulsion for brain-targeting: preparation, characterization, pharmacokinetic evalution and tissue distribution," *Drug Delivery*, vol. 26, no. 1, pp. 1191–1205, 2019.

[8] S. K. Tiwari, S. Agarwal, B. Seth et al., "Curcumin-loaded nanoparticles potently induce adult neurogenesis and reverse cognitive deficits in Alzheimer's disease model via canonical Wnt/β-catenin pathway," *ACS Nano*, vol. 8, no. 1, pp. 76–103, 2014.

[9] S. Massalini, S. Pellegatta, F. Pisati, G. Finocchiaro, M. G. Farace, and S. A. Ciafrè, "Reelin affects chain-migration and differentiation of neural precursor cells," *Molecular and Cellular Neurosciences*, vol. 42, no. 4, pp. 341–349, 2009.

[10] I. Knuesel, "Reelin-mediated signaling in neuropsychiatric and neurod egenerative diseases," *Progress in Neurobiology*, vol. 91, pp. 257–274, 2010.

[11] D. Park, A. P. Xiang, F. F. Mao et al., "Nestin is required for the proper self-renewal of neural stem cells," *Stem Cells*, vol. 28, no. 12, pp. 2162–2171, 2010.

[12] X. Zhang, C. T. Huang, J. Chen et al., "Pax6 is a human neuroectoderm cell fate determinant," *Cell Stem Cell*, vol. 7, no. 1, pp. 90–100, 2010.

[13] T. Kallur, R. Gisler, O. Lindvall, and Z. Kokaia, "Pax6 promotes neurogenesis in human neural stem cells," *Molecular and Cellular Neurosciences*, vol. 38, no. 4, pp. 616–628, 2008.

[14] M. Maekawa, N. Takashima, Y. Arai et al., "Pax6 is required for production and maintenance of progenitor cells in postnatal hippocampal neurogenesis," *Genes Cells*, vol. 10, no. 10, pp. 1001–1014, 2005.

[15] J. Nacher, E. Varea, J. M. Blasco-Ibañez et al., "Expression of the transcription factor Pax 6 in the adult rat dentate gyrus," *Journal of Neuroscience Research*, vol. 81, no. 6, pp. 753–761, 2005.

[16] M. Kojima and K. Kangawa, "Ghrelin: structure and function," *Physiological Reviews*, vol. 85, no. 2, pp. 495–522, 2005.

[17] I. Izquierdo, J. H. Medina, M. R. Vianna, L. A. Izquierdo, and D. M. Barros, "Separate mechanisms for short- and long-term memory," *Behavioural Brain Research*, vol. 103, no. 1, pp. 1–11, 1999.

[18] I. Izquierdo, D. M. Barros, T. M. E. Souza, M. M. de Souza, L. A. Izquierdo, and J. H. Medina, "Mechanisms for memory types differ," *Nature*, vol. 393, no. 6686, pp. 635-636, 1998.

[19] I. lzquierdo, L. A. Izquierdo, D. M. Barros et al., "Differential involvement of cortical receptor mechanisms in working, short-term and long-term memory," *Behavioural Pharmacology*, vol. 9, no. 5, pp. 421–427, 1998.

[20] R. Yang, B. C. Yuan, Y. S. Ma, S. Zhou, and Y. Liu, "The anti-inflammatory activity of licorice, a widely used Chinese herb," *Pharmaceutical Biology*, vol. 55, no. 1, pp. 5–18, 2017.

[21] J. P. Brown, S. Couillard-Després, C. M. Cooper-Kuhn, J. Winkler, L. Aigner, and H. G. Kuhn, "Transient expression of doublecortin during adult neurogenesis," *The Journal of Comparative Neurology*, vol. 467, no. 1, pp. 1–10, 2003.

[22] S. Couillard-Despres, B. Winner, S. Schaubeck et al., "Doublecortin expression levels in adult brain reflect neurogenesis," *The European Journal of Neuroscience*, vol. 21, no. 1, pp. 1–14, 2005.

[23] C. Liu, G. Cui, M. Zhu, X. Kang, and H. Guo, "Neuroinflammation in Alzheimer's disease: chemokines produced by astrocytes and chemokine receptors," *International Journal of Clinical and Experimental Pathology*, vol. 7, no. 12, pp. 8342–8355, 2014.

[24] S. Mandrekar-Colucci and G. E. Landreth, "Microglia and inflammation in Alzheimer's disease," *CNS & Neurological Disorders Drug Targets*, vol. 9, no. 2, pp. 156–167, 2010.

[25] L. R. Liu, J. C. Liu, J. S. Bao, Q. Q. Bai, and G. Q. Wang, "Interaction of Microglia and Astrocytes in the Neurovascular Unit," *Front Immunol*, vol. 11, Article ID 1024, 2020.

[26] H.-l. Gao, C. Li, H. Nabeka et al., "An 18-mer peptide derived from prosaposin ameliorates the effects of Aβ1-42 neurotoxicity on hippocampal neurogenesis and memory deficit in mice," *Journal of Alzheimer's Disease*, vol. 53, no. 3, pp. 1173–1192, 2016.

[27] S. Thuret, L. D. Moon, and F. H. Gage, "Therapeutic interventions after spinal cord injury," *Nature Reviews. Neuroscience*, vol. 7, no. 8, pp. 628–643, 2006.

[28] Y. Xu, Q. Wang, Z. Wu et al., "The effect of lithium chloride on the attenuation of cognitive impairment in experimental hypoglycemic rats," *Brain Research Bulletin*, vol. 149, pp. 168–174, 2019.

[29] B. A. Reynolds and S. Weiss, "Generation of neurons and astrocytes from isolated cells of the adult mammalian central nervous system," *Science*, vol. 255, no. 5052, pp. 1707–1710, 1992.

[30] Y. Xu, Q. Wang, D. Li et al., "Protective effect of lithium chloride against hypoglycemia-induced apoptosis in neuronal PC12 cell," *Neuroscience*, vol. 330, pp. 100–108, 2016.

[31] S. M. Lee, S. Tole, E. Grove, and A. P. McMahon, "A local Wnt-3a signal is required for development of the mammalian hippocampus," *Development*, vol. 127, no. 3, pp. 457–467, 2000.

[32] K. M. Crowe-White, T. A. Phillips, and A. C. Ellis, "Lycopene and cognitive function," *Journal of Nutritional Science*, vol. 8, 2019.

Hindawi
Neural Plasticity
Volume 2021, Article ID 9928232, 8 pages
https://doi.org/10.1155/2021/9928232

Research Article

Role of NADPH Oxidase-Induced Hypoxia-Induced Factor-1α Increase in Blood-Brain Barrier Disruption after 2-Hour Focal Ischemic Stroke in Rat

Yanping Wang,[1] Yufei Shen,[1] Xin Yu,[2] Jingxia Gu,[1] Xiaoling Zhang,[1] Beiqun Zhou,[1] Yanyun Sun,[3] Congying Xu,[1] and Shuxia Qian[1]

[1]*Department of Neurology, The Second Hospital of Jiaxing City, Jiaxing, 314000 Zhejiang, China*
[2]*Bengbu Medical College (Department of Neurology, The Second Hospital of Jiaxing City), China*
[3]*Institute of Neuroscience, Soochow University, Suzhou 215123, China*

Correspondence should be addressed to Congying Xu; xucongying0806@163.com and Shuxia Qian; shuxia_630@163.com

Received 15 March 2021; Accepted 1 August 2021; Published 16 August 2021

Academic Editor: Fushun Wang

We recently showed that inhibition of hypoxia-induced factor-1α (HIF-1α) decreased acute ischemic stroke-induced blood-brain barrier (BBB) damage. However, factors that induce the upregulation of HIF-1α expression remain unclear. Nicotinamide adenine dinucleotide phosphate (NADPH) oxidase played a critical role in reperfusion-induced BBB damage after stroke. However, the role of NADPH oxidase in BBB injury during the acute ischemia stage remains unclear. This study is aimed at investigating the role of NADPH oxidase in BBB injury and the expression of HIF-1α after acute ischemic stroke. A sutured middle cerebral artery occlusion (MCAO) model was used to mimic ischemic stroke in rats. Our results show that the inhibition of NADPH oxidase by apocynin can significantly reduce the BBB damage caused by 2 h ischemic stroke accompanied by reducing the degradation of tight junction protein occludin. In addition, treatment with apocynin significantly decreased the upregulation of HIF-1α induced by 2 h MCAO. More importantly, apocynin could also inhibit the MMP-2 upregulation. Of note, HIF-1α was not colocalized with a bigger blood vessel. Taken together, our results showed that inhibition of NADPH oxidase-mediated HIF-1α upregulation reduced BBB damage accompanied by downregulating MMP-2 expression and occludin degradation after 2 h ischemia stroke. These results explored the mechanism of BBB damage after acute ischemic stroke and may help reduce the associated cerebral hemorrhage transformation after thrombolysis and endovascular treatment after ischemic stroke.

1. Introduction

The blood-brain barrier (BBB) which is composed of microvascular endothelial cells, astrocytes, neurons, pericytes, and basement membrane could prevent blood components from entering the brain parenchyma and maintain the basic stability of the brain environment. Chronic stress could induce anxiety, depression, and schizophrenia, and stress could also damage the BBB integrity [1]. Previous studies have shown that BBB plays important roles not only in mental illnesses such as schizophrenia, autism, and depression [2] but also in neurological diseases such as stroke and dementia [3].

After acute ischemic stroke, protecting the BBB is a promising strategy [4, 5] to decrease cerebral hemorrhage, the most feared complication in patients with intravenous tissue plasminogen activator (tPA) thrombolysis [6] or post-endovascular treatment [7]. BBB damage within the reperfusion stage has been investigated widely as the restoration of ischemic cerebral blood flow is essential for the occurrence of the most devastating results of BBB damage: hemorrhage transformation and edema [8–10]. However, the mechanism of BBB disruption during the acute phase of ischemia, especially within the time window of thrombolysis [11], requires a lot of research.

Hypoxia-inducible factor-1 alpha (HIF-1α) expression upregulation was observed in noninfarcted ventromedial striatum and preoptical area (POA) where BBB damage was observed after 2 h MCAO [12], and our recent study reported

that YC-1, a HIF-1α inhibitor, decreased BBB damage by regulating matrix metalloproteinase-2 (MMP-2) and vascular endothelial growth factor (VEGF) during acute cerebral ischemia [13]. However, the factors that induce the upregulation of HIF-1α in the acute phase of ischemic stroke remain unclear.

Acidosis and free radicals have been shown to upregulate HIF-1α expression [14], and oxidative stress plays a critical role in BBB disruption during the reperfusion phase after ischemic stroke [15]. For example, nicotinamide adenine dinucleotide phosphate (NADPH) oxidase was shown to play a key role in reperfusion-induced BBB damage in experimental stroke [16], and inhibition of NADPH oxidase is neuroprotective after ischemic stroke [17]. In addition, apocynin, a NADPH oxidase inhibitor, significantly improved the endothelial function of rat and human blood vessels [18]. However, the role of NADPH oxidase in BBB injury within the thrombolytic time window of acute ischemic stroke remains unclear.

In the current study, a rat middle cerebral artery occlusion (MCAO) model was used to mimic ischemic stroke. The effect of NADPH oxidase inhibition on BBB injury and HIF-1α expression after acute ischemic stroke will be explored.

2. Material and Methods

2.1. Animal Model of Middle Cerebral Artery Occlusion. Thirty-four male Sprague-Dawley rats were purchased from SLAC Company (Shanghai, China). Under the condition of constant temperature (23 ± 1°C) and light-controlled vivarium (12-hour light/12-hour dark cycle), 2-3 rats are housed in each cage. Rats can get water and food for free. The Soochow University Animal Care University Committee approved animal procedures in accordance with the National Institutes of Health Laboratory Animal Care and Use Guidelines. Each effort is to reduce the number of animals and minimize their suffering. Rats (270-290 g body weight) underwent a 2-hour MCAO operation using a suture model. We followed the research method of Shen et al. in 2018 [13]. The success of the operation was further tested by 2,3,5-triphenyltetrazolium chloride (TTC) staining (Figure 1).

2.2. Apocynin Administration. Apocynin (Sigma) or vehicle was recruited to inhibit NADPH oxidase. It was dissolved in 1% DMSO, and 40 mg/kg body weight was given via femoral vein one hour before MCAO surgery. This dose has been shown to effectively inhibit NADPH oxidase and reduce BBB damage after stroke [16].

2.3. Evan's Blue Leakage Detection. Evan's blue (EB) dye extravasation is a reliable and widely used method to detect BBB injury. After 2 hours of MCAO, EB was injected through a tail vein (Sigma, St. Louis, MO, USA, 2% wt/vol in PBS, 3 mL/kg). After 10 minutes of reperfusion, the EB was fully circulated to the ischemic hemisphere; then, ice-cold PBS was perfused, and the brain was quickly removed [19]. We detect the severity of BBB damage through either quantifying the mean leakage area which was calculated as averaged area proportion of the sections measured [20] or measuring content in the tissue of nonischemic and ischemic brain hemisphere [21].

2.4. Immunofluorescence Staining. The rats were immediately perfused with PBS and 4% PFA after cerebral ischemia for 2 hours. We followed the previously published methods of Shen et al. in doing immunofluorescence staining [13]. In brief, 20 μm thick cryosections were preincubated for 1 hour at room temperature in PBS which contained 0.1% Triton X-100, 1% BSA, and 5% goat serum (Solarbio, Beijing, China) to cover nonspecific binding sites. The HIF-1α (1 : 200, Abcam) and RECA-1 (1 : 100, Abcam) primary antibodies were applied to the brain slices and incubated overnight at 4°C. Appropriate secondary antibodies that bind to Cy3 (anti-mouse, 1 : 800) or 488 (anti-rabbit, 1 : 800) were used for detection. The nucleus was stained with Dapi. The LSM 700 confocal laser scanning microscope (Zeiss) was used to take images from the ischemic area and the mirror nonischemic area [13].

2.5. Western Blot. We did this experiment following a recently published paper [21]. Briefly, after collecting the tissue of the ventral striatum and preoptic area (region of interest 1, ROI 1) as well as the cortex and dorsal striatum (region of interest 2, ROI 2) of the ischemic (I) and nonischemic (NI) hemispheres, we detected the protein concentration using a BCA protein detection kit (Beyotime, Haimen, Jiangsu, China). After boiling the aliquots of the homogenate (30 μg total protein), they were electrophoresed on a 10% SDS-PAGE acrylamide gel and then transferred to a 0.45 μm PVDF membrane (Millipore, Billerica, Massachusetts, USA). After blocking the membrane in PBS-T (phosphate-buffered saline and 0.1% Tween-20) containing 5% skim milk for 2 hours, it was incubated overnight with occludin (1 : 300, Invitrogen), HIF-α (1 : 300, Novus), or β-actin (1 : 5000, Hubei, China) primary antibodies. After washing three times with PBS-T, incubation with horseradish peroxidase- (HRP-) conjugated anti-rabbit or anti-mouse secondary antibody (Boster, Wuhan, Hubei, China) followed for 2 hours at room temperature. The membrane was developed and photographed using the Super Signal West Pico HRP substrate kit (Thermo Fisher, Rockford, IL, USA). The protein band intensity was quantified after normalization with β-actin. Every measurement is repeated three times.

2.6. Zymography. The tissues of the ischemic (I) and nonischemic (NI) brain hemispheres are homogenized in the lysis buffer for matrix metalloproteinase, and the level of MMP-2/9 in the homogenate was determined by the gel-gelatin zymography method [13].

2.7. Statistical Analysis. The data were shown as the mean ± SEM. Statistical analysis adopts one- or two-way analysis of variance (SPSS software, version 17.0). The value of $P < 0.05$ is statistically significant.

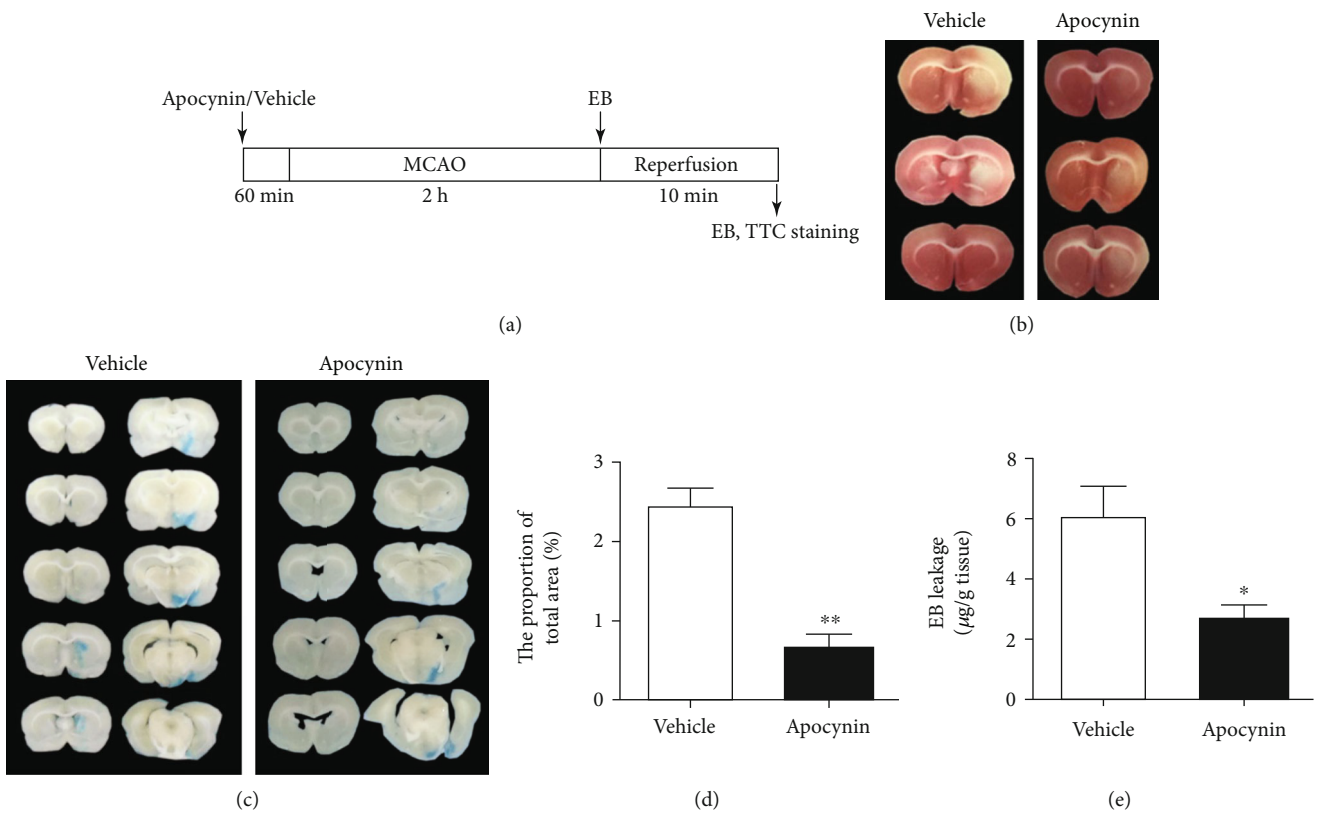

Figure 1: Effect of apocynin treatment on BBB injury induced by 2 h ischemia. (a) The experimental procedure diagram. (b) TTC staining showed the success of MCAO surgery. (c) Ten consecutive brain coronal sections demonstrated leakage of Evan's blue (EB) in the rats treated with vehicle or apocynin. (d) EB extravasation is quantitated and expressed as the average area ratio (%) of the measured brain slice section (%). $^{\#}P < 0.05$ versus the vehicle ctrl, $n = 6$ per group. (d) Another method to quantitatively determine the amount of EB leakage in brain tissue, and it was expressed as per gram of brain tissue (μg/g) by the external EB standard curve. $^{\#}P < 0.05$ versus vehicle ctrl. Data were demonstrated as the mean ± SEM, $n = 5$ per group.

3. Results

3.1. Apocynin Treatment Alleviates BBB Injury and Degradation of Tight Junction Protein Occludin Induced by 2-Hour MCAO. We first explored whether inhibiting NADPH oxidase could decrease the disruption of BBB integrity induced by 2 hours of MCAO. The experimental program diagram is shown in Figure 1(a). Apocynin was administered 60 min before 2 h MCAO. EB was recruited to determine BBB permeability [22]. We first used TTC staining to confirm the success of our MCAO surgery (Figure 1(b)). A set of representative images of EB dye in the sliced brain is provided in Figure 1(c). Extravasation of EB was obviously seen in the ROI 1 of ipsilateral cerebral hemisphere of rats subjected to 2-hour MCAO (Figure 1(c)). Treatment with NADPH oxidase inhibitor apocynin dramatically reduced the EB leakage area (Figure 1(c)), and quantitative data demonstrated that apocynin reduced EB extravasation by approximately 75% (Figure 1(d)), indicating that inhibition of NADPH oxidase can effectively reduce BBB damage within 2 hours after the onset of ischemia stroke.

Degradation of occludin is a key factor in BBB injury after 2 hours of MCAO [21]. In order to check if the upregulation of free radicals degraded the occludin, we used western blot to examine the expression of occludin in the interest region. We demonstrated that after 2 hours of ischemia, occludin degradation was seen in the ventral striatum and preoptical area (ROI 1, Figure 2(a)), but not in the cortex and dorsal striatum (ROI 2, Figure 2(b)). Pretreatment with apocynin significantly decreased occludin degradation induced by 2 hours of MCAO in ROI 1 (Figure 2(a)), indicating that NADPH oxidase had a key role in the degradation of occludin after 2 hours of ischemia stroke.

3.2. Effect of Apocynin on 2 h MCAO-Induced HIF-1α Expression. Upregulated HIF-1α has been shown to contribute to the disruption of BBB integrity after 2 h MCAO [12, 13]. In this study, we tested whether inhibition of NADPH oxidase could reduce BBB damage through downregulating HIF-1α. Our results showed that after 2 hours of ischemia, HIF-1α in ROI 1 was significantly upregulated (Figure 2(c)), while HIF-1α in ROI 2 was not upregulated (Figure 2(d)), and inhibition of NADPH oxidase with apocynin could significantly prevent this increase (Figure 2(c)), indicating that NADPH oxidase played an important role in HIF-1α upregulation induced by 2 hours of ischemia stroke.

3.3. Effect of Apocynin on MMP-2 Expression after 2 h Ischemia. The MMP-2/9 level after 2 hours of MCAO was detected by gelation zymography (Figure 3). In the

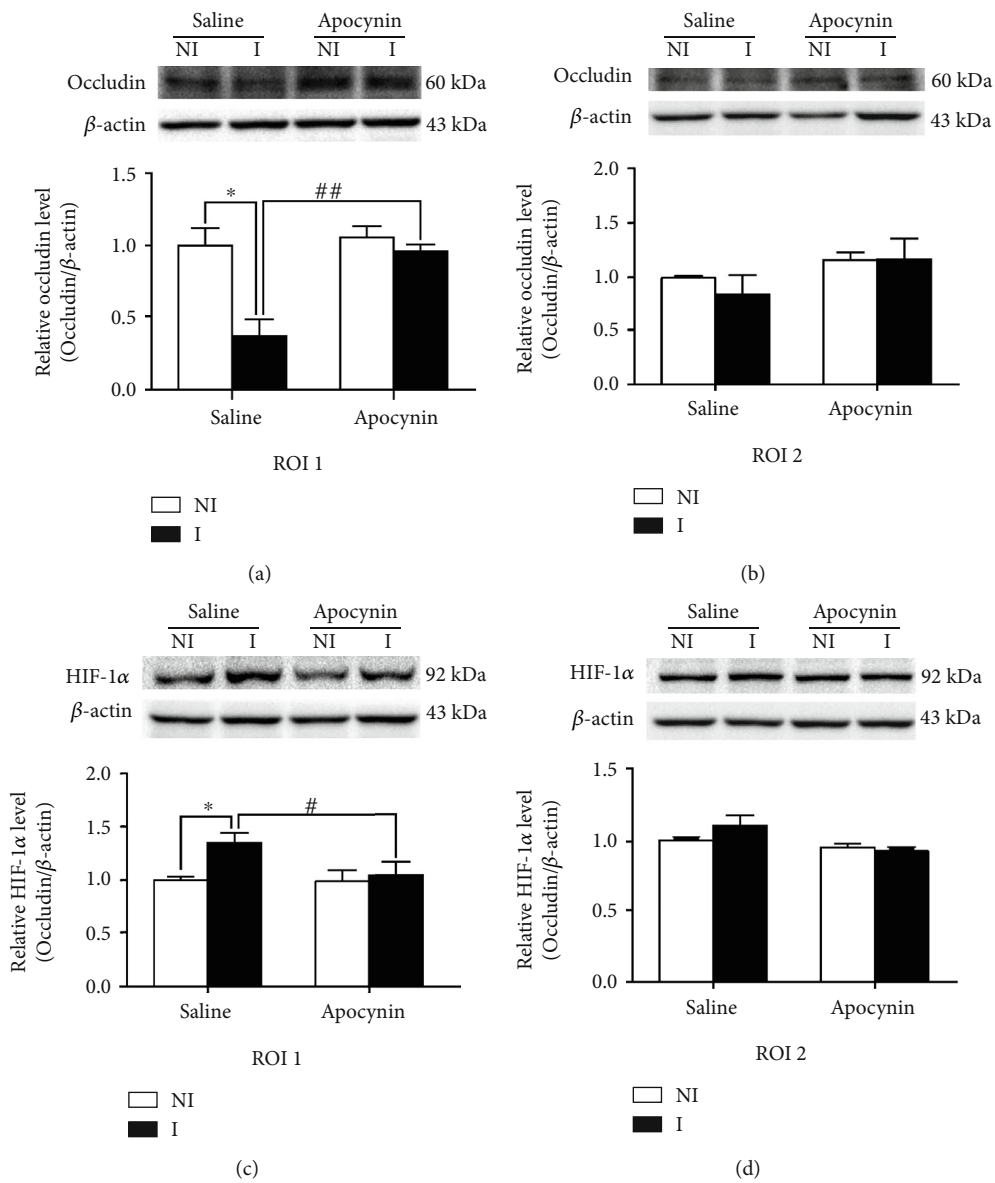

Figure 2: Effect of apocynin on occludin degradation and HIF-1α upregulation after 2 h MCAO. Western blot was recruited to detect occludin expression in nonischemic (NI) and ischemic (I) brain tissues. (a, b) Representative blots showed expression of occludin in regions of interest (ROI) 1 (a) and 2 (b) in apocynin- or vehicle-treated rats (upper panel). After the normalization, the relative band intensity of occludin to β-actin was quantified (lower panel). After two hours of MCAO, the occludin level in ROI 1 was significantly reduced ($^*P < 0.05$, compared with the vehicle group in ROI 1), while the occludin level in ROI 2 did not significantly decrease ($P > 0.05$). Apocynin treatment significantly alleviated the degradation of occludin ($P < 0.05$). (c, d) Representative blots demonstrated the expression of HIF-1α in ROI 1 (c) and ROI 2 (d) of apocynin- or vehicle-treated rats (upper panel). HIF-1α expression was quantified after normalization to β-actin (bottom panel). The expression of HIF-1α in ROI 1 ($^*P < 0.05$) but not in ROI 2 ($P > 0.05$) was significantly increased in the vehicle group after two hours of MCAO. Apocynin treatment significantly reduced the HIF-1α increase ($P < 0.05$). The data are expressed as the mean ± SEM, $n = 5$ per group.

nonischemic (NI) hemisphere, the levels of MMP-2 were not significantly different, and the results of MMP-9 were similar (Figure 3(a)). Consistent with our previous study, in the ischemic hemisphere (I), the level of MMP-2 increased significantly after 2 hours of MCAO (Figure 3), and treatment with apocynin significantly prevented the upregulation of MMP-2 induced by 2 hours of MCAO (Figure 3(b)), suggesting that NADPH oxidase was critically involved in HIF-1α-mediated MMP-2 upregulation by 2 hours of ischemia stroke.

3.4. Expression of HIF-1α in Blood Vessel after 2 Hours of MCAO. Using double labeling of HIF-1α and the endothelial cell marker RECA-1 [12], we demonstrated that HIF-1α was not expressed in endothelial cells (Figure 4(a)) in either striatum (Str) or cortex (Ctx); in addition, HIF-1α was not expressed in bigger blood vessels either (Figure 4(b)); this is consistent with our previous study showing that the upregulated HIF-1α after acute ischemia stroke was from neurons but not astrocytes or endothelial cells.

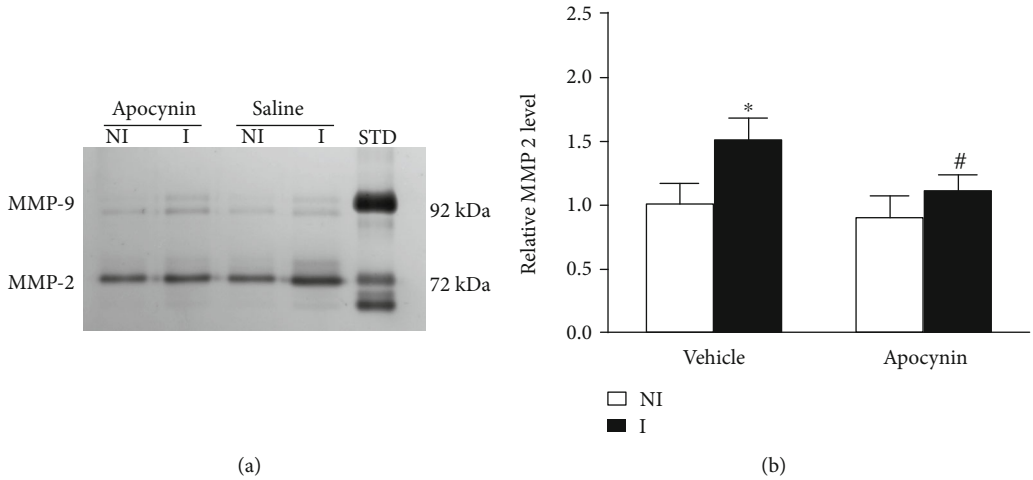

Figure 3: Effect of apocynin on 2 h ischemia-induced MMP-2 upregulation. After 2 hours of ischemia, the expression of MMP-2/9 was induced in the ischemic brain tissue. (a) Representative gelatin zymogram demonstrated the MMP-2/9 levels in the brain tissue of nonischemic (NI) and ischemic (I) sites. The MMP-2 level was quantitated (b). After 2 hours of ischemia, MMP-2 in ischemic tissues increased significantly (compared to NI, $P < 0.05$, $n = 5$), and apocynin treatment can significantly prevent the increase of MMP-2 (compared to vehicle, $P < 0.05$, $n = 5$). Data were expressed as the mean ± SEM.

4. Discussion

The BBB permeability after acute ischemic stroke is critical to determine the outcome of reperfusion by tissue plasminogen activator (tPA) thrombolysis [6] or endovascular mechanical thrombus removal [7]. This critical role of BBB status prompted us to examine BBB injury at the early phase of ischemic stroke in order to provide strategies to improve acute stroke management and show clues for further tPA thrombolysis. This study demonstrated that (1) pretreatment with NADPH oxidase inhibitor apocynin significantly reduced the injury of BBB integrity and disruption of occludin induced by 2 hours of ischemia, (2) pretreatment with apocynin reduced increase of HIF-1α expression induced by 2 hours of ischemia, (3) apocynin could also inhibit the MMP-2 upregulation after 2 h ischemic stroke, and (4) HIF-1α is not colocalized with bigger blood vessels. The results demonstrate that in the case of acute cerebral ischemia, inhibiting NADPH oxidase can reduce the increase of HIF-1α and upregulation of MMP-2, thereby reducing the BBB injury.

NADPH oxidase played a key role in BBB disruption in experimental stroke [16], and its inhibition with inhibitor apocynin improved endothelial function in rat and human blood vessels [18]. Our results showed that apocynin significantly reduced 2 h MCAO-induced BBB injury, providing evidence showing that NADPH oxidase plays a key role in BBB injury not only in the reperfusion stage during which a lot of free radicals were produced but also in the ischemia phase. Since BBB injury was observed in noninfarcted striatum and preoptical area which have moderately reduced cerebral blood flow [20], moderately decreased cerebral blood flow may induce reperfusion-like disruption events such as upregulated reactive oxygen species generations in hypoperfused tissue to accelerate BBB injury [16, 23]. Since our aim is to find a target and strategy to extend the time window and reduce tPA thrombolysis-associated hemorrhage transformation, we investigated the mechanism underlying BBB damage within the thrombolytic time window and we did not investigate the effect of the apocynin on infarction size either.

Apocynin has shown neuroprotective effect after ischemia-reperfusion [17]. For example, coadministration of NADPH plus apocynin provided greater anti-inflammatory and neuroprotective effects on a mouse model of stroke [24], and combination of apocynin with lipoic acid increased the neuroprotection effect on a rat model of stroke [25]. However, apocynin has been shown to improve stroke outcomes with a narrow dose range [26], and apocynin also showed worse outcomes after stroke in aged rats [27]. Therefore, the application of apocynin to reduce ischemia-induced BBB damage and protect the brain must be very careful.

Several factors have shown important roles in regulating HIF-1α expression after stroke. For example, HIF-1α could be regulated by β2-adrenergic receptor after focal ischemia stroke [12]. In addition, C1q contributed to poststroke angiogenesis via the LAIR1-HIF1α-VEGF pathway [28], and LncRNA SNHG1 regulated cerebrovascular injury through HIF-1α/VEGF after ischemia stroke [29]. In addition, Bu Yang Huan Wu decoction prevented ischemic stroke-induced reperfusion injury in rats by downregulating HIF-1α and VEGF and upregulating β-ENaC expression [30]. Our results showed that NADPH oxidase inhibition with inhibitor apocynin significantly reduced HIF-1α increase induced by 2 hours of MCAO, providing another strategy to regulate HIF-1α expression after ischemic stroke.

We have previously found that MMP-2 induction is significantly upregulated in the ventral striatum and preoptic area and the interaction of HIF-1α and MMP-2 was critically involved in BBB injury after acute ischemic stroke. Downregulation of HIF-1α can reduce BBB injury through inhibiting MMP-2 activity [13]. The results showed that the apocynin

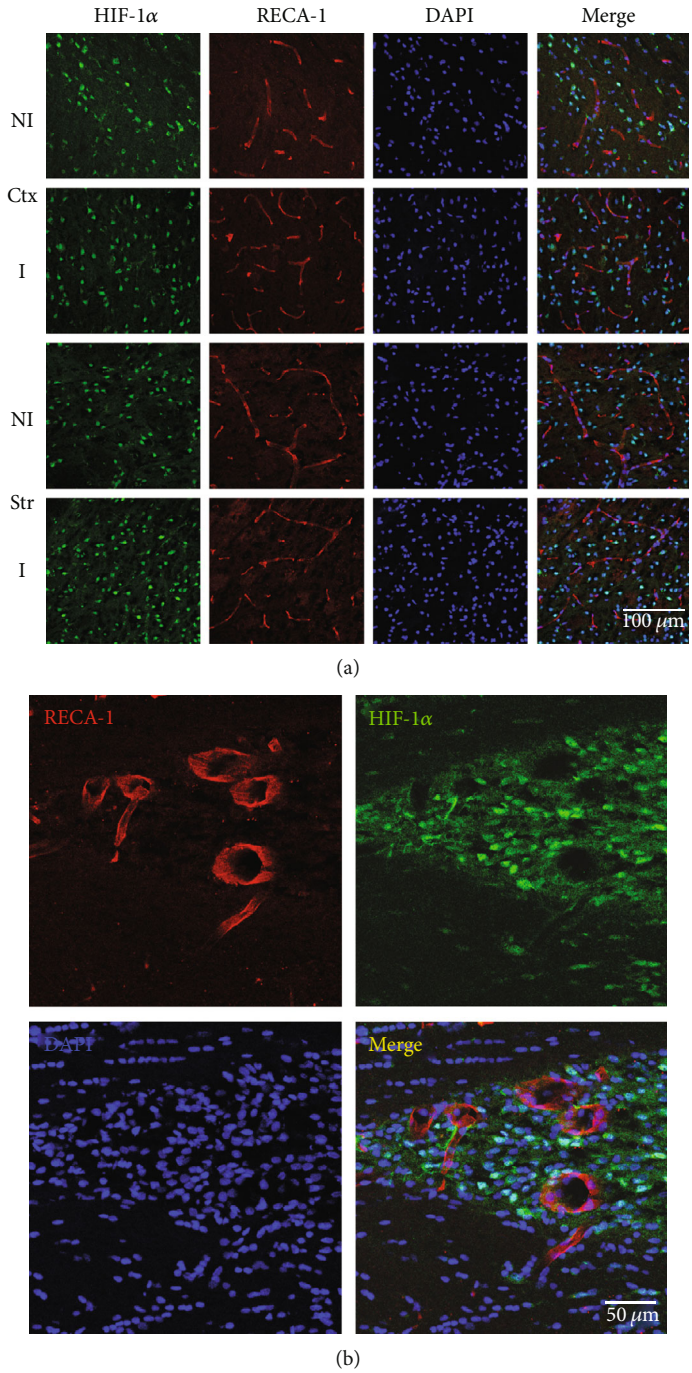

Figure 4: Expression of HIF-1α in the blood vessel after 2 hours of MCAO. Using RECA-1 (endothelial cell marker) immunohistochemical staining method to detect HIF-1α expression in endothelial cells of the cortex (Ctx) and striatum (Str) in nonischemic (NI) and ischemic (I) hemispheres after 2 hours of ischemia stroke. (a) Double immunostaining of HIF-1α (green) and RECA-1 (red) showed that HIF-1α did not colocalize with endothelial cells. $n = 3$ per group. Scale bar = 100 μm. (b) Double immunostaining of HIF-1α (green) and RECA-1 (red) showed no expression of HIF-1α in bigger blood vessels. Scale bar = 50 μm. $n = 3$ per group.

significantly reduced the upregulation of MMP-2 induced by 2 h ischemia, suggesting that inhibition of NADPH oxidase-mediated HIF-1α upregulation can reduce the BBB injury by reducing the MMP-2 induction.

Our results showed that HIF-1α was not colocalized with a bigger vessel, and a previous study has showed that HIF-1α was not colocalized with endothelial cells [12], suggesting that HIF-1α played an important role in BBB damage, but its upregulation was not induced by the blood vessel after acute ischemia stroke. During the reperfusion stage, the blood vessel may contribute to HIF-1α upregulation since HIF-1α played a key role in the protection of BBB from reperfusion injury [31, 32]. HIF-1α downregulation reduced acute hyperglycemia-induced cerebral hemorrhage

transformation in the ischemic hemisphere [33, 34] and decrease BBB injury induced by rat neonatal stroke [35]. Effect of YC-1 treatment on reduction of BBB leakage and reduction of occludin has been shown by our collaborator [12] and us [13].

The findings may provide a new clue to prevent the damage of the integrity of BBB from ischemic damage and to extend the thrombolytic time window of tPA or endovascular treatment and reduce cerebral hemorrhage.

In summary, our results show that during acute cerebral ischemia, inhibiting NADPH oxidase with apocynin reduced BBB damage by regulating HIF-1α upregulation and MMP-2 induction. The results gave new clues for preventing ischemic brain injury by protecting the integrity of the BBB and for prolonging the time window of tPA thrombolysis or endovascular treatment and reducing cerebral hemorrhage transformation.

Abbreviations

BBB: Blood-brain barrier
EB: Evan's blue
ECA: External carotid artery
HIF-1α: Hypoxia-inducible factor-1 alpha
HT: Hemorrhagic transformation
I: Ischemic hemisphere
ICA: Internal carotid artery
MCAO: Middle cerebral artery occlusion
MMP: Matrix metalloproteinase
NADPH: Nicotinamide adenine dinucleotide phosphate
NI: Nonischemic
POA: Preoptical area
ROI: Region of interest
tPA: Tissue plasminogen activator
TTC: 2,3,5-Triphenyltetrazolium chloride
VEGF: Vascular endothelial growth factor.

Data Availability

Data and material will be provided upon request.

Ethical Approval

The study protocol was approved by the ethical committee of Soochow University.

Conflicts of Interest

The authors declare no conflict of interest.

Authors' Contributions

The work was performed and accomplished by all authors. YW, YS, SQ, ZL, JG, YS, XZ, BZ, and YS contributed to the execution of the entire project and the statistical analyses. CX, SQ, YS, and YW wrote the manuscript. All authors have read and approved the final manuscript. Yanping Wang and Yufei Shen are co-first authors.

Acknowledgments

This work was supported by grants from the Zhejiang Provincial Natural Science Foundation of China under Grant nos. LGF20H090018 and 2018C37093 and Health and Family Planning Commission of Zhejiang Province (grant no. 2017KY653).

References

[1] M. O. Welcome and N. E. Mastorakis, "Stress-induced blood brain barrier disruption: molecular mechanisms and signaling pathways," *Pharmacological Research*, vol. 157, 2020.

[2] J. Kealy, C. Greene, and M. Campbell, "Blood-brain barrier regulation in psychiatric disorders," *Neuroscience Letters*, vol. 726, 2020.

[3] M. D. Sweeney, Z. Zhao, A. Montagne, A. R. Nelson, and B. V. Zlokovic, "Blood-brain barrier: from physiology to disease and back," *Physiological Reviews*, vol. 99, no. 1, pp. 21–78, 2019.

[4] X. Jin, J. Liu, and W. Liu, "Early ischemic blood brain barrier damage: a potential indicator for hemorrhagic transformation following tissue plasminogen activator (tPA) thrombolysis?," *Current Neurovascular Research*, vol. 11, no. 3, pp. 254–262, 2014.

[5] J. Liu, J. Weaver, X. Jin et al., "Nitric oxide interacts with caveolin-1 to facilitate autophagy-lysosome-mediated claudin-5 degradation in oxygen-glucose deprivation-treated endothelial cells," *Molecular Neurobiology*, vol. 53, no. 9, pp. 5935–5947, 2016.

[6] R. Leigh, S. S. Jen, A. E. Hillis et al., "Pretreatment blood-brain barrier damage and post-treatment intracranial hemorrhage in patients receiving intravenous tissue-type plasminogen activator," *Stroke*, vol. 45, no. 7, pp. 2030–2035, 2014.

[7] R. Leigh, S. Christensen, B. C. Campbell et al., "Pretreatment blood-brain barrier disruption and post-endovascular intracranial hemorrhage," *Neurology*, vol. 87, no. 3, pp. 263–269, 2016.

[8] J. M. Simard, T. A. Kent, M. Chen, K. V. Tarasov, and V. Gerzanich, "Brain oedema in focal ischaemia: molecular pathophysiology and theoretical implications," *Lancet Neurology*, vol. 6, no. 3, pp. 258–268, 2007.

[9] S. Hafez, M. Coucha, A. Bruno, S. C. Fagan, and A. Ergul, "Hyperglycemia, acute ischemic stroke, and thrombolytic therapy," *Translational Stroke Research*, vol. 5, no. 4, pp. 442–453, 2014.

[10] Y. Shi, R. K. Leak, R. F. Keep, and J. Chen, "Translational stroke research on blood-brain barrier damage: challenges, perspectives, and goals," *Translational Stroke Research*, vol. 7, no. 2, pp. 89–92, 2016.

[11] W. Hacke, M. Kaste, E. Bluhmki et al., "Thrombolysis with alteplase 3 to 4.5 hours after acute ischemic stroke," *The New England Journal of Medicine*, vol. 359, no. 13, pp. 1317–1329, 2008.

[12] Y. Sun, X. Chen, X. Zhang et al., "β2-adrenergic receptor-mediated HIF-1α upregulation mediates blood brain barrier damage in acute cerebral ischemia," *Frontiers in Molecular Neuroscience*, vol. 10, p. 257, 2017.

[13] Y. Shen, J. Gu, Z. Liu et al., "Inhibition of HIF-1α reduced blood brain barrier damage by regulating MMP-2 and VEGF during acute cerebral ischemia," *Frontiers in Cellular Neuroscience*, vol. 12, p. 288, 2018.

[14] J. Xu, Z. Peng, R. Li et al., "Normoxic induction of cerebral HIF-1α by acetazolamide in rats: Role of acidosis," *Neuroscience Letters*, vol. 451, no. 3, pp. 274–278, 2009.

[15] W. Wang, M. Li, Q. Chen, and J. Wang, "Hemorrhagic transformation after tissue plasminogen activator reperfusion therapy for ischemic stroke: mechanisms, models, and biomarkers," *Molecular Neurobiology*, vol. 52, no. 3, pp. 1572–1579, 2015.

[16] T. Kahles, P. Luedike, M. Endres et al., "NADPH oxidase plays a central role in blood-brain barrier damage in experimental stroke," *Stroke*, vol. 38, no. 11, pp. 3000–3006, 2007.

[17] H. Chen, Y. S. Song, and P. H. Chan, "Inhibition of NADPH oxidase is neuroprotective after ischemia-reperfusion," *Journal of Cerebral Blood Flow and Metabolism*, vol. 29, no. 7, pp. 1262–1272, 2009.

[18] C. A. Hamilton, M. J. Brosnan, S. Al-Benna, G. Berg, and A. F. Dominiczak, "NAD(P)H oxidase inhibition improves endothelial function in rat and human blood vessels," *Hypertension*, vol. 40, no. 5, pp. 755–762, 2002.

[19] Y. Liu, W. C. Liu, Y. Sun et al., "Normobaric hyperoxia extends neuro- and vaso-protection of N-acetylcysteine in transient focal ischemia," *Molecular Neurobiology*, vol. 54, no. 5, pp. 3418–3427, 2017.

[20] X. Jin, J. Liu, Y. Yang, K. J. Liu, Y. Yang, and W. Liu, "Spatiotemporal evolution of blood brain barrier damage and tissue infarction within the first 3 h after ischemia onset," *Neurobiology of Disease*, vol. 48, no. 3, pp. 309–316, 2012.

[21] Y. Wang, X. Wang, X. Zhang et al., "D1 receptor-mediated endogenous tPA upregulation contributes to blood-brain barrier injury after acute ischaemic stroke," *Journal of Cellular and Molecular Medicine*, vol. 24, no. 16, pp. 9255–9266, 2020.

[22] X. Wang, G. X. Xue, W. C. Liu et al., "Melatonin alleviates lipopolysaccharide-compromised integrity of blood-brain barrier through activating AMP-activated protein kinase in old mice," *Aging Cell*, vol. 16, no. 2, pp. 414–421, 2017.

[23] T. J. Abbruscato and T. P. Davis, "Combination of hypoxia/aglycemia compromises in vitro blood-brain barrier integrity," *The Journal of Pharmacology and Experimental Therapeutics*, vol. 289, no. 2, pp. 668–675, 1999.

[24] Y. Y. Qin, M. Li, X. Feng et al., "Combined NADPH and the NOX inhibitor apocynin provides greater anti- inflammatory and neuroprotective effects in a mouse model of stroke," *Free Radical Biology & Medicine*, vol. 104, pp. 333–345, 2017.

[25] B. J. Connell and T. M. Saleh, "Co-administration of apocynin with lipoic acid enhances neuroprotection in a rat model of ischemia/reperfusion," *Neuroscience Letters*, vol. 507, no. 1, pp. 43–46, 2012.

[26] X. N. Tang, B. Cairns, N. Cairns, and M. A. Yenari, "Apocynin improves outcome in experimental stroke with a narrow dose range," *Neuroscience*, vol. 154, no. 2, pp. 556–562, 2008.

[27] K. A. Kelly, X. Li, Z. Tan, R. L. VanGilder, C. L. Rosen, and J. D. Huber, "NOX2 inhibition with apocynin worsens stroke outcome in aged rats," *Brain Research*, vol. 1292, pp. 165–172, 2009.

[28] A. V. Terry and P. M. Callahan, "Nicotinic acetylcholine receptor ligands, cognitive function, and preclinical approaches to drug discovery," *Nicotine & Tobacco Research*, vol. 21, pp. 383–394, 2019.

[29] L. Zhang, X. Luo, F. Chen et al., "LncRNA SNHG1 regulates cerebrovascular pathologies as a competing endogenous RNA through HIF-1α/VEGF signaling in ischemic stroke," *Journal of Cellular Biochemistry*, vol. 119, no. 7, pp. 5460–5472, 2018.

[30] A. A. Conti, L. McLean, S. Tolomeo, J. D. Steele, and A. Baldacchino, "Chronic tobacco smoking and neuropsychological impairments: a systematic review and meta-analysis," *Neuroscience and Biobehavioral Reviews*, vol. 96, pp. 143–154, 2018.

[31] J. Yan, B. Zhou, S. Taheri, and H. Shi, "Differential effects of HIF-1 inhibition by YC-1 on the overall outcome and blood-brain barrier damage in a rat model of ischemic stroke," *PLoS One*, vol. 6, no. 11, article e27798, 2011.

[32] W. L. Yeh, D. Y. Lu, C. J. Lin, H. C. Liou, and W. M. Fu, "Inhibition of hypoxia-induced increase of blood-brain barrier permeability by YC-1 through the antagonism of HIF-1alpha accumulation and VEGF expression," *Molecular Pharmacology*, vol. 72, no. 2, pp. 440–449, 2007.

[33] C. Chen, R. P. Ostrowski, C. Zhou, J. Tang, and J. H. Zhang, "Suppression of hypoxia-inducible factor-1alpha and its downstream genes reduces acute hyperglycemia-enhanced hemorrhagic transformation in a rat model of cerebral ischemia," *Journal of Neuroscience Research*, vol. 88, no. 9, pp. 2046–2055, 2010.

[34] Z. Zhang, J. Yan, and H. Shi, "Role of hypoxia inducible factor 1 in hyperglycemia-exacerbated blood-brain barrier disruption in ischemic stroke," *Neurobiology of Disease*, vol. 95, pp. 82–92, 2016.

[35] D. Mu, X. Jiang, R. A. Sheldon et al., "Regulation of hypoxia-inducible factor 1α and induction of vascular endothelial growth factor in a rat neonatal stroke model," *Neurobiology of Disease*, vol. 14, no. 3, pp. 524–534, 2003.

Hindawi
Neural Plasticity
Volume 2021, Article ID 4504363, 11 pages
https://doi.org/10.1155/2021/4504363

Research Article

Destructive Effects of Pyroptosis on Homeostasis of Neuron Survival Associated with the Dysfunctional BBB-Glymphatic System and Amyloid-Beta Accumulation after Cerebral Ischemia/Reperfusion in Rats

Zhongkuan Lyu,[1] Yuanjin Chan,[1] Qiyue Li,[1] Qiang Zhang,[2] Kaili Liu,[2] Jun Xiang,[3] Xiangting Li,[3] Dingfang Cai,[3] Yaming Li,[1] Bing Wang,[2] and Zhonghai Yu[2]

[1]*Geriatrics Department of Chinese Medicine, Huadong Hospital, Fudan University, Shanghai 200040, China*
[2]*Department of Traditional Chinese Medicine, Shanghai Jiao Tong University Affiliated Sixth People's Hospital, Shanghai 200233, China*
[3]*Department of Integrative Medicine, Zhongshan Hospital, Fudan University, Shanghai 200032, China*

Correspondence should be addressed to Zhongkuan Lyu; 18111280008@fudan.edu.cn, Yaming Li; doctorymli@163.com, Bing Wang; bingliver@163.com, and Zhonghai Yu; yuzhonghai0715@126.com

Received 17 May 2021; Revised 4 July 2021; Accepted 30 July 2021; Published 16 August 2021

Academic Editor: Fang Pan

Neuroinflammation-related amyloid-beta peptide (Aβ) accumulation after cerebral ischemia/reperfusion (I/R) accounts for cerebral I/R injuries and poststroke dementia. Recently, pyroptosis, a proinflammatory cell death, has been identified as a crucial pathological link of cerebral I/R injuries. However, whether pyroptosis acts as a trigger of Aβ accumulation after cerebral I/R has not yet been demonstrated. Blood-brain barrier (BBB) and glymphatic system mediated by aquaporin-4 (AQP-4) on astrocytic endfeet are important pathways for the clearance of Aβ in the brain, and pyroptosis especially occurring in astrocytes after cerebral I/R potentially damages BBB integrity and glymphatic function and thus influences Aβ clearance and brain homeostasis. In present study, the method of middle cerebral artery occlusion/reperfusion (MCAO/R) was used for building models of focal cerebral I/R injuries in rats. Then, we used lipopolysaccharide and glycine as the agonist and inhibitor of pyroptosis, respectively, Western blotting for detections of pyroptosis, AQP-4, and A$\beta_{1\text{-}42}$ oligomers, laser confocal microscopy for observations of pyroptosis and Aβ locations, and immunohistochemical stainings of SMI 71 (a specific marker for BBB integrity)/AQP-4 and Nissl staining for evaluating, respectively, BBB-glymphatic system and neuronal damage. The results showed that pyroptosis obviously promoted the loss of BBB integrity and AQP-4 polarization, brain edema, Aβ accumulation, and the formation of A$\beta_{1\text{-}42}$ oligomers and thus increased neuronal damage after cerebral I/R. However, glycine could inhibit cerebral I/R-induced pyroptosis by alleviating cytomembrane damage and downregulating expression levels of cleaved caspase-11/1, N-terminal gasdermin D, NLRP3 (nucleotide-binding domain, leucine-rich repeat containing protein 3), interleukin-6 (IL-6) and IL-1β and markedly abate above pathological changes. Our study revealed that pyroptosis is a considerable factor causing toxic Aβ accumulation, dysfunctional BBB-glymphatic system, and neurological deficits after cerebral I/R, suggesting that targeting pyroptosis is a potential strategy for the prevention of ischemic stroke sequelae including dementia.

1. Introduction

Ischemic stroke, a common cerebrovascular disease, constitutes most strokes and is among the leading causes of long-term disability and dementia worldwide [1, 2]. For patients suffered from acute cerebral ischemia, there is a pressing need to restore blood flow of the ischemic cerebral tissue in a short-time window. However, the additional injuries following ischemia/reperfusion (I/R) greatly influence the therapeutic efficacy of restoring blood flow and induce ischemic

stroke sequelae including dementia. As one of the key factors causing Alzheimer's disease (AD), neuroinflammation-related amyloid-beta peptide (Aβ) massively accumulates around astrocytes in ischemic brain tissues, accounting for cerebral I/R injuries and the occurrence of dementia induced by ischemic stroke [3–6].

Astrocytes in the brain are star-shaped cells with a range of functions, among which are to supply energy for neurons, underscoring the importance of astrocytes in neuroglial vascular coupling named neurovascular unit (NVU) [7]. Moreover, aquaporin-4 (AQP-4) on astrocytic endfeet functions as an important part of both blood-brain barrier (BBB) and glymphatic system to clear metabolic wastes such as Aβ and maintains the homeostasis of central nervous system (CNS) environment [8].

Pyroptosis is a newly discovered proinflammatory form of cell death distinguished from apoptosis, and it has been demonstrated that pyroptosis plays an important role during I/R injuries in multiple vital organs including the brain [9–11]. And the known signaling molecules involved in pyroptosis mainly include certain cysteine-dependent aspartate-directed proteases (caspase), proinflammatory factors such as interleukin-1β (IL-1β), nucleotide-binding oligomerization domain-like receptors pyrin domain containing 3 (NLRP3), and the gasdermin family [12]. Various studies have demonstrated that the gasdermin D (GSDMD) can be cleaved by activated caspase-4/5/11 (caspase-4/5 in humans, and the orthologous caspase-11 in rodents) or caspase-1 to form N-terminal (GSDMD-N) fragment which determines pyroptotic cell death by forming membrane pores [13–15].

Astrocytic and microglial pyroptosis induced by cerebral I/R has been reported [16, 17]. Therefore, we hypothesized and designed this study to identify that pyroptosis, especially occurring in astrocytes, aggravates the damage of BBB-glymphatic system, triggers the accumulation of toxic Aβ, and thus destroys homeostasis of neurons survival after cerebral I/R, and that inhibition of pyroptosis could ameliorate these pathological changes.

2. Materials and Methods

2.1. Animals. A total of sixty specific pathogen-free (SPF) male Sprague-Dawley rats, weighing 200-230 g, were obtained from Shanghai Laboratory Animal Research Center and housed in SPF animal rooms of Shanghai Jiao Tong University Affiliated Sixth People's Hospital, under the standard laboratory conditions with controlled humidity and constant temperature. Experimental operations were carried out after the acclimation of animals for several days with unlimited food and water. Both animal handling procedures and experimental protocols were consistent with the guidelines for the management of laboratory animals and approved by the Animal Ethics Committee of Shanghai Jiao Tong University Affiliated Sixth People's Hospital.

2.2. Groups and Interventions. Lipopolysaccharide (LPS) and glycine (Gly) are usually used as the activator and inhibitor of pyroptosis, respectively [18, 19]. Accordingly, the rats in this study were randomly divided into four groups including the sham group, cerebral ischemia/reperfusion group (I/R), cerebral ischemia/reperfusion plus LPS group (I/R + LPS), and cerebral ischemia/reperfusion plus Gly group (I/R + Gly). And LPS (125 μg/ml) and Gly (200 mg/ml) (#L2630, #G7126, Sigma-Aldrich, USA) dissolved in distilled water were intraperitoneally injected (LPS, 500 μg/kg; Gly, 800 mg/kg) at 3 h after cerebral I/R according to previous studies [20, 21]. Rats in other groups were injected with equivalent volume of distilled water.

2.3. Models of Focal Cerebral I/R Injuries and Neurological Function Assessment. The method of left middle cerebral artery occlusion/reperfusion (MCAO/R) was used for building models of focal cerebral I/R injuries in rats as described in our previous work [22, 23]. Rats in I/R, I/R + LPS, and I/R + Gly groups were subjected to MCAO/R surgeries, while rats in the sham group underwent the same operation with no insertion of the monofilament. Neurological examinations were performed after reperfusion. And in order to exclude the interference of operative failures, the rats subjected to MCAO/R with no detectable neurological deficits were eliminated from the following researches and analyses. During the whole course, rectal temperature and cardiovascular rate of all rats were monitored and maintained. Finally, eight rats were died or ruled out from the experiments. And neurological deficits score of rats at 24 h after reperfusion in present study were evaluated on a 5-point scale as described previously [24].

2.4. Brain Water Content Measurement. Brain water content was measured with the dry-wet weight method. Briefly, after being anesthetized with pentobarbital sodium (0.5%, 1 ml/100 g), the animals were sacrificed, and the brain tissues were removed and separated into ischemic and nonischemic hemispheres, which were immediately weighed to obtain the wet weight (WW). Then, the tissues were placed in an oven at 60°C for 24 h and reweighed to obtain the dry weight (DW). The brain water content was assessed with the following formula: $100\% \times (\mathrm{WW} - \mathrm{DW})/\mathrm{WW}$.

2.5. Western Blotting Analysis for Detections of Pyroptosis, AQP-4, and A$\beta_{1\text{-}42}$ Oligomers. After 24 h reperfusion, the rats were deeply anesthetized, and the brains were quickly removed after cardiac perfusion with 200 ml normal saline. The expression levels of pyroptosis-related proteins, AQP-4, and A$\beta_{1\text{-}42}$ oligomers were detected by Western blotting. In brief, after concentrations measurement, equal amounts of protein extracted from ischemic penumbra and equivalent area under sham were separated by 10% sodium dodecyl sulfate-polyacrylamide gel electrophoresis (SDS-PAGE) and electrotransferred onto the polyvinylidnene fluoride membranes (#ISEQ00010, Millipore, USA). The membranes were blocked at room temperature with 5% bovine serum albumin (BSA) for 1 h and incubated with the following primary antibodies at 4°C overnight: caspase-11 (1 : 200, #sc-56038, Santa Cruz, USA), GSDMD (1 : 1000, #93709, Cell Signaling Technology, USA), NLRP3 (1 : 300, #19771-1-AP, Proteintech, USA), caspase-1 (1 : 500, #22915-1-AP, Proteintech), IL-6 (1 : 200, #sc-57315, Santa Cruz), IL-1β (1 : 200, #sc-12742,

Santa Cruz), AQP-4 (1 : 200, #sc-32739, Santa Cruz), A$\beta_{1\text{-}42}$ (1 : 1000, #ab201060, Abcam, UK), and β-actin (1 : 1000, #3700, Cell Signaling Technology). Then, the membranes were washed and incubated with corresponding secondary antibodies (1 : 5000, #L3012/L3032, Signalway Antibody, USA) for 1 h at room temperature. Western blotting bands were developed with the enhanced chemiluminescence kit (#WBKLS0500, Millipore), and then pictures were captured with a gel imaging instrument (Bio-Rad Laboratories, USA), and the intensities were analyzed by ImageJ software (National Institutes of Health, USA).

2.6. LDH Assay. Briefly, homogenates from cortex tissues in ischemic penumbra and equivalent area under sham were prepared and centrifuged at 1,2000 rpm and 4°C for 10 min, and then the supernatant was used to detect the content of LDH for preliminarily assessing the degree of pyroptosis by an LDH assay kit (#C0016, Beyotime, China) following the manufacturer's instructions.

2.7. Observations of Pyroptosis and Aβ Locations by Laser Confocal Microscopy. After anesthetization followed by infusion with normal saline and then 4% paraformaldehyde, the brains of rats were removed and immersed in 4% paraformaldehyde for 24 h fixation and then prepared for paraffin sections. According to the procedure described previously [25], we made an optimum proposal of PI staining in this study. Briefly, the paraffin sections were dewaxed and rehydrated (100% ethanol for 3 min, 95% ethanol for 2 min, 80% ethanol for 2 min, 75% ethanol for 2 min, H_2O for 1 min) followed by incubation with PI dye (5 μg/ml, #ST511, Beyotime) diluted by phosphate buffer solution (PBS) for 2 min at room temperature. Subsequently, PI dye was removed quickly and washed with PBS, and then 4′,6-diamidino-2-phenylindole (DAPI) staining solution was added onto the sections for 10 min at 37°C. For immunofluorescence stainings of protein colocalization, after dewaxing and rehydration with gradient ethanol, the sections further went through antigen retrieval, permeation by 0.3% triton-X 100, and then blockage with 5% BSA. Subsequently, the sections were incubated with the first antibodies mixed for caspase-11/ionized calcium-binding adapter molecule-1 (Iba-1) (#ab178847, Abcam), caspase-11/glial fibrillary acidic protein (GFAP) (#23935-1-AP, Proteintech), Aβ (#sc-28365, Santa Cruz)/GFAP, and GSDMD (#20770-1-AP, Proteintech)/GFAP (#60190-1-Ig, Proteintech) overnight at 4°C followed by incubations with corresponding mixed Alexa Fluor 488/647 secondary antibodies (1 : 500, #A0423/A0473, #A0428/A0468, Beyotime) for 1 h at room temperature. After DAPI staining, all the sections were covered with antiquenching agent for capturing fluorescent pictures by a laser scanning confocal microscope (Leica Wetzlar, Germany).

2.8. Evaluations of the BBB-Glymphatic System and Neuronal Damage. Endothelial barrier antigen (EBA, clone: SMI 71) is a specific marker for BBB integrity, and polarization loss of AQP-4 on astrocytic endfeet is the major cause of glymphatic dysfunction. Thus, we further made evaluations of BBB and glymphatic system by the immunohistochemical staining of SMI 71 and AQP-4. Briefly, the sections were dewaxed and rehydrated and went through antigen retrieval, permeation, and inactivation of the endogenous catalase by H_2O_2 and then blockage with 5% BSA. Subsequently, the sections were incubated, respectively, with anti-rat BBB antibody (SMI 71) (1 : 100, #836812, BioLegend, USA) and AQP-4 antibody (1 : 100, #sc-32739, Santa Cruz) overnight at 4°C followed by incubations with the secondary antibody in immunohistochemical kit (#KIHC-5, Proteintech) for 1 h at room temperature. Then, 3,3-diaminobenzidine tetrahydrochloride and hematoxylin were used as color developing reagents for visualizing the sections. Neuronal damage was evaluated by the method of Nissl staining as described in our previous study [22]. Briefly, the sections were dewaxed, rehydrated, and stained with Nissl staining solution (#E607316, Sangon Biotech, China) at room temperature for 20 min. Subsequently, the sections were rinsed and cleared in graded ethanol and xylene and coverslipped under permount. Finally, all sections were observed with a light microscope (Leica Wetzlar, Germany).

2.9. Statistical Analysis. All the data were expressed as the mean ± standard deviation (SD). Statistical analysis was performed using GraphPad Prism 8.0 (GraphPad Software Inc., USA). Statistical significance of difference among groups was analyzed by one-way ANOVA or unpaired Student's t-test. A value of $P < 0.05$ was considered to be statistically significant.

3. Results

3.1. Effects of LPS and Gly Interventions on Neurological Deficits. Figure 1 exhibited the schematic diagram of experimental protocol (Figure 1(a)) and neurological deficits score of rats at 24 h after reperfusion (Figures 1(b) and 1(c)) in present study. The neurological deficits were evaluated on a 5-point scale as described in Figure 1(b). And the result of neurological function assessment showed that cerebral I/R-induced neurological deficits were obviously exacerbated by LPS but reversed by Gly as described in Figure 1(c).

3.2. Effects of LPS and Gly Interventions on Degree of Pyroptosis. Detection of the LDH content in damaged tissues and PI staining is effective methods used for preliminarily assessing the degree of pyroptosis. In present study, compared with the sham group, the I/R group showed higher LDH content and more positive PI staining which were obviously increased by LPS and reduced by Gly (Figures 2(a) and 2(b)), implying that pyroptosis was aggravated in the I/R + LPS group but alleviated in the I/R + Gly group after reperfusion.

3.3. Pyroptosis Focuses on Microglia and Astrocytes after Reperfusion. Pyroptosis is initially found as an innate immune response with strong inflammatory reaction. Thus, in this study, locations of pyroptosis were locked on the immunocyte in the brain. As expected, pyroptosis mainly occurred in microglia and astrocytes of ischemic brain tissues, which was observed from the double immunofluorescence staining of caspase-11 colocalized with Iba-1

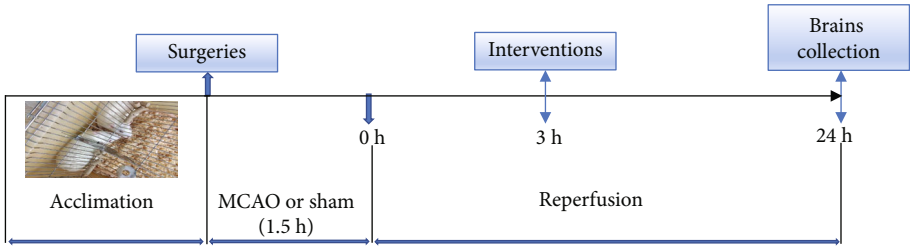

(a)

Score	Neurobehavioral manifestation
0	no deficit
1	failure to extend right forepaw
2	circling to the right
3	falling to the right
4	no spontaneous walking with a depressed level of consciousness

(b)

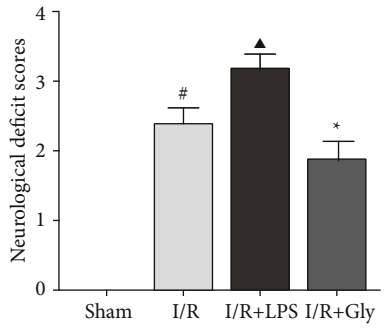

(c)

Figure 1: (a) Schematic diagram of the experimental protocol. (b) Longa's score and corresponding neurobehavioral manifestation. (c) Neurological deficit scores of each group according to Longa's score method, $n = 10$. Data are presented as mean ± SD. $^{\#}P < 0.05$, I/R group versus sham group; $^{\blacktriangle}P < 0.05$, I/R + LPS group versus I/R group; $^{*}P < 0.05$, I/R + Gly group versus I/R group.

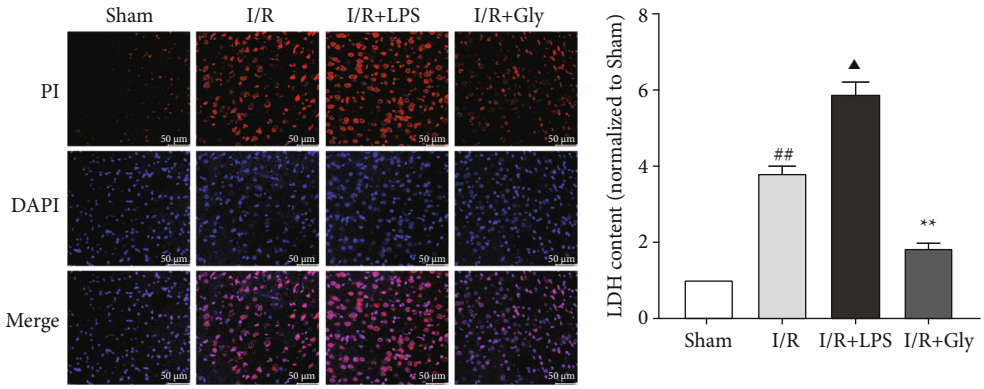

(a) (b)

Figure 2: Effects of LPS and Gly interventions on the degree of pyroptosis at 24 h after reperfusion. (a) Representative pictures of PI staining, the red dots represent positive PI staining; scale bars, 50 μm. (b) Relevant quantitative analysis of LDH content, $n = 4$. Data are presented as mean ± SD. $^{\#\#}P < 0.01$, I/R group versus sham group; $^{\blacktriangle}P < 0.05$, I/R + LPS group versus I/R group; $^{**}P < 0.01$, I/R + Gly group versus I/R group.

(microglial biomarker) and GFAP (astrocytic biomarker), respectively, and was obviously aggravated in the I/R + LPS group but alleviated in the I/R + Gly group (Figure 3(c)). Correspondingly, the expression levels of pyroptosis-related proteins such as pro-/cleaved-caspase-11, GSDMD-FL (full length GSDMD)/N (Figures 3(a) and 3(b)), NLRP3, cleaved caspase-1, IL-6, and cleaved IL-1β (Figures 3(d) and 3(e)) significantly increased in the I/R + LPS group but decreased in the I/R + Gly group compared with those in the I/R group.

3.4. Pyroptosis Influences BBB Integrity after Reperfusion. Astrocytic endfeet envelops the cerebral capillaries that form BBB. Our study showed that the damage of BBB integrity reflected by immunohistochemical staining of SMI 71 was

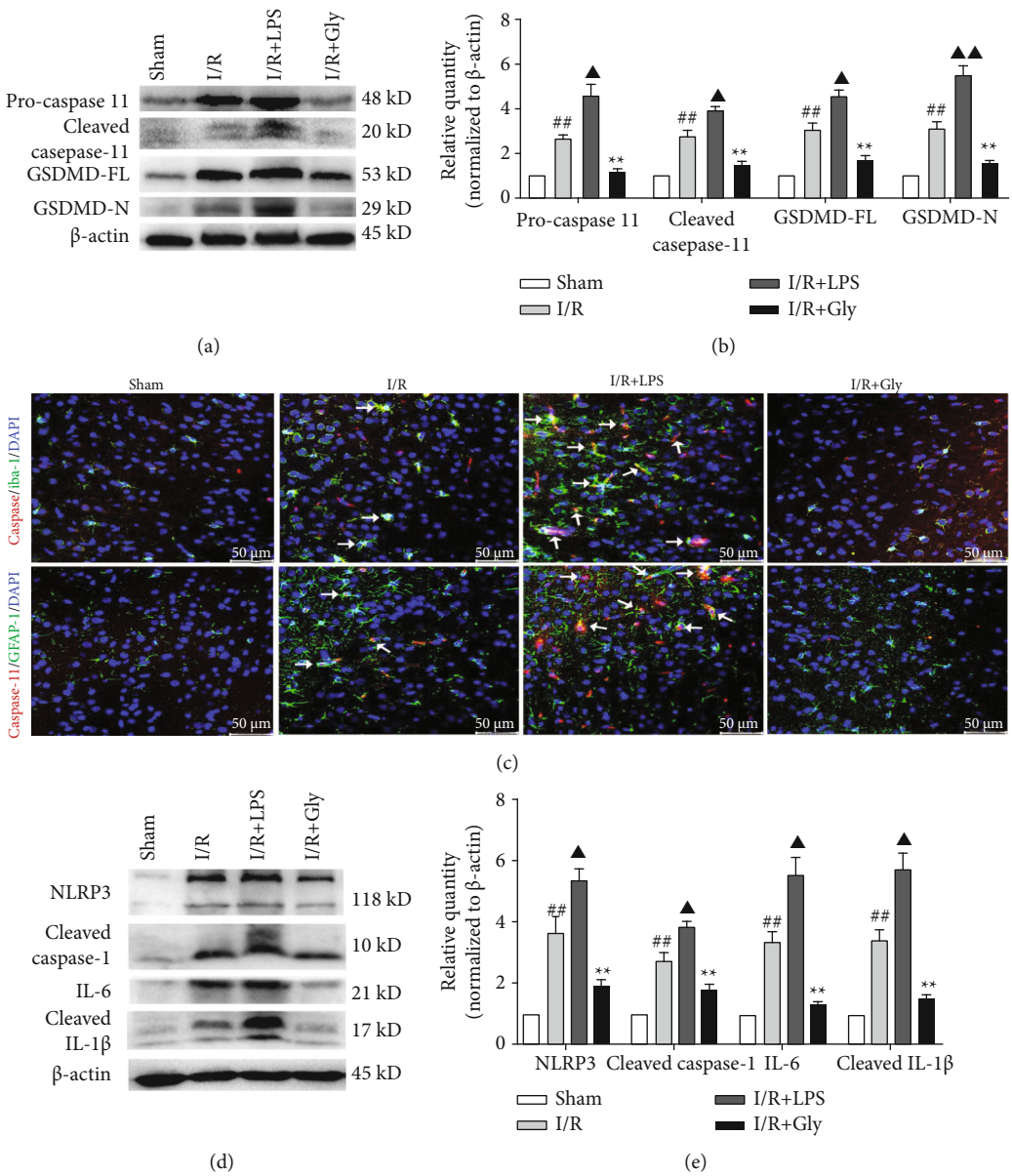

Figure 3: Effects of LPS and Gly interventions on expression levels of pyroptosis-related proteins and observations of pyroptosis locations. (a, b) Expression levels of pro-/cleaved caspase-11 and GSDMD-FL/N by Western blotting analysis, $n = 6$. (c) Representative pictures of the double immunofluorescence staining (white arrows) of caspase-11 (red) colocalized with Iba-1 or GFAP (green), respectively, scale bars, 50 μm. (d, e) Expression levels of NLRP3, cleaved caspase-1, IL-6, and cleaved IL-1β, $n = 6$. Data are presented as mean ± SD. $^{\#\#}P < 0.01$, I/R group versus sham group; $^{\blacktriangle}P < 0.05$, $^{\blacktriangle\blacktriangle}P < 0.01$, I/R + LPS group versus I/R group; $^{**}P < 0.01$, I/R + Gly group versus I/R group.

worsened with the exacerbation of astrocytic pyroptosis in the I/R + LPS group but alleviated with the mitigation of astrocytic pyroptosis in the I/R + Gly group, respectively (Figures 4(a) and 4(b)). Accordingly, the water content of ischemic hemisphere significantly increased in the I/R + LPS group but decreased in the I/R + Gly group compared with that in the I/R group (Figure 4(c)).

3.5. Pyroptosis Influences AQP-4 Polarization and Aβ Clearance after Reperfusion. The AQP-4-dependent glymphatic system is an important pathway for the clearance of Aβ in the brain. And glymphatic dysfunction is closely associated with the loss of AQP-4 polarization on astrocytic endfeet. In present study, the results showed that the loss of AQP-4 polarization after reperfusion with obvious dispersion and perturbed expression was worsened in the I/R + LPS group but apparently lightened in the I/R + Gly group (Figures 5(a), 5(c), and 5(d)). Accordingly, the accumulation of Aβ concentrated around astrocytes was also aggravated in the I/R + LPS group but alleviated in the I/R + Gly group (Figure 5(b)). Furthermore, A$\beta_{1\text{-}42}$ oligomer (the main form of toxic Aβ) obviously increased in the I/R + LPS group but decreased in the I/R + Gly group compared with that in the I/R group (Figures 5(e) and 5(f)).

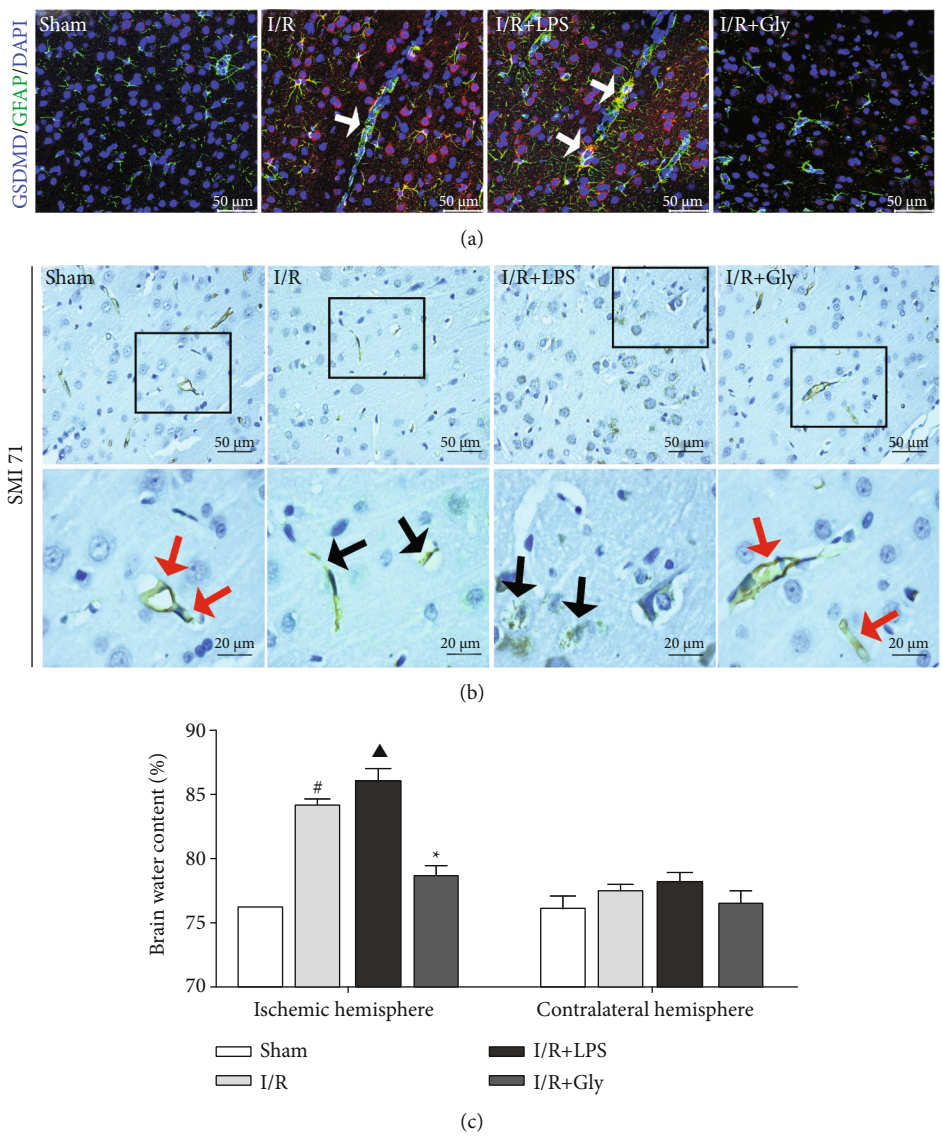

Figure 4: Influences of pyroptosis on BBB integrity at 24 h after reperfusion. (a) Representative pictures of double immunofluorescence stainings of GSDMD (red) colocalized with GFAP (green); white arrows represent astrocytic pyroptosis, scale bars, 50 μm. (b) Representative pictures of immunohistochemical staining of SMI 71. Red arrows show smooth and intact capillaries which represent normal BBB integrity, and black arrows represent the damage of BBB integrity with unsmoothed, shriveled, or ruptured capillaries, scale bars, 50/20 μm. (c) Brain water content analysis of ischemic hemisphere, $n = 4$. Data are presented as mean ± SD. $^{\#}P < 0.05$, I/R group versus sham group; $^{\blacktriangle}P < 0.05$, I/R + LPS group versus I/R group; $^{*}P < 0.05$, I/R + Gly group versus I/R group.

3.6. Pyroptosis Influences Neuron Survival after Reperfusion. The above results in present study have revealed that cerebral I/R-induced pyroptosis promotes dysfunctions of the BBB-glymphatic system and toxic Aβ accumulation and thus potentially influences the CNS homeostasis on which neurons survival depend. Accordingly, our study further showed that the damaged neurons in ischemic cortex (Figures 6(a) and 6(b)) and hippocampus (Figures 6(c) and 6(d)) tissues after reperfusion significantly increased in the I/R + LPS group but decreased in the I/R + Gly group compared with those in the I/R group, which was consistent with the results of neurological function assessment. Furthermore, Figure 7 summarizes internal relationships of pyroptosis promoting neurological deficits associated with the dysfunctional BBB-glymphatic system and Aβ accumulation after I/R in this study, which would be expatiated detailedly in the following discussion.

4. Discussion

Damage of cell membrane is a common pathological change of I/R injuries [26, 27]. Cellular membrane permeabilization is a prominent feature of pyroptosis, and the GSDMD in the gasdermin family is identified as the key executor of pyroptosis to damage the integrity of cellular membranes by forming nanopores which cause cellular swelling and death [13–15]. Therefore, recently, the roles of pyroptosis and its related signaling molecules such as caspase-11/1 and GSDMD in I/R

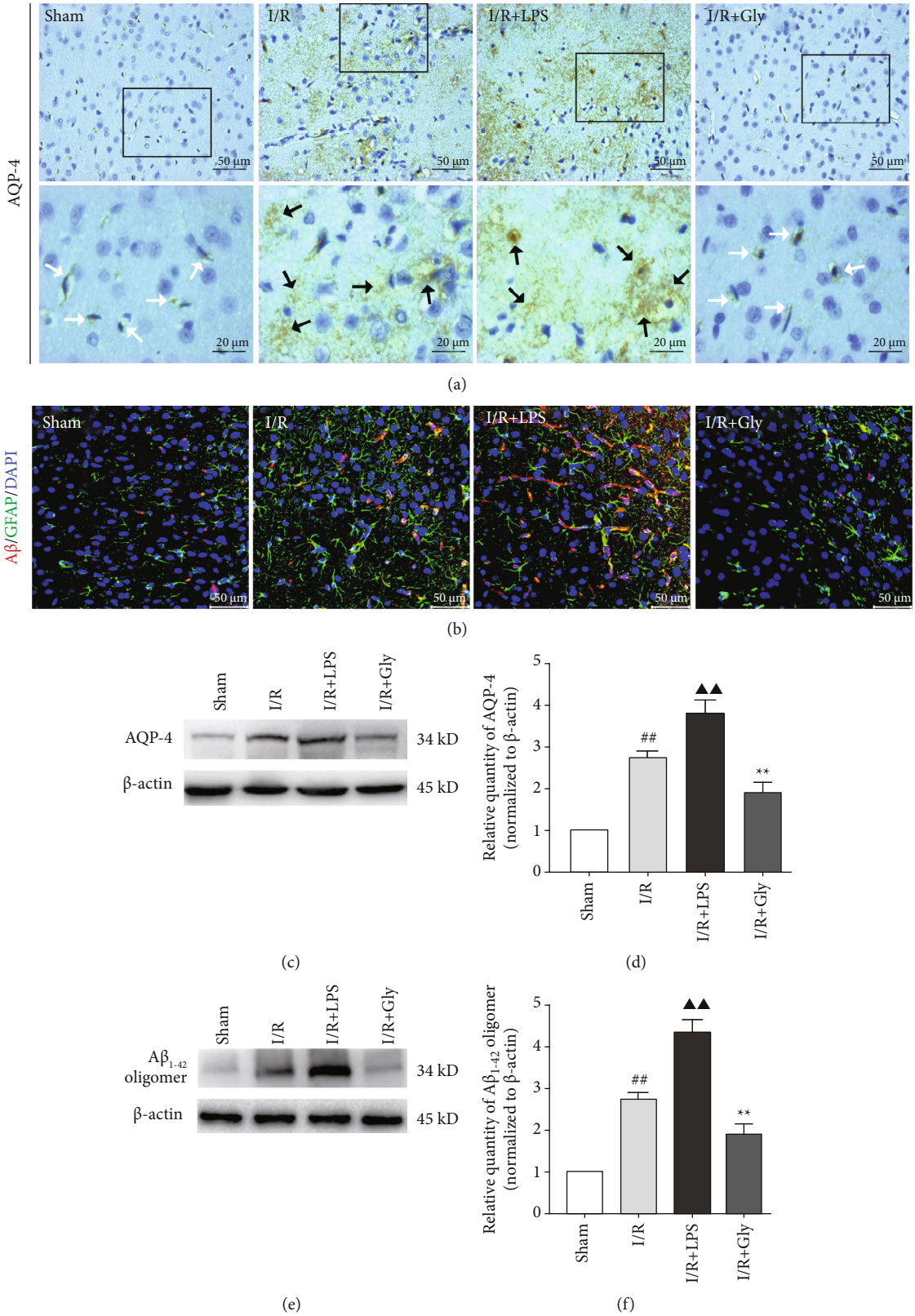

Figure 5: Influences of pyroptosis on AQP-4 polarization and Aβ clearance at 24 h after reperfusion. (a) Representative pictures of immunohistochemical staining of AQP-4. White arrows represent normal AQP-4 polarization, and black arrows represent the loss of AQP-4 polarization with obvious dispersion and perturbed expression, scale bars, 50/20 μm. (b) Representative pictures of double immunofluorescence staining of Aβ (red) colocalized with GFAP (green), scale bars, 50 μm. (c, d) Protein levels of AQP-4 by Western blotting analysis, $n = 6$. (e, f) Protein levels of A$\beta_{1\text{-}42}$ oligomer by Western blotting analysis, $n = 6$. Data are presented as mean ± SD. $^{\#\#}P < 0.01$, I/R group versus sham group; $^{\blacktriangle\blacktriangle}P < 0.01$, I/R + LPS group versus I/R group; $^{**}P < 0.01$, I/R + Gly group versus I/R group.

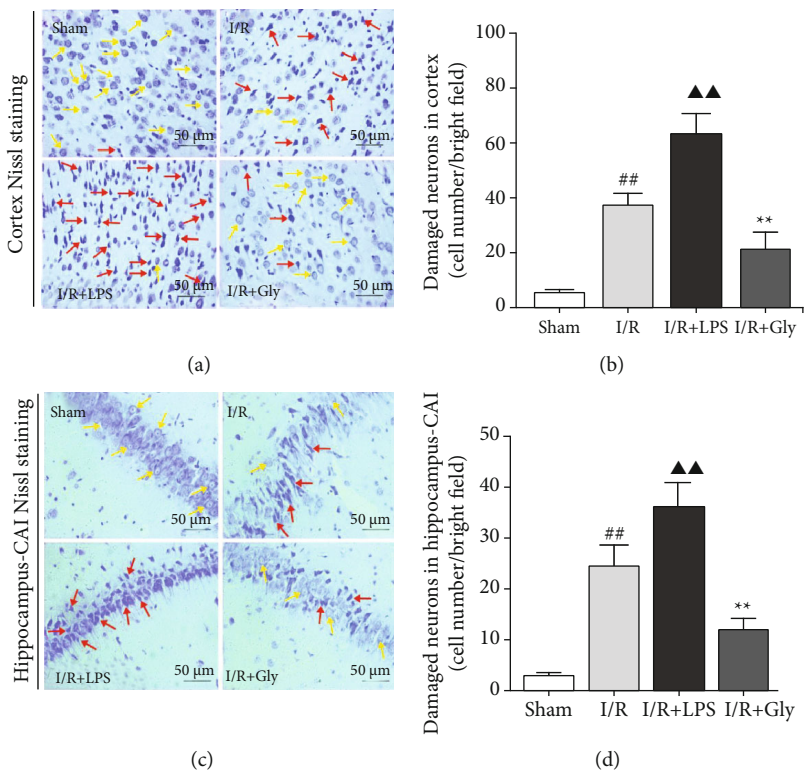

Figure 6: Influences of pyroptosis on neurons survival at 24 h after reperfusion. (a, c) Representative pictures of ischemic cortex and hippocampus-CA1 Nissl staining. Yellow arrows represent normal morphology of neurons with clear nucleolus, abundant cytoplasm, and intact structure. Red arrows represent abnormal neurons appeared shrunken and deep stained, scale bars, 50 μm. (b, d) Quantitative analysis of damaged neurons in the cortex and hippocampus-CA1 areas, $n = 6$. Data are presented as mean ± SD. $^{\#\#}P < 0.01$, I/R group versus sham group; $^{\blacktriangle\blacktriangle}P < 0.01$, I/R + LPS group versus I/R group; $^{**}P < 0.01$, I/R + Gly group versus I/R group.

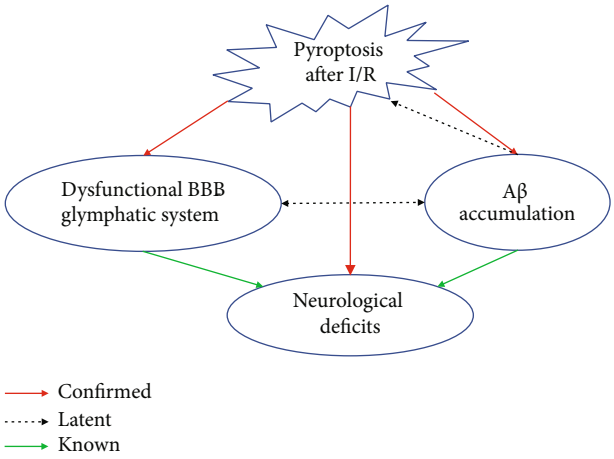

Figure 7: Schematic diagram about internal relationships among pathological changes in this study. Red arrows present relationships confirmed by this study among pathological changes including pyroptosis, Aβ accumulation, dysfunctional BBB-glymphatic system, and neurological deficits after I/R, and dotted arrows and green arrows, respectively, present latent and known relationships obtained on the basis of previous studies.

injuries have been attracting attention of researchers [9–11]. LPS is the common agonist of pyroptosis by activating caspase-11, and Gly is usually used as the protective agent of cellular membrane to inhibit pyroptosis [18, 19]. It has been demonstrated that pyroptosis is an important pathological link of cerebral I/R injuries [11], and our results in present study showed that the pyroptosis-related damage of cell membrane after cerebral I/R could be, respectively, aggravated and alleviated by LPS and Gly interventions.

Previous literatures have indicated that the summit of cerebral I/R induced pyroptosis occurs at 24 h after reperfusion [11]. Our study showed that both microglia and astrocytes are the main locations of noncanonical pyroptosis mediated by caspase-11 which could trigger the cleavage of GSDMD and then the activation of NLRP3/caspase-1 pathway, causing acute neuroinflammation at 24 h after cerebral I/R along with the release of proinflammatory factors such as IL-1β and IL-6. Astrocytic endfeet envelops the cerebral capillaries that form BBB to exert the transport function of nutrition or metabolic products [28], and BBB dysfunction in I/R injuries is closely related to abnormal astrocytes which cause brain edema formation and nonreflow phenomenon and promote neuronal damage, greatly influencing effects of restoring blood flow [29–31]. Therefore, astrocytic pyroptosis was specially highlighted and exhibited in this study; though, we noticed that pyroptosis may occur in a few neurons or other brain cells besides microglia and astrocytes which could be observed by the result of GSDMD staining after I/R. Furthermore, our study indicated that aggravating pyroptosis promotes the damage and dysfunction of BBB,

and inhibiting pyroptosis by Gly could abate the damage of BBB and significantly reduce brain edema after reperfusion.

Primary Gly at low level is an inhibitory neurotransmitter in CNS. However, interestingly, Gly at high level (800 mg/kg, intraperitoneal administration) inversely exerts protective effects against neuronal injury induced by I/R in rats according to the previous study [21]. Therefore, our current study adopted such level (800 mg/kg) of Gly as the intervention dosage administrated to rats, and we preliminarily observed the equal neuroprotective effect of Gly by assessing neurological function deficits. Then, our results further confirmed the inhibitory effects of Gly on pyroptosis after I/R. Multiple studies have demonstrated that Gly exerts cytoprotection against pyroptosis by targeting plasma membrane permeability barriers [19]. However, in current study, the results showed that Gly also exerts inhibitory effects on the expression levels of pyroptosis-related molecules such as cleaved caspase-11/1, N-terminal gasdermin D, and IL-1β. It is firstly considered that the protective effects of Gly on plasma membrane permeability barriers prevent the stimulators including abnormal iron current from aggravating pyroptosis in the setting of this study and thus mediately downregulate the expressions of pyroptosis-related signaling molecules. In addition, this phenomenon is also likely associated with the complex interrelated processes of pyroptosis. Recent evidence has revealed that IL-1β reversely induces the expression of caspase-11 during sterile inflammation [32]. Therefore, acting on one link tends to cause changes of its upstream or downstream processes during pyroptosis, which needs to be further exploration in specific experimental settings.

Recently, researches have demonstrated that toxic Aβ, one of crucial damage-associated molecular patterns (DAMPs) in AD, accumulates in brain and is responsible for brain edema formation and the occurrence of dementia induced by ischemic stroke and thus maintaining the clearance of Aβ after stroke could offer a new therapeutic approach to prevent poststroke cognitive impairment and development into dementia [5, 6, 33]. Numerous studies revealed that neuroinflammation is the fundamental factor triggering the generation of Aβ [34–36], and the accumulation of toxic Aβ is not only the outcome of BBB dysfunction but also the important cause of BBB damage [33, 37], just as our previous researches indicated that A$\beta_{1\text{-}42}$ oligomers were the main form of Aβ toxicity inducing dysfunctional BBB [38, 39]. In this study, our results showed that cerebral I/R induces the concentration of Aβ around astrocytes and the formation of massive A$\beta_{1\text{-}42}$ oligomers within 24 h after reperfusion, and that aggravating pyroptosis obviously increases A$\beta_{1\text{-}42}$ oligomers while inhibiting pyroptosis by Gly could markedly reverse Aβ accumulation and the formation of A$\beta_{1\text{-}42}$ oligomers. Therefore, pyroptosis acts as a considerable trigger of toxic Aβ accumulation after cerebral I/R.

The glymphatic system is an important pathway besides BBB for the clearance of Aβ in the brain [33]. AQP-4, the main component of glymphatic system, is a water channel physiologically located with high polarization on astrocytic endfeet, and the loss of AQP-4 polarization can cause the dysfunction of glymphatic system in pathological changes including AD and ischemic stroke [40, 41]. Thus, AQP-4 is now recognized as essential for two unique functions, namely, neurovascular coupling and glymphatic flow, to facilitate the clearance of metabolic wastes such as Aβ [41, 42]. In present study, we observed that cerebral I/R-induced AQP-4 polarization loss with obvious dispersion and perturbed expression and Aβ concentration around astrocytes along with increased A$\beta_{1\text{-}42}$ oligomers were exacerbated by the further activation of pyroptosis but obviously abated by the inhibition of pyroptosis, indicating that pyroptosis is an important factor causing glymphatic dysfunction which accounts for the accumulation of Aβ.

Previous researches have revealed that chronic Aβ accumulation around astrocytes accompanies with not only BBB damage but delayed neuronal death (DND) within six months after cerebral I/R and even deposits to plaques with the further extension of time [43, 44], which provide experimental evidence for the occurrence of sporadic AD induced by ischemic stroke. Furthermore, a clinical study by Liu et al. [5] demonstrated that patients with Aβ deposition experienced a more severe and rapid cognitive decline over 3 years after stroke/transient ischemic attack compared with subjects without AD-like Aβ deposition, and Aβ was associated with changes in multiple cognitive domains. Recently, Martins et al. [6] have reported the acute accumulation of Aβ oligomers within 24 h in blood vessel walls including small capillaries and nearby brain tissues after cerebral I/R, and that such accumulation acts as a detrimental factor promoting brain damage. Additionally, the accumulation of toxic Aβ can produce swelling in astrocytes and their endfeet and also cause dysregulation of capillaries by acting on pericytes, influencing energy supply for neurons [45, 46]. Our study revealed that pyroptosis accounts for dysfunctions of the BBB-glymphatic system and the accumulation of toxic Aβ and thus destroys the CNS homeostasis on which neurons survival depend, aggravating the damage of neurons and neurological deficits after cerebral I/R. However, inhibiting pyroptosis could markedly abate these pathological changes. On the other hand, toxic Aβ has been identified as a trigger of pyroptosis and neuroinflammation [47, 48], which suggests a magnified effect of Aβ accumulation after cerebral I/R.

In the light of the above discussion, the outcome in present study firstly confirmed that cerebral I/R-induced pyroptosis significantly promotes the dysfunctional BBB-glymphatic system, Aβ accumulation, and the formation of toxic Aβ which have been known as crucial pathological factors influencing the CNS homeostasis on which neurons survival depend and thus increasing neurological deficits. Besides, after cerebral I/R, there exists a latent relationship with mutual stimulation between the dysfunctional BBB-glymphatic system and Aβ accumulation based on previous studies, and toxic Aβ potentially aggravating pyroptosis also deserves to be further demonstrated. Admittedly, the limitation of our current study may be that glycine could not exert a completely absolute blocking effect on pyroptosis of CNS. To solve this problem, we will further construct GSDMD gene knockout rats to indepth study pyroptosis and related pathological changes after cerebral I/R. Furthermore, we

speculate and will confirm in the following study that pyroptosis and the acute accumulation of Aβ form a vicious circle in cerebral I/R injuries, which triggers the chronic Aβ accumulation after reperfusion and induces poststroke cognitive impairment.

5. Conclusion

The present study demonstrated that pyroptosis is a considerable factor causing the dysfunctional BBB-glymphatic system and the accumulation of toxic Aβ (A$\beta_{1\text{-}42}$ oligomers) and thus aggravating the neuronal damage and neurological deficits after cerebral I/R in rats. And our study not only further identifies pyroptosis as an important link in cerebral I/R injuries but also suggests that targeting pyroptosis is a potential strategy for the prevention of ischemic stroke sequelae including dementia.

Data Availability

The data used to support the findings of this study are available from the corresponding author upon request.

Conflicts of Interest

The authors declare no conflict of interest.

Authors' Contributions

Z.Y. and Z.L. designed and performed most of the experiments, analyzed the data, and wrote the manuscript. Y.C., Q.Z., and K.L. contributed to the implementation of experiments. Q.L., J.X., and X.L. contributed to data analysis and editorial support on the manuscript. Y.L., B.W., and D.C. assisted with the design of this project.

Acknowledgments

The authors would like to express gratitude and respect to the animals sacrificed in our study. This work was funded by the National Natural Science Foundation of China (grant number 81703857).

References

[1] H. Amani, E. Mostafavi, M. R. Alebouyeh et al., "Would colloidal gold nanocarriers present an effective diagnosis or treatment for ischemic stroke?," *International Journal of Nanomedicine*, vol. Volume 14, pp. 8013–8031, 2019.

[2] A. Chamorro, U. Dirnagl, X. Urra, and A. M. Planas, "Neuroprotection in acute stroke: targeting excitotoxicity, oxidative and nitrosative stress, and inflammation," *Lancet Neurology*, vol. 15, no. 8, pp. 869–881, 2016.

[3] T. Nihashi, S. Inao, Y. Kajita et al., "Expression and distribution of beta amyloid precursor protein and beta amyloid peptide in reactive astrocytes after transient middle cerebral artery occlusion," *Acta Neurochirurgica*, vol. 143, no. 3, pp. 287–295, 2001.

[4] R. Pluta, "Astroglial expression of the β-Amyloid in ischemia-reperfusion brain injury," *Annals of the New York Academy of Sciences*, vol. 977, no. 1, pp. 102–108, 2002.

[5] W. Liu, A. Wong, L. Au et al., "Influence of Amyloid-β on cognitive decline after stroke/transient ischemic Attack," *Stroke*, vol. 46, no. 11, pp. 3074–3080, 2015.

[6] A. H. Martins, A. Zayas-Santiago, Y. Ferrer-Acosta et al., "Accumulation of amyloid beta (Aβ) peptide on blood vessel walls in the damaged brain after transient middle cerebral artery occlusion," *Biomolecules*, vol. 9, no. 8, p. 350, 2019.

[7] N. J. Allen and D. A. Lyons, "Glia as architects of central nervous system formation and function," *Science*, vol. 362, no. 6411, pp. 181–185, 2018.

[8] M. K. Rasmussen, H. Mestre, and M. Nedergaard, "Fluid transport in the brain," *Physiological Reviews*, 2021.

[9] N. Miao, F. Yin, H. Xie et al., "The cleavage of gasdermin D by caspase-11 promotes tubular epithelial cell pyroptosis and urinary IL-18 excretion in acute kidney injury," *Kidney International*, vol. 96, no. 5, pp. 1105–1120, 2019.

[10] S. Toldo, A. G. Mauro, Z. Cutter, and A. Abbate, "Inflammasome, pyroptosis, and cytokines in myocardial ischemia-reperfusion injury," *American Journal of Physiology. Heart and Circulatory Physiology*, vol. 315, no. 6, pp. H1553–H1568, 2018.

[11] D. Zhang, J. Qian, P. Zhang et al., "Gasdermin D serves as a key executioner of pyroptosis in experimental cerebral ischemia and reperfusion model both in vivo and in vitro," *Journal of Neuroscience Research*, vol. 97, no. 6, pp. 645–660, 2019.

[12] S. Matikainen, T. A. Nyman, and W. Cypryk, "Function and regulation of noncanonical Caspase-4/5/11 Inflammasome," *Journal of Immunology*, vol. 204, no. 12, pp. 3063–3069, 2020.

[13] L. Sborgi, S. Ruhl, E. Mulvihill et al., "GSDMD membrane pore formation constitutes the mechanism of pyroptotic cell death," *The EMBO Journal*, vol. 35, no. 16, pp. 1766–1778, 2016.

[14] R. A. Aglietti, A. Estevez, A. Gupta et al., "GsdmD p30 elicited by caspase-11 during pyroptosis forms pores in membranes," *Proceedings of the National Academy of Sciences of the United States of America*, vol. 113, no. 28, pp. 7858–7863, 2016.

[15] M. M. Gaidt and V. Hornung, "Pore formation by GSDMD is the effector mechanism of pyroptosis," *The EMBO Journal*, vol. 35, no. 20, pp. 2167–2169, 2016.

[16] Y. Zhou, Y. Gu, and J. Liu, "BRD4 suppression alleviates cerebral ischemia-induced brain injury by blocking glial activation via the inhibition of inflammatory response and pyroptosis," *Biochemical and Biophysical Research Communications*, vol. 519, no. 3, pp. 481–488, 2019.

[17] P. An, J. Xie, S. Qiu et al., "Hispidulin exhibits neuroprotective activities against cerebral ischemia reperfusion injury through suppressing NLRP3-mediated pyroptosis," *Life Sciences*, vol. 232, p. 116599, 2019.

[18] C. Wu, W. Lu, Y. Zhang et al., "Inflammasome activation triggers blood clotting and host death through pyroptosis," *Immunity*, vol. 50, no. 6, pp. 1401–1411.e4, 2019.

[19] J. M. Weinberg, A. Bienholz, and M. A. Venkatachalam, "The role of glycine in regulated cell death," *Cellular and Molecular Life Sciences*, vol. 73, no. 11-12, pp. 2285–2308, 2016.

[20] H. Xu, W. Qin, X. Hu et al., "Lentivirus-mediated overexpression of OTULIN ameliorates microglia activation and neuroinflammation by depressing the activation of the NF-κB signaling pathway in cerebral ischemia/reperfusion rats," *Journal of Neuroinflammation*, vol. 15, no. 1, p. 83, 2018.

[21] W. Yao, F. Ji, Z. Chen et al., "Glycine exerts dual roles in ischemic injury through distinct mechanisms," *Stroke*, vol. 43, no. 8, pp. 2212–2220, 2012.

[22] Z. H. Yu, M. Cai, J. Xiang et al., "PI3K/Akt pathway contributes to neuroprotective effect of Tongxinluo against focal cerebral ischemia and reperfusion injury in rats," *Journal of Ethnopharmacology*, vol. 181, pp. 8–19, 2016.

[23] Z. Yu, M. Cai, X. Li et al., "Neuroprotective effects of Tongxinluo on focal cerebral ischemia and reperfusion injury in rats associated with the activation of the MEK1/2/ERK1/2/p90RSK signaling pathway," *Brain Research*, vol. 1685, pp. 9–18, 2018.

[24] E. Z. Longa, P. R. Weinstein, S. Carlson, and R. Cummins, "Reversible middle cerebral artery occlusion without craniectomy in rats," *Stroke*, vol. 20, no. 1, pp. 84–91, 1989.

[25] L. Fu, D. X. Zhang, L. M. Zhang et al., "Exogenous carbon monoxide protects against mitochondrial DNA-induced hippocampal pyroptosis in a model of hemorrhagic shock and resuscitation," *International Journal of Molecular Medicine*, vol. 45, no. 4, pp. 1176–1186, 2020.

[26] D. Li, Z. Shao, T. L. Vanden Hoek, and J. R. Brorson, "Reperfusion accelerates acute neuronal death induced by simulated ischemia," *Experimental Neurology*, vol. 206, no. 2, pp. 280–287, 2007.

[27] P. Charlagorla, J. Liu, M. Patel, J. I. Rushbrook, and M. Zhang, "Loss of plasma membrane integrity, complement response and formation of reactive oxygen species during early myocardial ischemia/reperfusion," *Molecular Immunology*, vol. 56, no. 4, pp. 507–512, 2013.

[28] B. Nico and D. Ribatti, "Morphofunctional aspects of the blood-brain barrier," *Current Drug Metabolism*, vol. 13, no. 1, pp. 50–60, 2012.

[29] Y. Huang, S. Chen, Y. Luo, and Z. Han, "Crosstalk between inflammation and the BBB in stroke," *Current Neuropharmacology*, vol. 18, no. 12, pp. 1227–1236, 2020.

[30] J. Wang, C. Ma, J. Zhu, G. Rao, and H. Li, "Effect of 3-aminobenzamide on the ultrastructure of astrocytes and microvessels after focal cerebral ischemia in rats," *Dose Response*, vol. 18, no. 1, p. 155932581990124, 2020.

[31] S. Li, X. Hu, M. Zhang et al., "Remote ischemic postconditioning improves neurological function by AQP4 downregulation in astrocytes," *Behavioural Brain Research*, vol. 289, pp. 1–8, 2015.

[32] K. Caution, N. Young, F. Robledo-Avila et al., "Caspase-11 mediates neutrophil chemotaxis and extracellular trap formation during acute gouty arthritis through alteration of cofilin phosphorylation," *Frontiers in Immunology*, vol. 10, 2019.

[33] R. Goulay, L. Mena Romo, E. M. Hol, and R. M. Dijkhuizen, "From stroke to dementia: a comprehensive review exposing tight interactions between stroke and Amyloid-β formation," *Translational Stroke Research*, vol. 11, no. 4, pp. 601–614, 2020.

[34] M. Koistinaho and J. Koistinaho, "Interactions between Alzheimer's disease and cerebral ischemia–focus on inflammation," *Brain Research. Brain Research Reviews*, vol. 48, no. 2, pp. 240–250, 2005.

[35] F. Leng and P. Edison, "Neuroinflammation and microglial activation in Alzheimer disease: where do we go from here?," *Nature Reviews. Neurology*, vol. 17, no. 3, pp. 157–172, 2021.

[36] M. R. Minter, J. M. Taylor, and P. J. Crack, "The contribution of neuroinflammation to amyloid toxicity in Alzheimer's disease," *Journal of Neurochemistry*, vol. 136, no. 3, pp. 457–474, 2016.

[37] E. Ristori, S. Donnini, and M. Ziche, "New insights into blood-brain barrier maintenance: the homeostatic role of β-Amyloid precursor protein in cerebral vasculature," *Frontiers in Physiology*, vol. 11, 2020.

[38] W. Wan, L. Cao, L. Liu et al., "Aβ1-42oligomer-induced leakage in anin vitroblood-brain barrier model is associated with up-regulation of RAGE and metalloproteinases, and down-regulation of tight junction scaffold proteins," *Journal of Neurochemistry*, vol. 134, no. 2, pp. 382–393, 2015.

[39] W. Chen, Y. Chan, W. Wan, Y. Li, and C. Zhang, "A$\beta_{1\text{-}42}$ induces cell damage via RAGE-dependent endoplasmic reticulum stress in bEnd.3 cells," *Experimental Cell Research*, vol. 362, no. 1, pp. 83–89, 2018.

[40] C. Ji, X. Yu, W. Xu, C. Lenahan, S. Tu, and A. Shao, "The role of glymphatic system in the cerebral edema formation after ischemic stroke," *Experimental Neurology*, vol. 340, p. 113685, 2021.

[41] M. Valenza, R. Facchinetti, L. Steardo, and C. Scuderi, "Altered waste disposal system in aging and Alzheimer's disease: focus on astrocytic aquaporin-4," *Frontiers in Pharmacology*, vol. 10, 2019.

[42] T. Nakada, I. L. Kwee, H. Igarashi, and Y. Suzuki, "Aquaporin-4 Functionality and Virchow-Robin Space Water Dynamics: Physiological Model for Neurovascular Coupling and Glymphatic Flow," *International Journal of Molecular Sciences*, vol. 18, no. 8, p. 1798, 2017.

[43] R. Pluta, S. Januszewski, M. Jablonski, and M. Ulamek, "Factors in creepy delayed neuronal death in hippocampus following brain ischemia-reperfusion injury with long-term survival," *Acta Neurochirurgica. Supplement*, vol. 106, pp. 37–41, 2010.

[44] T. van Groen, K. Puurunen, H. M. Maki, J. Sivenius, and J. Jolkkonen, "Transformation of diffuse beta-amyloid precursor protein and beta-amyloid deposits to plaques in the thalamus after transient occlusion of the middle cerebral artery in rats," *Stroke*, vol. 36, no. 7, pp. 1551–1556, 2005.

[45] D. M. Wilcock, M. P. Vitek, and C. A. Colton, "Vascular amyloid alters astrocytic water and potassium channels in mouse models and humans with Alzheimer's disease," *Neuroscience*, vol. 159, no. 3, pp. 1055–1069, 2009.

[46] R. Nortley, N. Korte, P. Izquierdo et al., "Amyloid β Oligomers Constrict Human Capillaries in Alzheimer's Disease Via Signaling to Pericytes," *Science*, vol. 365, no. 6450, p. eaav9518, 2019.

[47] A. Halle, V. Hornung, G. C. Petzold et al., "The NALP3 inflammasome is involved in the innate immune response to amyloid-β," *Nature Immunology*, vol. 9, no. 8, pp. 857–865, 2008.

[48] F. Shi, M. Kouadir, and Y. Yang, "NALP3 inflammasome activation in protein misfolding diseases," *Life Sciences*, vol. 135, pp. 9–14, 2015.

Hindawi
Neural Plasticity
Volume 2021, Article ID 8643129, 12 pages
https://doi.org/10.1155/2021/8643129

Review Article

Contribution of Neuronal and Glial Two-Pore-Domain Potassium Channels in Health and Neurological Disorders

Yuncheng Luo, Lu Huang, Ping Liao, and Ruotian Jiang

Laboratory of Anesthesia and Critical Care Medicine, National-Local Joint Engineering Research Center of Translational Medicine of Anesthesiology, West China Hospital, Sichuan University, Chengdu 610000, China

Correspondence should be addressed to Ruotian Jiang; ruotianjiang@scu.edu.cn

Received 28 June 2021; Accepted 3 August 2021; Published 15 August 2021

Academic Editor: Fang Pan

Two-pore-domain potassium (K2P) channels are widespread in the nervous system and play a critical role in maintaining membrane potential in neurons and glia. They have been implicated in many stress-relevant neurological disorders, including pain, sleep disorder, epilepsy, ischemia, and depression. K2P channels give rise to leaky K^+ currents, which stabilize cellular membrane potential and regulate cellular excitability. A range of natural and chemical effectors, including temperature, pressure, pH, phospholipids, and intracellular signaling molecules, substantially modulate the activity of K2P channels. In this review, we summarize the contribution of K2P channels to neuronal excitability and to potassium homeostasis in glia. We describe recently discovered functions of K2P channels in glia, such as astrocytic passive conductance and glutamate release, microglial surveillance, and myelin generation by oligodendrocytes. We also discuss the potential role of glial K2P channels in neurological disorders. In the end, we discuss current limitations in K2P channel researches and suggest directions for future studies.

1. Introduction

Ion channels in the cell membrane, particularly potassium channels, play a vital role in the resting membrane potential of neurons and in the transmission of action potentials [1–5]. An appropriate resting membrane potential requires a leaky K^+ current, and two-pore-domain potassium (K2P) channels appear crucial in providing such current. These channels remain open ("leaky") across the range of physiological voltages, as well as during action potentials [6–8].

The first mammalian K2P channel, TWIK-1, was identified in humans in 1996 [9], and since then, another 14 members sharing a similar structure have been identified and organized into six subfamilies (TWIK, TREK, TASK, TALK, THIK, and TRESK) [7, 8]. In contrast to other K^+ channels, which feature one pore domain per subunit, K2P channels contain two pore domains per subunit. TWIKs give rise to a weakly inwardly rectifying K^+ current, while TREKs are sensitive to mechanical and thermal stimuli as well as lipids. TASKs and TALKs respond strongly to changes in extra- or intracellular pH, while THIKs are sensitive to halothane.

K2P channels are widely expressed in the nervous system, including the dorsal root ganglion (DRG), trigeminal ganglion (TG), spinal cord, cerebrum, and cerebellum [10, 11]. In the peripheral nervous system, K2P channels are expressed in sensory neurons of the DRG and TG. In the brain, TWIK-1, TREK-1, TREK-2, TRAAK, TASK-1, and TASK-3 are preferentially expressed in specific regions. K2P channels are also expressed in various patterns in different cell types in other brain regions.

Perhaps the best-understood functions of K2P channels are passive K^+ conductance and maintenance of resting membrane potential. Activation of K2P channels leads to the extrusion of K^+ into the extracellular space, hyperpolarizing the neuronal membrane and dampening neuronal excitability. Various endogenous and exogenous stimuli can regulate the activity of these ion channels, including membrane stretching, voltage, temperature, extra- and

intracellular pH, phospholipids, and other intracellular signaling molecules generated through the activation of G protein-coupled receptors (GPCRs) [12].

Some K2P members are expressed not only in neurons but also in glial cells. Glia are nonneuronal cells in the nervous system that do not produce electrical impulses. Instead, they maintain homeostasis of certain ions, particularly K^+, in the extracellular environment. In the brain, TASK-1 has been detected in astrocytes and oligodendrocytes, while TWIK-1 and TREK-1 are expressed in astrocytes, and THIK-1 was identified in microglia [13].

This review summarizes recent studies of K2P channel functions in neurons and glia of the central and peripheral nervous systems. These studies have relied primarily on genetic and pharmacological tools to elucidate channel function. We focus on how K2P channels in neurons help maintain resting membrane potential and regulate excitability, and on how K2P channels in glia help maintain potassium homeostasis.

2. K2P Channels and the Excitability of Neurons

2.1. Peripheral Nervous System (PNS). Some K2P channels mediate nociception and pathological pain, and knocking them out in mice increases sensitivity to noxious stimuli [14, 15]. These findings indicate a strong association between K2P channels and neuronal excitability. Indeed, animal models of pathological pain show downregulation of K2P channels in the DRG or TG, as well as increased excitability of nociceptive neurons [16] (Figure 1).

2.1.1. TWIK-Related Spinal Cord K^+ Channels (TRESKs). TRESK was first found in the human spinal cord, then discovered in mouse cerebrum [17]. In DRG neurons, this channel contributes strongly to background K^+ currents: mutating Gly339 to Arg in TRESK in mice significantly reduced standing outward current in DRG neurons, without affecting resting membrane potential [18, 19]. At the same time, the mutation increased excitability of DRG neurons: it reduced the rheobase to elicit an action potential, and it increased the rate of action potential firing [18, 20, 21]. Knocking out TRESK in mice sensitized the animals to mechanical stress and cold, based on assessments of inflammatory and neuropathic pain responses, without substantially affecting their sensitivity to heat [20, 21]. Bone metastasis in mice has been linked to depolarization of nociceptive neurons and to pain hypersensitivity, which were partially reversed by overexpressing TRESK in DRG neurons and exacerbated by knocking down TRESK [22]. Similarly, treating isolated DRG neurons with the TRESK inhibitor isobutylalkenyl amide depolarized the cells and evoked action potential [23].

TRESK has been linked to migraine pathophysiology, and a frameshift mutation (F139WfsX24) has been identified in patients suffering from migraine with aura [24]. In mice, this frameshift mutation showed a dominant-negative effect of reducing the rheobase and increasing the rate of action potential firing in TG, without altering resting membrane potential [25]. The frameshift may cause these effects by giving rise to a truncated protein, TRESK-MT2 [26]. Expression of TRESK-MT2 in TG neurons of mice inhibited TREK-1 and TREK-2, reduced the rheobase, and increased the firing rate, indicating greater excitability. Using CRISPR-Cas9 to correct the frameshift in induced pluripotent stem cells from migraine patients reversed the hyperexcitability of the resulting differentiated nociceptors. Activating TRESK using cloxyquin in a mouse model of migraine alleviated pain hypersensitivity to mechanical and thermal stimuli [27]. Future studies are needed to examine coexpression of TRESK and TREK, to determine whether endogenous levels of TRESK-MT2 in human nociceptors inhibit TREK-1/2, and to evaluate the contribution of TREK-1/2 to migraine pathogenesis.

TRESK is also expressed in the nodose ganglia (NG), and NG neurons in diabetic rats show hyperpolarization as well as upregulated TRESK relative to NG neurons in healthy controls. [28, 29]. Silencing TRESK in diabetic animals partially restored normal excitability of NG neurons and thereby the animal's sensitivity to satiety signals [28, 29].

The fact that TRESK is expressed primarily in sensory neurons makes it a potential target for treating allodynia and migraine. Developing specific activators of this channel may expand on the range of analgesic agents currently available.

2.1.2. TREKs (TWIK-Related K^+ Channels). TREKs belong to another subfamily of K2P channels comprising TREK-1, TREK-2, and TRAAK. TREKs are sensitive to membrane stretching, pH, arachidonic acid, and temperature, making them polymodal pain perception channels. In the DRG, TREKs are expressed in small-diameter neurons and to a small extent in medium- and large-diameter neurons [30]. Knocking out TREK-1, TREK-2, or TRAAK from mice rendered them more sensitive to thermal and mechanical stimuli [31–33], which indicated enhanced neuronal excitability. Downregulating TREK-2 in C-fiber nociceptors depolarized the membrane by about 10 mV and increased spontaneous firing frequency. Downregulating TREK-2 also increased spontaneous pain behavior in a mouse model of complete Freund's adjuvant (CFA) [34].

Activating TREKs using the neuroprotective agent riluzole hyperpolarized the resting membrane in the superior cervical ganglion [35, 36]. Similarly, activating TREK-1/2 in DRG neurons with BL-1249 or GI-530159 hyperpolarized the resting membrane and reduced firing frequency [37]. These results suggest that TREK activation in the peripheral nervous system can alleviate polymodal pathological pain, but the selectivity of those TREK activators has not been rigorously established. Potentially more reliable support for the therapeutic potential of TREK activation comes from studies with the recently developed TREK-1/2 activator C3001a [38]. C3001a was found to activate TREK-1 with a half-maximal effective concentration (EC_{50}) of 12.81 μM, and it activated TREK-2 with similar efficacy, while it did not appreciably activate TRAAK or other human K2P channels (TASK-3, TASK-1, TRESK, and THIK-1). Applying c3001a to dissociated DRG neurons produced weak hyperpolarization, increased the rheobase, and reduced the number of action potentials in small-sized neurons [38]. Applying the compound to mice with spared nerve injury or complete Freund's adjuvant alleviated spontaneous pain and cold hyperalgesia. The compound also alleviated mechanical allodynia and

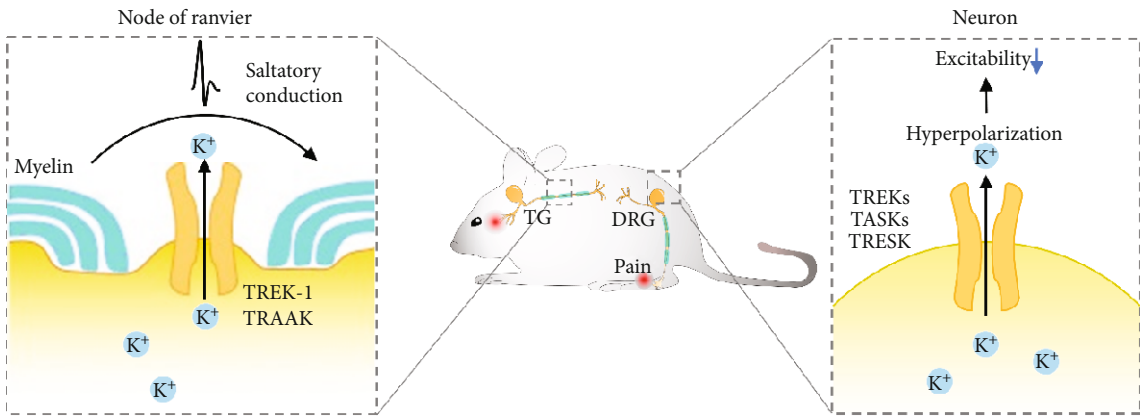

Figure 1: Functions of K2P channels in the peripheral nervous system. Left: TREK-1 and TRAAK are enriched in nodes of Ranvier on myelinated afferent nerves. The channels rapidly regenerate action potentials, allowing fast action potential conduction along the nerve. Right: K2P channels are expressed in neurons of the dorsal root ganglion and trigeminal ganglion. They extrude K^+ and hyperpolarize the membrane of neurons at rest, decreasing their excitability.

inflammation in a mouse model of pancreatitis. Thus, activating TREKs may be a useful therapeutic strategy.

TREK-1 and TRAAK are enriched at nodes of Ranvier on myelinated afferent nerves. These nodes display unusual action potentials and quite leaky K^+ conductance that is thermo- and mechanosensitive. The nodes of Ranvier on nearly all trigeminal Aβ-afferent nerves express both TREK-1 and TRAAK [39]. Knocking down or pharmacologically inhibiting either channel widened action potentials at the nodes, increased nodal membrane input resistance, and depolarized the resting membrane. Thus, these channels are probably required for rapid action potential repolarization at the nodes of Ranvier. The channels also permit rapid, high-frequency action potentials along myelinated afferent nerves. Consistent with these ideas, knocking down TREK-1 or TRAAK in TG of rat significantly reduced tactile responses, suggesting sensory behavioral deficit [39]. These channels may play similar roles in other parts of the mammalian nervous system that contain rapidly conducting somatosensory afferent nerves or motor nerves. Further study is needed to determine whether other K2P channels are also involved in rapid action potential conduction at nodes of Ranvier in myelinated nerves in the peripheral and central nervous systems.

2.1.3. TWIK-Related Acid-Sensitive K^+ Channels (TASKs). TASK-1 and TASK-3 belong to a subfamily of K2P channels sensitive to changes in extracellular pH [40], and they are expressed in DRG [11, 41]. TASK-3 is primarily expressed in small-sized DRG neurons, where it colocalizes with TRMP8, TRPV1, and tyrosine hydroxylase, suggesting selective expression in nociceptive neurons [42]. In the peripheral nervous system, TASK-3 is expressed in TRPM8-positive neurons, and knocking it out from mice rendered them hypersensitive to cold, and this effect was associated with depolarization of the resting membrane and increased amplitude of action potentials in TRPM8-positive neurons [42].

More details about the *in vivo* function of TASK-3 under physiological and pathological conditions began to emerge with the structure-based design of a selective TASK-3 activator, CHET3 [43]. Administering CHET3 to animal models of acute and chronic pain alleviated spontaneous pain as well as hyperalgesia in response to cold, heat, and mechanical stress. Applying CHET3 to isolated DRG neurons increased the rheobase and decreased action potential frequency, without altering resting membrane potential [43]. These genetic and pharmacological studies reveal a role for TASK-3 in membrane excitability of nociceptive neurons.

Since TASK-3 is expressed at much higher levels in the TG than DRG [43], future research should evaluate the potential role of TASK-3 in trigeminal diseases and facial sensation.

2.2. Central Nervous System. In the central nervous system, mRNAs encoding K2P channels have been detected in the cerebrum, cerebellum, brainstem, and spinal cord [10, 11]. Neuronal K2P channels have been implicated in chronic pain [44], ischemia, epilepsy [45], sleep disorder, and major depressive disorder [46] (Figure 2).

2.2.1. TRESK. High expression of TRESK has been found in several areas of the central nervous system, including the cortex, periaqueductal gray (PAG), and dorsal horn of the spinal cord [47]. Spinal nerve ligation in mice to induce neuropathic pain is associated with TRESK upregulation in the superficial dorsal horn [48], and overexpressing TRESK in such animals alleviated their hyperalgesia, inflammation, and neuronal apoptosis [49, 50]. These results suggest that TRESK in the spinal cord plays an essential role in pain perception, which needs to be confirmed in electrophysiological studies.

Recent evidence suggests that TRESK helps regulate nocturnal dynamics of the suprachiasmatic nucleus (SCN) and light-adaptive responses [51]. The SCN is the key circadian pacemaker, which synchronizes internal circadian rhythms to the external day-night cycle. TRESK expression increases in the early evening and remains high throughout the night, suggesting a rhythmic expression pattern. In the animal study, neurons at rest in the SCN of control animals were

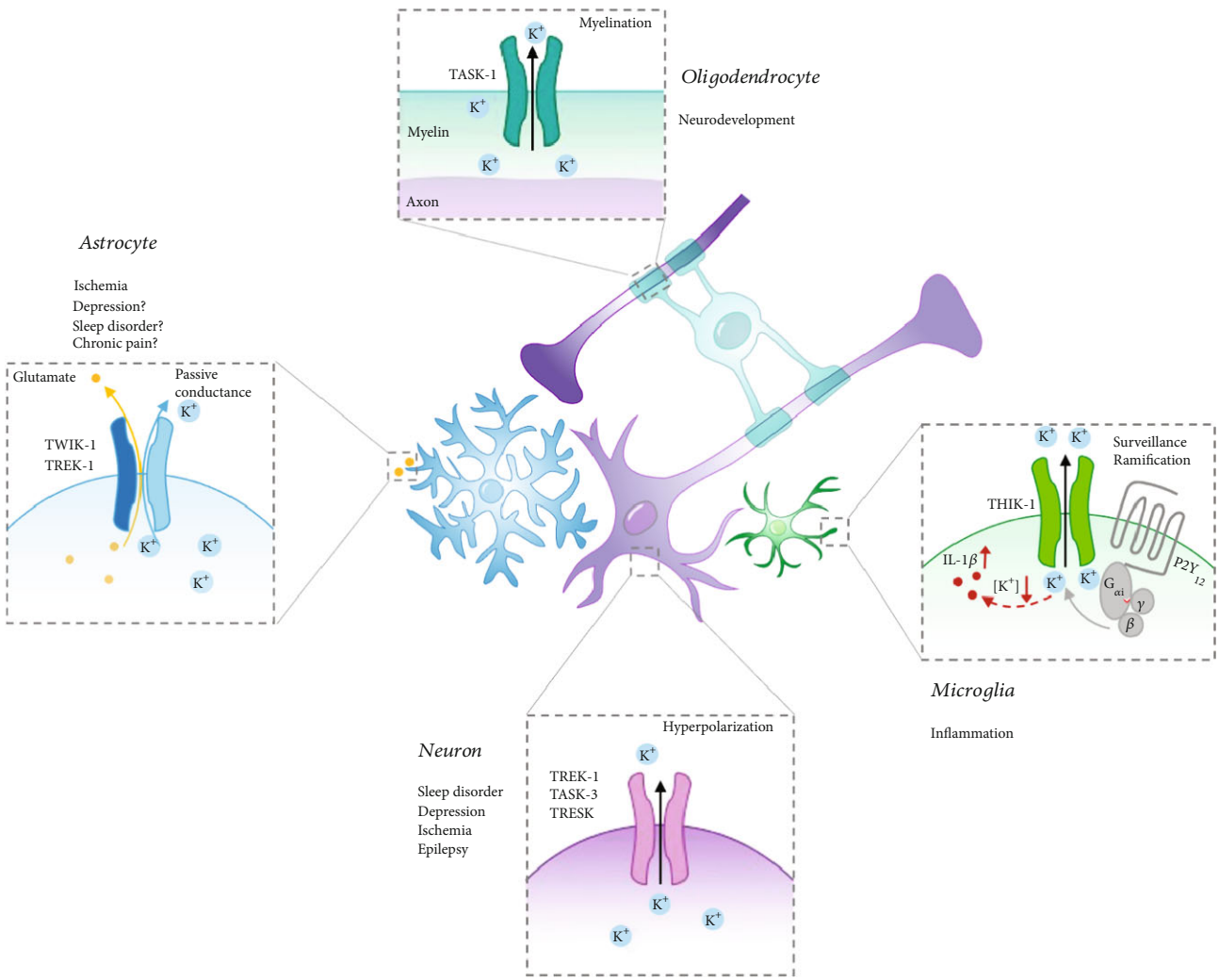

Figure 2: Roles of K2P channels in the central nervous system. K2P channels regulate neuronal excitability and contribute to many normal and disease processes, including sleep, epilepsy, ischemia, and depression. In glia, K2P channels maintain glial membrane potential and are involved in astrocytic passive conductance and glutamate release, microglial surveillance, myelin generation by oligodendrocytes, and K^+ homeostasis.

more depolarized during the day than at night, whereas the same neurons in animals lacking TRESK remained constantly in a depolarized state, and their nocturnal spike rate was higher than in controls. In addition, knocking out TRESK led to a much weaker Ca^{2+} response to glutamate [51].

2.2.2. TREKs. TREK-1 and TRAAK are widely expressed across the central nervous system, with TREK-1 most abundant in the striatum, cortex and hippocampus. TRAAK is most abundant in the cortex. TREK-2 is restricted to the cerebellar granule cell layer [11, 52, 53].

(1) TREK-1. TREK-1 can regulate the excitability of neurons, but its precise roles may depend on the type of neuron. In pyramidal neurons of the CA1 region of the hippocampus, TREK-1 deficiency depolarized resting neurons, reduced the rheobase, and increased action potential frequency [54]. Similarly, in serotonergic neurons of the dorsal raphe nucleus (DRN), TREK-1 knockout increased discharge frequency in mice [55]. The channel does not, however, appear to affect resting membrane potential of GABAergic neurons in the striatum [56]. Treating brain slices with the endogenous TREK-1 inhibitor spadin or the inhibitor SID1900 increased the firing rate of serotonergic neurons in the DRN [57, 58]. Spadin also depolarized cortical neurons at rest [59]. The various effects of TREK-1 have been implicated in nervous system disorders as described below:

(1) *Depression*: knocking out TREK-1 from several mouse models of depression alleviated depression symptoms, as measured in the forced swimming test, tail suspension test, conditioned suppression of motility test, and learned helplessness test [55]. In fact, the knockout animals showed similar behavior as wild-type mice treated with the antidepressants fluoxetine or paroxetine. Knockout was associated

with higher firing rates of serotonergic neurons, which likely increased the release of serotonin into target structures. Mice lacking TREK-1 were insensitive to selective serotonin reuptake inhibitors, suggesting that the efficacy of such inhibitors involves TREK-1 inhibition [55]. Indeed, these inhibitors appear to inhibit TREK-1 in a dose-dependent manner [55, 60]. Both spadin and SID1900 enhanced the excitability of serotonergic neurons in mice, alleviating depressive symptoms [57, 58]. TREK-1 knockdown in hippocampal neurons alleviated depressive symptoms in a mouse model of lipopolysaccharide-induced depression [61]. Consistent with the studies on rodent models, four single nucleotide polymorphisms in TREK-1 were also identified in some patients with treatment resistance in major depressive disorders [62]

These observations suggest that TREK-1 may be a useful therapeutic target in depression. Future study is needed to determine whether TREK-1 actively regulates serotonin release and is involved in the mechanism of action of selective serotonin reuptake inhibitors.

(2) *Ischemia and seizure*: knocking out TREK-1 from mice increased their risk of ischemia due to transient bilateral occlusion of the common carotid arteries or due to occlusion of the aortic arch and left subclavian artery [56]. This ischemia was associated with higher mortality. Knockout also increased risk of epileptic seizures triggered by kainite or pentylenetetrazol; the mutant animals showed increased morbidity as well as increased spike amplitude and frequency, based on electroencephalography [56]. Administering spadin to mice did not reduce infarct size following focal ischemia or alleviate kainate-induced seizures [63]

TREK-1 in serotonergic neurons of the dorsal raphe has recently been implicated in the circadian photoperiod [64]. Longer photoperiods may reduce TREK-1 function, since pharmacological inhibition of TREK-1 significantly increased spike frequency in animals exposed to short or equinox photoperiods but not in animals exposed to long photoperiods, which expressed lower levels of the channel [64].

(2) TREK-2/TRAAK. TREK-2 is a downstream mediator of $GABA_B$ receptors in neurons of the entorhinal cortex, giving the channel a strong influence over spatial learning. Treating the stellate neuron of the entorhinal cortex with the $GABA_B$ receptor activator baclofen activated TREK-2, which blocked action potentials and hyperpolarized the membrane through mechanisms involving the G_{ai}, G_{ao}, and PKA pathways [65]. This decrease in neuronal excitability led to impaired spatial learning, which was abolished when TREK-2 was knocked down. Knockdown did not alter the resting membrane potential of stellate neurons in the entorhinal cortex.

In another study, norepinephrine was shown to activate TREK-2 and thereby hyperpolarize neurons at rest in the superficial layers of the entorhinal cortex. This mechanism appeared to involve α-$_{2A}$ adrenergic receptors as well as the $G_{\alpha i}$ and PKA pathways [66].

In humans, FHEIG (facial dysmorphism, hypertrichosis, epilepsy, intellectual disability/developmental delay, and gingival overgrowth) was associated with a missense mutation in TRAAK. The recombinant mutant TRAAK channel showed a significant gain of function basally and damaged sensitivity to mechanical stimulus and arachidonic acid [67].

2.2.3. TASKs. TASKs are widely expressed across the central nervous system [10, 68]. TASK-1 may be most abundant in the cerebellum, while TASK-3 may be more abundant in the hippocampus, cortex, cerebellum, and certain nuclei, such as the paraventricular nuclei of the thalamus, locus coeruleus, and the dorsal raphe [11]. TASK electrophysiology has been studied in cerebellar granule neurons of rats and serotonergic raphe neurons of mice [69, 70]. Knocking out TASK-1 from mice did not alter resting membrane potential of cerebellar granule neurons or the properties of their action potentials [71]. In contrast, knocking out TASK-3 depolarized cerebellar granule neurons by 10 mV and decreased both the rheobase and action potential amplitude [72]. These results suggest that TASK-3 may contribute more to the resting membrane potential of cerebellar granule neurons than TASK-1.

In mature neurons, transmembrane chloride gradients are mainly regulated by KCC2 and NKCC1, two cation-chloride cotransporters, which, respectively, mediate outward and inward cotransport of Cl^- and K^+ under physiological conditions. Consistent with this idea, chronic knockdown of KCC2 in rat hippocampus increased neuronal excitability by downregulating levels of TASK-3 at the membrane [73]. Altogether, these studies indicate that TASKs stabilize neuronal membrane potential and regulate their activity. As a result, these channels likely play roles in epilepsy, sleep disorder, and depression, as described below.

(1) Epilepsy. In the rat entorhinal cortex, application of serotonin depolarized GABAergic interneurons at rest, increased action potential firing frequency, and increased GABA release [74]. As a result, pyramidal cells showed lower excitability. These effects of serotonin were associated with inhibition of TASK-3 in interneurons, suggesting that the channel may be a target in treating epilepsy. Future research is required to determine whether selective inhibition of TASK-3 can alleviate one or more subtypes of epilepsy.

The *Kcnk9* gene coding for TASK-3 is located at chromosomal position 8q24, a locus associated with absence epilepsy [75, 76], although the association is somewhat controversial [77]. A mutation in TASK-3 has been linked to absence epilepsy in a rat model, but mutant and wild-type animals showed similar leaky K^+ currents [78]. Further work is needed to clarify whether and how this mutation contributes to absence seizures.

(2) Sleep Disorder. Sleep is essential to emotional health, but the molecular processes that determine daily sleep duration and the sleep-wake cycle remain elusive. Thalamocortical neuronal networks alternate between burst activity during sleep and tonic single-spike activity during wakefulness [79]. Inhibition of TASK-1 and TASK-3 depolarized thalamic relay neurons, leading them to engage preferentially in tonic single-spike activity [80, 81]. Similarly, inhibiting TASK-3 using spermine during repetitive activity or hypoxia depolarized the thalamic neurons by about 8 mV and switched the firing mode from burst to tonic [82]. Thus, TASKs have potential roles in the sleep-wake cycle.

Consistent with this idea, animals expressing TASK-3 mutants showed increased nocturnal activity and shorter REM sleep [83, 84]. Animals deficient in TASK-3 lacked an θ oscillation that was seen in the cortical electroencephalogram of control animals and that resembled type II θ. The deficient animals also progressed much more slowly from wakefulness to sleep, and their sleep episodes and REM θ oscillations were more fragmented [79]. Knocking out TASK-3 severely shortened sleep [85]. Exposing mice to chronic sleep fragmentation depolarized medial habenula cholinergic output neurons at rest and increased the frequency of their spontaneous firing. Inhibition of TASK-3 mimicked the sleep fragmentation effects in control mice, while the effects of TASK-3 inhibition were absent in sleep fragmentation mice [86]. These results suggest that TASK-3 mediates the ability of sleep fragmentation to increase the excitability of medial habenula cholinergic output neurons.

These findings identify TASK-3 as a mediator of sleep disturbance, but how TASK-3 regulates firing patterns is still unclear. Further study is needed to investigate how TASK-3 contributes to the normal sleep cycle and how its impairment contributes to emotional disorders related to sleep disturbance, such as depression and anxiety.

(3) Depression. Knocking out TASK-3 from mice impaired working memory, based on the T-maze spontaneous alternation test, and it damaged spatial memory, based on the Morris water maze test [83]. At the same time, TASK-3 knockout alleviated depressive behaviors, as assessed in the forced swimming test and tail suspension test [84]. These observations identify TASK-3 as a potential target in the treatment of depression. In fact, the receptor may help mediate the antidepressive effects of cannabinoid receptor agonists in mouse models [87–89]: knocking out TASK-3 rendered the animals less responsive to the agonist WIN55212-2 mesylate [83]. Future research is needed to validate how TASK-3 regulates depression.

Dysfunction of TASK-3 was also identified to cause neurological disorders in humans. A missense mutation in TASK-3 was identified to abolish the channel's currents and resulted in a maternally transmitted genomic-imprinting syndrome characterized by mental retardation, hypotonia, and dimorphisms in patients [90, 91].

2.2.4. Tandem of Pore Domains in a Weak Inward Rectifying K^+ Channel (TWIK). TWIK-1 appears to be expressed widely across the central nervous system [92], but few studies have examined its physiological roles in neurons. In the entorhinal cortex, serotonin activated TWIK-1, which hyperpolarized stellate and pyramidal neurons at rest in superficial layers, and it slowed their action potential firing [93]. It is unclear whether TWIK-1 in the entorhinal cortex acts as a homodimer or as a heterodimer with another K2P channel isotype.

In dentate gyrus granule cells, downregulating TWIK-1 depolarized the cells at rest and increased their firing rate [94]. TASK-3 appeared to localize in the proximal dendrites and soma of those cells, similar to the localization of TWIK-1. Knocking down both TWIK-1 and TASK-3 depolarized the cells at rest and increased their action potential firing rate [95]. These results suggest that TWIK-1 and TASK-3 contribute to the intrinsic excitability of dentate gyrus granule cells.

3. K2P and the Potassium Homeostasis of Glia

Glia support neuronal functions *via* various mechanisms in the central nervous system, and K2P channels are expressed in glia. A transcriptome analysis detected the mRNAs encoding TWIK-1 and TREK-1 in astrocytes [96], and immunohistochemistry detected TASK-1 protein in astrocytes of hippocampus and oligodendrocytes in the mouse brain [97]. Several studies have examined the functions of K2P channels in glia (Figure 2), though much more work remains to be done.

3.1. Astrocytes. Astrocytes are star-shaped, specialized glia that differentiate from a neural stem cell pool. They primarily mediate ionic homeostasis and provide structural support to neurons. They also contribute to neurotransmitter release and synaptic development. Astrocyte dysfunction, termed reactive astrogliosis, is common in injury or disease affecting the central nervous system, including some neurological diseases related to aging: Huntington's disease, Alzheimer's disease (AD), and Parkinson's disease [98].

3.1.1. Astrocyte and Passive Conductance. TREK-1 and TWIK-1 in astrocytes contribute to the large K^+ conductance of cultured cortical astrocytes [13]. While knocking out TWIK-1 from mice did not significantly alter astrocytic passive conductance [99], depleting it from cultured astrocytes led to more negative resting membrane potential [100]. In contrast, eliminating TREK-1 from cultured astrocytes did not alter either resting membrane potential or passive potassium conductance [99]. On the other hand, treating cultured astrocytes or hippocampal slices with spadin reduced their passive conductance by inhibiting the activity of TWIK-1/TREK-1 heterodimers [101]. These data suggest that TREK-1 mildly contributes to the passive conductance of astrocytes. Knocking out TREK-1 alone or together with TWIK-1 did not alter the expression of other potassium channels, suggesting that the other channels do not compensate for K2P channel activity [102].

3.1.2. Glutamate Release. Glutamate is one of the most important neurotransmitters that are released from excitatory presynaptic neurons and that mediate neuronal transmission. Emerging evidence suggests that astrocytes can also release glutamate to modulate synaptic plasticity, neuronal excitability, and transmitter release in physiological and pathophysiological states [103–105]. How astrocytes release glutamate is controversial: for example, does it depend on channels, transporters, or vesicular exocytosis? Several studies in cultured astrocytes and brain slices suggest that increased intracellular Ca^{2+} concentration induces glutamate release *via* a pathway involving the exocytotic machinery [106]. However, these findings may not be entirely reliable, given that the supporting experiments relied on nonspecific methods to manipulate intracellular Ca^{2+} concentration and glutamate transport in astrocytes. For example, the rise of intracellular Ca^{2+} also activates the Ca^{2+}-activated K^+ channels in astrocytes and extrudes K^+ onto surrounding neurons, depolarizing them and probably resulting in glutamate release [106]. Using a metabotropic glutamate receptor agonist to induce a change in Ca^{2+} concentration in astrocytes may also trigger other changes due to activation of the same receptor on neurons. Indeed, pharmacological inhibition of certain anion channels can reduce glutamate release from astrocytes independently of the exocytotic machinery [103].

Brief synaptic activity can trigger K^+ uptake via K2P channels containing TREK-1, leading to a temporary increase in astrocyte volume. The volume returns to normal when bestrophin-1 allows Cl^- out of the cell [107]. TREK-1 is responsible for fast glutamate release from astrocytes, and the Ca^{2+}-activated Cl^- channel bestrophin-1 is responsible for slow glutamate release [108]. Fast release depends on activation of $G_{\alpha i}$ and dissociation of $G_{\beta\gamma}$, followed by interaction between $G_{\beta\gamma}$ and TREK-1, leading to the opening of glutamate-permeable TREK-1 [109]. This overall pathway is mediated by G_i-type G protein-coupled receptors including cannabinoid receptor 1, adenosine receptor A1, and μ-opioid receptor. Like TREK-1, TWIK-1 can directly interact with the G_γ subunit; in the presence of G_γ, the heterodimer TWIK-1/TREK-1, which is expressed in astrocytes [13, 96, 100, 110], becomes permeable to glutamate and K^+ [100]. These data suggest that $G_{\beta\gamma}$ alters the pore region of the K2P channel. Further studies are needed to determine how TWIK-1/TREK-1 heterodimers are permeable to glutamate.

3.1.3. Ischemia. Astrocytic TREK-1 is also involved in the pathology of ischemia. In an animal model of focal ischemia induced by arterial occlusion, reperfusion was associated with upregulation of TREK-1 [111]. Inhibition of TREK-1 impaired astrocytic clearance and exacerbated inflammation after ischemia, resulting in neuronal apoptosis [112]. During ischemia, the ischemic metabolite lactate upregulates TREK-1 in astrocytes via the PKA pathway [113]. Astrocyte elevated gene-1 (AEG-1) also induces TREK-1 expression in astrocytes during ischemia [114].

These observations suggest that K2P channels, particularly TREK-1, may be involved in passive K^+ conductance, glutamate release, and ischemia pathology. Future work, such as using conditional knockout mice, should focus on establishing which K2P channels are expressed in astrocytes and what are their functions.

3.2. Microglia. Microglia fulfill various functions within the central nervous system, which are related mainly to immune responses and homeostasis. Microglia monitor for damage, injury, or disease, and they contribute to synaptic pruning. Disruption of microglial function leads to several diseases, and microglia-mediated neuroinflammation, associated with synaptic loss and cognitive decline [115], is a characteristic of late AD. Dysregulation of synaptic pruning is associated with cognitive defects in autism [116].

Little is known regarding the expression and function of K2P channels in microglia. THIK-1 appears to play a critical role in microglial ramification and immune surveillance in the brain [117]. Microglia in rat brain slices showed a more depolarized potential (-40.6 mV) and higher input resistance than neurons or other glia. Locally puffing 100 mM ATP onto microglia activated the $P2Y_{12}$ receptor and hyperpolarized their membrane by ~30 mV [117]. Pharmacological blockade or genetic ablation of THIK-1 depolarized the microglia at rest, inhibiting microglial ramification and surveillance. These results suggest that by modulating resting membrane potential of microglia, THIK-1 may help regulate microglia function. Blocking THIK-1 in brain slices with quinine, bupivacaine, or tetrapentylammonium abolished the release of interleukin-1β from microglia [117]. This implies that THIK-1 may be involved in the pathological function of microglia in brain diseases. Future studies should investigate the link between resting membrane potential and microglial function, especially since the resting membrane potential of microglia varies across brain regions. Future research should also clarify the region and cell type specificity of THIK-1 expression in the brain.

3.3. Oligodendrocytes. The primary function of oligodendrocytes is to insulate the neuronal axon by creating a myelin sheath, which contributes to rapid signal transduction. TASK-1 can induce currents in oligodendrocytes in response to extracellular acidification, and lack of TASK-1 depolarizes oligodendroglial precursor cells [97]. Inhibition of TASK-1 can protect oligodendrocytes from ischemic injury [118]. TASK-1 may be involved in multiple sclerosis, but the details are unclear. In multiple sclerosis, insufficient recruitment and differentiation of oligodendroglial precursor cells leads to incomplete remyelination. The demyelination and inflammation in the central nervous system of the mice model of multiple sclerosis was alleviated by treatment with bupivacaine, which acts against TASK-1 as well as other channels [97], but not by specific TASK-1 knockout or inhibition [119, 120]. In another mouse model of multiple sclerosis, TASK-1 knockout increased the number of mature oligodendrocytes and accelerated developmental myelination, yet it did not affect oligodendroglial differentiation during remyelination after pathological demyelination [97]. Future studies should clarify whether and how TASK-containing K2P channels help mediate oligodendroglial differentiation and remyelination in normal and disease contexts.

4. Future Perspectives

K2P channels, which differ from K_v and K_{ir} channels, produce leaky K^+ currents to regulate neuronal excitability. K2P channels are distributed widely in the peripheral and central nervous systems, where their expression patterns vary. In neurons, K2P channels modulate resting membrane potential and action potentials, allowing them to influence multiple biological functions. In the peripheral nervous system, TRESK, TASK, and TREK are involved in nociception and pathological pain. Activation of these channels reduces neuronal excitability and thereby alleviates allodynia in several animal models of pain, suggesting that these channels might be potent targets in pain management. In the central nervous system, activation of G protein-coupled receptors induces K2P channels to regulate neuronal excitability in ways that can influence chronic pain, ischemia, epilepsy, sleep disorder, and major depressive disorder.

While neuronal K2P channels regulate excitability, glial K2P channels are likely more involved in K^+ and neurotransmitter homeostasis. TREK-1, TWIK-1, THIK-1, and TASK-1 are thought to be expressed in glia, but further investigation is needed to confirm the regional and cell-type distribution of K2P channels. Indeed, much more work is needed to elucidate the functions of K2P channels in glia as well as in neurons, such as through animal studies in which channels are knocked out of specific cell types under physiological and pathological conditions.

Conflicts of Interest

The authors have no conflict of interest regarding this article.

Acknowledgments

This study was supported by grants to R.J. from the National Natural Science Foundation of China (32071003), the Department of Science and Technology of Sichuan Province (2020ZYD006), and the 1·3·5 Project for Disciplines of Excellence of West China Hospital, Sichuan University (ZYJC21034).

References

[1] D. J. Adams, S. J. Smith, and S. H. Thompson, "Ionic currents in molluscan soma," *Annual Review of Neuroscience*, vol. 3, no. 1, pp. 141–167, 1980.

[2] A. M. Katz, F. C. Messineo, and L. Herbette, "Ion channels in membranes," *Circulation*, vol. 65, 1, Part 2, pp. I2–10, 1982.

[3] O. M. Sejersted and G. Sjogaard, "Dynamics and consequences of potassium shifts in skeletal muscle and heart during exercise," *Physiological Reviews*, vol. 80, no. 4, pp. 1411–1481, 2000.

[4] L. Y. Jan and Y. N. Jan, "Voltage-gated potassium channels and the diversity of electrical signalling," *Journal of Physiology*, vol. 590, no. 11, pp. 2591–2599, 2012.

[5] N. Schmitt, M. Grunnet, and S. P. Olesen, "Cardiac potassium channel subtypes: new roles in repolarization and arrhythmia," *Physiological Reviews*, vol. 94, no. 2, pp. 609–653, 2014.

[6] F. Lesage and M. Lazdunski, "Molecular and functional properties of two-pore-domain potassium channels," *American Journal of Physiology: Renal Physiology*, vol. 279, no. 5, pp. F793–F801, 2000.

[7] F. V. Sepulveda, L. Pablo Cid, J. Teulon, and M. I. Niemeyer, "Molecular aspects of structure, gating, and physiology of pH-sensitive background K2P and Kir K+-transport channels," *Physiological Reviews*, vol. 95, no. 1, pp. 179–217, 2015.

[8] P. Enyedi and G. Czirjak, "Molecular background of leak K+ currents: two-pore domain potassium channels," *Physiological Reviews*, vol. 90, no. 2, pp. 559–605, 2010.

[9] F. Lesage, E. Guillemare, M. Fink et al., "TWIK-1, a ubiquitous human weakly inward rectifying K+ channel with a novel structure," *EMBO Journal*, vol. 15, no. 5, pp. 1004–1011, 1996.

[10] A. D. Medhurst, G. Rennie, C. G. Chapman et al., "Distribution analysis of human two pore domain potassium channels in tissues of the central nervous system and periphery," *Molecular Brain Research*, vol. 86, no. 1-2, pp. 101–114, 2001.

[11] E. M. Talley, G. Solorzano, Q. Lei, D. Kim, and D. A. Bayliss, "CNS distribution of members of the two-pore-domain (KCNK) potassium channel family," *Journal of Neuroscience*, vol. 21, no. 19, pp. 7491–7505, 2001.

[12] N. Decher, S. Rinne, M. Bedoya, W. Gonzalez, and A. K. Kiper, "Molecular pharmacology of K_{2P} potassium channels," *Cell Physiol Biochem*, vol. 55, no. S3, pp. 87–107, 2021.

[13] M. Zhou, G. Xu, M. Xie et al., "TWIK-1 and TREK-1 are potassium channels contributing significantly to astrocyte passive conductance in rat hippocampal slices," *Journal of Neuroscience*, vol. 29, no. 26, pp. 8551–8564, 2009.

[14] C. Tsantoulas, "Emerging potassium channel targets for the treatment of pain," *Current Opinion in Supportive & Palliative Care*, vol. 9, no. 2, pp. 147–154, 2015.

[15] A. Mathie and E. L. Veale, "Two-pore domain potassium channels: potential therapeutic targets for the treatment of pain," *Pflügers Archiv - European Journal of Physiology*, vol. 467, no. 5, pp. 931–943, 2015.

[16] X. Y. Li and H. Toyoda, "Role of leak potassium channels in pain signaling," *Brain Research Bulletin*, vol. 119, Part A, pp. 73–79, 2015.

[17] Y. Sano, K. Inamura, A. Miyake et al., "A Novel Two-pore Domain K^+ Channel, TRESK, Is Localized in the Spinal Cord," *Journal of Biological Chemistry*, vol. 278, no. 30, pp. 27406–27412, 2003.

[18] T. Dobler, A. Springauf, S. Tovornik et al., "TRESK two-pore-domain K^+ channels constitute a significant component of background potassium currents in murine dorsal root ganglion neurones," *Journal of Physiology*, vol. 585, no. 3, pp. 867–879, 2007.

[19] D. Kang and D. Kim, "TREK-2 (K2P10.1) and TRESK (K2P18.1) are major background K^+ channels in dorsal root ganglion neurons," *American Journal of Physiology-Cell Physiology*, vol. 291, no. 1, pp. C138–C146, 2006.

[20] A. Castellanos, A. Pujol-Coma, A. Andres-Bilbe et al., "TRESK background K^+ channel deletion selectively uncovers enhanced mechanical and cold sensitivity," *Journal of Physiology*, vol. 598, no. 5, pp. 1017–1038, 2020.

[21] Z. Guo, C. S. Qiu, X. Jiang et al., "TRESK K^+ Channel activity regulates trigeminal nociception and headache," *eNeuro*, vol. 6, no. 4, 2019.

[22] Y. Yang, S. Li, Z. R. Jin et al., "Decreased abundance of TRESK two-pore domain potassium channels in sensory neurons underlies the pain associated with bone metastasis," *Science Signaling*, vol. 11, no. 552, article eaao5150, 2018.

[23] A. Tulleuda, B. Cokic, G. Callejo, B. Saiani, J. Serra, and X. Gasull, "TRESK channel contribution to nociceptive sensory neurons excitability: modulation by nerve injury," *Molecular Pain*, vol. 7, p. 1744-8069-7-30, 2011.

[24] R. G. Lafrenière, M. Z. Cader, J. F. Poulin et al., "A dominant-negative mutation in the TRESK potassium channel is linked to familial migraine with aura," *Nature Medicine*, vol. 16, no. 10, pp. 1157–1160, 2010.

[25] P. Liu, Z. Xiao, F. Ren et al., "Functional analysis of a migraine-associated TRESK K^+ channel mutation," *Journal of Neuroscience*, vol. 33, no. 31, pp. 12810–12824, 2013.

[26] P. Royal, A. Andres-Bilbe, P. Ávalos Prado et al., "Migraine-associated TRESK mutations increase neuronal excitability through alternative translation initiation and inhibition of TREK," *Neuron*, vol. 101, no. 2, pp. 232–245.e6, 2019.

[27] P. Pettingill, G. A. Weir, T. Wei et al., "A causal role for TRESK loss of function in migraine mechanisms," *Brain*, vol. 142, no. 12, pp. 3852–3867, 2019.

[28] G. Grabauskas, X. Wu, S. Zhou, J. Y. Li, J. Gao, and C. Owyang, "High-fat diet-induced vagal afferent dysfunction via upregulation of 2-pore domain potassium TRESK channel," *JCI Insight*, vol. 4, no. 17, 2019.

[29] G. Grabauskas, X. Wu, I. Song, S. Y. Zhou, T. Lanigan, and C. Owyang, "Increased Activation of the TRESK K^+ Mediates Vago-Vagal Reflex Malfunction in Diabetic Rats," *Gastroenterology*, vol. 151, no. 5, pp. 910–922.e7, 2016.

[30] V. Viatchenko-Karpinski, J. Ling, and J. G. Gu, "Characterization of temperature-sensitive leak K^+ currents and expression of TRAAK, TREK-1, and TREK2 channels in dorsal root ganglion neurons of rats," *Molecular Brain*, vol. 11, no. 1, p. 40, 2018.

[31] A. Alloui, K. Zimmermann, J. Mamet et al., "TREK-1, a K^+ channel involved in polymodal pain perception," *EMBO Journal*, vol. 25, no. 11, pp. 2368–2376, 2006.

[32] V. Pereira, J. Busserolles, M. Christin et al., "Role of the TREK2 potassium channel in cold and warm thermosensation and in pain perception," *Pain*, vol. 155, no. 12, pp. 2534–2544, 2014.

[33] J. Noël, K. Zimmermann, J. Busserolles et al., "The mechano-activated K^+ channels TRAAK and TREK-1 control both warm and cold perception," *EMBO Journal*, vol. 28, no. 9, pp. 1308–1318, 2009.

[34] C. Acosta, L. Djouhri, R. Watkins, C. Berry, K. Bromage, and S. N. Lawson, "TREK2 expressed selectively in IB4-binding C-fiber nociceptors hyperpolarizes their membrane potentials and limits spontaneous pain," *Journal of Neuroscience*, vol. 34, no. 4, pp. 1494–1509, 2014.

[35] P. Rivas-Ramirez, A. Cadaveira-Mosquera, J. A. Lamas, and A. Reboreda, "Muscarinic modulation of TREK currents in mouse sympathetic superior cervical ganglion neurons," *European Journal of Neuroscience*, vol. 42, no. 2, pp. 1797–1807, 2015.

[36] D. Fernández-Fernández, A. Cadaveira-Mosquera, L. Rueda-Ruzafa et al., "Activation of TREK currents by riluzole in three subgroups of cultured mouse nodose ganglion neurons," *PLoS One*, vol. 13, no. 6, article e0199282, 2018.

[37] A. J. C. Loucif, P. P. Saintot, J. Liu et al., "GI-530159, a novel, selective, mechanosensitive two-pore-domain potassium (K2P) channel opener, reduces rat dorsal root ganglion neuron excitability," *British Journal of Pharmacology*, vol. 175, no. 12, pp. 2272–2283, 2018.

[38] Y. Qiu, L. Huang, J. Fu et al., "TREK channel family activator with a well-defined structure-activation relationship for pain and neurogenic inflammation," *Journal of Medicinal Chemistry*, vol. 63, no. 7, pp. 3665–3677, 2020.

[39] H. Kanda, J. Ling, S. Tonomura, K. Noguchi, S. Matalon, and J. G. Gu, "TREK-1 and TRAAK Are Principal K^+ Channels at the Nodes of Ranvier for Rapid Action Potential Conduction on Mammalian Myelinated Afferent Nerves," *Neuron*, vol. 104, no. 5, pp. 960–971.e7, 2019.

[40] Y. Kim, H. Bang, and D. Kim, "TASK-3, a New Member of the Tandem Pore K^+ Channel Family," *Journal of Biological Chemistry*, vol. 275, no. 13, pp. 9340–9347, 2000.

[41] B. Marsh, C. Acosta, L. Djouhri, and S. N. Lawson, "Leak K^+ channel mRNAs in dorsal root ganglia: Relation to inflammation and spontaneous pain behaviour," *Molecular and Cellular Neurosciences*, vol. 49, no. 3, pp. 375–386, 2012.

[42] C. Morenilla-Palao, E. Luis, C. Fernández-Peña et al., "Ion channel profile of TRPM8 cold receptors reveals a role of TASK-3 potassium channels in thermosensation," *Cell Reports*, vol. 8, no. 5, pp. 1571–1582, 2014.

[43] P. Liao, Y. Qiu, Y. Mo et al., "Selective activation of TWIK-related acid-sensitive K^+ 3 subunit-containing channels is analgesic in rodent models," *Science Translational Medicine*, vol. 11, no. 519, article eaaw8434, 2019.

[44] G. García, R. Noriega-Navarro, V. A. Martínez-Rojas, E. J. Gutiérrez-Lara, N. Oviedo, and J. Murbartián, "Spinal TASK-1 and TASK-3 modulate inflammatory and neuropathic pain," *European Journal of Pharmacology*, vol. 862, p. 172631, 2019.

[45] R. Kohling and J. Wolfart, "Potassium channels in epilepsy," *Cold Spring Harbor Perspectives in Medicine*, vol. 6, no. 5, 2016.

[46] M. Borsotto, J. Veyssiere, H. Moha ou Maati, C. Devader, J. Mazella, and C. Heurteaux, "Targeting two-pore domain K^+ channels TREK-1 and TASK-3 for the treatment of depression: a new therapeutic concept," *British Journal of Pharmacology*, vol. 172, no. 3, pp. 771–784, 2015.

[47] S. Yoo, J. Liu, M. Sabbadini, P. Au, G. X. Xie, and C. S. Yost, "Regional expression of the anesthetic-activated potassium channel TRESK in the rat nervous system," *Neuroscience Letters*, vol. 465, no. 1, pp. 79–84, 2009.

[48] H. Y. Hwang, E. Zhang, S. Park et al., "TWIK-related spinal cord K^+ Channel expression is increased in the spinal dorsal horn after spinal nerve ligation," *Yonsei Medical Journal*, vol. 56, no. 5, pp. 1307–1315, 2015.

[49] J. Zhou, W. Lin, H. Chen, Y. Fan, and C. Yang, "TRESK contributes to pain threshold changes by mediating apoptosis via MAPK pathway in the spinal cord," *Neuroscience*, vol. 339, pp. 622–633, 2016.

[50] G. T. Kim, A. S. Siregar, E. J. Kim et al., "Upregulation of TRESK channels contributes to motor and sensory recovery after spinal cord injury," *International Journal of Molecular Sciences*, vol. 21, no. 23, p. 8997, 2020.

[51] T. Lalic, A. Steponenaite, L. Wei et al., "TRESK is a key regulator of nocturnal suprachiasmatic nucleus dynamics and

light adaptive responses," *Nature Communications*, vol. 11, no. 1, p. 4614, 2020.

[52] G. J. Hervieu, J. E. Cluderay, C. W. Gray et al., "Distribution and expression of TREK-1, a two-pore-domain potassium channel, in the adult rat CNS," *Neuroscience*, vol. 103, no. 4, pp. 899–919, 2001.

[53] W. Gu, G. Schlichthörl, J. R. Hirsch et al., "Expression pattern and functional characteristics of two novel splice variants of the two-pore-domain potassium channel TREK-2," *Journal of Physiology*, vol. 539, no. 3, pp. 657–668, 2002.

[54] W. Wang, C. M. Kiyoshi, Y. du et al., "TREK-1 null impairs neuronal excitability, synaptic plasticity, and cognitive function," *Molecular Neurobiology*, vol. 57, no. 3, pp. 1332–1346, 2020.

[55] C. Heurteaux, G. Lucas, N. Guy et al., "Deletion of the background potassium channel TREK-1 results in a depression-resistant phenotype," *Nature Neuroscience*, vol. 9, no. 9, pp. 1134–1141, 2006.

[56] C. Heurteaux, N. Guy, C. Laigle et al., "TREK-1, a K^+ channel involved in neuroprotection and general anesthesia," *EMBO Journal*, vol. 23, no. 13, pp. 2684–2695, 2004.

[57] J. Mazella, O. Pétrault, G. Lucas et al., "Spadin, a sortilin-derived peptide, targeting rodent TREK-1 channels: a new concept in the antidepressant drug design," *PLoS Biology*, vol. 8, no. 4, article e1000355, 2010.

[58] D. Ye, Y. Li, X. Zhang et al., "TREK1 channel blockade induces an antidepressant-like response synergizing with 5-HT_{1A} receptor signaling," *European Neuropsychopharmacology*, vol. 25, no. 12, pp. 2426–2436, 2015.

[59] C. Devader, A. Khayachi, J. Veyssière et al., "In vitro and in vivo regulation of synaptogenesis by the novel antidepressant spadin," *British Journal of Pharmacology*, vol. 172, no. 10, pp. 2604–2617, 2015.

[60] L. E. Kennard, J. R. Chumbley, K. M. Ranatunga, S. J. Armstrong, E. L. Veale, and A. Mathie, "Inhibition of the human two-pore domain potassium channel, TREK-1, by fluoxetine and its metabolite norfluoxetine," *British Journal of Pharmacology*, vol. 144, no. 6, pp. 821–829, 2005.

[61] A. Kim, H. G. Jung, Y. E. Kim et al., "The knockdown of TREK-1 in hippocampal neurons attenuate lipopolysaccharide-induced depressive-like behavior in mice," *International Journal of Molecular Sciences*, vol. 20, no. 23, p. 5902, 2019.

[62] R. H. Perlis, P. Moorjani, J. Fagerness et al., "Pharmacogenetic analysis of genes implicated in rodent models of antidepressant response: association of *TREK1* and treatment resistance in the STAR*D study," *Neuropsychopharmacology*, vol. 33, no. 12, pp. 2810–2819, 2008.

[63] H. Moha ou Maati, J. Veyssiere, F. Labbal et al., "Spadin as a new antidepressant: absence of TREK-1-related side effects," *Neuropharmacology*, vol. 62, no. 1, pp. 278–288, 2012.

[64] M. A. Giannoni-Guzmán, A. Kamitakahara, V. Magalong, P. Levitt, and D. G. McMahon, "Circadian photoperiod alters TREK-1 channel function and expression in dorsal raphe serotonergic neurons via melatonin receptor 1 signaling," *Journal of Pineal Research*, vol. 70, no. 2, article e12705, 2021.

[65] P. Y. Deng, Z. Xiao, C. Yang et al., "$GABA_B$ Receptor Activation Inhibits Neuronal Excitability and Spatial Learning in the Entorhinal Cortex by Activating TREK-2 K^+ Channels," *Neuron*, vol. 63, no. 2, pp. 230–243, 2009.

[66] Z. Xiao, P. Y. Deng, L. Rojanathammanee et al., "Noradrenergic Depression of Neuronal Excitability in the Entorhinal Cortex via Activation of TREK-2 K^+ Channels," *Journal of Biological Chemistry*, vol. 284, no. 16, pp. 10980–10991, 2009.

[67] C. K. Bauer, P. Calligari, F. C. Radio et al., "Mutations in KCNK4 that affect gating cause a recognizable neurodevelopmental syndrome," *American Journal of Human Genetics*, vol. 103, no. 4, pp. 621–630, 2018.

[68] Z. Rusznák, K. Pocsai, I. Kovács et al., "Differential distribution of TASK-1, TASK-2 and TASK-3 immunoreactivities in the rat and human cerebellum," *Cellular and Molecular Life Sciences*, vol. 61, no. 12, pp. 1532–1542, 2004.

[69] J. Han, J. Truell, C. Gnatenco, and D. Kim, "Characterization of four types of background potassium channels in rat cerebellar granule neurons," *Journal of Physiology*, vol. 542, no. 2, pp. 431–444, 2002.

[70] C. P. Washburn, J. E. Sirois, E. M. Talley, P. G. Guyenet, and D. A. Bayliss, "Serotonergic raphe neurons express TASK channel transcripts and a TASK-like pH- and halothane-sensitive K^+ conductance," *Journal of Neuroscience*, vol. 22, no. 4, pp. 1256–1265, 2002.

[71] M. I. Aller, E. L. Veale, A. M. Linden et al., "Modifying the subunit composition of TASK channels alters the modulation of a leak conductance in cerebellar granule neurons," *Journal of Neuroscience*, vol. 25, no. 49, pp. 11455–11467, 2005.

[72] S. G. Brickley, M. I. Aller, C. Sandu et al., "TASK-3 two-pore domain potassium channels enable sustained high-frequency firing in cerebellar granule neurons," *Journal of Neuroscience*, vol. 27, no. 35, pp. 9329–9340, 2007.

[73] M. Goutierre, S. al Awabdh, F. Donneger et al., "KCC2 regulates neuronal excitability and hippocampal activity via interaction with TASK-3 channels," *Cell Reports*, vol. 28, no. 1, pp. 91–103.e7, 2019.

[74] P. Y. Deng and S. Lei, "Serotonin increases GABA release in rat entorhinal cortex by inhibiting interneuron TASK-3 K^+ channels," *Molecular and Cellular Neurosciences*, vol. 39, no. 2, pp. 273–284, 2008.

[75] F. A. de Falco, P. Striano, A. de Falco et al., "Benign adult familial myoclonic epilepsy: genetic heterogeneity and allelism with ADCME," *Neurology*, vol. 60, no. 8, pp. 1381–1385, 2003.

[76] Y. Sugimoto, R. Morita, K. Amano et al., "Childhood absence epilepsy in 8q24: refinement of candidate region and construction of physical map," *Genomics*, vol. 68, no. 3, pp. 264–272, 2000.

[77] C. Kananura, T. Sander, S. Rajan et al., "Tandem pore domain K^+-channel TASK-3 (KCNK9) and idiopathic absence epilepsies," *American Journal of Medical Genetics*, vol. 114, no. 2, pp. 227–229, 2002.

[78] J. Holter, D. Carter, N. Leresche, V. Crunelli, and P. Vincent, "A *TASK3* channel (*KCNK9*) mutation in a genetic model of absence epilepsy," *Journal of Molecular Neuroscience*, vol. 25, no. 1, pp. 037–052, 2005.

[79] T. C. Gent, M. Bandarabadi, C. G. Herrera, and A. R. Adamantidis, "Thalamic dual control of sleep and wakefulness," *Nature Neuroscience*, vol. 21, no. 7, pp. 974–984, 2018.

[80] S. G. Meuth, T. Budde, T. Kanyshkova, T. Broicher, T. Munsch, and H. C. Pape, "Contribution of TWIK-related acid-sensitive K^+ channel 1 (TASK1) and TASK3 channels to the control of activity modes in thalamocortical neurons," *Journal of Neuroscience*, vol. 23, no. 16, pp. 6460–6469, 2003.

[81] S. G. Meuth, T. Kanyshkova, P. Meuth et al., "Membrane resting potential of thalamocortical relay neurons is shaped by the interaction among TASK3 and HCN2 channels," *Journal of Neurophysiology*, vol. 96, no. 3, pp. 1517–1529, 2006.

[82] B. Musset, S. G. Meuth, G. X. Liu et al., "Effects of divalent cations and spermine on the K^+ channel TASK-3 and on the outward current in thalamic neurons," *Journal of Physiology*, vol. 572, no. 3, pp. 639–657, 2006.

[83] A. M. Linden, C. Sandu, M. I. Aller et al., "TASK-3 knockout mice exhibit exaggerated nocturnal activity, impairments in cognitive functions, and reduced sensitivity to inhalation anesthetics," *Journal of Pharmacology and Experimental Therapeutics*, vol. 323, no. 3, pp. 924–934, 2007.

[84] A. L. Gotter, V. P. Santarelli, S. M. Doran et al., "TASK-3 as a potential antidepressant target," *Brain Research*, vol. 1416, pp. 69–79, 2011.

[85] D. S. Pang, C. J. Robledo, D. R. Carr et al., "An unexpected role for TASK-3 potassium channels in network oscillations with implications for sleep mechanisms and anesthetic action," *Proceedings of the National Academy of Sciences of the United States of America*, vol. 106, no. 41, pp. 17546–17551, 2009.

[86] F. Ge, P. Mu, R. Guo et al., "Chronic sleep fragmentation enhances habenula cholinergic neural activity," *Molecular Psychiatry*, vol. 26, no. 3, pp. 941–954, 2021.

[87] G. Gobbi and P. Blier, "Effect of neurokinin-1 receptor antagonists on serotoninergic, noradrenergic and hippocampal neurons: comparison with antidepressant drugs," *Peptides*, vol. 26, no. 8, pp. 1383–1393, 2005.

[88] W. Jiang, Y. Zhang, L. Xiao et al., "Cannabinoids promote embryonic and adult hippocampus neurogenesis and produce anxiolytic- and antidepressant-like effects," *Journal of Clinical Investigation*, vol. 115, no. 11, pp. 3104–3116, 2005.

[89] Z. Zhang, W. Wang, P. Zhong et al., "Blockade of 2-arachidonoylglycerol hydrolysis produces antidepressant-like effects and enhances adult hippocampal neurogenesis and synaptic plasticity," *Hippocampus*, vol. 25, no. 1, pp. 16–26, 2015.

[90] J. M. Graham Jr., N. Zadeh, M. Kelley et al., "KCNK9 imprinting syndrome-further delineation of a possible treatable disorder," *American Journal of Medical Genetics. Part A*, vol. 170, no. 10, pp. 2632–2637, 2016.

[91] O. Barel, S. A. Shalev, R. Ofir et al., "Maternally Inherited Birk Barel Mental Retardation Dysmorphism Syndrome Caused by a Mutation in the Genomically Imprinted Potassium Channel _KCNK9_," *American Journal of Human Genetics*, vol. 83, no. 2, pp. 193–199, 2008.

[92] F. Lesage, I. Lauritzen, F. Duprat et al., "The structure, function and distribution of the mouse TWIK-1 K^+ channel," *FEBS Letters*, vol. 402, no. 1, pp. 28–32, 1997.

[93] P. Y. Deng, S. K. Poudel, L. Rojanathammanee, J. E. Porter, and S. Lei, "Serotonin inhibits neuronal excitability by activating two-pore domain K+ channels in the entorhinal cortex," *Molecular Pharmacology*, vol. 72, no. 1, pp. 208–218, 2007.

[94] O. Yarishkin, D. Y. Lee, E. Kim et al., "TWIK-1 contributes to the intrinsic excitability of dentate granule cells in mouse hippocampus," *Molecular Brain*, vol. 7, no. 1, p. 80, 2014.

[95] J. H. Choi, O. Yarishkin, E. Kim et al., "TWIK-1/TASK-3 heterodimeric channels contribute to the neurotensin-mediated excitation of hippocampal dentate gyrus granule cells," *Experimental and Molecular Medicine*, vol. 50, no. 11, pp. 1–13, 2018.

[96] J. D. Cahoy, B. Emery, A. Kaushal et al., "A transcriptome database for astrocytes, neurons, and oligodendrocytes: a new resource for understanding brain development and function," *Journal of Neuroscience*, vol. 28, no. 1, pp. 264–278, 2008.

[97] S. Albrecht, S. Korr, L. Nowack et al., "The K2P-channel TASK1 affects oligodendroglial differentiation but not myelin restoration," *Glia*, vol. 67, no. 5, pp. 870–883, 2019.

[98] S. Liddelow and B. Barres, "SnapShot: astrocytes in health and disease," *Cell*, vol. 162, no. 5, pp. 1170–1170.e1, 2015.

[99] W. Wang, A. Putra, G. P. Schools et al., "The contribution of TWIK-1 channels to astrocyte K^+ current is limited by retention in intracellular compartments," *Frontiers in Cellular Neuroscience*, vol. 7, p. 246, 2013.

[100] E. Mi Hwang, E. Kim, O. Yarishkin et al., "A disulphide-linked heterodimer of TWIK-1 and TREK-1 mediates passive conductance in astrocytes," *Nature Communications*, vol. 5, no. 1, p. 3227, 2014.

[101] Y. Bae, J. H. Choi, K. Ryoo et al., "Spadin modulates astrocytic passive conductance via inhibition of TWIK-1/TREK-1 heterodimeric channels," *International Journal of Molecular Sciences*, vol. 21, no. 24, p. 9639, 2020.

[102] Y. du, C. M. Kiyoshi, Q. Wang et al., "Genetic deletion of TREK-1 or TWIK-1/TREK-1 potassium channels does not alter the basic electrophysiological properties of mature hippocampal astrocytes in situ," *Frontiers in Cellular Neuroscience*, vol. 10, p. 13, 2016.

[103] A. Verkhratsky and M. Nedergaard, "Physiology of astroglia," *Physiological Reviews*, vol. 98, no. 1, pp. 239–389, 2018.

[104] M. D. Scofield, "Exploring the role of astroglial glutamate release and association with synapses in neuronal function and behavior," *Biological Psychiatry*, vol. 84, no. 11, pp. 778–786, 2018.

[105] T. A. Fiacco, C. Agulhon, and K. D. McCarthy, "Sorting out astrocyte physiology from pharmacology," *Annual Review of Pharmacology and Toxicology*, vol. 49, pp. 151–174, 2009.

[106] N. B. Hamilton and D. Attwell, "Do astrocytes really exocytose neurotransmitters?," *Nature Reviews Neuroscience*, vol. 11, no. 4, pp. 227–238, 2010.

[107] J. Woo, M. W. Jang, J. Lee, W. Koh, K. Mikoshiba, and C. J. Lee, "The molecular mechanism of synaptic activity-induced astrocytic volume transient," *Journal of Physiology*, vol. 598, no. 20, pp. 4555–4572, 2020.

[108] D. H. Woo, K. S. Han, J. W. Shim et al., "TREK-1 and Best1 channels mediate fast and slow glutamate release in astrocytes upon GPCR activation," *Cell*, vol. 151, no. 1, pp. 25–40, 2012.

[109] D. H. Woo, J. Y. Bae, M. H. Nam et al., "Activation of astrocytic μ-opioid receptor elicits fast glutamate release through TREK-1-containing K2P channel in hippocampal astrocytes," *Frontiers in Cellular Neuroscience*, vol. 12, p. 319, 2018.

[110] J. Benesova, V. Rusnakova, P. Honsa et al., "Distinct expression/function of potassium and chloride channels contributes to the diverse volume regulation in cortical astrocytes of GFAP/EGFP mice," *PLoS One*, vol. 7, no. 1, article e29725, 2012.

[111] M. Wang, J. Song, W. Xiao et al., "Changes in lipid-sensitive two-pore domain potassium channel TREK-1 expression and

its involvement in astrogliosis following cerebral ischemia in rats," *Journal of Molecular Neuroscience*, vol. 46, no. 2, pp. 384–392, 2012.

[112] X. Wu, Y. Liu, X. Chen et al., "Involvement of TREK-1 activity in astrocyte function and neuroprotection under simulated ischemia conditions," *Journal of Molecular Neuroscience*, vol. 49, no. 3, pp. 499–506, 2013.

[113] A. Banerjee, S. Ghatak, and S. K. Sikdar, "l-Lactate mediates neuroprotection against ischaemia by increasing TREK1 channel expression in rat hippocampal astrocytes in vitro," *Journal of Neurochemistry*, vol. 138, no. 2, pp. 265–281, 2016.

[114] A. Kim, H. G. Jung, S. C. Kim et al., "Astrocytic AEG-1 regulates expression of TREK-1 under acute hypoxia," *Cell Biochem Funct*, vol. 38, no. 2, pp. 167–175, 2020.

[115] S. Hong, V. F. Beja-Glasser, B. M. Nfonoyim et al., "Complement and microglia mediate early synapse loss in Alzheimer mouse models," *Science*, vol. 352, no. 6286, pp. 712–716, 2016.

[116] I. Voineagu, X. Wang, P. Johnston et al., "Transcriptomic analysis of autistic brain reveals convergent molecular pathology," *Nature*, vol. 474, no. 7351, pp. 380–384, 2011.

[117] C. Madry, V. Kyrargyri, I. L. Arancibia-Cárcamo et al., "Microglial Ramification, Surveillance, and Interleukin-1β Release Are Regulated by the Two-Pore Domain K^+ Channel THIK-1," *Neuron*, vol. 97, no. 2, pp. 299–312.e6, 2018.

[118] V. Hawkins and A. Butt, "TASK-1 channels in oligodendrocytes: a role in ischemia mediated disruption," *Neurobiology of Disease*, vol. 55, pp. 87–94, 2013.

[119] S. Bittner, M. A. Bauer, P. Ehling et al., "The TASK1 channel inhibitor A293 shows efficacy in a mouse model of multiple sclerosis," *Experimental Neurology*, vol. 238, no. 2, pp. 149–155, 2012.

[120] S. Bittner, S. G. Meuth, K. Göbel et al., "TASK1 modulates inflammation and neurodegeneration in autoimmune inflammation of the central nervous system," *Brain*, vol. 132, no. 9, pp. 2501–2516, 2009.

Hindawi
Neural Plasticity
Volume 2021, Article ID 7806370, 16 pages
https://doi.org/10.1155/2021/7806370

Research Article

Astrocytes in the Ventromedial Hypothalamus Involve Chronic Stress-Induced Anxiety and Bone Loss in Mice

Yunhui Liu,[1] **Jie Shao**,[1,2] **Dashuang Gao**,[1,2] **Lu Zhang**,[1] **and Fan Yang**[1,2]

[1]*The Brain Cognition and Brain Disease Institute, Shenzhen Institute of Advanced Technology, Chinese Academy of Sciences, Shenzhen-Hong Kong Institute of Brain Science-Shenzhen Fundamental Research Institutions, Shenzhen 518055, China*
[2]*University of Chinese Academy of Sciences, Beijing 100049, China*

Correspondence should be addressed to Fan Yang; fan.yang@siat.ac.cn

Yunhui Liu and Jie Shao contributed equally to this work.

Received 19 May 2021; Accepted 22 June 2021; Published 8 July 2021

Academic Editor: Alexei Verkhratsky

Chronic stress is one of the main risk factors of bone loss. While the neurons and neural circuits of the ventromedial hypothalamus (VMH) mediate bone loss induced by chronic stress, the detailed intrinsic mechanisms within the VMH nucleus still need to be explored. Astrocytes in brain regions play important roles in the regulation of metabolism and anxiety-like behavior through interactions with surrounding neurons. However, whether astrocytes in the VMH affect neuronal activity and therefore regulate chronic stress-induced anxiety and bone loss remain elusive. In this study, we found that VMH astrocytes were activated during chronic stress-induced anxiety and bone loss. Pharmacogenetic activation of the Gi and Gq pathways in VMH astrocytes reduced and increased the levels of anxiety and bone loss, respectively. Furthermore, activation of VMH astrocytes by optogenetics induced depolarization in neighboring steroidogenic factor-1 (SF-1) neurons, which was diminished by administration of N-methyl-D-aspartic acid (NMDA) receptor blocker but not by alpha-amino-3-hydroxy-5-methyl-4-isoxazolepropionic acid (AMPA) receptor blocker. These results suggest that there may be a functional "glial-neuron microcircuit" in VMH nuclei that mediates anxiety and bone loss induced by chronic stress. This study not only advances our understanding of glial cell function but also provides a potential intervention target for chronic stress-induced anxiety and bone loss therapy.

1. Introduction

Chronic stress can lead to different mental disorders, manifesting as anxiety, depression, panic, and other symptoms [1–3]. Importantly, chronic stress-induced anxiety often causes a variety of metabolic problems, including glucose [4, 5], lipid [6, 7], and bone metabolism disorders [8, 9]. In particular, abnormal bone metabolism is a common symptom of stress and anxiety [10, 11]. Clinical studies have shown that the probability of osteoporosis and fractures in patients with anxiety and depression is significantly higher than that in normal controls [12–14], suggesting that an individual's anxiety state is closely related to bone metabolism. Although evidence indicates that anxiety can affect bone loss, the underlying neural mechanism is still unclear.

The VMH is closely related to mood disorders such as anxiety and depression. Studies have shown that VMH brain activity is significantly increased in cats with anxiety-like symptoms [15, 16], while blocking VMH glutamate signals can effectively reduce anxiety in animals [17], suggesting that the VMH is involved in the regulation of mood disorders. Furthermore, cannabinoid [18, 19] and serotonin receptors [19, 20] in steroidogenic factor-1- (SF-1-) positive neurons, the main neuronal subtype in the VMH, mediate regulation of anxiety behavior in mice. Research has also shown that bone mass increases significantly after chemical damage to SF-1 neurons in the VMH, suggesting a role of VMH in the regulation of bone metabolism [21]. Subsequent studies have demonstrated that leptin and serotonin act on SF-1 neurons to regulate bone metabolism by regulating sympathetic nerve

activity [22–25]. Thus, SF-1 neurons in the VMH are crucial for central regulation of anxiety and bone metabolism. We previously revealed a $BNST^{SOM}$-VMH^{SF-1}-NTS^{Vglut2} neural circuit that regulates the activities of the peripheral sympathetic nervous system and mediates bone loss caused by chronic stress [26]. As a key link in this circuit, the VMH is responsible for integrating "anxiety information" sent by the upstream bed nucleus of the stria terminalis (BNST) and "bone regulation information" from the downstream—the nucleus of the solitary tract (NTS). To date, however, the underlying neural mechanism within the VMH nucleus remains uncertain regarding regulation of chronic stress-induced anxiety and bone loss.

Astrocytes, which are the most abundant cell type in the brain, are considered to play an auxiliary and supportive role in advanced cognitive functions in the brain. However, increasing evidence suggests that astrocytes are directly involved in the mediation of advanced emotions and metabolic regulation [27–30]. Astrocytes in the lateral habenula (LHb) regulate depressive behavior in rats via the Kir4.1 potassium channel, which is selectively expressed in astrocytes [27]. Hippocampal astrocytes regulate major depression in mice via astrocyte-derived adenosine triphosphate (ATP) [28], suggesting an important role in the regulation of negative emotions such as anxiety and depression. Importantly, hypothalamic VMH astrocytes regulate activities of hypothalamic agouti-related peptide (AgRP) and proopiomelanocortin (POMC) neurons through cannabinoid (CBR1) and adenosine receptors and thereby regulate feeding and metabolism in mice [29, 30]. Thus, given the important role of astrocytes in anxiety and metabolic regulation, we hypothesized that VMH astrocytes likely play a critical role in the regulation of bone loss induced by chronic stress.

In this study, we achieved bidirectional regulation of chronic stress-induced anxiety and bone loss in mice by the chemogenetic manipulation of VMH astrocytes. Specifically, activation of the Gi pathway in VMH astrocytes prevented chronic stress-induced anxiety-like behavior and bone loss, whereas activation of the Gq pathway exerted the opposite effects. Furthermore, the neuronal electrophysiological recordings suggested that these effects may be mediated by astrocyte to SF1 neuron signaling via NMDA receptors but not AMPA receptors. Collectively, this study indicated that VMH astrocytes not only participate in the regulation of mood disorders but can intervene in bone metabolism, thus providing a potential interventional target for the therapeutic treatment of chronic stress-induced anxiety and bone loss.

2. Results

2.1. Chronic Stress-Induced Anxiety and Bone Loss Promote c-fos Expression in VMH Nuclei. We previously identified a BNST-VMH-NTS neural circuit that mediates chronic stress-induced bone loss, whereby the VMH integrates "anxiety information" from the BNST and "bone regulation information" from the NTS [26]. To investigate the role of the VMH in chronic stress-induced anxiety and bone loss, we established a chronic unpredictable mild stress-induced anxiety model in mice. After 8 weeks of chronic stress, mice displayed a decrease in the frequency of entries and time spent in the central area in the open field test compared with the control mice (Figures 1(a) and 1(b)). In addition, compared with the control mice, stressed mice entered less often and spent significantly less time in the open arms of the elevated plus maze (Figures 1(c) and 1(d)). These results indicate that chronic stress (8 weeks) can induce anxiety-like behavior in mice. Importantly, dual-energy X-ray scanning analysis showed that bone density of the proximal tibia was significantly lower in stressed mice than in control mice (Figures 1(e) and 1(f)). Furthermore, H&E staining also indicated a significantly lower number of proximal tibia trabeculae in the stressed group than in the control group (Figure 1(g)). Based on immunohistochemical staining, expression of c-fos in the VMH brain area of the stressed group was significantly higher than that in the control group (Figures 1(h) and 1(i)), suggesting that neural activity in the VMH nucleus is involved in the maintenance of the anxiety state and decrease in bone mineral density (BMD).

2.2. Activation of VMH Astrocytes in Chronic Stress-Induced Anxiety and Bone Loss. Astrocytes are involved in the regulation of emotional disorders and metabolic functions [24–27]. Thus, we examined the role of astrocytes in the VMH nucleus in chronic stress-induced anxiety and bone loss. Based on immunostaining, the number of c-fos and glial fibrillary acidic protein (GFAP) coexpressing astrocytes in the VMH of stressed mice increased significantly compared with that in the control group (Figures 2(a)–2(e)). These results suggest that VMH astrocyte activity is closely related to maintenance of the anxiety state and decreased BMD. In addition, increased GFAP signals and GFAP fibers were observed in the VMH astrocytes of the stress group compared with that of control mice, suggesting alteration in the structure of astrocytes after chronic stress (Figures 2(f) and 2(g)). Therefore, we hypothesized that chronic stress impacts VMH astrocyte activity to regulate the activities of SF-1 neurons in the VMH and thereby modulating the process of bone loss induced by chronic stress.

2.3. Activation of Gi Pathway in VMH Astrocytes Reduces Anxiety and Prevents Bone Loss. To test the hypothesis that VMH astrocyte activity mediates chronic stress-induced anxiety-like behavior and decreases the BMD, we injected AAV2-DIO-hM4Di-mCherry or AAV2-DIO-mCherry into the VMH of S100β-Cre mice, which enabled the selective activation of the Gi pathway in VMH astrocytes by clozapine N-oxide (CNO) administration (Figures 3(a) and 3(b)). After 4 weeks of viral expression and 8 weeks of daily stress, mice received an intraperitoneal injection of CNO (1 mg/kg) to investigate the behavioral effects of Gi pathway activation in VMH astrocytes (Figure 3(a)). Results showed that selective activation of the Gi pathway in VMH astrocytes effectively prevented the induction of anxiety-like behavior following chronic stress. Compared with the control group mice, the hM4Di-expressing mice entered more frequently and spent more time in the central area of the open field (Figures 3(c) and 3(e)). In addition, compared with the control group, the hM4Di-expressing mice preferred to enter

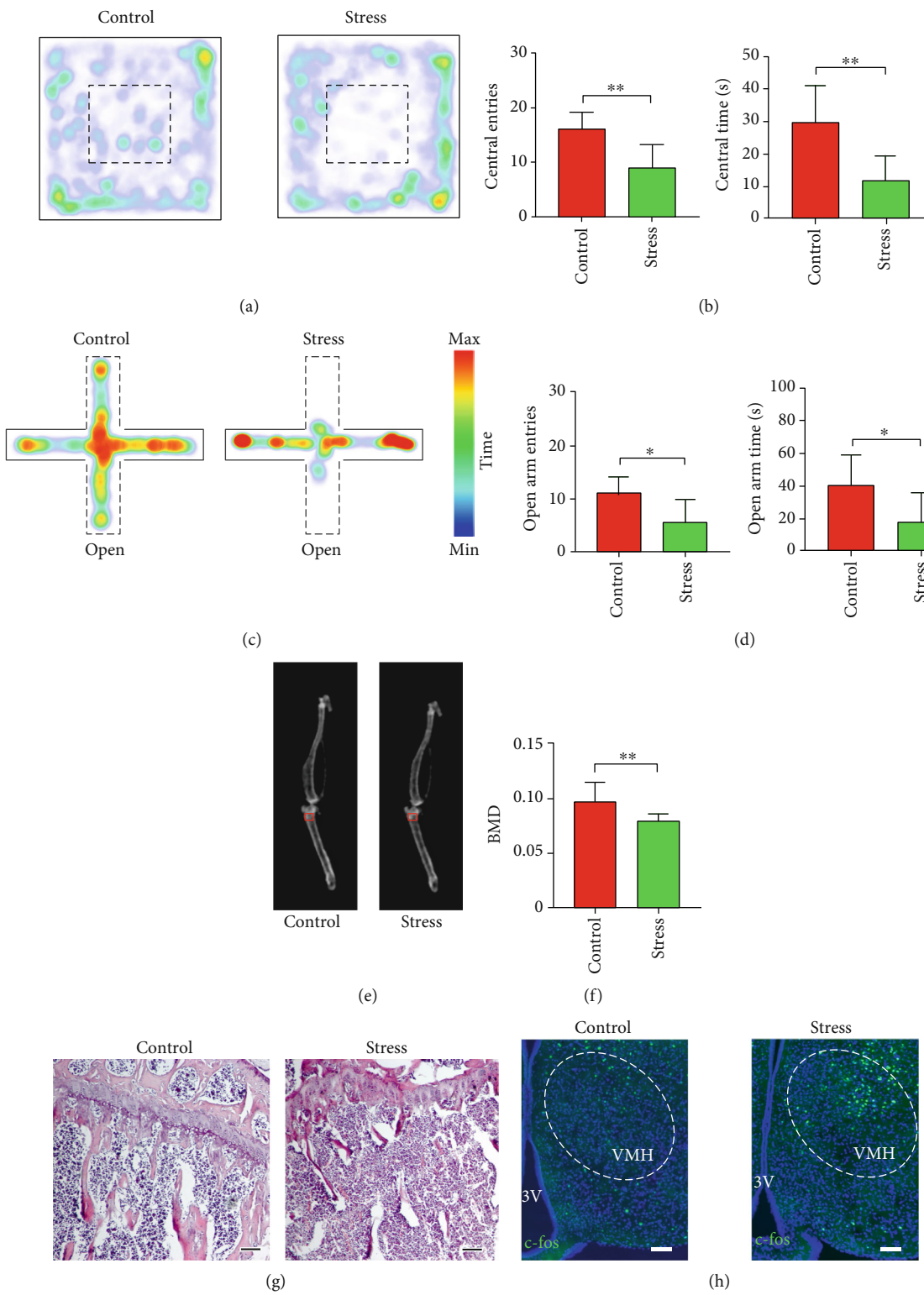

Figure 1: Continued.

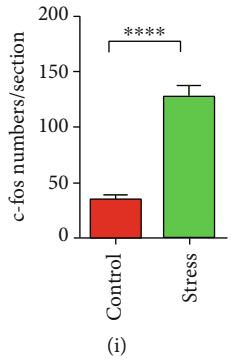

Figure 1: Chronic stress induced anxiety-like behavior and bone loss in mice. (a) Representative heat maps of control and stress groups in different positions in open field test (OFT), with warmer color indicating more time spent at that location. (b) Quantification of entries into and time spent in central area in control and stress groups; values represent mean ± SD ($n = 8$ for control and $n = 7$ for stressed group; $^{**}p < 0.01$; unpaired t-test). (c) Representative heat maps of control and stress groups in different positions in elevated plus maze test (EPM), with warmer color indicating more time spent at that location. (d) Quantification of entries into and time spent in open arm in control and stress groups; values represent mean ± SD ($n = 8$ for control and $n = 7$ for stress group; $^{*}p < 0.05$; unpaired t-test). (e) Representative dual-energy X-ray image showing bone mineral density (BMD) of control and stress groups. BMD in red box was collected for statistical analysis. (f) Quantification of BMD in control and stress groups; values represent mean ± SD ($n = 10$ per group from 5 mice per group; $^{**}p < 0.01$; unpaired t -test). (g) Representative hematoxylin and eosin (H&E) staining of proximal tibia in control and stress groups. Number of proximal tibia trabeculae in stressed mice is less than in control mice; scale bar, 100 μm. (h) c-fos staining of VMH in control and stress groups; scale bar, 100 μm. (i) Quantification of c-fos-positive cells in control and stress groups; values represent mean ± SD ($n = 20$ sections from 5 mice per group; $^{****}p < 0.0001$; unpaired t-test).

and stay in the open arms of the elevated plus maze (Figures 3(d) and 3(f)). To determine the effect of Gi pathway activation in VMH astrocytes on the BMD of mice, we injected CNO into mice three times a week for 4 weeks. Dual energy X-ray bone scanning showed that the BMD of the proximal tibia of the hM4Di group was significantly higher than that of the control group (Figures 3(g) and 3(h)). Furthermore, the number of proximal tibia trabeculae in the hM4Di group was significantly greater than that in the mCherry-expressing control group (Figure 3(i)). In summary, selective activation of the Gi pathway in VMH astrocytes effectively reduced anxiety-like behavior and prevented BMD decrease induced by chronic stress.

2.4. Activation of Gq Pathway in VMH Astrocytes Induces Anxiety and Promotes Bone Loss. We next explored whether the Gq pathway in VMH astrocytes also participates in the regulation of anxiety-induced bone loss. First, we selectively expressed hM3Dq or mCherry in the astrocytes of the VMH nucleus by stereotactic injection in S100β-Cre mice (Figures 4(a) and 4(b)). Following intraperitoneal injection of CNO (1 mg/kg), Gq pathway activation in the VMH astrocytes induced obvious anxiety-like behavior in mice. The number of entries and time spent exploring the central area of the open field was significantly lower in the hM3Dq-expressing mice than in the control mice (Figures 4(c) and 4(e)). Consistently, compared with the control group, hM3Dq-expressing mice entered less often and spent significantly less time in the open arms of the elevated plus maze (Figures 4(d) and 4(f)). Notably, dual energy X-ray analysis showed that BMD of the proximal tibia was significantly lower in the hM3Dq-expressing mice than in the control group (Figures 4(g) and 4(h)). The H&E staining results showed that the number of proximal tibia trabeculae was significantly lower in the hM3Dq-expressing group than in the mCherry-expressing control group (Figure 4(i)). These results suggest that activation of the Gq pathway in VMH astrocytes can induce significant anxiety-like behavior and promote BMD decrease in mice. Thus, pharmacogenetic activation of the Gi and Gq pathways in VMH astrocytes can bidirectionally regulate anxiety-like behavior and bone loss in mice.

2.5. Optical Stimulation of Astrocytes Induced an Excitatory Response in SF-1 Neurons via NMDA Receptor. To clarify the neural mechanism underlying VMH astrocyte regulation of anxiety-like behavior and bone metabolism, we applied optogenetics to test the effects of astrocyte activation on SF-1 neurons, which are crucial regulators of anxiety and bone metabolism [21, 25, 31]. By injecting AAV-GFAP-ChR2-mCherry into the VMH of mice, we achieved optical activation of astrocytes in brain slices during patch recordings (Figures 5(a) and 5(b)). Results indicated that optical stimulation of astrocytes depolarized SF-1 neurons and induced action potential firing (Figure 5(c)). As glutamate is considered a primary excitatory neurotransmitter, we applied glutamate receptor antagonists to brain slices to explore the interactions between astrocytes and SF-1 neurons. Among glutamate receptors, ionotropic glutamate receptors (iGluRs), including NMDA, AMPA, and kainate receptors, can mediate rapid depolarization by glutamate [32]. Given that NBQX and D-APV can block most iGluRs, we added these antagonists to perfused artificial cerebrospinal fluid (aCSF) and found that action potential firing of SF-1 neurons caused by optical activation of astrocytes was significantly suppressed (Figure 5(d)), suggesting that depolarization was primarily due to activation of glutamate receptors. Therefore, we applied NBQX and D-APV separately into aCSF to clarify

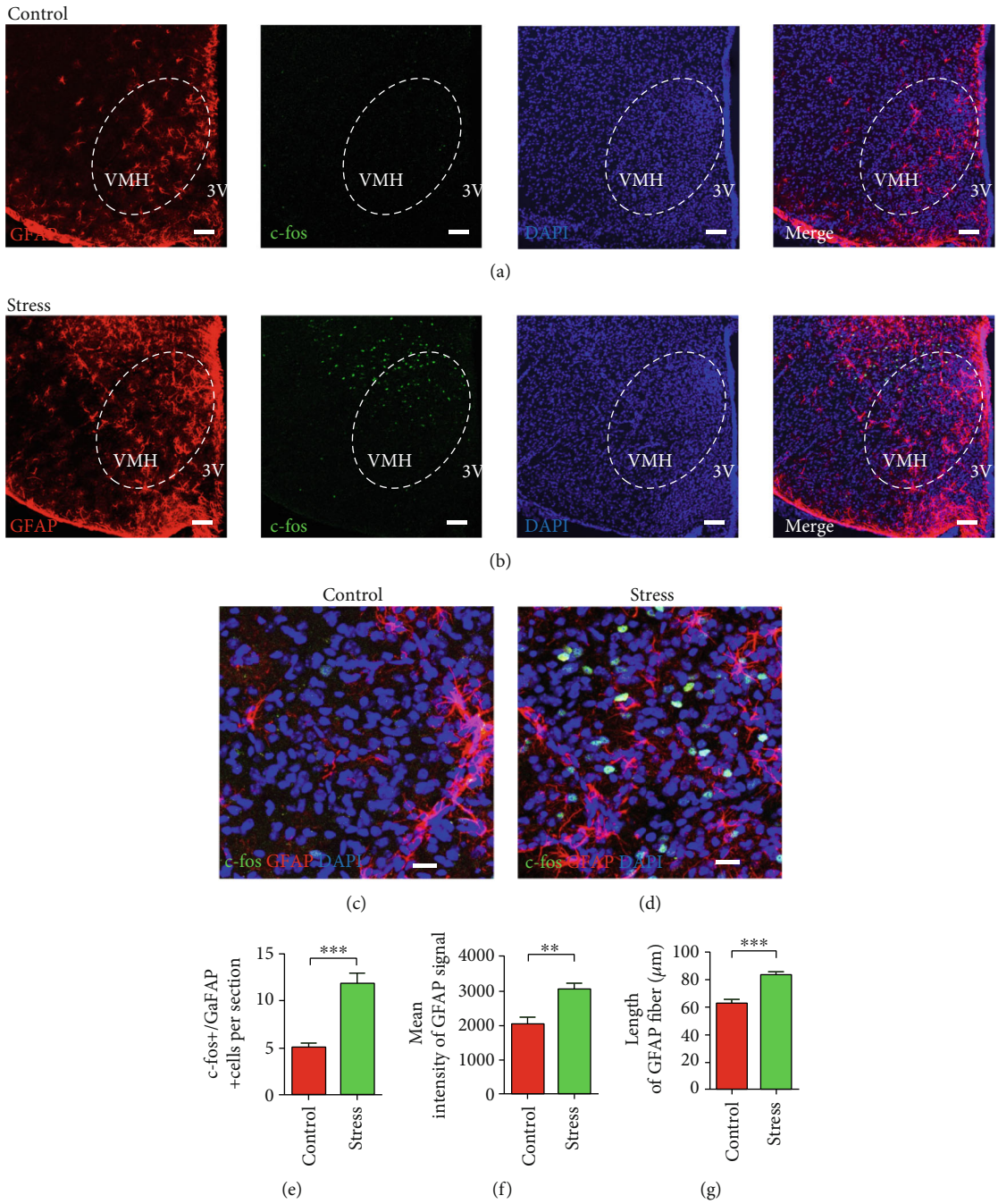

FIGURE 2: Astrocytes in VMH are activated in chronic stress-treated mice. (a) Representative low magnification image showing triple staining of GFAP (red), c-fos (green), and DAPI (blue) in VMH of control group; scale bar, 100 μm. (b) Representative low magnification image showing triple staining of GFAP (red), c-fos (green), and DAPI (blue) in VMH of stress group; scale bar, 100 μm. (c) Representative high magnification image showing triple staining of GFAP (red), c-fos (green), and DAPI (blue) in VMH of control group; scale bar, 20 μm. (d) Representative high magnification image showing triple staining of GFAP (red), c-fos (green), and DAPI (blue) in VMH of stress group; scale bar, 20 μm. (e) Quantification of c-fos$^+$ and GFAP$^+$ coexpressed cells in control and stress groups; values represent mean ± SD ($n = 20$ sections from 5 mice per group; $^{***}p < 0.001$; unpaired t-test). (f) Mean signal intensities of GFAP staining in VMH of control and stress groups; values represent mean ± SD ($n = 5$ mice per group; $^{**}p < 0.01$; unpaired t-test). (g) The length of GFAP fiber in VMH astrocytes of control and stress groups; values represent mean ± SD ($n = 20$ cells; 4 cells from each mouse, 5 mice per group; $^{***}p < 0.001$; unpaired t-test).

the main glutamate receptor subtype involved in astrocyte activation-induced SF-1 neuronal firing. As shown in Figure 5, application of D-APV, but not NBQX, significantly blocked SF-1 neuronal firing caused by optical activation of astrocytes. We also recorded changes in membrane potential in SF-1 neurons before and after the application of blue light and found that D-APV markedly diminished the membrane potential depolarization induced by astrocyte activation,

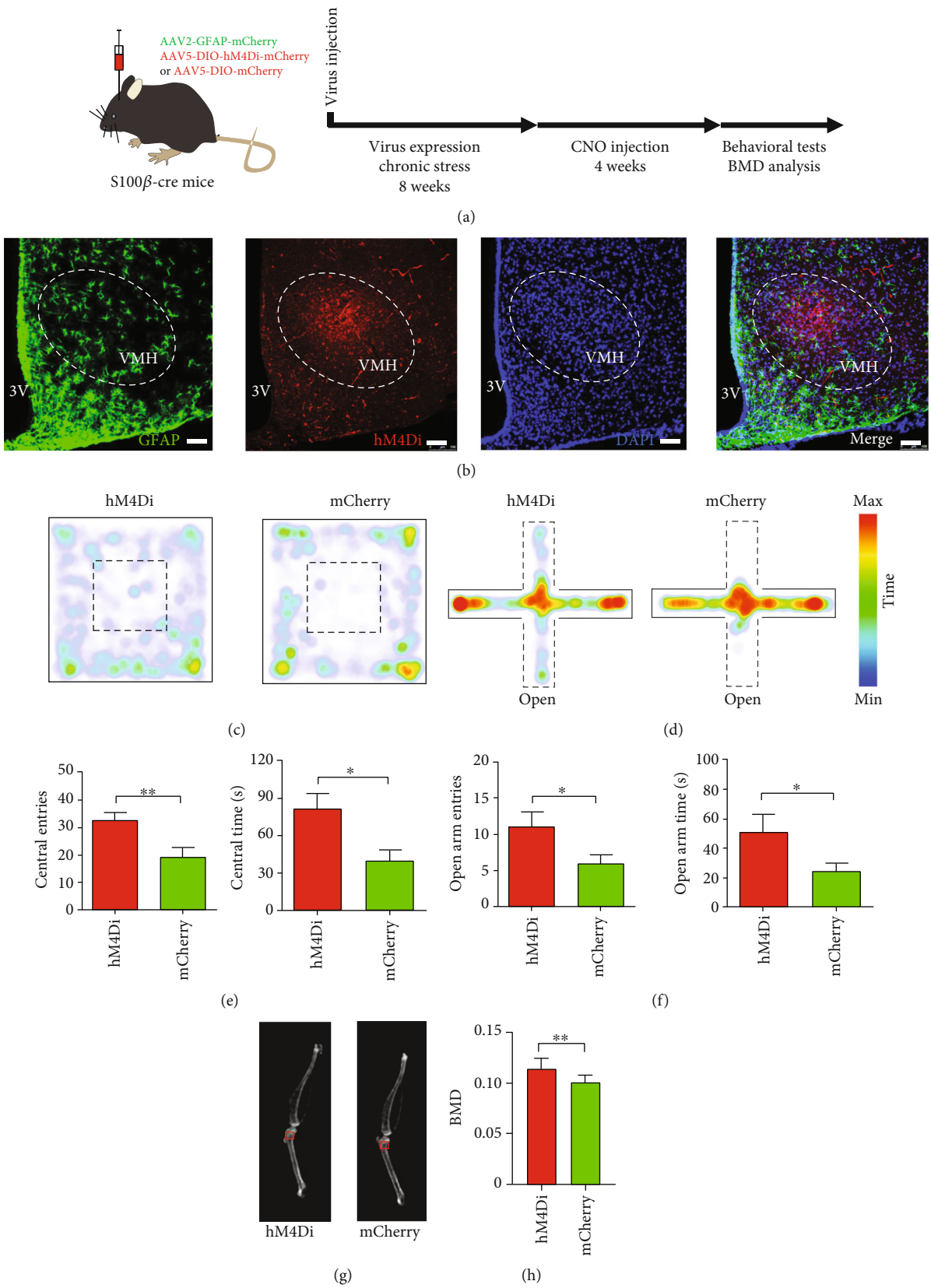

Figure 3: Continued.

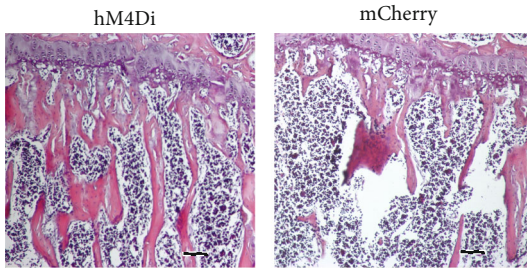

(i)

Figure 3: Activation of Gi pathway in VMH astrocytes decreases anxiety-like behavior and prevents bone loss. (a) Schematic of experimental procedure for mice with chronic stress and chemogenetic inhibition. (b) Representative image showing GFAP and hM4Di virus expression in VMH of S100B-Cre mouse (green, GFAP; red, hM4Di-mCherry; blue, DAPI; scale bars, 60 μm). (c) Representative heat maps of hM4Di and mCherry mice in different positions in OFT. (d) Representative heat maps of hM4Di and mCherry mice in different positions in EPM. (e) Quantification of entries into and time spent in central area in hM4Di and mCherry groups; values represent mean ± SD ($n = 10$ for hM4Di and $n = 8$ for mCherry group; $^{*}p < 0.05$; $^{**}p < 0.01$; unpaired t-test). (f) Quantification of entries into and time spent in open arm in hM4Di and mCherry groups; values represent mean ± SD ($n = 10$ for hM4Di and $n = 8$ for mCherry group; $^{*}p < 0.05$; unpaired t-test). (g) Representative dual-energy X-ray image showing BMD in hM4Di and mCherry groups. BMD in red box was collected for statistical analysis. (h) Quantification of BMD in hM4Di and mCherry groups; values represent mean ± SD ($n = 14$ from 7 hM4Di mice and $n = 10$ from 5 mCherry mice; $^{**}p < 0.01$; unpaired t-test). (i) Representative images of H&E staining showing chemogenetic inhibition of VMH astrocytes rescued the decrease in proximal tibia trabeculae caused by chronic stress (scale bar, 100 μm).

while NBQX exerted no obvious effect (Figures 5(e) and 5(f)). Taken together, we concluded that astrocytes regulate SF-1 neuronal activity, which, in turn, regulates anxiety-like behavior and bone loss via NMDA receptors.

3. Discussion

Stress-induced emotional disorders, such as anxiety and depression, are closely related to bone loss [8, 11–13]. Denes and colleagues identified fluorescent signals in several brain regions following injection of pseudorabies virus (PRV) into the bone marrow cavity of rats, thereby proving a physical neural connection between bone and brain [33]. These findings suggest that the central nervous system may be involved in the regulation of bone metabolism. The hypothalamus is a crucial brain area for regulating visceral and endocrine activities, which not only regulates body temperature [34], food intake [35], energy metabolism [36], and other basic functions closely related to biological survival but also participates in animal emotion and biological rhythm regulation [37, 38]. The VMH plays a crucial role in energy metabolism [39], bone metabolism [22, 24], and emotional regulation [15, 16]. We previously identified a BNST-VMH-NTS neural circuit mediating chronic stress-induced anxiety and bone loss [26] and revealed the regulatory mechanism of anxiety-induced bone loss at the central circuit level. However, the mechanism related to chronic stress-induced anxiety and bone loss regulation by the VMH nucleus as an intermediate linker of the neural circuit remains unclarified.

Using DREADD (designer receptors exclusively activated by designer drugs) manipulation, we found that selective activation of the Gi pathway in the VMH astrocytes prevented chronic stress-induced anxiety-like behavior and bone loss, whereas activation of the Gq pathway in VMH astrocytes induced anxiety-like behavior and bone loss in normal wild-type mice. Combining optogenetics and electrophysiological recordings, we found that selective activation of VMH astrocytes induced an excitatory response in SF-1 neurons, which was mediated through the NMDA receptor. Although our results cannot confirm the mechanism by which astrocytes regulate the NMDA receptor of SF-1 neurons, astrocytes may potentially induce an excitatory response in SF-1 neurons by enhancing the uptake of GABA or secreting more glial-derived glutamate. Based on the ability of astrocytes to regulate glutamate concentration in the extracellular space and elevate extrasynaptic NMDA receptor expression and/or activation in disease states [40, 41], we hypothesized that photoactivation of astrocytes may excite SF-1 neurons via extrasynaptic NMDA receptors. Furthermore, our results also showed enhanced GFAP signals in the VMH after chronic stress. Altered expression of GFAP is reported to affect extrasynaptic gliotransmission due to the interaction between scaffold protein GFAP and transporters on the membrane, thus affecting neuronal activity [42].

3.1. Regulation of Astrocyte Activity by Chemogenetics and Optogenetics. Astrocytes, a major glial cell type in the brain, respond to neuronal activities by increasing intracellular calcium events, which, in turn, trigger gliotransmitter secretion and neural activities [43–45]. Astrocytes also modulate the excitability of neurons through K^{+} clearance via the potassium channel Kir4.1, which changes the concentration of potassium ions in the extracellular environment [46]. Kir4.1, which is upregulated in LHb astrocytes in depressed rats, tightly regulates the degree of membrane hyperpolarization and amount of bursting activity in LHb neurons, and astrocyte-specific gain and loss of Kir4.1 in the LHb bidirectionally regulates neuronal bursting and depressive-like symptoms [27]. By secreting diverse gliotransmitters, astrocytes are also involved in regulation of behavior in mice [28, 47]. Astrocytes are capable of expressing virtually all types of neurotransmitter receptors. These receptors can be activated by synaptically released

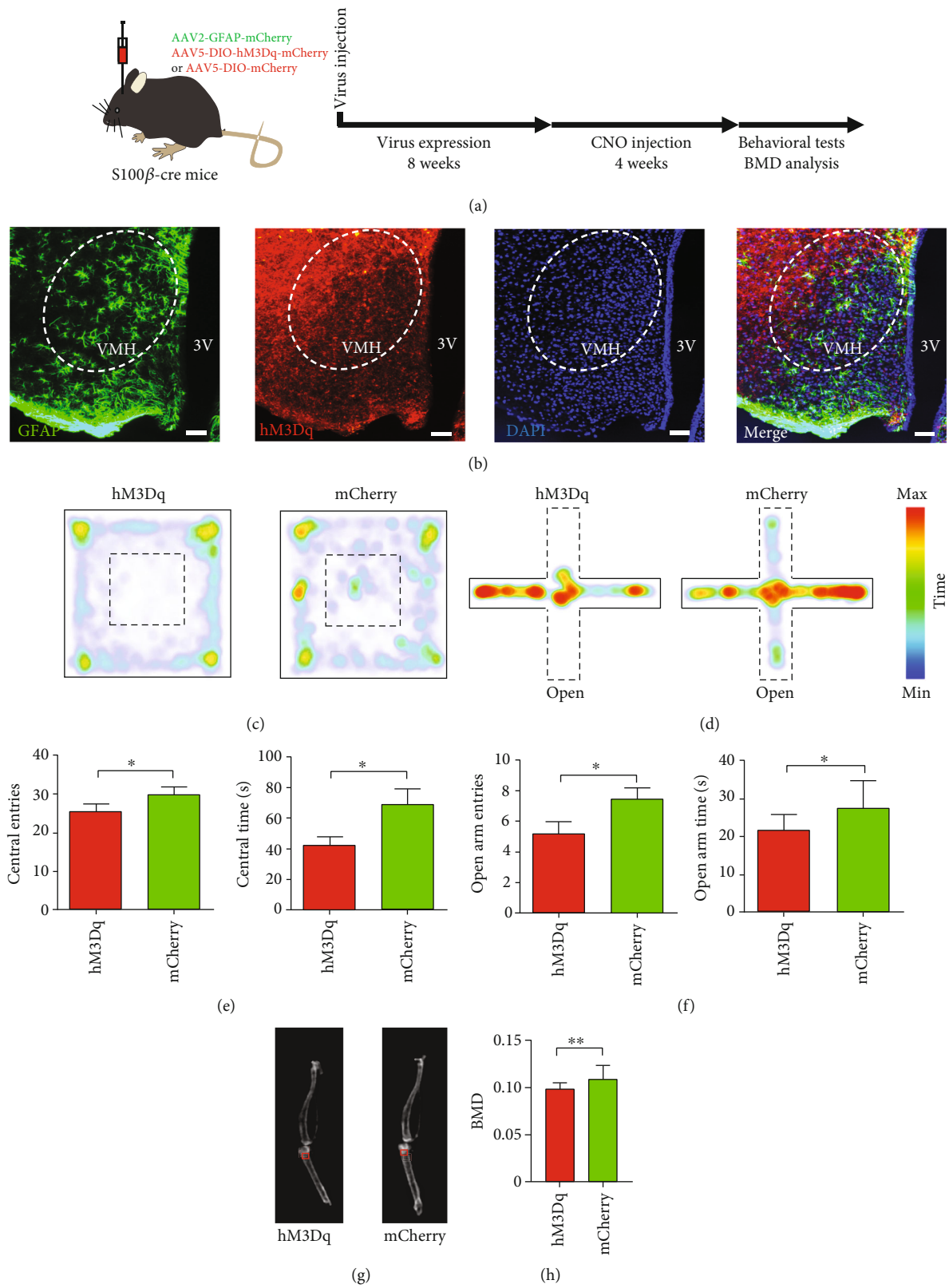

Figure 4: Continued.

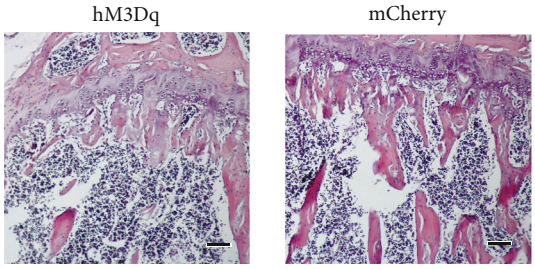

(i)

Figure 4: Activation of Gq pathway in VMH astrocytes increases anxiety-like behavior and promotes bone loss. (a) Schematic of experimental procedure for mice with chemogenetic activation. (b) Representative image showing GFAP and hM3Dq virus expression in VMH of S100B-Cre mouse (green, GFAP; red, hM3Dq-mCherry; blue, DAPI; scale bars, 60 μm). (c) Representative heat maps of hM3Dq and mCherry mice in different positions in OFT. (d) Representative heat maps of hM3Dq and mCherry mice in different positions in EPM. (e) Quantification of entries into and time spent in central area in hM3Dq and mCherry groups; values represent mean ± SD ($n = 10$ for hM3Dq and $n = 10$ for mCherry group; $^{*}p < 0.05$; $^{**}p < 0.01$; unpaired t-test). (f) Quantification of entries into and time spent in open arm in hM3Dq and mCherry groups; values represent mean ± SD ($n = 10$ for hM4Di and $n = 10$ for mCherry group; $^{*}p < 0.05$; unpaired t-test). (g) Representative dual-energy X-ray image showing BMD of hM3Dq and mCherry groups. BMD in red box was collected for statistical analysis. (h) Quantification of BMD in hM3Dq and mCherry groups; values represent mean ± SD ($n = 14$ from 7 hM3Dq mice and $n = 16$ from 8 mCherry mice; $^{**}p < 0.01$; unpaired t-test). (i) Representative image of H&E staining showing that chemogenetic activation of VMH astrocytes mimicked the decrease in proximal tibia trabeculae caused by chronic stress (scale bar, 100 μm).

neurotransmitters, which makes astrocytes indispensable for many physical functions [48–50].

Optogenetics have been widely used to control neuronal activities [51], as well as to regulate the activities and functions of cells other than neurons, including islet cells [52–54], cardiomyocytes [55, 56], and astrocytes [57, 58]. Due to the regulation effects of astrocytes on neuronal activity, considerable effort has been made to study the optogenetic regulation of astrocytes, including on neuronal activity, neural circuit function, and animal behavior [27, 59, 60]. Pharmacogenetics (e.g., DREADD), also known as chemogenetics, can be applied to express artificially constructed receptor channels on specific cells and manipulate receptor channels through artificial application of specific ligand CNO to affect cellular activity [57]. Pharmacogenetics can also change the concentration of intracellular calcium ions and the activity of intracellular kinase, thus influencing cell activity regulation [61]. The most widely used DREADD elements include mutated human muscarinic receptors hM3Dq and hM4Di. hM3Dq can activate the intracellular Gq signaling pathway for excitatory stimulation of neurons, while hM4Di can activate the intracellular Gi pathway for inhibitory stimulation of neurons. Both are widely used in mice and nonhuman primates [62, 63].

Compared with highly spatiotemporal-specific optogenetic regulation technology, chemogenetics usually takes about 30 min to work, so time specificity is weaker than that of optogenetics. However, because long-term chronic stimulation is not a real-time response, and intraperitoneal injection of CNO is noninvasive, it is often used in chronic behavioral research: Adamsky and colleagues applied DREADD technology to selectively activate the Gq pathway in astrocytes from the hippocampal CA1 subregion, which enhanced the formation of short-term memory in mice [64]. However, they also found that chemogenetic activation of the Gi pathway in astrocytes from the hippocampal CA1 region prevents long-term memory in mice [65]. These studies indicate that chemogenetic manipulation of astrocytes is a feasible approach for studying their physiological functions.

By delivering the AAV-DIO virus into the VMH of S100β-Cre mice, we specifically expressed hM3Dq or hM4Di in the astrocytes of the VMH nucleus. After intraperitoneal injection of CNO, we found that chemogenetic regulation of VMH astrocytes bidirectionally regulated anxiety and bone loss in mice. Specifically, activation of the Gi pathway prevented stress-induced anxiety in mice, while activation of the Gq pathway induced anxiety-like behavior in normal mice. After 4 weeks of intraperitoneal administration of CNO, chemogenetic regulation also had distinctive effects on BMD: notably, activation of the Gi and Gq pathways promoted and reduced BMD, respectively. Both hM3Dq and hM4Di can also induce intracellular calcium events in astrocytes [65]. These results suggest that astrocytes are functionally heterogenous in different brain regions [60, 66], and chemogenetic manipulation of astrocytes in different brain areas can cause complicated effects on cell activity.

3.2. VMH Astrocytes Regulate Excitability of SF-1 Neurons through Glutamate Receptors. In recent years, interactions between astrocytes and neurons have become a research hotspot [67]. Abnormal astrocytes can lead to neuronal dysfunction and the subsequent occurrence of various diseases. For example, astrocyte abnormalities can induce a variety of central nervous system diseases, including stroke, Alzheimer's disease, Parkinson's disease, Huntington's disease, and schizophrenia [68]. Furthermore, astrocytes not only provide energy support to neurons but also participate in the formation processing and pruning of synapses of neurons [69]. Moreover, astrocytes secrete a variety of gliotransmitters to regulate neuronal function and participate in extracellular neurotransmitter feedback in neurons to ensure the efficiency of information transmission. Astrocytes are known to secrete thrombospondin, which drives the formation of

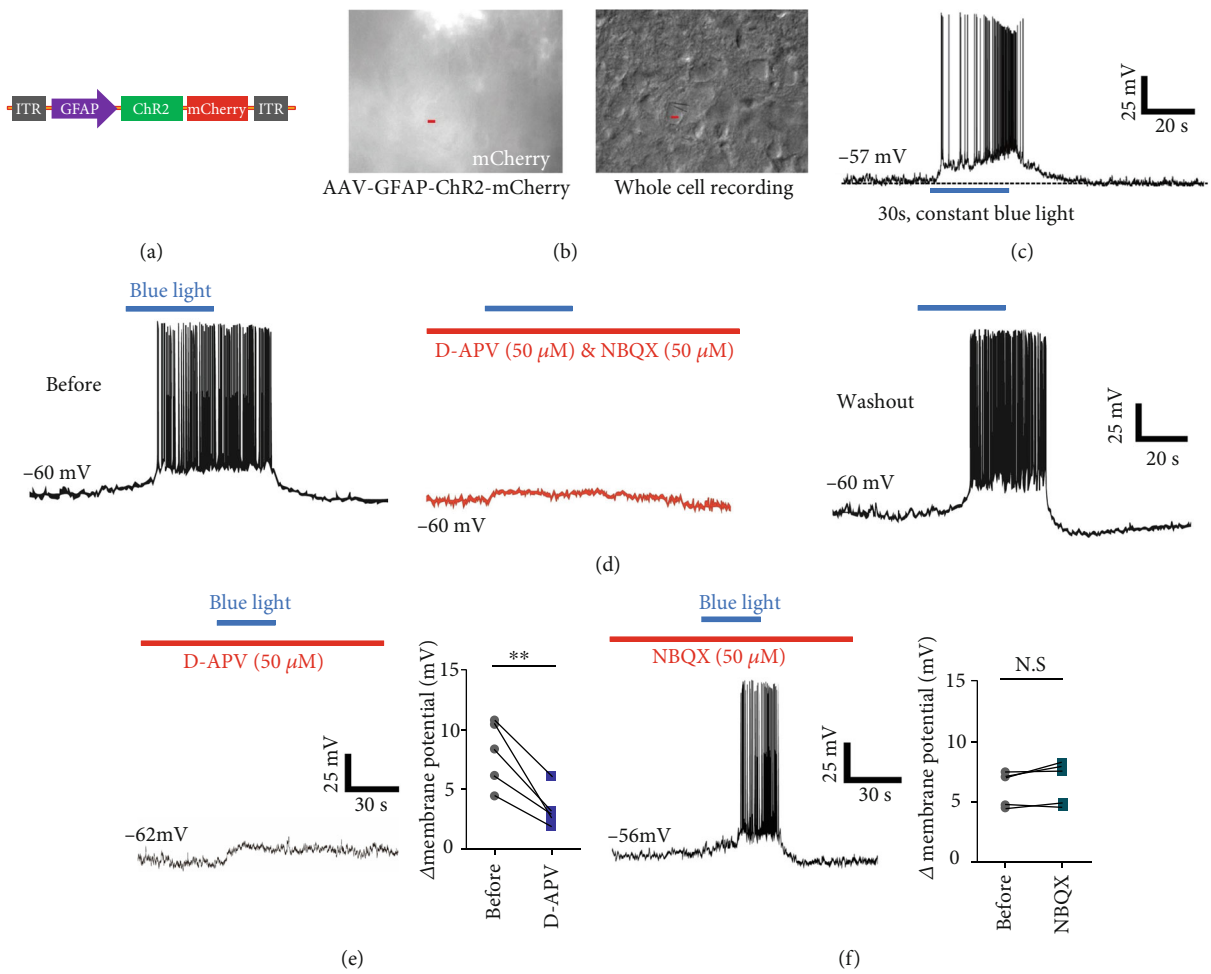

Figure 5: Continued.

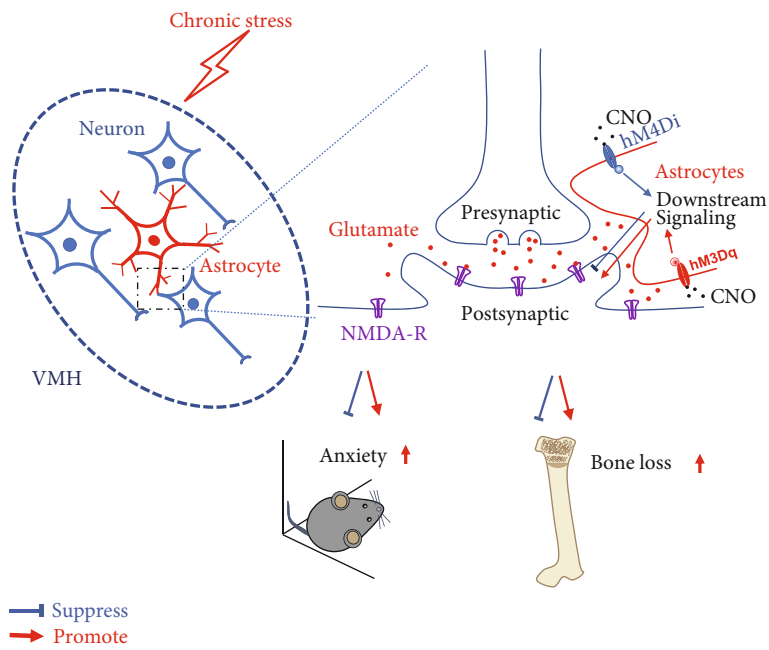

(g)

Figure 5: Optogenetically activated astrocytes induced excitatory response in SF-1 neurons, mainly via NMDA receptor. (a) Schematic representing viral construct of ChR2 specifically expressed in astrocytes. (b) Whole-cell recording of VMH neurons near ChR2-expressing astrocytes. (c) Representative recordings illustrating VMH SF-1 neurons depolarized by optical stimulation of astrocytes. (d) Application of glutamatergic receptor antagonists NBQX (50 μM) and D-APV (50 μM) suppressed action potential firing caused by optical stimulation of astrocytes, which was recovered after aCSF washout ($n = 6$). (e) Application of D-APV significantly diminished membrane potential depolarization induced by astrocyte activation ($n = 5$, $^{**}p < 0.01$; paired t-test). (f) NBQX did not influence interaction between astrocytes and SF-1 neurons ($n = 5$, $^{*}p < 0.05$; paired t-test). (g) Schematic showing that manipulation of astrocytes in VMH could bidirectionally regulate chronic stress-induced anxiety and bone loss by affecting neural excitatory through NMDA receptors.

intact glutamatergic synapses by calcium channel regulation, thereby promoting the formation of structural synapses [70].

In this study, we found that selective regulation of astrocytes in the VMH bidirectionally regulated animal anxiety and bone loss. The most likely mechanism is that astrocyte activity changed the excitability of neurons, then regulated the relevant neural circuits, and finally exerted effects on animal anxiety and bone metabolism. To verify this hypothesis, we conducted electrophysiological recordings and found that optogenetically activated astrocytes induced SF-1 neuronal excitability by regulating NMDA receptors but not AMPA receptors, consistent with previous study on neurons cocultured with astrocytes [71]. NMDA receptors are obligatory heteromeric assemblies of two glycine-binding NR1 subunits and two other subunits (NR2A-D: glutamate-binding; NR3A-B: glycine-binding) [72]. Here, application of D-APV blocked the glutamate-binding site and significantly suppressed neuronal firing caused by astrocyte optogenetic activation, suggesting that glutamate-binding subunits are involved in this depolarization. Moreover, blockage of AMPA receptors did not suppress neuronal depolarization at the resting state induced by light illumination of astrocytes, indicating that Mg2 + -resistant NR2 subunits (like NR2C/D) are likely involved in this process as Mg2 + -sensitive subunits are blocked by Mg2+ at resting potentials [73]. However, our existing evidence could not determine the upstream mechanism underlying astrocyte regulation of anxiety-induced bone loss. For example, what kind of stimulation do these astrocytes receive in the state of anxiety, and what leads to the increase in their own activity and effects on SF-1 neuronal activity? These questions will be the focus of our future work.

3.3. Potential Mechanism of VMH Astrocytes in Regulating Anxiety-Induced Bone Loss. Our data support that VMH astrocytes regulate SF-1 neuronal activity through the NMDA receptor, which regulates anxiety and bone loss induced by chronic stress. However, the underlying mechanism by which chronic stress changes the function of astrocytes remains unclear. We previously showed that the concentration of VMH GABA is significantly higher in stressed mice than in control mice [26]. Whether astrocytes release glutamate under physiological conditions is controversial; however, recent studies have shown that GABA-induced upregulation of astrocyte calcium promotes the release of glutamate and ATP, and short-term high-concentration GABA stimulation induces astrocytes to release glutamate, which causes an excitatory response in neurons [44]. On the other hand, when astrocytes are stimulated with high concentrations of GABA long-term, glutamate and ATP are released to regulate the balance between excitability and inhibition of adnexal neurons [44, 74–77]. Therefore, high concentrations of GABA in the VMH brain area of chronically stressed mice could

induce astrocytes to release glutamate and ATP to coordinate the function of SF-1 neurons and neural circuits by acting on different receptors, thereby regulating animal behavior and bone metabolism [28, 43, 78].

We also found that somatostatin- (SOM-) positive neurons in the BNST nucleus emit nerve projections to the astrocyte body of the VMH (data not shown). SOM neurons are reported to regulate intracellular calcium release of astrocytes by secreting GABA and SOM, thus regulating astrocyte activity [79]. These results suggest that BNST-VMH is not only composed of SOM and SF-1 neurons but also astrocytes from the VMH.

In conclusion, this study demonstrated that astrocytes in the VMH play an important role in regulating chronic stress-induced anxiety and bone loss. Optogenetic activation of VMH astrocytes induced an excitatory response in SF-1 neurons, which was mediated by NMDA receptors (Figure 5(g)). This study is the first to prove that VMH astrocytes not only participate in the regulation of emotional disorders but also regulate the process of bone metabolism. This expands our understanding of the function of astrocytes and provides a potential clinical intervention target for chronic stress-induced bone loss.

4. Materials and Methods

4.1. Animals. The animal experiments in this study were reviewed and approved by the Animal Ethics Committee of the Shenzhen Institute of Advanced Technology, Chinese Academy of Sciences. All animals used in this study were male. All bone analyses were performed on six-month-old mice, whereas electrophysiological recordings were performed on two-month-old mice. The S100β-Cre mice were purchased from KANGWEIDA Gene Technology Co., Ltd, Wuhan, China. Adult (6 weeks old) male C57BL/6 mice were purchased from the Guangdong Medical Laboratory Animal Center, Guangzhou, China. Animals were housed at 22–25°C on a 12 h : 12 h light-dark circadian cycle (lights on from 07 : 00 am to 19 : 00 pm) with food and water provided *ad libitum*. The animals were randomly allocated to experimental and control groups, and experimenters were blind to the experimental group during behavioral experiments. Experimental data were collected during the daytime period.

4.2. Unpredictable Chronic Mild Stress Procedure (UCMS). The UCMS protocol was performed as described previously, with minor modifications [26]. The C57BL/6 or S100β-Cre mice were exposed to environmental stressors for 8 weeks, including the following: (i) tight squeeze: four mice were housed in a relatively small box ($3 \times 5 \times 7$ cm) for 2 h; (ii) wet environment: water was added to home cages to dampen bedding without generating large pools for 6 h; and (iii) high position stress: mice were placed on a platform raised 100 cm above floor height for 2 h. The stressors were randomized and counterbalanced so that each mouse received the same number of each stressor across consecutive days over 8 weeks. Efficacy of the induced anxiety procedures was confirmed by animal behavior studies.

4.3. Virus Injection and Manipulation. The viral vectors used in this study included AAV5-EF1a-DIO-hM4Di-mCherry, AAV5-EF1a-DIO-hM3Dq-mCherry, AAV5-EF1a-DIO-mCherry, AAV2-GFAP-ChR2-mCherry, and AAV2-GFAP-mCherry. Mice were fixed in a stereotaxic apparatus (RWD, China) once general anesthesia was achieved by pentobarbital sodium (intraperitoneal injection, 100 mg/kg). During surgery, the mice were anesthetized with isoflurane (1%) and kept warm with an electric blanket. A small hole in the skull above the targeted area was made with a dental drill, and injections were performed using a microsyringe pump (UMP3/Micro4, USA) with a 10 μl syringe connected to a 33G needle (Neuros; Hamilton, Reno, USA) at a slow flow rate of 50 nl/min. To specifically infect astrocytes in the VMH with hM4Di-mCherry, hM3Dq-mCherry, or mCherry (control group) for DREADD manipulation, AAV5-EF1a-DIO-hM4Di-mCherry, AAV5-EF1a-DIO-hM3Dq-mCherry, or AAV5-EF1a-DIO-mCherry was injected into the VMH of S100β-Cre mice (virus titers: 1×10^{13} gc/ml, 0.3 μl/injection; AP = −1.58 mm; ML = ±0.3 mm; DV = −5.35 mm); the coordinates of injection site were determined with the guide of brain atlas [80]. To specifically infect astrocytes in the VMH with ChR2-mCherry or mCherry for electrophysiological recordings, AAV2-GFAP-ChR2-mCherry or AAV2-GFAP-mCherry was injected into the VMH of C57BL/6 mice (virus titers: 1×10^{13} gc/ml, 0.3 μl/injection; AP = −1.58 mm; ML = ±0.3 mm; DV = −5.35 mm). The volume and injection site of AAV virus were designed to ensure expression mainly constrained in VMH; data acquired from mice without expression of AAV in VMH had been excluded. After injection, mice infected with AAV vector were housed in specific-pathogen-free area to prevent possible infection.

When the injection was complete, the needle was left in place for 10 min and then extracted slowly to avoid virus leakage in the track. The wound was sutured, and antibiotics (bacitracin and neomycin) were applied to the surgical wound, with ketoprofen (5 mg/kg) injected subcutaneously. The animals recovered from anesthesia under a heat lamp before being returned to their cages. Mice were housed for 8–9 weeks following injection for viral expression concurrent with daily stress. Clozapine N-oxide (CNO) (1 mg/kg, Sigma, USA, C0832) was dissolved in 0.6% dimethyl sulfoxide (DMSO) in saline solution and delivered by intraperitoneal injection. For optogenetics manipulation, blue light (constant, 30 s) was delivered by a Lambda DG-4 (Sutter, USA) system under the control of Digidata 1440A (Molecular Devices, USA).

4.4. Immunostaining and Hematoxylin and Eosin (H&E) Staining. Brains were perfused with and fixed in 4% paraformaldehyde (PFA) at 4°C overnight and cryosectioned at a thickness of 30 μm. Sections were then rehydrated and blocked by goat serum. The sections were incubated with primary antibodies to GFAP (1 : 1000, Abcam, ab7260 or ab10062, UK) and anti-S100β (1 : 500, Abcam, ab868, UK). The sections were then washed and labeled with fluorescence-conjugated corresponding secondary antibodies (Jackson ImmunoResearch, 111-545-003, 315-545-003, 1 : 500, USA). The sections were counterstained with Hoechst

33342 and then mounted for image acquisition. Images were taken under a microscope (LSM880, Zeiss, Germany). The numbers of c-fos-positive cells or c-fos/GFAP colocated in the VMH were counted in four sections (adjacent levels) from each mouse, with each group containing 5 mice. The c-fos expression is considered an indirect marker of recent astrocyte activity, and many studies have shown that c-fos is expressed in astrocytes in response to various extracellular signals [81, 82]. The cell numbers per section were compared among experimental groups during data analyses. The signal intensities and fiber length of GFAP staining were quantified by the ZEN software (Zeiss, Germany). H&E staining was performed as described previously [23].

4.5. Slice Preparation. Mice were deeply anesthetized with isoflurane and decapitated rapidly. Brains were then removed and placed to cold oxygenated cutting solution (95% O_2 and 5% CO_2) with the following composition (in mM): choline chloride 110, KCl 2.5, Na-pyruvate 0.6, $MgCl_2$ 7.0, $CaCl_2$ 0.5, NaH_2PO_4 1.3, $NaHCO_3$ 25, and glucose 20 (pH 7.4). Coronal slices (250–300 mm thick) were cut with a vibratome (Series 1000, Warner Instruments, Berlin, Germany) and incubated at 34°C for 30 min in oxygenated artificial cerebrospinal fluid (aCSF, in mM): NaCl 125, KCl 2.5, Na-pyruvate 0.6, $MgCl_2$ 1.3, $CaCl_2$ 2.0, NaH_2PO_4 1.3, $NaHCO_3$ 25, and glucose 10 (pH 7.4). After incubation, all slices were equilibrated in aCSF at room temperature (24–26°C) for at least 40 min. Single slices were transferred to the recording chamber perfused with oxygenated aCSF at room temperature. Unless stated otherwise, drugs were applied with perfused aCSF.

4.6. Electrophysiology. All VMH neurons were recorded with whole-cell patch clamp recording configuration. Recordings were obtained with multiclamp 700B amplifiers (Molecular Devices, San Jose, USA) under visual guidance using a Nikon FN1 microscope (Tokyo, Japan). Electrophysiological data were acquired and analyzed using the pClamp 10 software (Molecular Devices, San Jose, USA). Whole-cell recording pipettes were pulled (model PC-100, Narishige, Tokyo, Japan) from borosilicate glass (0.69 mm OD, 5–7 MΩ) and filled with solution containing (in mM): K-gluconate 135.0, KCl 4.0, NaCl 2.0, HEPES 10, EGTA 4.0, Mg-ATP 4.0, and Na-GTP 5.0. Osmolality was adjusted to 290–310 mOsm kg^{-1} with sucrose, and pH was adjusted to 7.4 with KOH. The liquid junctional potential was compensated for by using the "Pipette Offset" setting of the multiclamp 700B amplifier when the pipette contacted the bath solution.

After forming a high-resistance seal (GΩ), the cell was held in current-clamp mode for 7–10 min until access resistance stabilized. To elucidate how astrocytes in the VMH affect the electrophysiology of neurons, we applied blue light illumination with the Lambda DG-4 system (Sutter, Novato, USA) to activate ChR2-expressing astrocytes. NBQX (50 μM, MCE, Shanghai, China) and D-APV (50 μM, MCE Shanghai, China) were used in perfused aCSF to block the function of AMPA and NMDA receptors, respectively.

4.7. Animal Behavior Studies. Littermate mice were randomly allocated to experimental and control groups. Experimenters were blind to the experimental group allocation. To reduce experimenter-introduced interference, all mice were handled for 15–30 min per day for 3 d before behavioral tests. In this study, the open-field and elevated plus maze tests were employed for measuring anxiety in mice.

4.8. Open-Field Test. Anxiety level was measured in a white plastic open-field square chamber (50 cm length × 50 cm width × 40 cm height). Briefly, the mice were placed in a random corner of the arena at the start of each test and allowed to explore for 10 min. All animal activity was recorded with an infrared camera placed above the box. The arena was conceptually divided into a central field (25 × 25 cm) and a peripheral field. The number of entries into and time spent in the central area during the 10 min of exploration was measured (ANY-maze software). The chamber was cleaned with 30% alcohol and dried thoroughly after each test session to remove any odor cues left by the former mice.

4.9. Elevated Plus Maze Test. We also used the elevated plus maze apparatus to measure anxiety, which entailed a plastic maze consisting of a central platform (5 × 5 cm) with two white open arms (25 × 5 × 25 cm) and two white closed arms (25 × 5 × 25 cm) extending from the center in a plus shape. The maze was elevated 65 cm above the floor. The mice were individually placed in the center with their heads facing a closed arm and were allowed to explore the maze for 5 min. A high-definition camera was set above the apparatus to record animal activity. The number of entries into and amount of time spent in each arm was recorded (ANY-maze software). The maze was cleaned with 30% alcohol and dried thoroughly after each test session to remove any odor cues left by the former mice.

4.10. Bone Mineral Density (BMD) Measurement. The perfused or separated leg bones were placed in a small animal body composition analyzer (InAlyzer, South Korea), and BMD was determined using a dual-energy X-ray analysis system. The samples were placed in the same horizontal plane and direction for dual-energy X-ray scanning; after scanning, the area of interest (5 × 5 mm) was uniformly circled to calculate the BMD of the samples, and the differences in BMD in each group were statistically analyzed by the GraphPad Prism (GraphPad Software, USA) software.

4.11. Statistics. All statistics were performed using the GraphPad Prism 8.0 software. Unless otherwise specified, when appropriate, paired Student*t* -tests and unpaired Student*t* -tests were used. Bonferroni *post hoc* comparisons were conducted to detect significant effects or interactions. In all statistical indicators, $p < 0.05$ was statistically significant. Unless stated otherwise, values represent mean ± standard deviation (SD).

Data Availability

The datasets used and analyzed in the current study are available from the corresponding author upon reasonable request.

Conflicts of Interest

The authors declare that no conflicts of interest exist.

Authors' Contributions

F.Y supervised the project. Y.H.L, J.S, and F.Y prepared the manuscript with comments from all authors. Y.H.L, J.S, D.S.G, L.Z, and F.Y designed the experiments, performed the experiments, and/or analyzed the data. The order of the co-authors was assigned based on their relative contributions to the study. Yunhui Liu and Jie Shao contributed equally to this work.

Acknowledgments

We thank Bingfeng Liu and Ningning Li for experimental assistance. This project was partly supported by the National Natural Science Foundation of China (31800881 and 82072489), the Key Research Program of Frontier Sciences of Chinese Academy of Sciences (QYZDB-SSW-SMC056), the Science and Technology Program of Guangzhou (202007030001), and the Shenzhen Governmental Basic Research Grant (JCYJ20180507182301299).

References

[1] E. Anthony Todd, N. Dee, A. Bernard, W. Lerchner, N. Heintz, and D. J. Anderson, "Control of stress-induced persistent anxiety by an extra-amygdala septohypothalamic circuit," *Cell*, vol. 156, no. 3, pp. 522–536, 2014.

[2] Y. Yang, Y. Cui, K. Sang et al., "Ketamine blocks bursting in the lateral habenula to rapidly relieve depression," *Nature*, vol. 554, no. 7692, pp. 317–322, 2018.

[3] X. Zhu, H.-D. Tang, W.-Y. Dong et al., "Distinct thalamocortical circuits underlie allodynia induced by tissue injury and by depression-like states," *Nature Neuroscience.*, vol. 24, no. 4, pp. 542–553, 2021.

[4] V. K. Tsenkova, M. A. Albert, A. Georgiades, and C. D. Ryff, "Trait anxiety and glucose metabolism in people without diabetes: vulnerabilities among black women," *Diabetic Medicine*, vol. 29, no. 6, pp. 803–806, 2012.

[5] V. Villamil-Salcedo, B. E. Vargas-Terrez, J. Caraveo-Anduaga et al., "Glucose and cholesterol stabilization in patients with type 2 diabetes mellitus with depressive and anxiety symptoms by problem-solving therapy in primary care centers in Mexico City," *Primary Health Care Research & Development*, vol. 19, no. 1, pp. 33–41, 2018.

[6] J. C. Chuang, H. Cui, B. L. Mason et al., "Chronic social defeat stress disrupts regulation of lipid synthesis[S]," *Journal of Lipid Research*, vol. 51, no. 6, pp. 1344–1353, 2010.

[7] C. P. Muller, M. Reichel, C. Muhle, C. Rhein, E. Gulbins, and J. Kornhuber, "Brain membrane lipids in major depression and anxiety disorders," *Biochimica et Biophysica Acta*, vol. 1851, no. 8, pp. 1052–1065, 2015.

[8] C. A. Calarge, J. A. Mills, K. F. Janz et al., "The effect of depression, generalized anxiety, and selective serotonin reuptake inhibitors on change in bone metabolism in adolescents and emerging adults," *Journal of Bone and Mineral Research*, vol. 32, no. 12, pp. 2367–2374, 2017.

[9] C. Hong-Jhe, K. Chin-Yuan, T. Ming-Shium et al., "The incidence and risk of osteoporosis in patients with anxiety disorder: a population-based retrospective cohort study," *Medicine*, vol. 95, no. 38, p. e4912, 2016.

[10] E. T. Callegari, N. Reavley, S. M. Garland, A. Gorelik, and J. D. Wark, "Vitamin D status, bone mineral density and mental health in young Australian women: the Safe-D Study," *Journal of Public Health Research*, vol. 4, no. 3, p. 594, 2015.

[11] H. B. Erez, A. Weller, N. Vaisman, and S. Kreitler, "The relationship of depression, anxiety and stress with low bone mineral density in post-menopausal women," *Archives of Osteoporosis*, vol. 7, no. 1-2, pp. 247–255, 2012.

[12] R. Coelho, C. Silva, A. Maia, J. Prata, and H. Barros, "Bone mineral density and depression: a community study in women," *Journal of Psychosomatic Research*, vol. 46, no. 1, pp. 29–35, 1999.

[13] C. R. Gale, E. M. Dennison, M. Edwards, A. A. Sayer, and C. Cooper, "Symptoms of anxiety or depression and risk of fracture in older people: the Hertfordshire Cohort Study," *Archives of Osteoporosis*, vol. 7, no. 1-2, pp. 59–65, 2012.

[14] K. L. Holloway, L. J. Williams, S. L. Brennan-Olsen et al., "Anxiety disorders and falls among older adults," *Journal of Affective Disorders*, vol. 205, pp. 20–27, 2016.

[15] R. E. Adamec, "Lasting effects of FG-7142 on anxiety, aggression and limbic physiology in the cat," *Journal of Psychopharmacology*, vol. 7, no. 3, pp. 232–248, 1993.

[16] R. E. Adamec, "Evidence that NMDA-dependent limbic neural plasticity in the right hemisphere mediates pharmacological stressor (FG-7142)-induced lasting increases in anxiety-like behavior. Study 1–role of NMDA receptors in efferent transmission from the cat amygdala," *Journal of Psychopharmacology*, vol. 12, no. 2, pp. 122–128, 1998.

[17] C. C. Cheung, W. C. Krause, R. H. Edwards et al., "Sex-dependent changes in metabolism and behavior, as well as reduced anxiety after eliminating ventromedial hypothalamus excitatory output," *Mol Metab.*, vol. 4, no. 11, pp. 857–866, 2015.

[18] K. W. Kim, L. Zhao, and K. L. Parker, "Central nervous system-specific knockout of steroidogenic factor 1," *Molecular and Cellular Endocrinology*, vol. 300, no. 1-2, pp. 132–136, 2009.

[19] K. W. Kim, Y. H. Jo, L. Zhao, N. R. Stallings, S. C. Chua Jr., and K. L. Parker, "Steroidogenic factor 1 regulates expression of the cannabinoid receptor 1 in the ventromedial hypothalamic nucleus," *Molecular Endocrinology*, vol. 22, no. 8, pp. 1950–1961, 2008.

[20] E. S. da Silva, S. C. Poltronieri, J. O. Nascimento, H. Zangrossi Jr, and M. B. Viana, "Facilitation of 5-$HT_{2A/2C}$-mediated neurotransmission in the ventromedial hypothalamic nucleus decreases anxiety in the elevated T-maze," *Behavioural brain research*, vol. 216, no. 2, pp. 692–698, 2011.

[21] S. Takeda, F. Elefteriou, R. Levasseur et al., "Leptin regulates bone formation via the sympathetic nervous system," *Cell*, vol. 111, no. 3, pp. 305–317, 2002.

[22] P. Ducy, M. Amling, S. Takeda et al., "Leptin inhibits bone formation through a hypothalamic relay: a central control of bone mass," *Cell*, vol. 100, no. 2, pp. 197–207, 2000.

[23] Y. Shi, V. K. Yadav, N. Suda et al., "Dissociation of the neuronal regulation of bone mass and energy metabolism by leptin in vivo," *Proceedings of the National Academy of Sciences of the United States of America*, vol. 105, no. 51, pp. 20529–20533, 2008.

[24] F. Oury, V. K. Yadav, Y. Wang et al., "CREB mediates brain serotonin regulation of bone mass through its expression in ventromedial hypothalamic neurons," *Genes & Development*, vol. 24, no. 20, pp. 2330–2342, 2010.

[25] V. K. Yadav, F. Oury, N. Suda et al., "A serotonin-dependent mechanism explains the leptin regulation of bone mass, appetite, and energy expenditure," *Cell*, vol. 138, no. 5, pp. 976–989, 2009.

[26] F. Yang, Y. Liu, S. Chen et al., "A GABAergic neural circuit in the ventromedial hypothalamus mediates chronic stress–induced bone loss," *The Journal of clinical investigation.*, vol. 130, no. 12, pp. 6539–6554, 2020.

[27] Y. Cui, Y. Yang, Z. Ni et al., "Astroglial Kir4.1 in the lateral habenula drives neuronal bursts in depression," *Nature*, vol. 554, no. 7692, pp. 323–327, 2018.

[28] X. Cao, L. P. Li, Q. Wang et al., "Astrocyte-derived ATP modulates depressive-like behaviors," *Nature Medicine*, vol. 19, no. 6, pp. 773–777, 2013.

[29] N. Chen, H. Sugihara, J. Kim et al., "Direct modulation of GFAP-expressing glia in the arcuate nucleus bi-directionally regulates feeding," *eLife*, vol. 5, 2016.

[30] P. Sweeney, Y. Qi, Z. Xu, and Y. Yang, "Activation of hypothalamic astrocytes suppresses feeding without altering emotional states," *Glia*, vol. 64, no. 12, pp. 2263–2273, 2016.

[31] P. S. Kunwar, M. Zelikowsky, R. Remedios et al., "Ventromedial hypothalamic neurons control a defensive emotion state," *eLife*, vol. 4, article e06633, 2015.

[32] N. Scheefhals and H. D. MacGillavry, "Functional organization of postsynaptic glutamate receptors," *Molecular and Cellular Neurosciences*, vol. 91, pp. 82–94, 2018.

[33] Á. Dénes, Z. Boldogkoi, G. Uhereczky et al., "Central autonomic control of the bone marrow: multisynaptic tract tracing by recombinant pseudorabies virus," *Neuroscience*, vol. 134, no. 3, pp. 947–963, 2005.

[34] S. Rodbard, "Body temperature, blood pressure, and hypothalamus," *Science*, vol. 108, no. 2807, pp. 413–415, 1948.

[35] J. H. Jeong, D. K. Lee, and Y.-H. Jo, "Cholinergic neurons in the dorsomedial hypothalamus regulate food intake," *Molecular Metabolism.*, vol. 6, no. 3, pp. 306–312, 2017.

[36] M. J. Waterson and T. L. Horvath, "Neuronal regulation of energy homeostasis: beyond the hypothalamus and feeding," *Cell Metabolism*, vol. 22, no. 6, pp. 962–970, 2015.

[37] A. Kennedy, P. S. Kunwar, L. Y. Li, S. Stagkourakis, D. A. Wagenaar, and D. J. Anderson, "Stimulus-specific hypothalamic encoding of a persistent defensive state," *Nature*, vol. 586, no. 7831, pp. 730–734, 2020.

[38] C. B. Saper, T. E. Scammell, and J. Lu, "Hypothalamic regulation of sleep and circadian rhythms," *Nature*, vol. 437, no. 7063, pp. 1257–1263, 2005.

[39] M. López, L. Varela, M. J. Vázquez et al., "Hypothalamic AMPK and fatty acid metabolism mediate thyroid regulation of energy balance," *Nature Medicine.*, vol. 16, no. 9, pp. 1001–1008, 2010.

[40] A. Verkhratsky, M. S. Ho, N. Vardjan, R. Zorec, and V. Parpura, "General pathophysiology of astroglia," *Adv. Exp. Med. Biol.*, vol. 1175, pp. 149–179, 2019.

[41] G. E. Hardingham, Y. Fukunaga, and H. Bading, "Extrasynaptic NMDARs oppose synaptic NMDARs by triggering CREB shut-off and cell death pathways," *Nature Neuroscience*, vol. 5, no. 5, pp. 405–414, 2002.

[42] D. Li, X. Liu, T. Liu et al., "Neurochemical regulation of the expression and function of glial fibrillary acidic protein in astrocytes," *Glia*, vol. 68, no. 5, pp. 878–897, 2020.

[43] S. Guerra-Gomes, N. Sousa, L. Pinto, and J. F. Oliveira, "Functional roles of astrocyte calcium elevations: from synapses to behavior," *Frontiers in Cellular Neuroscience*, vol. 11, 2018.

[44] A. Covelo and A. Araque, "Neuronal activity determines distinct gliotransmitter release from a single astrocyte," *eLife*, vol. 7, 2018.

[45] A. Semyanov, "Spatiotemporal pattern of calcium activity in astrocytic network," *Cell Calcium*, vol. 78, pp. 15–25, 2019.

[46] A. Bellot-Saez, O. Kekesi, J. W. Morley, and Y. Buskila, "Astrocytic modulation of neuronal excitability through K^+ spatial buffering," *Neuroscience and Biobehavioral Reviews*, vol. 77, pp. 87–97, 2017.

[47] L. B. Haim and D. H. Rowitch, "Functional diversity of astrocytes in neural circuit regulation," *Nature Reviews. Neuroscience*, vol. 18, no. 1, pp. 31–41, 2017.

[48] B. A. Barres, "Glial ion channels," *Current Opinion in Neurobiology*, vol. 1, no. 3, pp. 354–359, 1991.

[49] A. Verkhratsky, "Neurotransmitter receptors in astrocytes," in *Astrocytes in (Patho)Physiology of the Nervous System*, pp. 49–67, Springer, Boston, MA, 2009.

[50] B. E. Yoon, J. Woo, and C. Justin Lee, "Astrocytes as GABAergic and GABA-ceptive cells," *Neurochemical Research*, vol. 37, no. 11, pp. 2474–2479, 2012.

[51] F. Zhang, L.-P. Wang, M. Brauner et al., "Multimodal fast optical interrogation of neural circuitry," *Nature*, vol. 446, no. 7136, pp. 633–639, 2007.

[52] H. Ye, M. D.-E. Baba, R.-W. Peng, and M. Fussenegger, "A synthetic optogenetic transcription device enhances blood-glucose homeostasis in mice," *Science*, vol. 332, no. 6037, pp. 1565–1568, 2011.

[53] N. R. Johnston, R. K. Mitchell, E. Haythorne et al., "Beta cell hubs dictate pancreatic islet responses to glucose," *Cell Metabolism*, vol. 24, no. 3, pp. 389–401, 2016.

[54] T. M. Reinbothe and I. G. Mollet, "Optogenetic Control of Pancreatic Islets," in *Optogenetics: Methods and Protocols*, A. Kianianmomeni, Ed., pp. 107–123, Springer New York, New York, NY, 2016.

[55] C. M. Ambrosi and E. Entcheva, "Optogenetic Control of Cardiomyocytes via Viral Delivery," in *Methods in Molecular Biology*, M. Radisic and L. D. Black Iii, Eds., pp. 215–228, Springer New York, New York, NY, 2014.

[56] P. Makowka, T. Bruegmann, V. Dusend et al., "Optogenetic stimulation of G_s-signaling in the heart with high spatiotemporal precision," *Nature Communications*, vol. 10, no. 1, p. 1281, 2019.

[57] J. Bang, H. Y. Kim, and H. Lee, "Optogenetic and chemogenetic approaches for studying astrocytes and gliotransmitters," *Experimental Neurobiology.*, vol. 25, no. 5, pp. 205–221, 2016.

[58] M. Figueiredo, S. Lane, F. Tang et al., "Optogenetic experimentation on astrocytes," *Experimental Physiology*, vol. 96, no. 1, pp. 40–50, 2011.

[59] F. L. Y. Yang, Y. Liu, J. Tu et al., "Activated astrocytes enhance the dopaminergic differentiation of stem cells and promote brain repair through bFGF," *Nature Communications*, vol. 5, no. 1, 2014.

[60] B. S. Khakh and M. V. Sofroniew, "Diversity of astrocyte functions and phenotypes in neural circuits," *Nature Neuroscience.*, vol. 18, no. 7, pp. 942–952, 2015.

[61] D. J. Urban and B. L. Roth, "DREADDs (designer receptors exclusively activated by designer drugs): chemogenetic tools with therapeutic utility," *Annual Review of Pharmacology and Toxicology.*, vol. 55, no. 1, pp. 399–417, 2015.

[62] Y. Nagai, N. Miyakawa, H. Takuwa et al., "Deschloroclozapine, a potent and selective chemogenetic actuator enables rapid neuronal and behavioral modulations in mice and monkeys," *Nature Neuroscience.*, vol. 23, no. 9, pp. 1157–1167, 2020.

[63] C. M. Mazzone, D. Pati, M. Michaelides et al., "Acute engagement of G_q-mediated signaling in the bed nucleus of the stria terminalis induces anxiety-like behavior," *Molecular Psychiatry*, vol. 23, no. 1, pp. 143–153, 2018.

[64] A. K. A. Adamsky, A. Kol, T. Kreisel et al., "Astrocytic Activation Generates _De Novo_ Neuronal Potentiation and Memory Enhancement," *Cell*, vol. 174, no. 1, pp. 59–71.e14, 2018.

[65] A. A. A. Kol, A. Adamsky, M. Groysman, T. Kreisel, M. London, and I. Goshen, "Astrocytes contribute to remote memory formation by modulating hippocampal- cortical communication during learning," *Nature Neuroscience*, vol. 23, no. 10, pp. 1229–1239, 2020.

[66] E. Hansson, P. Eriksson, and M. Nilsson, "Amino acid and monoamine transport in primary astroglial cultures from defined brain regions," *Neurochemical Research*, vol. 10, no. 10, pp. 1335–1341, 1985.

[67] N. J. E. C. Allen and C. Eroglu, "Cell biology of astrocyte-synapse interactions," *Neuron*, vol. 96, no. 3, pp. 697–708, 2017.

[68] E. C. A. Blanco-Suárez, A. L. M. Caldwell, and N. J. Allen, "Role of astrocyte-synapse interactions in CNS disorders," *The Journal of Physiology*, vol. 595, no. 6, pp. 1903–1916, 2017.

[69] C. Escartin, O. Guillemaud, and M. A. Carrillo-de Sauvage, "Questions and (some) answers on reactive astrocytes," *Glia*, vol. 67, no. 12, pp. 2221–2247, 2019.

[70] M. M. F. M. Corty and M. R. Freeman, "Cell biology in neuroscience: architects in neural circuit design: glia control neuron numbers and connectivity," *The Journal of Cell Biology*, vol. 203, no. 3, pp. 395–405, 2013.

[71] V. Parpura, T. A. Basarsky, F. Liu, K. Jeftinija, S. Jeftinija, and P. G. Haydon, "Glutamate-mediated astrocyte-neuron signalling," *Nature*, vol. 369, no. 6483, pp. 744–747, 1994.

[72] K. B. Hansen, F. Yi, R. E. Perszyk, F. S. Menniti, and S. F. Traynelis, "NMDA receptors in the central nervous system," in *Methods in Molecular Biology*, pp. 1–80, Humana Press, New York, NY, 2017.

[73] H. Monyer, R. Sprengel, R. Schoepfer et al., "Heteromeric NMDA receptors: molecular and functional distinction of subtypes," *Science*, vol. 256, no. 5060, pp. 1217–1221, 1992.

[74] A. Serrano, N. Haddjeri, J. C. Lacaille, and R. Robitaille, "GABAergic network activation of glial cells underlies hippocampal heterosynaptic depression," *The Journal of Neuroscience*, vol. 26, no. 20, pp. 5370–5382, 2006.

[75] J. Tu, F. Yang, J. Wan et al., "Light-controlled astrocytes promote human mesenchymal stem cells toward neuronal differentiation and improve the neurological deficit in stroke rats," *Glia*, vol. 62, no. 1, pp. 106–121, 2014.

[76] L. Mariotti, G. Losi, M. Sessolo, I. Marcon, and G. Carmignoto, "The inhibitory neurotransmitter GABA evokes long-lasting Ca (2+) oscillations in cortical astrocytes," *Glia*, vol. 64, no. 3, pp. 363–373, 2016.

[77] G. Perea, R. Gómez, S. Mederos et al., "Activity-dependent switch of GABAergic inhibition into glutamatergic excitation in astrocyte-neuron networks," *eLife*, vol. 5, 2016.

[78] M. Martin-Fernandez, S. Jamison, L. M. Robin et al., "Synapse-specific astrocyte gating of amygdala-related behavior," *Nature Neuroscience*, vol. 20, no. 11, pp. 1540–1548, 2017.

[79] L. Mariotti, G. Losi, A. Lia et al., "Interneuron-specific signaling evokes distinctive somatostatin-mediated responses in adult cortical astrocytes," *Nature Communications*, vol. 9, no. 1, p. 82, 2018.

[80] J.-P. Konsman, "The mouse brain in stereotaxic coordinates: second edition (deluxe) by Paxinos G. and Franklin, K.B.J., academic press, New York, 2001, ISBN 0-12-547637-X," *Psychoneuroendocrinology*, vol. 28, no. 6, pp. 827-828, 2003.

[81] Y. Edling, M. Ingelman-Sundberg, and A. Simi, "Glutamate activates c-fos in glial cells via a novel mechanism involving the glutamate receptor subtype mGlu5 and the transcriptional repressor DREAM," *Glia*, vol. 55, no. 3, pp. 328–340, 2007.

[82] G. E. Hermann and R. C. Rogers, "TNF activates astrocytes and catecholaminergic neurons in the solitary nucleus: implications for autonomic control," *Brain research.*, vol. 1273, pp. 72–82, 2009.

Hindawi
Neural Plasticity
Volume 2023, Article ID 9795436, 1 page
https://doi.org/10.1155/2023/9795436

Retraction

Retracted: Sustained Auditory Attentional Load Decreases Audiovisual Integration in Older and Younger Adults

Neural Plasticity

Received 29 August 2023; Accepted 29 August 2023; Published 30 August 2023

This article has been retracted by Hindawi following an investigation undertaken by the publisher [1]. This investigation has uncovered evidence of one or more of the following indicators of systematic manipulation of the publication process:

(1) Discrepancies in scope
(2) Discrepancies in the description of the research reported
(3) Discrepancies between the availability of data and the research described
(4) Inappropriate citations
(5) Incoherent, meaningless and/or irrelevant content included in the article
(6) Peer-review manipulation

The presence of these indicators undermines our confidence in the integrity of the article's content and we cannot, therefore, vouch for its reliability. Please note that this notice is intended solely to alert readers that the content of this article is unreliable. We have not investigated whether authors were aware of or involved in the systematic manipulation of the publication process.

Wiley and Hindawi regrets that the usual quality checks did not identify these issues before publication and have since put additional measures in place to safeguard research integrity.

We wish to credit our own Research Integrity and Research Publishing teams and anonymous and named external researchers and research integrity experts for contributing to this investigation.

The corresponding author, as the representative of all authors, has been given the opportunity to register their agreement or disagreement to this retraction. We have kept a record of any response received.

References

[1] Y. Ren, Y. Hou, J. Huang et al., "Sustained Auditory Attentional Load Decreases Audiovisual Integration in Older and Younger Adults," *Neural Plasticity*, vol. 2021, Article ID 4516133, 10 pages, 2021.

Hindawi
Neural Plasticity
Volume 2021, Article ID 4516133, 10 pages
https://doi.org/10.1155/2021/4516133

Research Article

Sustained Auditory Attentional Load Decreases Audiovisual Integration in Older and Younger Adults

Yanna Ren,[1] **Yawei Hou**,[1] **Jiayu Huang**,[1] **Fanghong Li**,[1] **Tao Wang**,[2] **Yanling Ren**,[2] **and Weiping Yang**[3]

[1]*Department of Psychology, College of Humanities and Management, Guizhou University of Traditional Chinese Medicine, Guiyang 550025, China*
[2]*Department of Light and Chemical Engineering, Guizhou Light Industry Technical College, Guiyang 550025, China*
[3]*Department of Psychology, Faculty of Education, Hubei University, Wuhan 430062, China*

Correspondence should be addressed to Weiping Yang; swywp@163.com

Yanna Ren and Yawei Hou contributed equally to this work.

Received 10 April 2021; Accepted 29 May 2021; Published 17 June 2021

Academic Editor: J. Michael Wyss

The modulation of attentional load on the perception of auditory and visual information has been widely reported; however, whether attentional load alters audiovisual integration (AVI) has seldom been investigated. Here, to explore the effect of sustained auditory attentional load on AVI and the effects of aging, nineteen older and 20 younger adults performed an AV discrimination task with a rapid serial auditory presentation task competing for attentional resources. The results showed that responses to audiovisual stimuli were significantly faster than those to auditory and visual stimuli (AV > V ≥ A, all $p < 0.001$), and the younger adults were significantly faster than the older adults under all attentional load conditions (all $p < 0.001$). The analysis of the race model showed that AVI was decreased and delayed with the addition of auditory sustained attention (no_load > load_1 > load_2 > load_3 > load_4) for both older and younger adults. In addition, AVI was lower and more delayed in older adults than in younger adults in all attentional load conditions. These results suggested that auditory sustained attentional load decreased AVI and that AVI was reduced in older adults.

1. Introduction

Individuals are constantly exposed to information from different sensory sources; however, they can select to attend to some of the available information and suppress useless information to identify outside events. The procedure that integrates information from different sensory sources is called multisensory integration [1, 2]. Studies have found that responses to audiovisual stimuli were faster and more accurate than those to auditory-only or visual-only stimuli, and this process has been called audiovisual integration (AVI) [3–5]. However, cognitive energy resources are limited for each person, and only certain amount of information-seized attention can be processed [6]. According to the "perceptual load theory," if the cognitive demand is higher for one task, less attentional resources will be left to process other tasks [7, 8]. Macdonald and Lavie found that visual perceptual load severely affected auditory perception and even induced "inattentional deafness," showing that the participant failed to notice the tone (~79%) during the visual detection task under high visual perceptual load [9]. Under high cognitive demand (high attentional load), how individuals integrate available auditory and visual information has seldom been investigated.

To study the effect of visual attentional load on AVI, Alsius et al. instructed participants to conduct the classic McGurk test under low (single task) and high (dual task) attentional load conditions, and both behavioral and EEG results showed decreased AVI under high attentional load conditions than under low attentional load conditions [10,

11]. Similar results were obtained using meaningless auditory/visual stimuli that removed the influence of high-order cognitive speech processes [12]. In the studies by Alsius et al. [10, 11] and Ren et al. [12], rapid serial visual presentation (RSVP) was employed as the secondary task to add to the attentional load, which was simultaneously and temporally presented the AV discrimination task and mainly induced transient visual attention [13]. In contrast to transient attention, in which the participant was occasionally cued to the stimulated location, sustained attention requires one to maintain attention on a specific task over time, which differentially affects information perception [14, 15]. To investigate the influence of sustained visual attention on AVI, Wahn and König instructed participants to continuously track visually moving balls when performing the audiovisual redundancy task [16], and their results revealed that AVI was comparable under high visual sustained perceptual-load conditions and low visual sustained perceptual-load conditions, indicating that sustained visual attentional load did not significantly affect AVI.

Wahn and König reported that distinctions between or sharing of auditory attention and visual attention are task dependent [17]; in particular, distinctions have been shown to occur during stimulus attribute discrimination tasks [18, 19] but sharing occurred during stimulus location identification tasks [20–24]. Stimulus attribute discrimination was involved in the studies by Alsius et al. [10, 11], Ren et al. [12], and Wahn and König [16]; that is, auditory attention and visual attention were distinct to some degree. Although visual dominance has been widely reported during AVI [25, 26], the integration of auditory information and visual information will be processed based on incoming auditory information [27–29], and AVI will not occur until the arrival of both auditory and visual information [30]. Therefore, investigations on how auditory attentional load influences AVI are important to fully clarify the interactions between attention and AVI, which is the main aim of the current study.

In addition to attentional load, aging is also an important factor that alters an individual's perception of auditory information and visual information and includes decreased visual sensitivity [31] and increased auditory thresholds [32]. Studies examining age-related AVI showed that the AVI was lower or higher in older adults than in younger adults and was task and stimulus dependent [33, 34]. Ren et al. first studied the influence of visual attentional load on AVI and found lower AVI in older adults than in younger adults under all visual attentional load conditions at the behavioral level [12]. During the integration of auditory information and visual information, older adults showed a higher visual dominance effect [35], and the effects of auditory attentional load on AVI in older adults might be different from the effects of visual attentional load conditions. Therefore, another aim of the current study was to test the effects of aging on AVI under different auditory sustained attentional loads.

2. Methods

2.1. Subjects. Twenty healthy older adults and 20 young adults were recruited to participate in the current study. All of the older adults were recruited from Huaxi University Town of Guiyang City, and all of the younger adults were college students at Guizhou University of Traditional Chinese Medicine. All participants provided written informed consent for the procedure, which had been previously approved by the Second Affiliated Hospital of Guizhou University of Traditional Chinese Medicine. All participants were free of neurological diseases, had normal hearing, had normal or corrected-to-normal vision, were right-handed, and were naive to the purpose of the experiment. Participants were excluded if their Mini-Mental State Examination (MMSE) scores were greater than 2.5 SDs from the mean for their age and education level [36]. Additionally, participants who reported a history of cognitive disorder or had an accuracy lower than 70% were also excluded from the experiment. Finally, 19 healthy older adults (55-67 years; mean age ± SD , 59.8 ± 3.6) and 20 young adults (19-22 years; mean age ± SD, 19.6 ± 1.1) successfully completed the experiment, and their data were used for further analysis.

2.2. Stimuli. Similar to our previous study [12], two tasks were employed in the current study: an AV discrimination task for evaluating the AVI and a rapid serial auditory presentation (RSAP) task for manipulating auditory attentional load (Figure 1). Based on the attentional load condition, the two tasks could be presented simultaneously or independently.

For the AV discrimination task, the auditory nontarget was a 1000 Hz sinusoidal tone, and the auditory target was white noise. The visual nontarget was a black and white checkerboard image (B/W checkerboard, 52 × 52 mm, with a visual angle of 5°), and the visual target was a B/W checkerboard image with two black dots contained within each white checkerboard (Figure 1(a)). The audiovisual target was the simultaneously presented visual target and auditory target, and the audiovisual nontarget was the simultaneously presented visual nontarget and auditory nontarget. There were no other combinations of auditory and visual stimuli. The visual stimuli (V) were presented on a computer monitor in front of participants' eyes at a 60 cm distance in the upper/-lower left or right quadrant of the screen for 200 ms with a 12-degree visual angle (Figure 1(a), gray square). Auditory stimuli (A) were presented through two speakers located on the left and right sides of the monitor at approximately 60 dB SPL for a duration of 200 ms (10 ms of the rise/fall cosine gate).

For the RSAP task (Figure 1(c)), the auditory stimuli consisted of 9 distractor characters taken from 3 digits (7, 8, and 9) and 6 letters (B, C, D, P, T, and V) presented through speakers located on the left and right sides of the monitor (Figure 1(a)).

2.3. Procedure. The stimulus presentations and data collection were controlled using MATLAB R2013b (MathWorks, Inc., Natick, MA, United States). Subjects were performed the experiment in a dimly lit and sound-attenuated room (Laboratory room, Guizhou University of Traditional Chinese Medicine, China). To fully understand alterations in AVI with the addition of attentional load, AVI was assessed

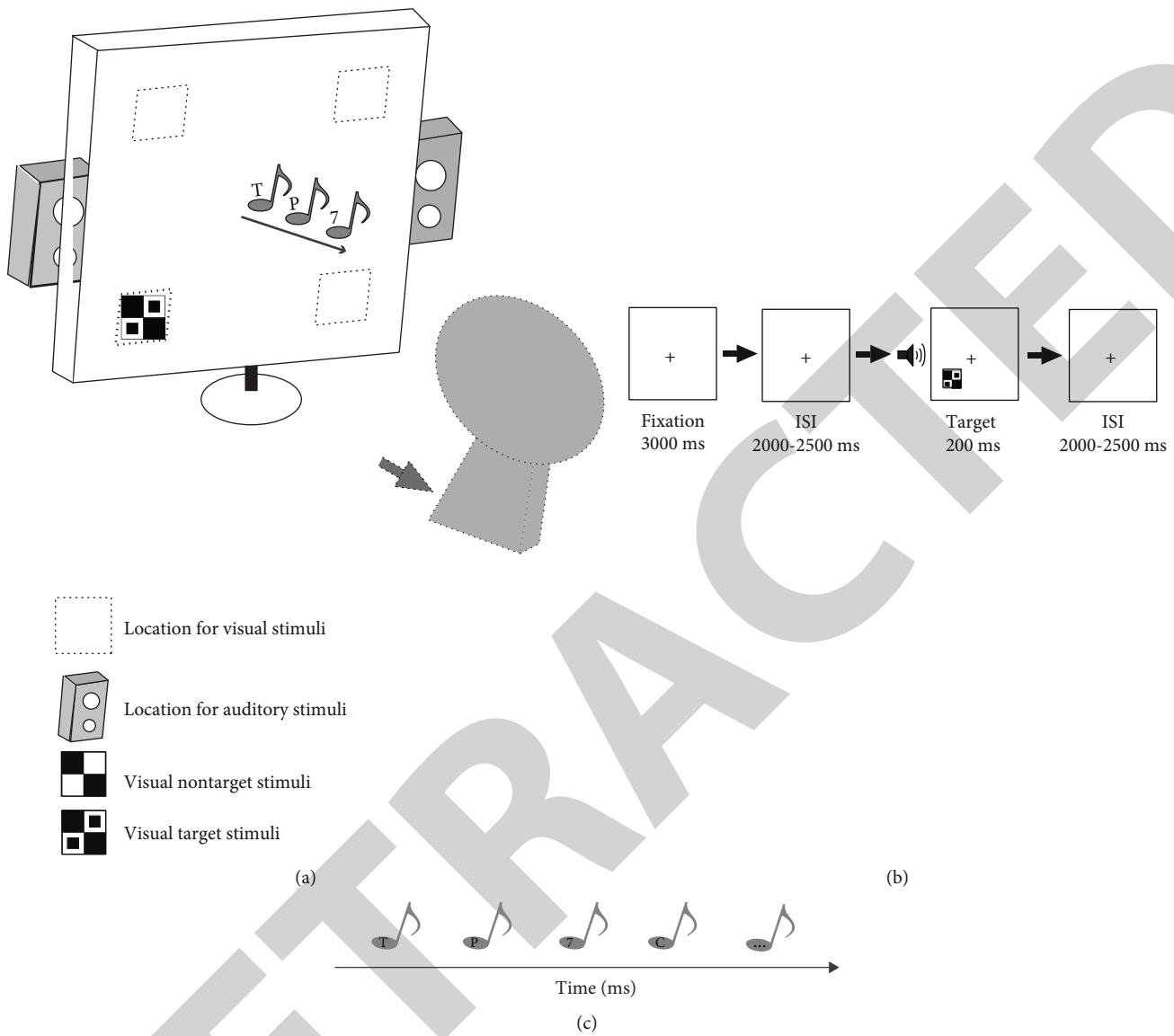

Figure 1: (a) The experimental scenario; a possible sequence for the (b) AV discrimination task and the (c) RSAP task. The AV discrimination task and RSAP task were presented independently.

in five different attentional load conditions. In all attentional load conditions, the AV discrimination task was identical (Figure 1(b)), but the reactive mode to the RSAP task was purposively controlled. In the no-attentional-load condition, only the AV discrimination task was presented; however, random combinations of the AV discrimination task and the RSAP task were simultaneously presented in the other attentional load conditions.

For the AV discrimination task, a fixation cross was presented for 3000 ms, and then, the A, V, and AV stimuli were randomly presented with a random interstimulus interval (ISI) of 2000-2500 ms (Figure 1(b)). The participants were instructed to press the left button of the mouse to respond to the target stimuli as rapidly and as accurately as possible. In total, there were 60 trials for each target stimulus type (A, V, and AV) and 20 trials for each nontarget stimulus type (A, V, and AV) in each session (240 trials), which lasted for 10 min with an appropriate rest break based on the specific situation of each subject.

For RSAP task, 90 characters with 10 times for each character were randomly presented with a 2000-2500 ms interstimulus interval. In the no-attentional-load condition, the RSAP task was not presented, but it was presented simultaneously with the AV discrimination task in all other attentional load conditions. In the attentional load_1 condition, the participants were instructed to respond only to the target in the AV discrimination task but to withhold responses associated with the RSAP task. In the attentional load_2 condition, the participants were instructed to respond to the target in the AV discrimination task by pressing the left button of the mouse and to the target (7, 8, and 9) in the RSAP task by pressing the right button of the mouse. In the attentional load_3 condition, the participants were instructed to respond to the target in the AV discrimination task by pressing the left

button of the mouse and to the target (B, 8) in the RSAP task by pressing the right button of the mouse. In the attentional load_4 condition, the participants were instructed to respond to the target in the AV discrimination task by pressing the left button of the mouse and to the target (B, T, and 8) in the RSAP task by pressing the right button of the mouse. During the experiment, the participants were instructed to treat the AV discrimination task and the RSAP task equally, and the five attentional load sessions were conducted in a random order for each participant. In the attentional load_2, load_3, and load_4 conditions, when the target of AV discrimination task and the target of RSAP task were presented simultaneously, the participants were instructed to press the left and right button of the mouse simultaneously.

2.4. Analysis. The accuracy and response times (RTs; response times falling within the average time duration ± 2.5 SD were included) were computed separately for each subject under each condition, and then, the data were submitted to a 2_{group} (older, younger) × $5_{\text{attentional load}}$ (no, load_1, load_2, load_3, load_4) × 3_{stimulus} (A, V, AV) ANOVA (Greenhouse-Geisser corrections with corrected degrees of freedom). The statistical significance level was set at $p \leq 0.05$, and the effect size estimates, η_p^2, are also reported.

The occurrence of AVI was assessed using a race model by cumulative distribution functions (CDFs) [1, 37]. The phenomenon that responses to an AV stimulus were significantly faster than to A-only or V-only stimuli was defined as a "redundant effect" [1]. Two hypotheses have been proposed to explain this phenomenon: race model and coactivation model. The race model hypothesizes that the A stimulus and the V stimulus are independently processed; the faster one would win the race and trigger the response. The probability of the response to AV [P(AV)] will never exceed the probability of the race model [$P(\text{A}) + P(\text{V}) - P(\text{A}) \times P(\text{V})$]. The coactivation model hypothesizes that the A stimulus and the V stimulus integrate together to achieve the criterion and trigger the response. Therefore, if the probability of the response to AV was significantly faster than that in the race model, it was assumed that the race model was violated and the coactivation model was supported, that is, AVI occurred. P(A), P(V), and P(AV) denote the probability of responding within a given time during auditory trials, visual trials, and audiovisual trials, respectively. To compare the difference in the amount of AVI in various attentional load conditions, a difference probability curve was generated by subtracting a subject's race model CDF from his/her AV CDF in each 10 ms bin [38–41]. The peak of the difference probability curve (peak benefit) and the positive area under the difference probability curve (pAUC) within the time course that AVI occurred were computed separately for each participant in each attentional load condition to assess the amount of AVI. The time point of peak benefit was defined as the peak latency, and the time interval that a significant difference occurred between the AV CDF and the race model CDFs was defined as the time window of AVI, which was used to assess when the AVI occurred.

3. Results

3.1. Accuracy and RTs. The accuracy of one older participant was 54% and was not included in further analysis. For other 19 older and 20 younger adults, the excluded trials were less than 5% in all attentional load conditions, and their accuracy and RTs were calculated separately (Table 1) and then submitted to 2_{group} (older, younger) × $5_{\text{attentional load}}$ (no, load_1, load_2, load_3, load_4) × 3_{stimulus} (A, V, AV) ANOVA. The results of the accuracy analysis showed a significant main effect of group [$F(1, 37) = 75.729$, $p < 0.001$, $\eta_p^2 = 0.671$], revealing higher accuracy by the younger adults than by the older adults, and a significant main effect of attentional load [$F(4, 148) = 99.600$, $p < 0.001$, $\eta_p^2 = 0.729$], revealing the highest accuracy in the no-attentional-load condition (no > load_1 = load_2 > load_3 > load_4), which indicated that the establishment of attentional load was reasonable. In addition, a significant main effect of stimulus [$F(2, 74) = 34.380$, $p < 0.001$, $\eta_p^2 = 0.482$] revealed higher accuracy when responding to AV stimuli than when responding to A or V stimuli (AV > V > A, all $p \leq 0.03$), which indicated response facilitation to AV stimuli.

The 2_{group} (older, younger) × $5_{\text{attentional load}}$ (no, load_1, load_2, load_3, load_4) × 3_{stimulus} (A, V, AV) ANOVA on RTs showed a significant main effect of group [$F(1, 37) = 55.846$, $p < 0.001$, $\eta_p^2 = 0.601$], attentional load [$F(4, 148) = 59.410$, $p < 0.001$, $\eta_p^2 = 0.616$], and stimulus [$F(2, 74) = 95.160$, $p < 0.001$, $\eta_p^2 = 0.720$]. The analysis revealed faster responses by younger adults than by older adults, faster responses in the no-attentional-load condition than in other attentional load conditions (no ≥ load_1 > load_2 ≥ load_3 > load_4), and faster responses to the AV stimuli than the A and V stimuli (AV > V > A, all $p \leq 0.007$). There was a significant interaction between attentional load and group [$F(4, 148) = 5.850$, $p < 0.001$, $\eta_p^2 = 0.137$]. The *post hoc* analysis of pairwise comparison showed that responses by the younger adults were faster than those by the older adults in all attentional load conditions (Bonferroni correction, all $p < 0.05$). Responses were faster in the attentional load_3 condition than in the attentional load_4 condition for older adults (no = load_1 > load_2 = load_3 ≥ load_4) but not for younger adults (no = load_1 > load_2 = load_3 = load_4). Additionally, the interaction between attentional load and stimulus was also significant [$F(8, 296) = 5.438$, $p < 0.001$, $\eta_p^2 = 0.128$]. The *post hoc* analysis of pairwise comparison showed faster responses to the V stimuli than to the A stimuli in the load_2, load_3, and load_4 conditions (Bonferroni correction, AV > V > A, all $p < 0.001$) but not in the no-attentional-load condition and attentional load_1 condition (AV > V = A). The pairwise comparison analysis across stimuli revealed faster responses to the V stimuli in the attentional load_3 condition than in the attentional load_4 condition (no = load_1 > load_2 = load_3 > load_4) but not when responding to the A and AV stimuli (no = load_1 > load_2 = load_3 = load_4).

Table 1: Mean response time (ms) and accuracy (%) for older and younger adults in each condition.

	Older						Younger					
	Response time			Accuracy			Response time			Accuracy		
	A	V	AV	A	V	AV	A	V	AV	A	V	AV
No_load	580 (75)	579 (65)	525 (78)	100 (1)	99 (1)	100 (1)	485 (72)	469 (60)	400 (72)	100 (0)	98 (2)	100 (1)
Load_1	595 (83)	595 (69)	513 (65)	98 (3)	98 (3)	100 (1)	523 (109)	491 (53)	419 (69)	98 (3)	98 (2)	100 (1)
Load_2	707 (80)	688 (67)	630 (58)	96 (4)	97 (4)	99 (2)	577 (105)	534 (62)	468 (77)	98 (3)	98 (3)	100 (1)
Load_3	733 (72)	682 (82)	623 (82)	82 (10)	90 (4)	95 (5)	599 (105)	536 (64)	474 (79)	98 (3)	98 (2)	99 (2)
Load_4	763 (75)	722 (72)	663 (59)	75 (9)	83 (9)	89 (5)	590 (104)	554 (61)	473 (68)	93 (6)	93 (4)	95 (4)

Data are presented as means with standard deviations (SDs). A = auditory; V = visual; AV = audiovisual.

3.2. Race Model. As shown in Figure 2(a) for younger adults and in Figure 2(c) for older adults in the no-attentional-load condition, AVI was assessed using a race model based on the CDFs of A, V, and AV stimuli. As shown in Figure 2(b) for younger adults and in Figure 2(d) for older adults, the probability difference was generated by subtracting race model CDFs from AV CDFs in the no-attentional-load condition.

Significant AVI was found in all attentional load conditions for both older and younger adults, except in the attentional load_4 condition for older adults (Figure 3, Table 2). The peak benefit decreased with the addition of attentional load and was higher in younger adults than in older adults, with peak benefits of 12.36% vs. 8.77%, 10.08% vs. 8.62%, 8.64% vs. 5.57%, and 8.62% vs. 2.29% in the no-attentional-load, attentional load_1, attentional load_2, and attentional load_3 conditions, respectively. The peak benefit was 5.79% for younger adults in the attentional load_4 condition, but no significant AVI was found for older adults. In addition, the pAUC also decreased with the addition of attentional load and was higher in younger adults than in older adults, with values of 200 ms vs. 93 ms, 152 ms vs. 79 ms, 107 ms vs. 72 ms, and 96 ms vs. 23 ms for the no-attentional-load, attentional load_1, attentional load_2, and attentional load_3 conditions, respectively. The peak benefit was 63 ms for younger adults in the attentional load_4 condition, but no significant AVI was found for older adults. These results indicated that AVI decreased with the addition of attentional load and that AVI was lower in older adults than in younger adults under all attentional load conditions.

The peak latency was delayed in the older adults compared with the younger adults in all attentional load conditions, with latencies of 460 ms vs. 370 ms, 470 ms vs. 440 ms, 480 ms vs. 390 ms, and 510 ms vs. 450 ms for the no-attentional-load, attentional load_1, attentional load_2, and attentional load_3 conditions, respectively. The peak latency was 450 ms for the younger adults in the attentional load_4 condition. The time window was also delayed in the older adults compared with the younger adults in all attentional load conditions, with time windows of 350-500 ms vs. 250-450 ms, 400-500 ms vs. 300-510 ms, 450-490 ms vs. 320-450 ms, and 500-550 ms vs. 350-500 ms for the no-attentional-load, attentional load_1, attentional load_2, and attentional load_3 conditions, respectively. The time window was 380-500 ms for the younger adults in the attentional load_4 condition. These results suggested that AVI was delayed with the addition of attentional load and was more delayed for the older adults compared with the younger adults in all attentional load conditions.

4. Discussion

The aim of the present study was to investigate how sustained auditory attention affects AVI and the effect of aging. The results showed that AVI was decreased and delayed with the addition of sustained auditory attentional load. In addition, AVI was lower and more delayed in the older adults than in the younger adults under all sustained auditory attentional loads.

Consistent with some previous studies [10–12], AVI was higher in the low-attentional-load condition than in the high-attentional-load condition. According to perceptual load theory [6–8], attentional resources are limited for each person, and if one task occupies more attentional resources, less will be available to process other tasks. During the experiment, the participants were instructed to treat the AV discrimination task and RSAP task equally. With the addition of attentional load, greater attentional demand was needed to complete the secondary RSAP task; therefore, less attentional resources were available for processing the AV discrimination task. Talsma and colleagues conducted several studies on the interaction between attention and AVI and found that AVI was higher in the attended condition than in the unattended condition [42–45]. Therefore, decreased AVI might be mainly attributed to the reduction in attentional resources available for processing auditory and visual information in the AV discrimination task. Additionally, Ren et al. found higher AVI in the low visual attentional load condition than in the no-attentional-load condition [12], but there was lower AVI in the low auditory attentional load condition than in the no-attentional-load condition in the present study. Numerous studies have revealed that the response to stimuli in one sensory modality was not disrupted by stimuli in another modality but was disrupted by stimuli in the same sensory modality, suggesting that attention acted unimodally [18, 46, 47]. Although shared auditory attention and visual attention have been found [20–24], they were also widely reported to be independent of each other [18, 19]. Auditory information diverts individuals' attention faster and more easily than visual information [48], suggesting that the same distractors might occupy more attentional resources under auditory attentional load conditions than under visual attentional load conditions. In addition, in the

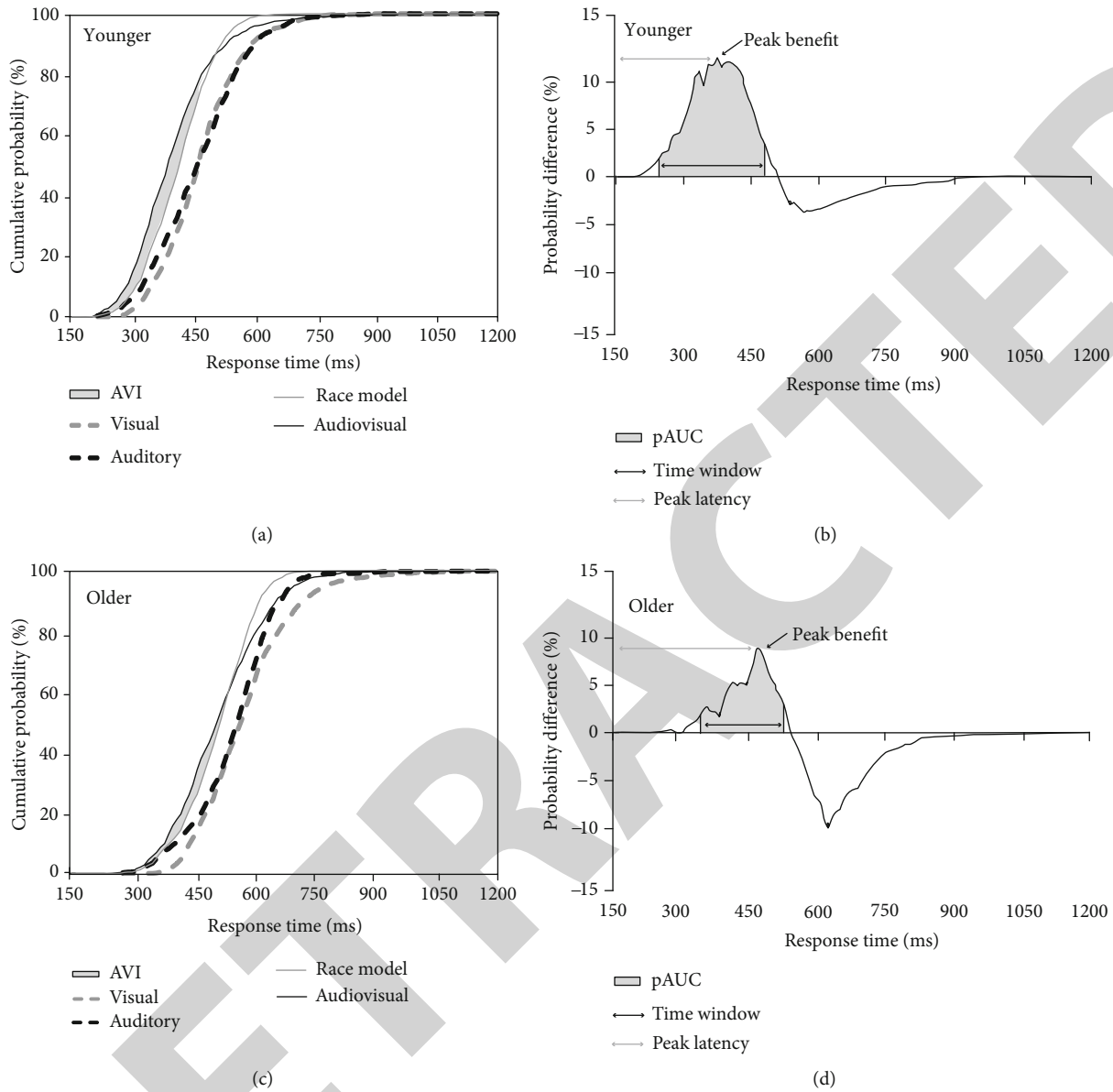

Figure 2: Cumulative distribution functions (CDFs) for the discrimination response times to auditory, visual, and audiovisual stimuli and the race model in (a) younger adults and (c) older adults. Probability difference between audiovisual CDFs and race model CDFs in (b) younger adults and (d) older adults.

current study, the distractor was randomly presented during the participants' performance in the AV discrimination task, which required the participants to maintain their attention on monitoring auditory distractors and mainly induced sustained attention. However, in the study conducted by Ren et al., stimuli in the AV discrimination task and visual distractors were presented simultaneously, and the participant was required to temporarily monitor the visual distractor, which mainly induced transient attention. Therefore, the differences in results compared with Ren et al. [12] might be mainly attributed to the different mechanisms between auditory attention and visual attention and between sustained attention and transient attention. Additionally, the current findings were different from the results by Wahn and König, who found no significant difference between low and high visual sustained attentional load conditions [16], which further indicated different mechanisms between auditory attention and visual attention and between sustained attention and transient attention, but further imaging studies are needed.

With the increase in attentional load, AVI was delayed. Responses were slower in conditions with distractors than in conditions without distractors [49, 50], so responses were slower in the auditory attentional load conditions than in the no-attentional-load condition. In the current study, the participants were instructed to respond to the AV discrimination task only and neglect auditory distractors in the auditory attentional load_1 condition; however, simultaneous responses were required in the auditory attention load_2 (7, 8, and 9), load_3 (B, 8), and load_4 (B, T, and 8) conditions.

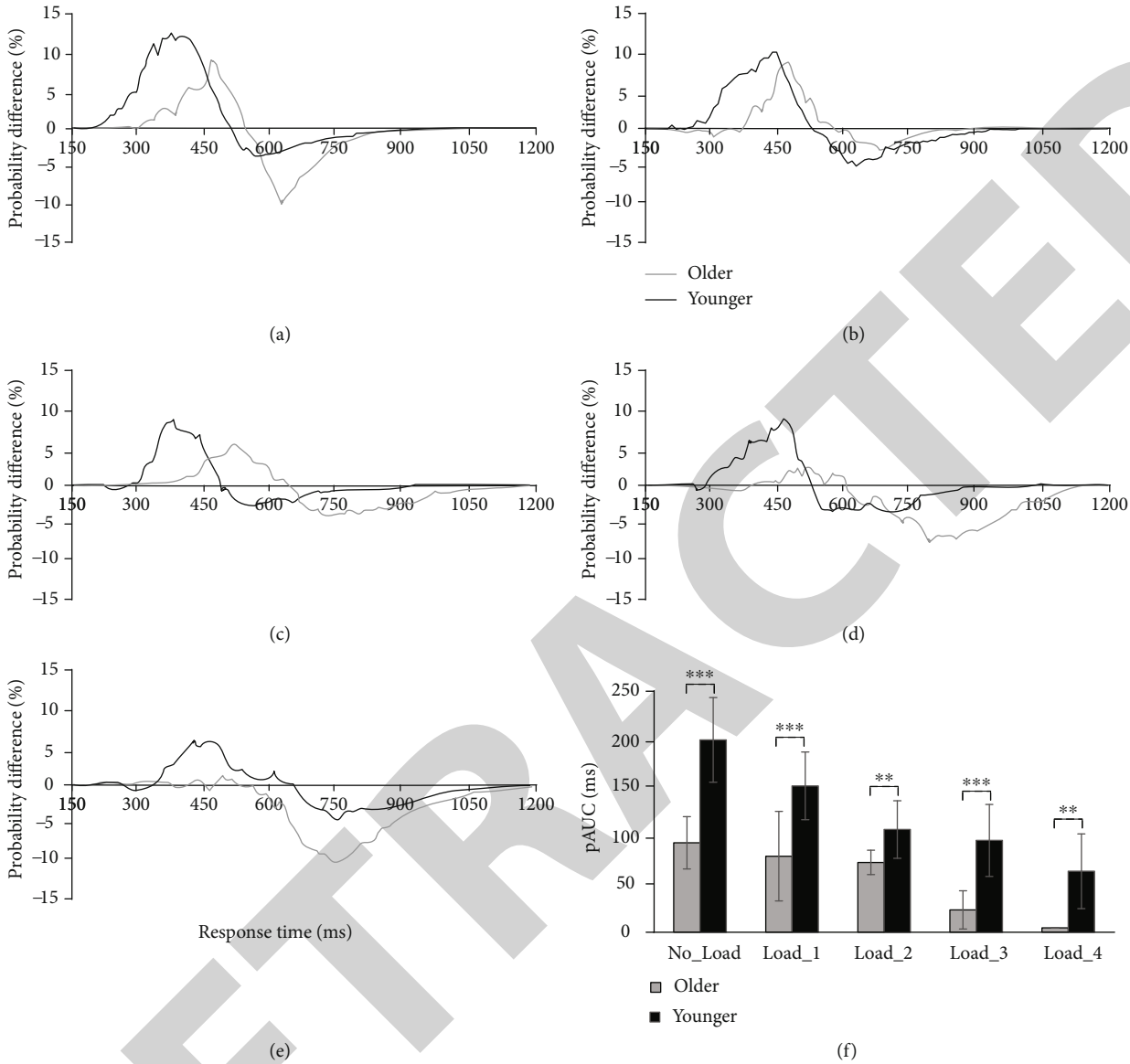

Figure 3: The comparison of probability differences between older and younger adults in the (a) no-attentional-load, (b) attentional load_1, (c) attentional load_2, (d) attentional load_3, and (e) attentional load_4 conditions; the positive area under the curve (pAUC) was decreased with the addition of attentional load, and AVI was lower in older adults than in younger adults (f). $^{**}p < 0.01$ and $^{***}p < 0.001$.

Table 2: The time window (ms), peak latency (ms), peak benefit (%), and area under the curve (pAUC, ms) for older and younger adults under each attentional load condition.

	Time window		Peak latency		Peak benefit		pAUC	
	Older	Younger	Older	Younger	Older	Younger	Older	Younger
No_load	350-500	250-450	460	370	8.77	12.36	93	200
Load_1	400-500	300-510	470	440	8.62	10.08	79	152
Load_2	450-490	320-450	480	390	5.57	8.64	72	107
Load_3	500-550	350-500	510	450	2.29	8.62	23	96
Load_4	—	380-500	—	450	—	5.79	—	63

Object classification was required in auditory attentional load_2 conditions, but object recognition was required in auditory attentional load_3 (B, 8) and load_4 (B, T, and 8) conditions. Object recognition is more difficult than object classification [51, 52], and the recognition of B and T is more prone to errors than that of only B [53]; therefore, responses were more difficult in auditory attentional load_4 conditions than in load_3 conditions and in auditory attentional load_3

conditions than in load_2 conditions, which showed that response speed decreased with increasing attentional load (response speed: no_load > load_1 > load_2 > load_3 > load_4). Colonius et al. proposed a "*time-window-of-integration model*," which presumed that the integration of auditory information and visual information included two stages: early afferent processing (first stage) and converging subprocesses (second stage) [30, 54]. The second stage is triggered only when the auditory information and visual information all terminate within a given time interval. With the addition of attentional load, the first stage was prolonged; therefore, AVI was also delayed.

AVI was lower in the older adults than in the younger adults in attentional load conditions. An enhanced AVI was found in studies by Laurienti et al. [39, 40] and Diederich et al. [54], in which the stimuli used to assess AVI were presented in the central field of vision; however, the stimuli were presented peripherally in the current study (upper/lower left/right 12°). The visual field was shown to be narrower and the peripheral information processing capacity lower in older adults than in younger adults [55–57], which might have further led to lower AVI in the older adults than in the younger adults. Additionally, with aging, there are clear declines in attention [58–60], and AVI was shown to be higher in attended conditions than in unattended conditions [42–45]. Therefore, another possible reason for the reduced AVI in older adults might also be attributed to the decline in attention. AVI was delayed in the older adults relative to the younger adults in all attentional load conditions, and this result was consistent with previous studies [12, 33, 39]. Responses of older adults were shown to be slower than those of younger adults in many cognitive tasks [61, 62], and there was a general functional decline with aging [63, 64]. AVI occurs based on the processing of auditory and visual information, and Colonius and Diederich even proposed that AVI might occur only when auditory information and visual information terminate within a certain time period [30, 54]; therefore, it is reasonable that AVI is delayed in older adults.

Data Availability

The data are available from the corresponding author upon reasonable request.

Conflicts of Interest

The authors declare no conflicts of interest.

Authors' Contributions

Yanna Ren and Yawei Hou contributed equally to this work and should be considered co-first authors. Yanna Ren, Yawei Hou, and Weiping Yang conceived and designed the experiments. Jiayu Huang and Fanghong Li collected the data. Yawei Hou, Tao Wang, and Yanling Ren analyzed the data. Yanna Ren and Yawei Hou wrote the draft manuscript and received comments from Weiping Yang.

Acknowledgments

The study was supported by the National Natural Science Foundation of China (31800932 and 31700973), Science and Technology Planning Project of Guizhou Province (QianKeHeJiChu-ZK [2021] General 120), the Innovation and Entrepreneurship Project for High-level Overseas Talent of Guizhou Province ((2019)04), and the Humanity and Social Science Youth Foundation of the Ministry of Education of China (18XJC190003 and 16YJC190025).

References

[1] J. Miller, "Divided attention: evidence for coactivation with redundant signals," *Cognitive Psychology*, vol. 14, no. 2, pp. 247–279, 1982.

[2] D. H. Raab, "Division of Psychology: statistical facilitation of simple reaction times*," *Transactions of the New York Academy of Sciences*, vol. 24, no. 5 Series II, pp. 574–590, 1962.

[3] M. A. Meredith, J. W. Nemitz, and B. E. Stein, "Determinants of multisensory integration in superior colliculus neurons. I. Temporal factors," *The Journal of Neuroscience*, vol. 7, no. 10, pp. 3215–3229, 1987.

[4] B. E. Stein and M. Meredith, *The Merging of the Sense*, The MIT Press, Cambridge, MA, 1993.

[5] B. E. Stein, *The New Handbook of Multisensory Processing*, The MIT Press, Cambridge, MA, 2012.

[6] D. Kahneman and A. Tversky, "On the psychology of prediction," *Psychological Review*, vol. 80, no. 4, pp. 237–251, 1973.

[7] N. Lavie, "Perceptual load as a necessary condition for selective attention," *Journal of Experimental Psychology*, vol. 21, no. 3, pp. 451–468, 1995.

[8] N. Lavie and Y. Tsal, "Perceptual load as a major determinant of the locus of selection in visual attention," *Perception & Psychophysics*, vol. 56, no. 2, pp. 183–197, 1994.

[9] J. S. P. Macdonald and N. Lavie, "Visual perceptual load induces inattentional deafness," *Attention, Perception, & Psychophysics*, vol. 73, no. 6, pp. 1780–1789, 2011.

[10] A. Alsius, J. Navarra, R. Campbell, and S. Soto-Faraco, "Audiovisual integration of speech falters under high attention demands," *Current Biology*, vol. 15, no. 9, pp. 839–843, 2005.

[11] A. Alsius, R. Möttönen, M. E. Sams, S. Soto-Faraco, and K. Tiippana, "Effect of attentional load on audiovisual speech perception: evidence from ERPs," *Frontiers in Psychology*, vol. 5, p. 727, 2014.

[12] Y. Ren, S. Li, T. Wang, and W. Yang, "Age-related shifts in theta oscillatory activity during audio-visual integration regardless of visual attentional load," *Frontiers in Aging Neuroscience*, vol. 12, article 571950, 2020.

[13] T. Liu, F. Pestilli, and M. Carrasco, "Transient attention enhances perceptual performance and fMRI response in human visual cortex," *Neuron*, vol. 45, no. 3, pp. 469–477, 2005.

[14] M. Eimer, "ERP modulations indicate the selective processing of visual stimuli as a result of transient and sustained spatial attention," *Psychophysiology*, vol. 33, no. 1, pp. 13–21, 1996.

[15] M. Eimer and B. Forster, "Modulations of early somatosensory ERP components by transient and sustained spatial attention," *Experimental Brain Research*, vol. 151, no. 1, pp. 24–31, 2003.

[16] B. Wahn and P. König, "Audition and vision share spatial attentional resources, yet attentional load does not disrupt

audiovisual integration," *Frontiers in Psychology*, vol. 6, p. 1084, 2015.

[17] B. Wahn and P. König, "Is attentional resource allocation across sensory modalities task-dependent?," *Advances in Cognitive Psychology*, vol. 13, no. 1, pp. 83–96, 2017.

[18] D. Alais, C. Morrone, and D. Burr, "Separate attentional resources for vision and audition," *Proceedings of the Royal Society B: Biological Sciences*, vol. 273, no. 1592, pp. 1339–1345, 2006.

[19] R. Arrighi, R. Lunardi, and D. Burr, "Vision and audition do not share attentional resources in sustained tasks," *Frontiers in Psychology*, vol. 2, p. 56, 2011.

[20] C. Spence, "Crossmodal spatial attention," *Annals of the New York Academy of Sciences*, vol. 1191, no. 1, pp. 182–200, 2010.

[21] J. Driver and C. Spence, "Crossmodal attention," *Current Opinion in Neurobiology*, vol. 8, no. 2, pp. 245–253, 1998.

[22] C. Spence and J. Driver, *Crossmodal Space and Crossmodal Attention*, Ooxford University Press, Ooxford, 2004.

[23] J. Driver and C. Spence, "Attention and the crossmodal construction of space," *Trends in Cognitive Sciences*, vol. 2, no. 7, pp. 254–262, 1998.

[24] C. Spence, "Crossmodal attention," *Scholarpedia*, vol. 5, no. 5, p. 6309, 2010.

[25] H. McGurk and J. Macdonald, "Hearing lips and seeing voices," *Nature*, vol. 264, no. 5588, pp. 746–748, 1976.

[26] P. Bertelson and M. Radeau, "Cross-modal bias and perceptual fusion with auditory-visual spatial discordance," *Perception & Psychophysics*, vol. 29, no. 6, pp. 578–584, 1981.

[27] L. Shams, Y. Kamitani, and S. Shimojo, "Visual illusion induced by sound," *Cognitive Brain Research*, vol. 14, no. 1, pp. 147–152, 2002.

[28] Y. Ren, W. Yang, K. Nakahashi, S. Takahashi, and J. Wu, "Audiovisual integration delayed by stimulus onset asynchrony between auditory and visual stimuli in older adults," *Perception*, vol. 46, no. 2, pp. 205–218, 2017.

[29] J. Vroomen and B. De Gelder, "Sound enhances visual perception: cross-modal effects of auditory organization on vision," *Journal of Experimental Psychology. Human Perception and Performance*, vol. 26, no. 5, pp. 1583–1590, 2000.

[30] H. Colonius and A. Diederich, "Multisensory interaction in saccadic reaction time: a time-window-of-integration model," *Journal of Cognitive Neuroscience*, vol. 16, no. 6, pp. 1000–1009, 2004.

[31] J. L.-T. Hidalgo, I. P. Martílnez, B. N. Bravo, F. A. Pretel, A. V. Ferrer, and M. Á. L. Verdejo, "Visual function versus visual acuity in older people," *Ophthalmic Epidemiology*, vol. 16, no. 4, pp. 262–268, 2009.

[32] B. E. Weinstein, "Age-related hearing loss: how to screen for it, and when to intervene," *Geriatrics*, vol. 49, no. 8, pp. 40–45, 1994.

[33] Y. Ren, Z. Xu, S. Lu, T. Wang, and W. Yang, "Stimulus specific to age-related audio-visual integration in discrimination tasks," *Perception*, vol. 11, no. 6, p. 204166952097841, 2020.

[34] R. A. Stevenson and M. T. Wallace, "Multisensory temporal integration: task and stimulus dependencies," *Experimental Brain Research.experimentelle Hirnforschung.experimentation Cerebrale*, vol. 227, no. 2, pp. 249–261, 2013.

[35] N. Tye-Murray, M. Sommers, B. Spehar, J. Myerson, and S. Hale, "Aging, audiovisual integration, and the principle of inverse effectiveness," *Ear and Hearing*, vol. 31, no. 5, pp. 636–644, 2010.

[36] G. Bravo and R. Hébert, "Age- and education-specific reference values for the Mini-Mental and Modified Mini-Mental State Examinations derived from a non-demented elderly population," *International Journal of Geriatric Psychiatry*, vol. 12, no. 10, pp. 1008–1018, 1997.

[37] J. Miller, "Timecourse of coactivation in bimodal divided attention," *Perception & Psychophysics*, vol. 40, no. 5, pp. 331–343, 1986.

[38] P. J. Laurienti, R. A. Kraft, J. A. Maldjian, J. H. Burdette, and M. T. Wallace, "Semantic congruence is a critical factor in multisensory behavioral performance," *Experimental Brain Research*, vol. 158, no. 4, pp. 405–414, 2004.

[39] P. J. Laurienti, J. H. Burdette, J. A. Maldjian, and M. T. Wallace, "Enhanced multisensory integration in older adults," *Neurobiology of Aging*, vol. 27, no. 8, pp. 1155–1163, 2006.

[40] A. M. Peiffer, J. L. Mozolic, C. E. Hugenschmidt, and P. J. Laurienti, "Age-related multisensory enhancement in a simple audiovisual detection task," *Neuroreport*, vol. 18, no. 10, pp. 1077–1081, 2007.

[41] C. E. Hugenschmidt, J. L. Mozolic, and P. J. Laurienti, "Suppression of multisensory integration by modality-specific attention in aging," *Neuroreport*, vol. 20, no. 4, pp. 349–353, 2009.

[42] D. Talsma and M. G. Woldorff, "Selective attention and multisensory integration: multiple phases of effects on the evoked brain activity," *Journal of Cognitive Neuroscience*, vol. 17, no. 7, pp. 1098–1114, 2005.

[43] D. Talsma, D. Senkowski, and M. G. Woldorff, "Intermodal attention affects the processing of the temporal alignment of audiovisual stimuli," *Experimental Brain Research*, vol. 198, no. 2-3, pp. 313–328, 2009.

[44] D. Talsma, D. Senkowski, S. Soto-Faraco, and M. G. Woldorff, "The multifaceted interplay between attention and multisensory integration," *Trends in Cognitive Sciences*, vol. 14, no. 9, pp. 400–410, 2010.

[45] D. Talsma, T. J. Doty, and M. G. Woldorff, "Selective attention and audiovisual integration: is attending to both modalities a prerequisite for early integration?," *Cerebral Cortex*, vol. 17, no. 3, pp. 679–690, 2007.

[46] A. M. Bonnel and E. R. Hafter, "Divided attention between simultaneous auditory and visual signals," *Perception & Psychophysics*, vol. 60, no. 2, pp. 179–190, 1998.

[47] A. Larsen, W. McIlhagga, J. Baert, and C. Bundesen, "Seeing or hearing? Perceptual independence, modality confusions, and crossmodal congruity effects with focused and divided attention," *Perception & Psychophysics*, vol. 65, no. 4, pp. 568–574, 2003.

[48] T. A. Mondor and K. J. Amirault, "Effect of same- and different-modality spatial cues on auditory and visual target identification," *Journal of Experimental Psychology: Human Perception and Performance*, vol. 24, no. 3, pp. 745–755, 1998.

[49] J. Fan, B. D. McCandliss, T. Sommer, A. Raz, and M. I. Posner, "Testing the efficiency and independence of attentional networks," *Journal of Cognitive Neuroscience*, vol. 14, no. 3, pp. 340–347, 2002.

[50] J. Fan, X. Gu, K. G. Guise et al., "Testing the behavioral interaction and integration of attentional networks," *Brain and Cognition*, vol. 70, no. 2, pp. 209–220, 2009.

[51] F. Goldhammer, J. Naumann, A. Stelter, K. Tóth, H. Rölke, and E. Klieme, "The time on task effect in reading and problem solving is moderated by task difficulty and skill: insights from a

Hindawi
Neural Plasticity
Volume 2021, Article ID 5575090, 15 pages
https://doi.org/10.1155/2021/5575090

Research Article

Annexin A3 as a Marker Protein for Microglia in the Central Nervous System of Rats

Zengli Zhang,[1,2] Zhengyiqi Li,[1] Zhi Ma,[2] Meiling Deng,[1] Manyu Xing,[1] Jing Wu,[1] Shasha Jiang,[1] Qiang Wang,[2] Qulian Guo,[1] and Wangyuan Zou[1,3]

[1]*Department of Anesthesiology, Xiangya Hospital, Central South University, Changsha 410008, China*
[2]*Department of Anesthesiology, Center for Brain Science, The First Affiliated Hospital of Xi'an Jiaotong University, Xi'an, China*
[3]*National Clinical Research Center for Geriatric Disorders, Xiangya Hospital, Central South University, Changsha 410008, China*

Correspondence should be addressed to Wangyuan Zou; wangyuanzou@csu.edu.cn

Received 3 February 2021; Revised 21 April 2021; Accepted 1 June 2021; Published 10 June 2021

Academic Editor: Fushun Wang

The parenchymal microglia possess different morphological characteristics in cerebral physiological and pathological conditions; thus, visualizing these cells is useful as a means of further investigating parenchymal microglial function. Annexin A3 (ANXA3) is expressed in microglia, but it is unknown whether it can be used as a marker protein for microglia and its physiological function. Here, we compared the distribution and morphology of parenchymal microglia labeled by ANXA3, cluster of differentiation 11b (CD11b), and ionized calcium-binding adaptor molecule 1 (Iba1) and measured the expression of ANXA3 in nonparenchymal macrophages (meningeal and perivascular macrophages). We also investigated the spatiotemporal expression of ANXA3, CD11b, and Iba1 in vivo and in vitro and the cellular function of ANXA3 in microglia. We demonstrated that ANXA3-positive cells were abundant and evenly distributed throughout the whole brain tissue and spinal cord of adult rats. The morphology and distribution of ANXA3-labeled microglia were quite similar to those labeled by the microglial-specific markers CD11b and Iba1 in the central nervous system (CNS). ANXA3 was expressed in the cytoplasm of microglia, and its expression was significantly increased in activated microglia. ANXA3 was almost undetectable in the nonparenchymal macrophages. Meanwhile, the protein and mRNA expression levels of ANXA3 in different regions of the CNS were different from those of CD11b and Iba1. Moreover, knockdown of ANXA3 inhibited the proliferation and migration of microglia, while overexpression of ANXA3 enhanced these activities. This study confirms that ANXA3 may be a novel marker for parenchymal microglia in the CNS of adult rats and enriches our understanding of ANXA3 from expression patterns to physiological function.

1. Introduction

The parenchymal microglia are critical cells that constitute approximately 15%-20% of the total number of glial cells in the central nervous system (CNS) [1]. They are highly motile cells distributed throughout the cerebral tissue and constantly survey tissue homeostasis with micromovements of their distal processes [1, 2]. In addition, microglia are activated by various environmental stimuli caused by brain injury or neurological diseases and are responsible for the clearing of dead tissue and toxic substances to maintain tissue homeostasis [1, 3]. Microglial activation involves morphological changes in which the cells develop shortened cytoplasmic processes and large soma [2]. Thus, detecting the different states of cellular activation by visualizing the cell morphology of parenchymal microglia is vital in the field of microglial research.

Existing visualization techniques are based on surface molecules expressed in resting and activated parenchymal microglial cells. The widely used classical microglial-specific markers are the cluster of differentiation 11b (CD11b) and ionized calcium-binding adaptor molecule 1 (Iba1). They are constitutively expressed by all resting and activated microglial subpopulations, as well as by peripheral macrophages, such as splenic macrophages and Kupffer cells [4–7]. Annexin 3 (ANXA3) belongs to the structurally related annexin protein family, whose members bind to negatively charged phospholipids in the presence of calcium and

participate in membrane trafficking, endocytosis, and cytoskeletal modulation [8–10]. The study by Junker et al. [8] showed that ANXA3 is highly expressed in resting and activated microglia in the rat brain following reversible cerebral ischemia. We and other investigators also found that ANXA3 is abundantly expressed in the microglia in the spinal cord of rats and mice [9, 11, 12]. However, whether ANXA3 can be used as a marker protein for microglia and the physiological function of ANXA3 in microglia is mostly unknown.

In the present study, to confirm the possibility of ANXA3 as a novel parenchymal microglial marker for adult rats and to gain insight into its cellular functions, we investigated the immunostaining patterns and expression levels of ANXA3, CD11b, and Iba1 in different regions of the CNS at different developmental time points and the roles of microglial ANXA3 in cell migration and cell proliferation.

2. Material and Methods

2.1. Animals. Sprague-Dawley (SD) male rats aged 1, 3, 6, 9, and 12 months were obtained from the Experimental Animal Center of Central South University (Changsha, China). The animals were housed in a specific pathogen-free and temperature-controlled facility. The animals were kept under a 12-hour light-dark cycle and were given free access to food and water. All animal experimental procedures were approved by the Ethics Committee for Animal Experimentation of Central South University and followed the Chinese National Institutes of Health Guide for the Care and Use of Laboratory Animals.

2.2. Middle Cerebral Artery Occlusion (MCAO). MCAO was performed as previously described [13]. Briefly, general anesthesia was induced by inhalational isoflurane (2%). Then, the middle cerebral artery was occluded using a nylon monofilament inserted from the left common carotid artery (CCA). The cerebral blood flow was recovered by removing the filament 90 min after MCAO. Immunofluorescence staining was performed 3 days after reperfusion to observe the morphology of microglial cells in the ischemic penumbra.

2.3. Embryo Collection. Male and female adult SD rats (3 months) were paired overnight. The next morning was designated embryonic day 0.5 (E0.5) if a vaginal plug was present (7:00 am) at the vaginal opening of female rats. Rat brains of the embryos were collected at E9.5, E11.5, E13.5, E15.5, E17.5, and E19.5.

2.4. Cell Cultures. Immortalized murine microglial N9 cells were a gift from Dr. Zhi Ma (Department of Anesthesiology, the First Affiliated Hospital of Xi'an Jiaotong University, China). The N9 cells were cultured in Iscove's modified Dulbecco's medium (IMDM, HyClone) containing 10% fetal bovine serum (FBS, Gibco) and 1% penicillin/streptomycin. The cells were maintained in a 37°C sterile container containing a mixture of 95% atmospheric air and 5% CO_2. The medium was replaced every 3 days.

2.5. Lentiviral Transfection. Up- and downregulation of the ANXA3 protein expression in microglial N9 cells was achieved via lentiviral transfection (LV-ANXA3 and LV-shANXA3, respectively) as previously described [14], Briefly, N9 cells were seeded in 96-well culture plates. The lentivirus (diluted using DMEM) was added to infect the cells for 24 h (multiplicity of infection, MOI = 80). Puromycin (4.5 μg/ml; Sigma, USA) selection was then performed to kill the uninfected cells. The LV-ANXA3, LV-shANXA3 (5′-CGGCCA TCCAATCAGATACTT-3′) targeting the mouse ANXA3 sequence (GenBank Accession: NM_013470.2, gene name: annexin A3 or Anxa3), an additional scrambled sequence (LV-NC; 5′-TTCTCCGAACGTGTCACGT-3′), and LV-empty were synthesized by Suzhou GenePharma (China). Briefly, to produce the lentivirus, 70% confluent 293T cells were cotransfected with lentivirus vector and plasmids (PG-P1-VSVG, PG-P2-REV, and PG-P3-RRE) using RNAi-Mate (Suzhou GenePharma, China). The medium was replaced 6 h after transfection. Lentiviral particles were harvested from the supernatant 72 h after the transfection and purified by ultracentrifugation. These particles are hereafter referred to as LV-ANXA3, LV-shANXA3, LV-NC (negative control, a control for LV-shANXA3), and LV-empty (a control for LV-ANXA3). The transfection efficiency of the lentivirus was the number of successfully transfected cells/the number of total cells in the same field of view. Up- and downregulation of ANXA3 protein expression was identified by Western blotting.

2.6. Cytoplasmic and Nuclear Protein Extraction. The cytoplasmic and nuclear protein extraction of N9 cells was performed using a Minute™ Cytoplasmic and Nuclear Extraction Kit for Cells (SC-003, Invent Biotechnologies, China) strictly according to the product instructions.

2.7. Cell Cycle Analysis. The cell cycle distribution of N9 cells was assessed by flow cytometry as previously described [14]. Briefly, N9 cells were collected, fixed in ice-cold 75% ethanol, and stained with propidium iodide solution (BD Biosciences, China). The DNA content was determined by flow cytometry data using CellQuest Software. For each sample, 10,000 events were counted (FACSCalibur, Becton-Dickinson, USA). The percentage of cells that were in a particular cell cycle stage was calculated using FlowJo software.

2.8. EdU Proliferation Assay. The proliferation of the N9 cells was determined using a Cell-Light EdU (5-ethynyl-20-deoxyuridine) Apollo 567 In Vitro Kit (RiboBio, China) according to the product instructions. The percentage of EdU-positive cells was calculated from five random fields in three wells.

2.9. Transwell Migration Assays. Cell migration was evaluated using a Transwell chamber with an 8 μm pore filter membrane (Corning, USA) as previously described [15]. Approximately 2×10^5 cells in serum-free medium were seeded in the upper chamber, while 600 μl of IMDM medium supplemented with 20% FBS was added to the lower chamber. Cells were incubated at 37°C in a humidified incubator containing 5% CO_2 for 24 hours. Cells that migrated into the lower chamber were stained with 10% crystal violet

(Sigma, USA) and counted in five random areas under a light microscope.

2.10. Wound Healing Assay. A wound healing assay was performed to observe the cell migration of microglia as previously described [16]. Transverse lines were drawn at the back of the 6-well culture plate evenly with a marking pen, and N9 cells were seeded in the plates and allowed to reach 100% confluence. An artificial wound was made using a 10 μl pipette tip (the same pipette tip was used to make scratches for all the wells) across the cell monolayer perpendicular to the lines drawn with the marking pen. Cells were rinsed with PBS and cultured in serum-free medium. Images of the cells were captured at 0 and 24 hours after scratching. The cell migration index was quantified by (D0-D24)/D0, where D0 is the distance from the wound edges at 0 hours, and D24 is the distance from the wound edges at 24 hours.

2.11. Immunohistochemical Staining (IHC). Immunohistochemical staining was performed using a PV-9000 Kit (ZSBiO, China) according to the product instructions [17]. Briefly, brain and spinal cord sections from rats were sliced into 10 μm thick sections (Leica CM1900), which were then subjected to antigen retrieval in a heated citrate buffer (pH 6.0) and incubated with 3% H_2O_2 for 10 min at room temperature to block endogenous peroxidase activity. Rabbit anti-ANXA3 antibody (1 : 1000, Sigma, USA) was used as a primary antibody. After the sections were incubated with peroxidase-labeled goat anti-rabbit/mouse IgG antibody, diaminobenzidine (DAB) was used as a chromogen.

2.12. Immunofluorescence Staining Assay. Immunofluorescence staining was performed on either frozen coronal sections of rats or N9 cells plated on cover slips as previously described [18]. The following primary antibodies were used: mouse anti-CD206 antibody (GB13438, 1 : 200, Servicebio, China), mouse anti-CD11b antibody (ab1211, 1 : 200, Abcam, England), rabbit anti-ANXA3 antibody (HPA013398, 1 : 200, Sigma, USA), and goat anti-Iba1 antibody (ab5076, 1 : 200, Abcam, England). Then, the samples were incubated with mixtures of Alexa-488- (green, Invitrogen), Alexa-594- (red, Santa Cruz), and Alexa-647- (red, Invitrogen) conjugated donkey anti-goat, anti-rabbit, and anti-mouse secondary antibodies. Finally, the sections were viewed under a fluorescence microscope (Olympus BX51, Japan) and photographed.

2.13. Western Blotting. The ANXA3, CD11b, and Iba1 protein expression levels were measured by Western blotting as described previously [19]. The following primary antibodies were used: rabbit anti-CD11b antibody (ab133357, 1 : 1000, Abcam, England), rabbit anti-ANXA3 antibody (HPA013398, 1 : 1000, Sigma, USA), rabbit anti-Iba1 (1 : 500, Wako, Japan), and rabbit anti-tubulin antibody (1 : 1000, Cell Signaling Technology, USA). The membranes were then incubated with an HRP-conjugated anti-rabbit or anti-mouse secondary antibody (Thermo Scientific) for two hours. Protein bands were visualized using a LI-COR Odyssey System (LI-COR Biotechnology).

2.14. Quantitative (Real-Time) Polymerase Chain Reaction (Real-Time PCR). The ANXA3 mRNA expression levels in the olfactory bulb, cortex, hippocampus, thalamus, cerebellum, and spinal cord collected from SD rats aged 1, 3, 6, 9, and 12 months were measured by real-time PCR as previously described. Total RNA was isolated using a kit (ER501-01, Transgen, China) and reverse transcribed in a 20 μl reaction at 42°C for 15 min followed by 85°C for 5 sec using SuperMix (M10111, Transgen, China). Real-time PCR was performed according to the manufacturer's manual of the qPCR Kit (AQ141, Transgen, China). The reaction was performed at 94°C for 30 sec followed by 40 cycles of 94°C for 5 sec, 60°C for 15 sec, and 72°C for 19 sec on the ViiA7 Real-Time PCR Detection System (2720 Thermal Cycler, Applied Biosystems). The mRNA primer sequences used are listed in Table 1. The relative mRNA expression was analyzed using the formula $2^{-(\text{Ct target gene-Ct reference gene})}$.

2.15. Statistical Analysis. Statistical tests were performed using PRISM v7.0 software (GraphPad). Data were collected by an independent investigator who was blinded to the groups. Comparisons between two groups were performed using Student's t-tests whereas comparisons among more than two groups were performed using one-way ANOVA with Tukey's posttest. All values are presented as the means ± SD. Values of $p < 0.05$ were considered statistically significant.

3. Results

3.1. Colocalization of ANXA3, CD11b, and Iba1 within Microglia in Different Regions. Brain sections that were immunohistochemically processed for light microscopy showed that ANXA3 immunoreactive cells were abundant and evenly distributed in the cortex, hippocampus, thalamus, and spinal cord of the adult rats (3 months) (Figure 1). When viewed at a higher magnification, the ANXA3-positive cells presented a radial shape characterized by small soma, long processes, and multiple branches (Figure 1), particularly similar to the morphology of glial cells. To confirm the phenotype of ANXA3-positive cells, we performed double immunofluorescence staining with NeuN, the neuronal nuclei-specific marker, and GFAP, the astrocyte marker, in the cortex and spinal cord of adult rats (3 months). Immunostaining showed that ANXA3 was almost undetectable in astrocytes labeled with GFAP and neurons labeled with NeuN in the cortex and spinal cord (Figures 2(a) and 2(b)). As brain macrophages including microglia can be distinguished into parenchymal microglia and $CD206^+$ CNS-associated macrophages (CAMs), namely, the nonparenchymal macrophages (perivascular macrophages, meningeal macrophages) [20], we detected the expression of AXNA3 in perivascular macrophages and meningeal macrophages using immunofluorescence staining (Figure 2(c)). Immunostaining showed that ANXA3 was almost undetectable in macrophages labeled with CD206 in the perivascular and meningeal (Figure 2(c)). We then detected the colocalization of ANXA3 with the microglial-specific markers CD11b and Iba1 throughout the brain and spinal cord of adult rats.

Table 1: Sequence of primers used for real-time PCR.

Gene	Forward primer (5-3′)	Reverse primer (5-3′)
CD11b	CAAGGAGTGTGTTTGCGTGT	AGAAGGCTCGGACAACTGAG
ANXA3	CAAATTCACCGAGATCCTGT	TGCTGGAGTGCTGTACGAAA
Iba1	TCTGAATGGCAATGGAGATA	GTTGGCTTCTGGTGTTCT
GAPDH	GCTCTCTGCTCCTCCCTGTTCTA	TGGTAACCAGGCGTCCGATA

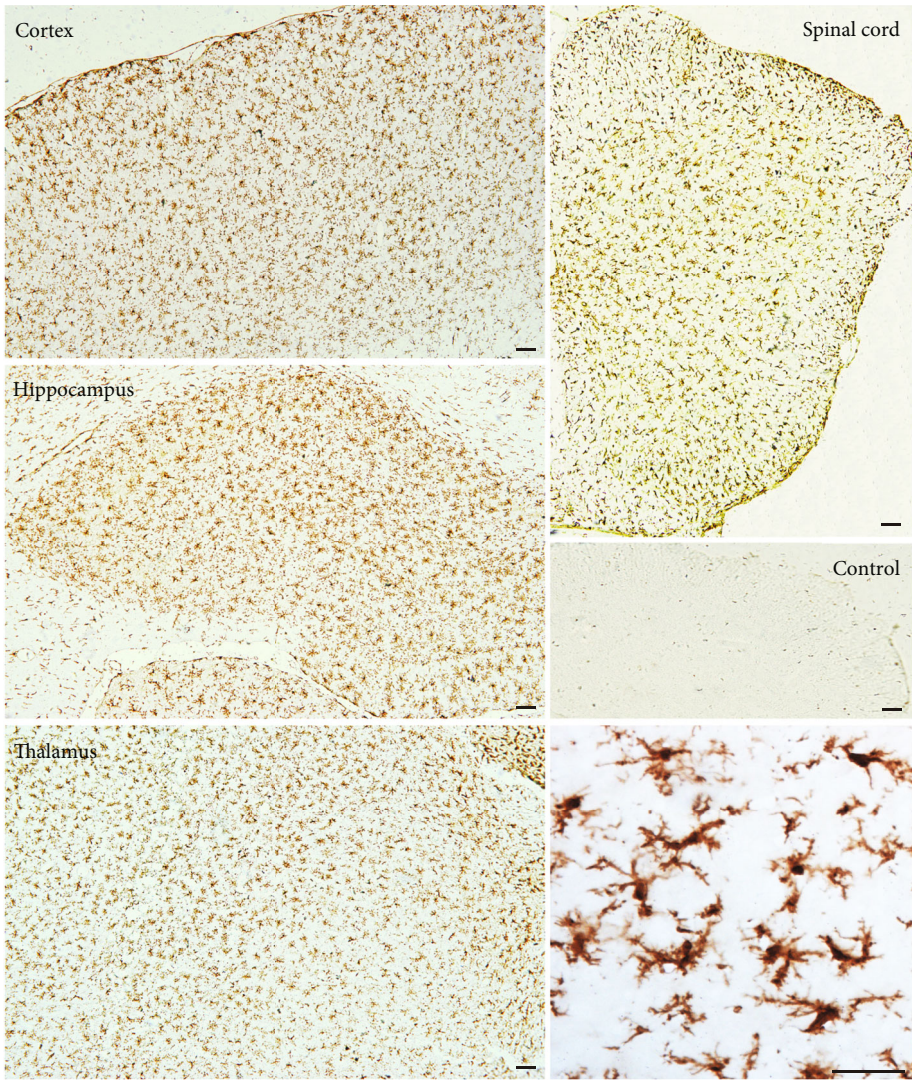

Figure 1: Overall pattern of ANXA3 immunoreactivity in the CNS of rats. Representative immunohistochemical images showing the immunoreactivity of ANXA3 in the cortex, hippocampus, thalamus, and spinal cord and the negative control. The negative control was the cortex tissue that was performed with IHC without a primary antibody. The image in the lower right corner shows the morphology of ANXA3-positive cells in the thalamus at a higher magnification. Scale bar = 100 μm.

The results indicate that ANXA3 and CD11b presented nearly complete colocalization in the microglia from the olfactory bulb, cortex, hippocampus, thalamus, cerebellum, and spinal cord of the adult rats (Figure 3(a)). Figure 3(b) shows images of the negative control (without primary antibody). Meanwhile, immunostaining showed that ANXA3 was nearly colocalized with Iba1 throughout the cerebrum, cerebellum, and spinal cord of the adult rats (Figure 4(a)). Figure 4(b) shows images of the negative control (without primary antibody). No significant differences in the ANXA3$^+$/CD11b$^+$ cells (Figure 3(c)) and ANXA3$^+$/Iba1$^+$ cells (Figure 4(c)) were observed among the different regions.

3.2. The Morphologies of Resting and Activated Microglia Labeled by ANXA3. As shown in Figure 5(a), the ischemic penumbra was the area between the infarct core and the unaffected (normal) tissue. At a higher magnification, the resting microglia labeled with ANXA3 in the unaffected

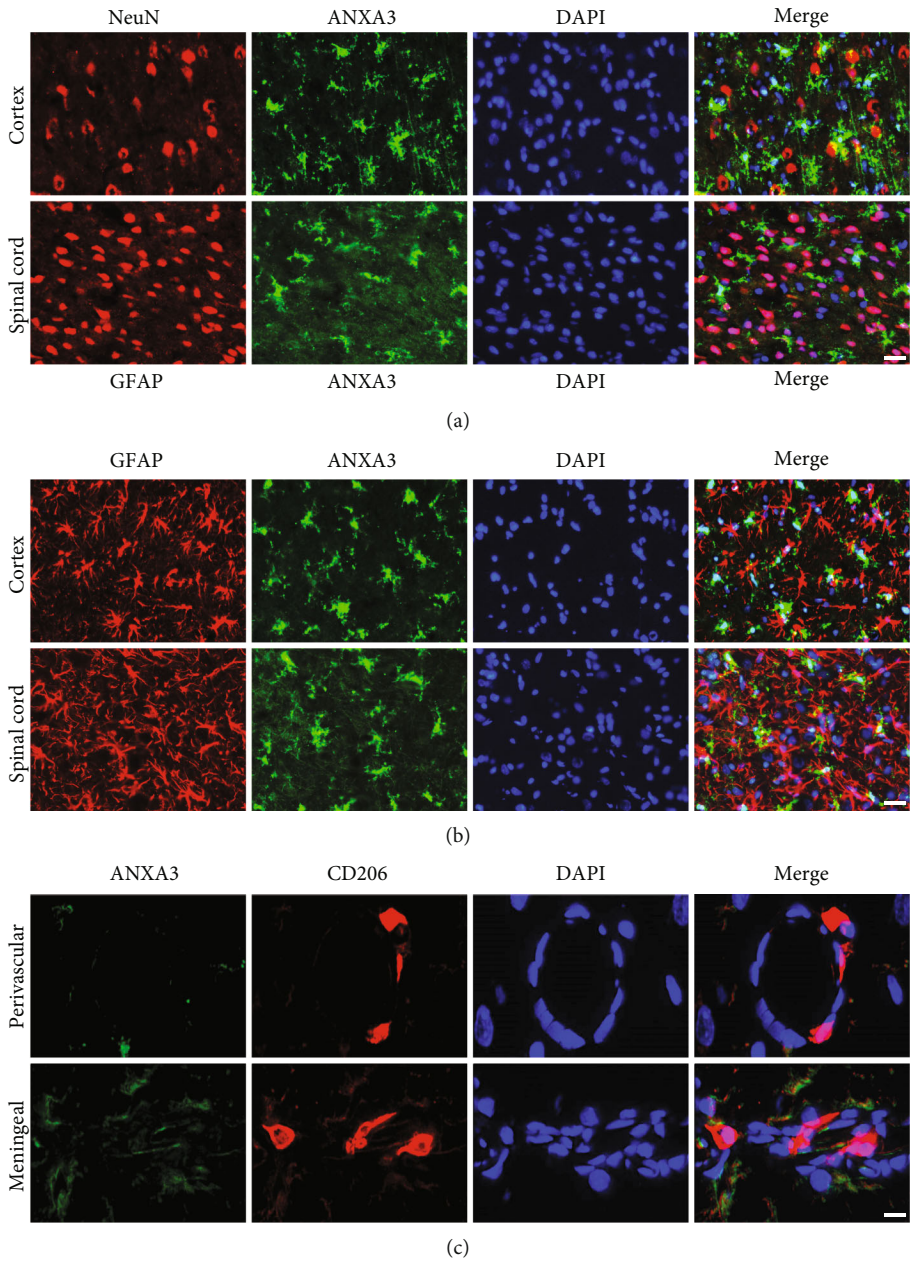

Figure 2: ANXA3 immunoreactivity in neurons, astrocytes, and nonparenchymal macrophages. (a, b) Representative immunofluorescence images showing the expression of ANXA3 in neurons (stained with NeuN) and astrocytes (stained with GFAP) from the cortex and spinal cord. Scale bar = 20 μm. (c) Representative immunofluorescence images showing the expression of ANXA3 in macrophages labeled with CD206 in the perivascular and meningeal. Scale bar = 50 μm.

tissue had a small perinuclear cytoplasm with long, thick processes extending in multiple directions, while the activated microglia labeled by ANXA3 in the penumbra displayed larger soma and shorter, coarser cytoplasmic processes, which were particularly similar to those of the microglial cells labeled by Iba1 (Figure 5(b)).

3.3. Protein Expression Levels of ANXA3, CD11b, and Iba1 in Different Regions. We performed Western blotting to measure the protein expression levels of ANXA3, CD11b, and Iba1 in the olfactory bulb, cortex, hippocampus, thalamus, cerebellum, and spinal cord of the adult rats (Figures 5(c) and 5(d)). The levels of ANXA3 protein expression in the olfactory bulb, cortex, thalamus, and spinal cord were much higher than those in the cerebellum, while no significant difference was observed between the hippocampus and cerebellum. The levels of CD11b protein expression in the olfactory bulb, thalamus, and spinal cord were much higher than those in the cerebellum, and no significant differences were observed among the cortex, hippocampus, and cerebellum. The level of Iba1 protein expression in the cerebellum was significantly lower than those in the other regions, and no significant differences were observed among the olfactory bulb, cortex, hippocampus, and spinal cord.

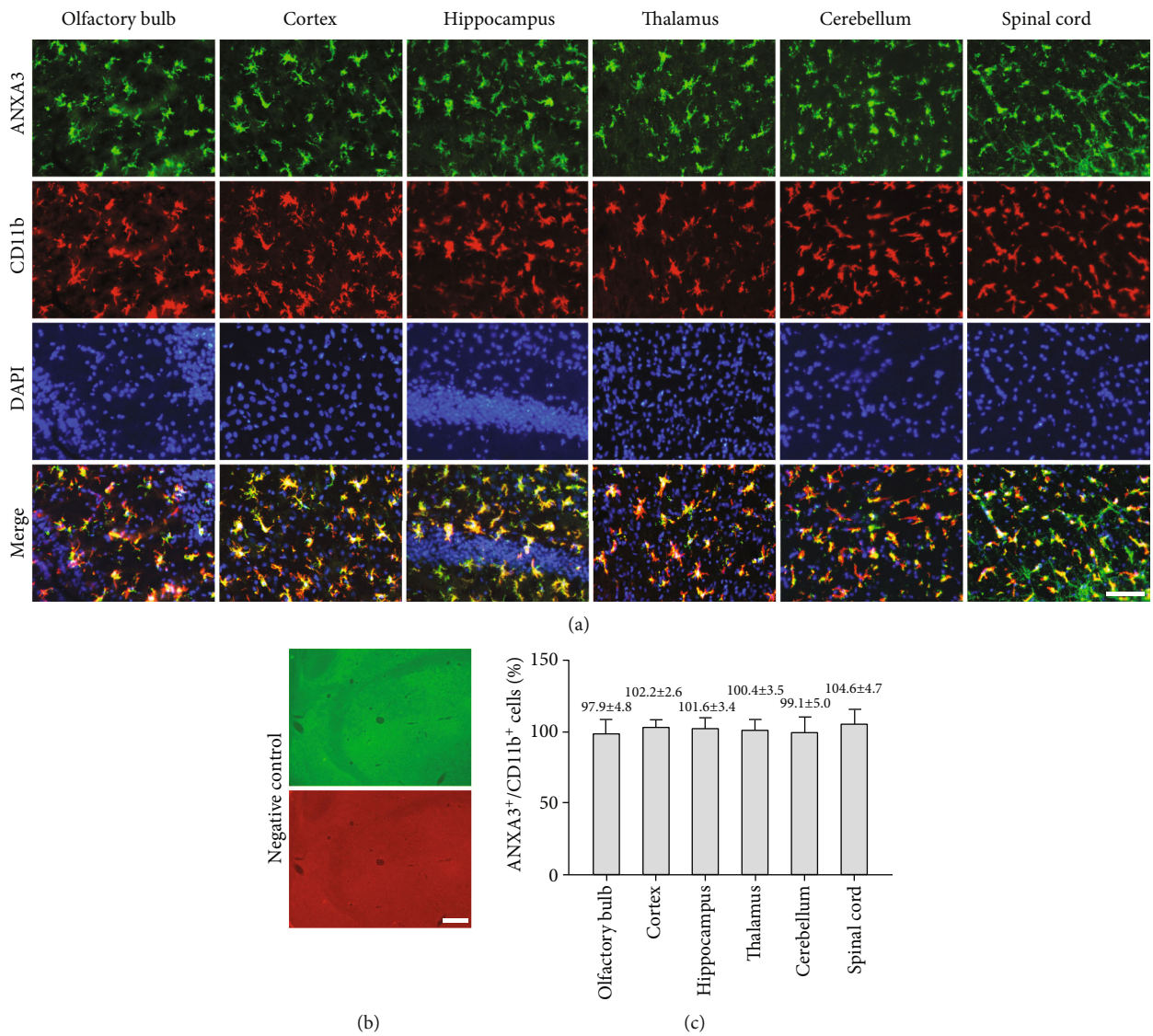

Figure 3: Colocalization of ANXA3 and CD11b in different regions of the CNS. (a) Representative immunofluorescence images of microglia labeled by ANXA3 and CD11b in the olfactory bulb, cortex, hippocampus, thalamus, cerebellum, and spinal cord of adult rats (3 months). Scale bar = 40 μm. (b) Images of the negative control (without primary antibody). Scale bar = 100 μm. (c) Quantitative analysis of $ANXA3^+/CD11b^+$ microglial cells in different regions of the CNS. The $ANXA3^+/CD11b^+$ are the number of ANXA3-positive cells/the number of CD11b-positive cells in the same randomly selected field of view. The data are presented as the means ± SD and were analyzed by one-way ANOVA with Tukey's post hoc test. $n = 5$ per group. Cells in five randomly selected fields were counted.

3.4. Spatiotemporal Expression of ANXA3 in the CNS of Rats. ANXA3 protein and mRNA expression levels were examined to determine the overall trend of the ANXA3 expression in embryos from E9.5 to E19.5 (Figures 6(a)–6(c)). The levels of the ANXA3 protein and mRNA expression were highest at E11.5 and lowest at E17.5 during brain development. No significant differences were observed among the E9.5, E13.5, E15.5, and E19.5 groups. We also measured the mRNA expression levels of ANXA3, CD11b, and Iba1 in the olfactory bulb, cortex, hippocampus, thalamus, cerebellum, and spinal cord of rats aged 1, 3, 6, 9, and 12 months (Figures 6(d)–6(i)). In the olfactory bulb and thalamus, the mRNA expression levels of ANXA3, CD11b, and Iba1 showed no significant changes in rats aged 1, 3, 6, 9, and 12 months (Figures 6(d) and 6(g)); however, mRNA expression levels of all three genes were significantly increased in the cortex and cerebellum of rats aged 12 months compared with rats aged 1 month (Figures 6(e) and 6(h)). In the hippocampus and spinal cord, the mRNA expression levels of ANXA3 and Iba1 were significantly increased starting at 6 months and gradually increased with age (Figures 6(f) and 6(i)). The mRNA expression levels of CD11b in the hippocampus were significantly increased in rats aged 12 months, and the mRNA levels of CD11b in the spinal cord were significantly increased from 6 months and gradually increased with age (Figures 6(f) and 6(i)).

3.5. Subcellular Localization of ANXA3 in Microglia. We then investigated the subcellular localization of ANXA3 in resting

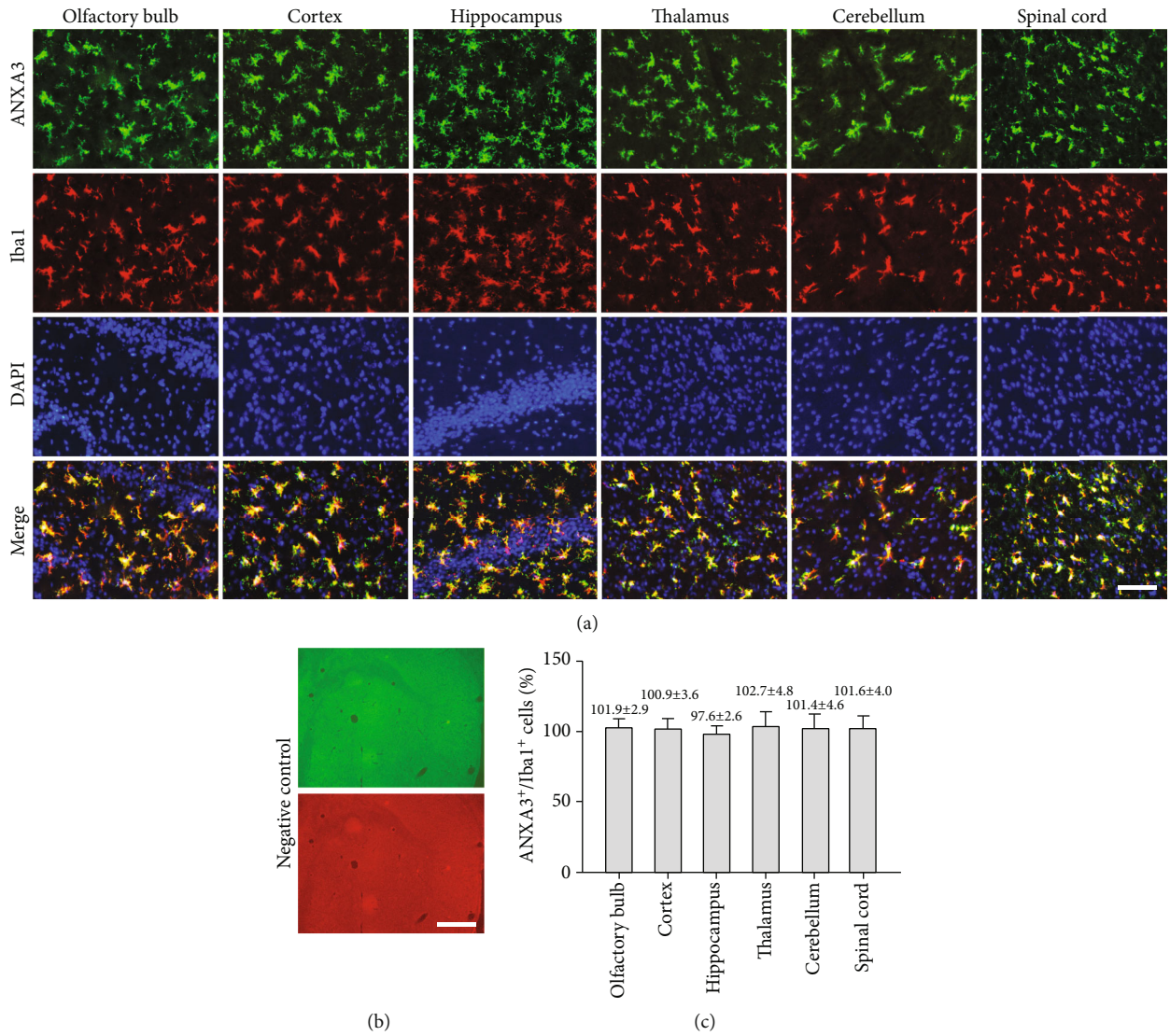

Figure 4: Colocalization of ANXA3 and Iba1 in different regions of the CNS. (a) Representative immunofluorescence images of microglia labeled by ANXA3 and Iba1 in the olfactory bulb, cortex, hippocampus, thalamus, cerebellum, and spinal cord of adult rats (3 months). Scale bar = 40 μm. (b) Images of the negative control (without primary antibody). Scale bar = 100 μm. (c) Quantitative analysis of $ANXA3^+/Iba1^+$ microglial cells in different regions of the CNS. The data are presented as the means ± SD and were analyzed by one-way ANOVA with Tukey's post hoc test. $n = 5$ per group. Cells in five randomly selected fields were counted.

and activated microglial N9 cells (Figures 7(a)–7(c)). Immunostaining showed that ANXA3 was expressed in N9 cells (Figure 7(a)), with higher magnifications showing that ANXA3 immunoreactivity was mainly present in the cytoplasm (Figure 7(a)). The N9 cells were treated with 500 ng/ml lipopolysaccharide (LPS) for 24 hours to achieve functional activation [21]. ANXA3 protein expression levels in the cytoplasmic and nuclear protein extractions of the resting (Con) and LPS-induced activated N9 cells were detected by Western blotting analysis (Figures 7(b) and 7(c)). The ANXA3 protein was detectable in the cytoplasm of both resting (Con) and LPS-induced activated N9 cells and was almost undetectable in the nuclei of N9 cells (Figures 7(b) and 7(c)). In addition, there was a significant increase in the ANXA3 protein expression in the cytoplasm of LPS-induced activated N9 cells compared with the control resting N9 cells (Figures 7(b) and 7(c)).

3.6. ANXA3 Participated in the Proliferation of Microglia. To gain insight into the cellular function of ANXA3 in microglia, overexpression and knockdown of ANXA3 in N9 microglial cells were performed via lentiviral transfection of LV-ANXA3 and ANXA3-targeting shRNA (LV-shANXA3), respectively, and evaluated using Western blotting (Fig. S1). The transfection efficiencies of LV-empty, LV-NC, LV-ANXA3, and LV-shANXA3 were more than 95% (Fig. S1A-S1B). The ANXA3 protein expression was significantly increased in the LV-ANXA3 group compared with the LV-empty group and was significantly decreased in the LV-shANXA3 group compared with the LV-NC group

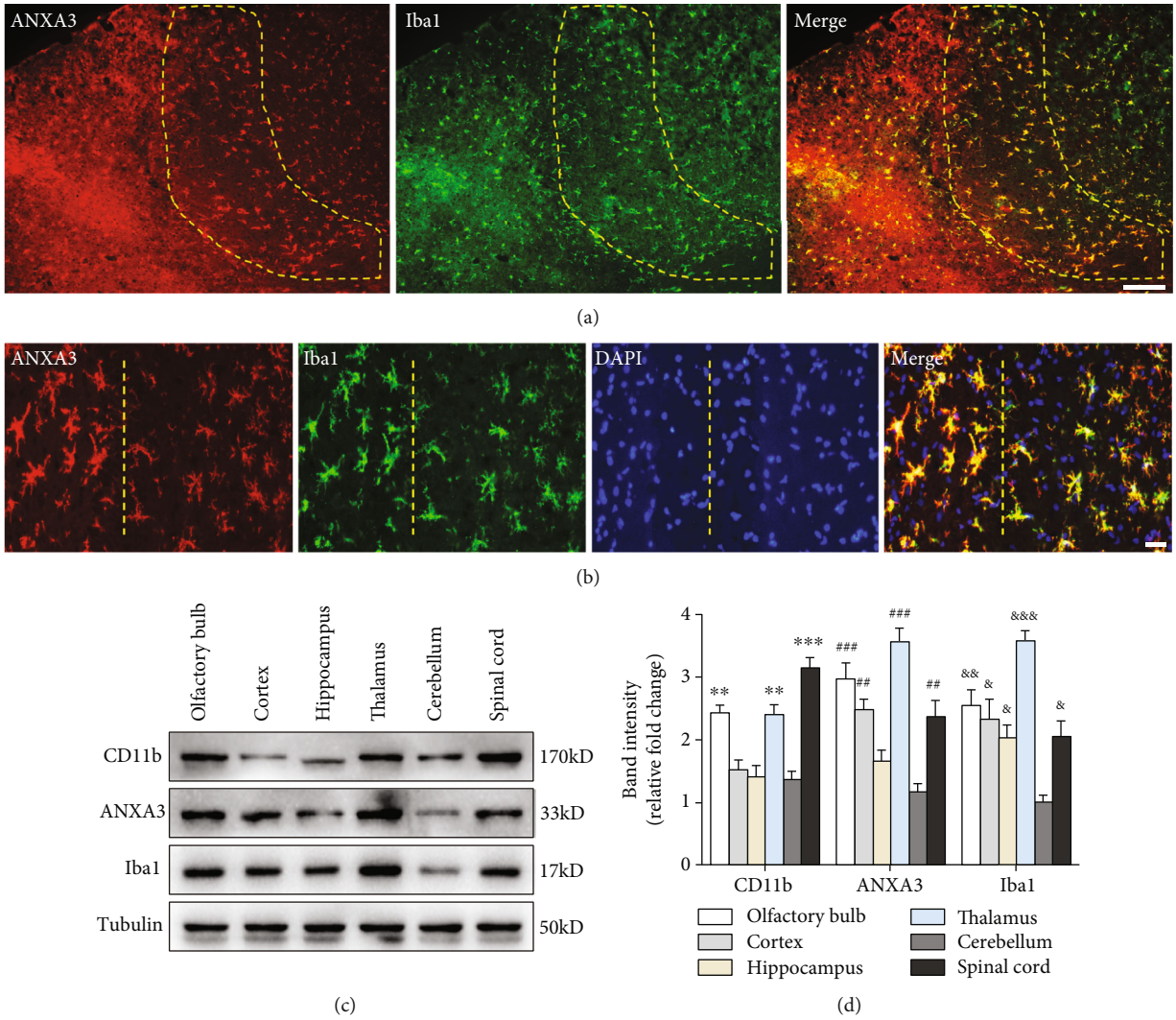

Figure 5: Morphologies of microglia labeled by ANXA3 and ANXA3 protein expression levels in different regions. (a) Low-magnification micrographs showing microglial cells in the ischemic penumbra 3 days after reperfusion. The yellow-dotted ring indicates the ischemic penumbra area between the infarct area and the normal area of the brain tissue. Scale bars = 200 μm. (b) Representative immunofluorescence images showing the morphology of activated microglia in the ischemic penumbra (on the left) and resting microglia in the healthy area (on the right) labeled by ANXA3 and Iba1 at high magnification. Scale bars = 50 μm. $n = 5$ per group. (c, d) The expression levels of ANXA3, CD11b, and Iba1 proteins in the olfactory bulb, cortex, hippocampus, thalamus, cerebellum, and spinal cord of adult rats (3 months) were determined by Western blotting analysis. The panel shows protein bands corresponding to ANXA3, CD11b, Iba1, and tubulin. The histogram shows the results of the densitometric analysis. The data are expressed as the means ± SD and were analyzed by one-way ANOVA with Tukey's post hoc test. $^{**}p < 0.01$ and $^{***}p < 0.001$ compared with the cerebellum group. $^{\#\#}p < 0.01$ and $^{\#\#\#}p < 0.001$ compared with the cerebellum group. $^{\&}p < 0.05$, $^{\&\&}p < 0.01$, and $^{\&\&\&}p < 0.001$ compared with the cerebellum group. $n = 6$ per group.

(Fig. S1C-S1D). Next, we measured the proliferative capacity of the overexpressing and knockdown N9 cells using both flow cytometry analysis and EdU incorporation assays. Overexpression of ANXA3 in the LV-ANXA3-treated N9 cells significantly increased the percentages of cells that were in the S phase and S+G2 phase compared to the LV-empty-treated N9 cells, and knockdown of ANXA3 in the LV-shANXA3-treated N9 cells significantly decreased the percentage of cells in the S phase and S+G2 phase compared to the LV-NC-treated N9 cells (Figures 8(a) and 8(b)). The EdU incorporation assay results were consistent with those of the flow cytometry analysis: overexpression of ANXA3 in LV-ANXA3-treated N9 cells significantly increased the percentage of EdU-positive cells compared with LV-NC-treated N9 cells, and knockdown of ANXA3 in LV-shANXA3-treated N9 cells significantly decreased the percentage of EdU-positive cells compared with LV-NC-treated N9 cells (Figures 8(c) and 8(d)).

3.7. ANXA3 Participated in the Migration of Microglia. Wound healing and Transwell assays were performed to determine the migration of microglia. The wound healing assay showed that overexpression of ANXA3 in LV-ANXA3-treated N9 cells significantly increased the

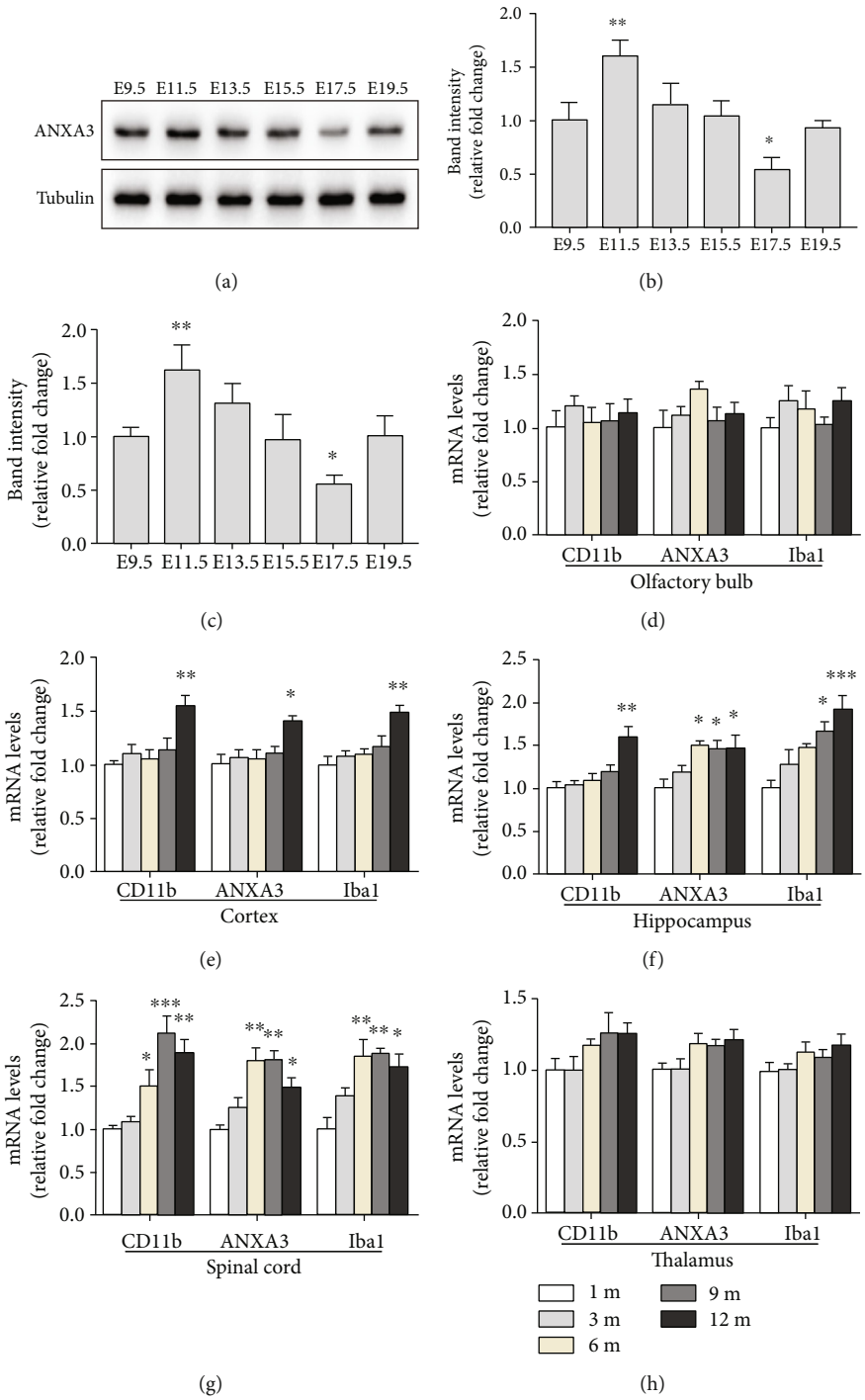

Figure 6: Continued.

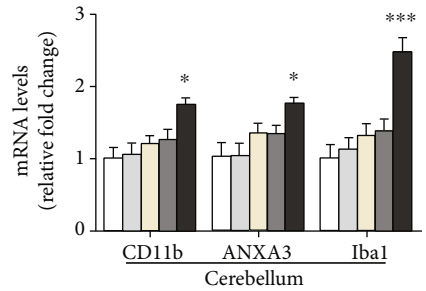

(i)

Figure 6: Spatiotemporal expression of ANXA3 protein and mRNA. (a, b) The expression levels of ANXA3 protein in rat embryos from E9.5 to E19.5 were determined by Western blotting analysis. The panel shows the protein bands corresponding to ANXA3 and tubulin. The histogram indicates the quantification of the densitometric analysis. The data are expressed as the means ± SD and were analyzed by one-way ANOVA with Tukey's post hoc test. $^{*}p < 0.05$ and $^{**}p < 0.01$ compared with the E9.5 group. $n = 6$ per group. (c) Real-time PCR analysis of ANXA3 mRNA expression in rat embryos from E9.5 to E19.5. The data are expressed as the means ± SD and were analyzed by one-way ANOVA with Tukey's post hoc test. $^{*}p < 0.05$ and $^{**}p < 0.01$ compared with the E9.5 group. $n = 6$ per group. (d–i) The levels of ANXA3 mRNA expression in the olfactory bulb, cortex, hippocampus, thalamus, cerebellum, and spinal cord of rats aged 1, 3, 6, 9, and 12 months were determined by qPCR analysis. The data are expressed as the means ± SD and were analyzed by one-way ANOVA with Tukey's post hoc test. $^{*}p < 0.05$, $^{**}p < 0.01$, and $^{***}p < 0.001$ compared with the 1 m group. $n = 6$ per group. 1 m: 1 month; 3 m: 3 months; 6 m: 6 months; 9 m: 9 months; 12 m: 12 months.

migration index of microglia compared with LV-empty-treated N9 cells, and knockdown of ANXA3 in LV-shANXA3-treated N9 cells significantly decreased the migration index of microglia compared with LV-NC-treated N9 cells (Figures 9(a) and 9(b)). The Transwell assay showed that overexpression of ANXA3 in LV-ANXA3-treated N9 cells significantly increased the number of migrating cells compared with LV-empty-treated N9 cells, and knockdown of ANXA3 in LV-shANXA3-treated N9 cells significantly decreased the number of migrating cells compared with LV-NC-treated N9 cells (Figures 9(c) and 9(d)).

4. Discussion

ANXA3 is a Ca^{2+}-dependent phospholipid-binding protein whose immunostaining patterns and physiological function in the CNS are mostly unknown. In the current study, we demonstrated that ANXA3-positive cells were abundantly and evenly distributed throughout the whole brain tissue and spinal cord of adult rats. The morphology and distribution of ANXA3-positive microglia were quite similar to those of CD11b- and Iba1-positive microglia in the CNS. ANXA3 expression was localized to the cytoplasm of microglia and was increased in activated microglia. Knockdown of ANXA3 inhibited the proliferation and migration of microglia, while overexpression promoted microglial proliferation and migration. The study confirms that ANXA3 may be a novel marker for the parenchymal microglia and can enrich our understanding of ANXA3 in the CNS from expression patterns to physiological functions.

CD11b and Iba1 are molecules used as markers to identify the parenchymal microglial cells in the CNS [4, 5, 22]. The parenchymal microglia labeled by CD11b and Iba1 present a relatively uniform distribution, with the exception of higher relative numbers in the olfactory telencephalon, dentate gyrus of the hippocampus, substantia nigra, and portions of the basal ganglia [3]. Using immunohistochemistry and immunofluorescence, we demonstrated that ANXA3-positive microglia were abundantly and evenly distributed throughout the CNS. Moreover, we found that ANXA3 and CD11b/Iba1 presented nearly complete colocalization in microglia throughout the whole brain tissue and the spinal cord of adult rats. Consistent with our results, a study from Smithson and Kawaja demonstrated that ANXA3-immunopositive cells are evenly distributed throughout the olfactory bulb of adult rats [22]. Microglia are known to undergo morphological transformation in response to various stimuli. Functional changes in microglia are often accompanied by morphological changes to cells with larger soma and shorter, coarser cytoplasmic processes displaying a bushy appearance; these changes can possibly progress to a full amoeboid morphology [3]. In this study, the ANXA3-positive activated microglia in the penumbra presented larger soma and shorter, coarser cytoplasmic processes, particularly similar to Iba1-positive glial cells. The morphology and distribution of ANXA3-positive microglia were quite similar to those of CD11b- and Iba1-positive microglia in the CNS, which appear to identify all the parenchymal microglia; thus, ANXA3 may be a novel marker for the parenchymal microglia. In addition, we found that ANXA3 was nearly undetectable in the perivascular macrophages and meningeal macrophages. Furthermore, we showed that ANXA3 protein expression significantly increased in the cytoplasm of LPS-induced activated microglial cells compared with resting microglia. ANXA3 has been recently reported to be highly upregulated in the postischemic rat brain [8], and ANXA3 knockdown inhibits the nuclear factor-kappa B (NF-κB) pathway by upregulating IκBα [23]. These findings indicate that ANXA3 may play a role in the process of microglia activation or microglia-mediated inflammation.

While characteristic features of the microglia structure and function have been identified as they relate to brain development and aging, there are limited experimental data about the changes in the expression of microglial markers

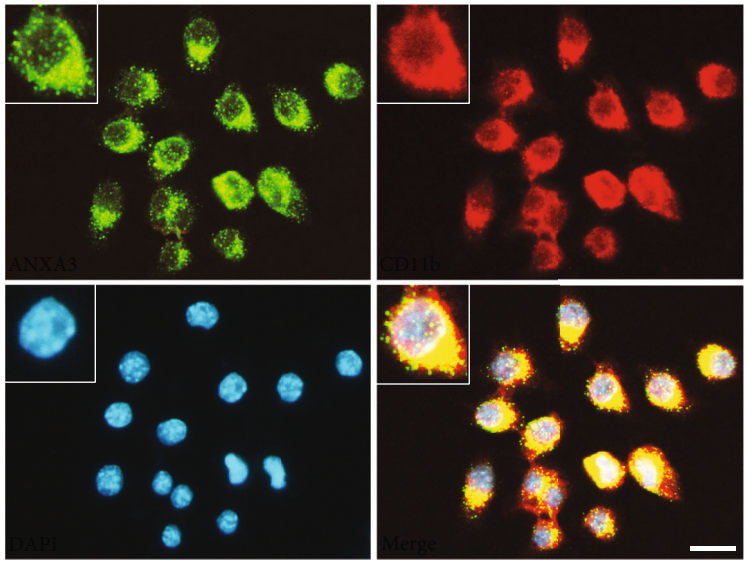

(a)

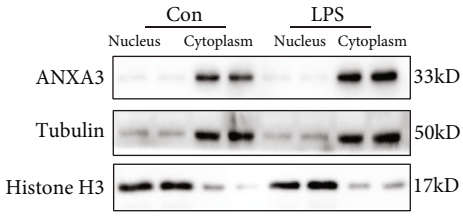

(b)

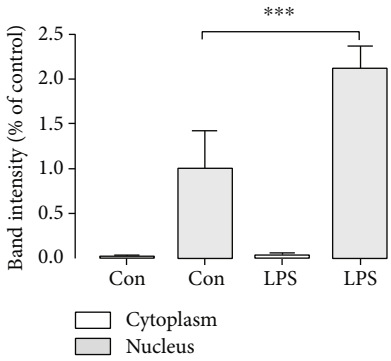

(c)

Figure 7: Subcellular localization of ANXA3 in resting and activated N9 microglial cells and lentiviral transfection of N9 cells. (a) Representative immunofluorescence images showing ANXA3 expression in microglial cells. N9 cells were also stained for CD11b expression. The inset shows the microglia at a higher magnification. Scale bar = 40 μm. (b, c) Western blotting analysis of ANXA3 protein expression levels in the cytoplasm and nuclei of resting (Con) and LPS-induced activated microglia (500 ng/ml LPS treatment for 24 hours). The panel shows the ANXA3, tubulin, and histone H3 protein bands, and the histogram reflects the results of the densitometric analysis. The data are expressed as the means ± SD and were analyzed by Student's t-tests. $^{***}p < 0.001$ compared with the control group. The data were pooled from six independent experiments.

across the lifespan of higher organisms. We found that the ANXA3 protein and mRNA expression levels were highest at E11.5 and lowest at E17.5 during the brain development of rats. Microglia originate from progenitor cells in the yolk sac at approximately embryonic day 7.5 (E7.5) and migrate into the rudimentary brain at approximately E9.5 [24]. ANXA3 protein and mRNA were detectable at E9.5 and lasted until E19.5, indicating that ANXA3 may participate in brain development at the embryonic stage. Studies by Dalmau et al. demonstrate that there is a low proportion of microglia undergoing apoptosis during brain development [3, 25]. The decreased expression of ANXA3 at E17.5 may either be due to microglial apoptosis or simply reflect the dramatic changes in volume expansion of the CNS during development. Future investigations will be essential to determine the functional significance of the temporal differential expression of ANXA3 during brain development. Aging is associated with an increase in microglial activation [3, 26]. In both rat and human brains, observations of altered microglia morphology have been observed and are associated with a more reactive/activated phenotype as a function of aging [3, 27–29]. Markers normally present in activated microglia, including MHC II antigens, CD11b, CD14, and pattern recognition receptors, are also elevated in aged microglia [3, 30–34]. In the olfactory bulb and thalamus, the mRNA expression levels of ANXA3, CD11b, and Iba1 showed no changes in rats aged 1, 3, 6, 9, and 12 months; however, in the cortex and cerebellum, the mRNA expression levels of ANXA3, CD11b, and Iba1 were increased in rats aged 12 months. In the hippocampus and spinal cord, the mRNA expression levels of ANXA3, CD11b, and Iba1 gradually increased with age. Differences in the expression levels of ANXA3, CD11b, and Iba1 throughout the brain and spinal cord are suggested to be associated with the

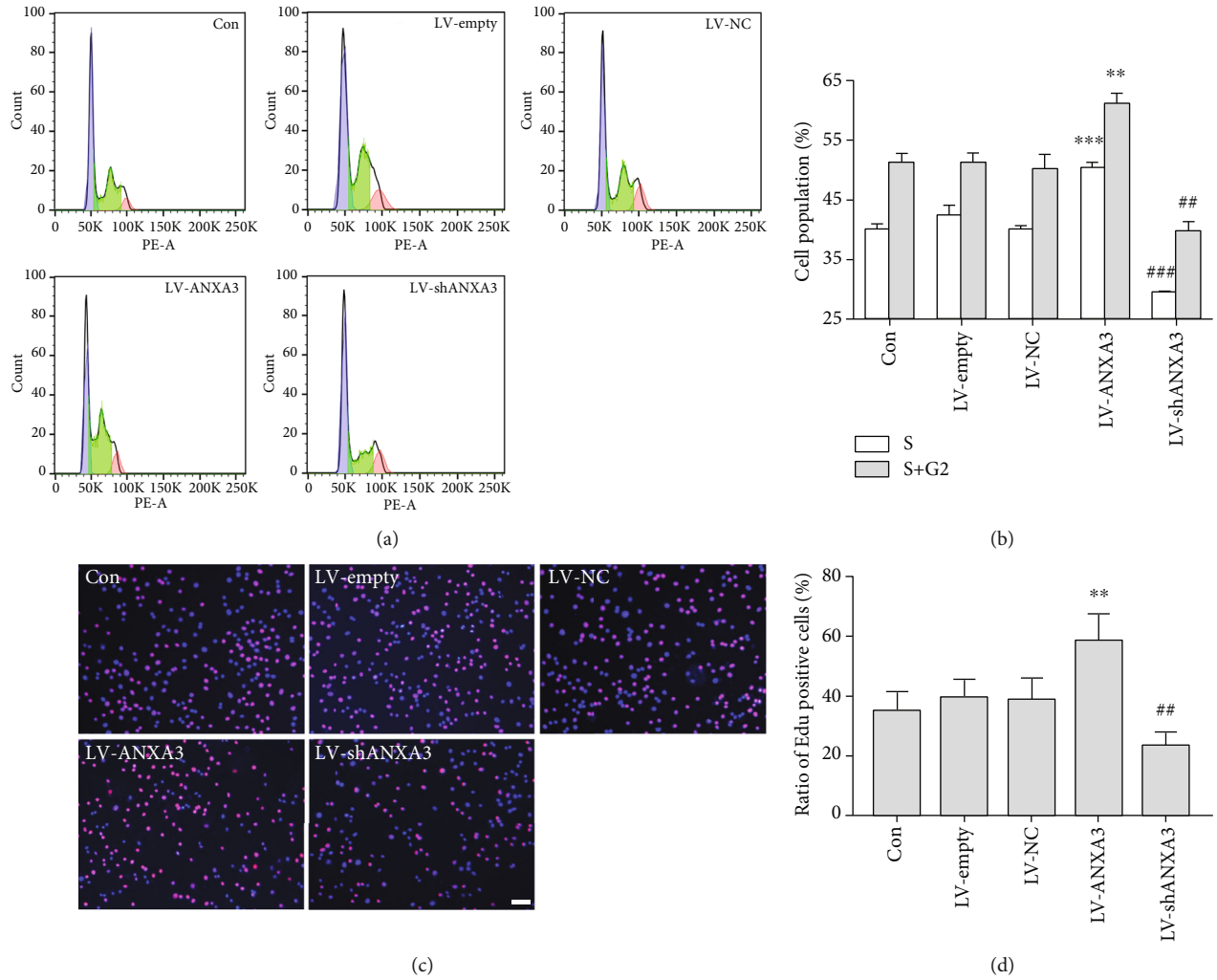

Figure 8: The proliferation of microglial N9 cells. (a, b) Flow cytometry analysis showing the proliferation of the Con, LV-empty, LV-NC, LV-ANXA3, and LV-shANXA3-treated N9 microglial cells. MultiCycle AV software was used to perform the fit analysis of the DNA cell cycle and to calculate the percentages of cells in each phase. The blue peak, the green arc-shaped hatched portion in the middle, and the red peak represent the G1, S, and G2 phases of the cell cycle, respectively. The data are expressed as the means ± SD and were analyzed by one-way ANOVA with Tukey's post hoc test. $^{**}p < 0.01$ and $^{***}p < 0.001$ compared with the LV-empty group. $^{\#\#}p < 0.01$ and $^{\#\#\#}p < 0.001$ compared with the LV-NC group. The data were pooled from five independent experiments. (c, d) The EdU incorporation assay showing the proliferation of the Con, LV-empty, LV-NC, LV-ANXA3, and LV-shANXA3-treated N9 microglial cells. The cell nuclei were stained with DAPI. EdU-positive cells are indicated in pink. The data are expressed as the means ± SD and were analyzed by one-way ANOVA with Tukey's post hoc test. $^{**}p < 0.01$ compared with the LV-empty group. $^{\#\#}p < 0.01$ compared with the LV-NC group. The data were pooled from five independent experiments. Scale bar = 20 μm. DAPI: 4′,6-diamidino-2-phenylindole; EdU: 5-ethynyl-2′-deoxyuridine.

microenvironment as well as with functional differences, including receptor expression patterns [35] and the expression of cell surface antigens [36]. In addition, one study has shown that in the hippocampus of mice, ANXA3 is undetectably low at the age of 3 days, significantly increases from 3 days to 3 weeks, and remains high at 3 months [37]. The results from our research and other investigators indicate that ANXA3 plays an important functional role in the CNS across the lifespan of higher organisms.

We also detected the expression levels of ANXA3, CD11b, and Iba1 proteins and mRNA in the olfactory bulb, cortex, hippocampus, thalamus, cerebellum, and spinal cord of adult rats. The expression levels of ANXA3, CD11b, and Iba1 are varied in different regions, indicating the heterogeneity of the marker expression patterns. Expression differences in these cell surface antigens throughout the brain are suggested to be associated with differences in the localization of microglia [3]. In addition, as microglial density has been shown to differ between males and females across stages of the lifespan and throughout brain regions under steady-state conditions and in response to chronic stress [38], future investigations are required to determine whether ANXA3 expression differs between males and females.

Our group originally found that ANXA3 is greatly upregulated in the spinal cord following chronic constriction injury- (CCI-) induced neuropathic pain [9]. Moreover, ANXA3 downregulation alleviates CCI-induced mechanical allodynia and thermal hyperalgesia, indicating that ANXA3

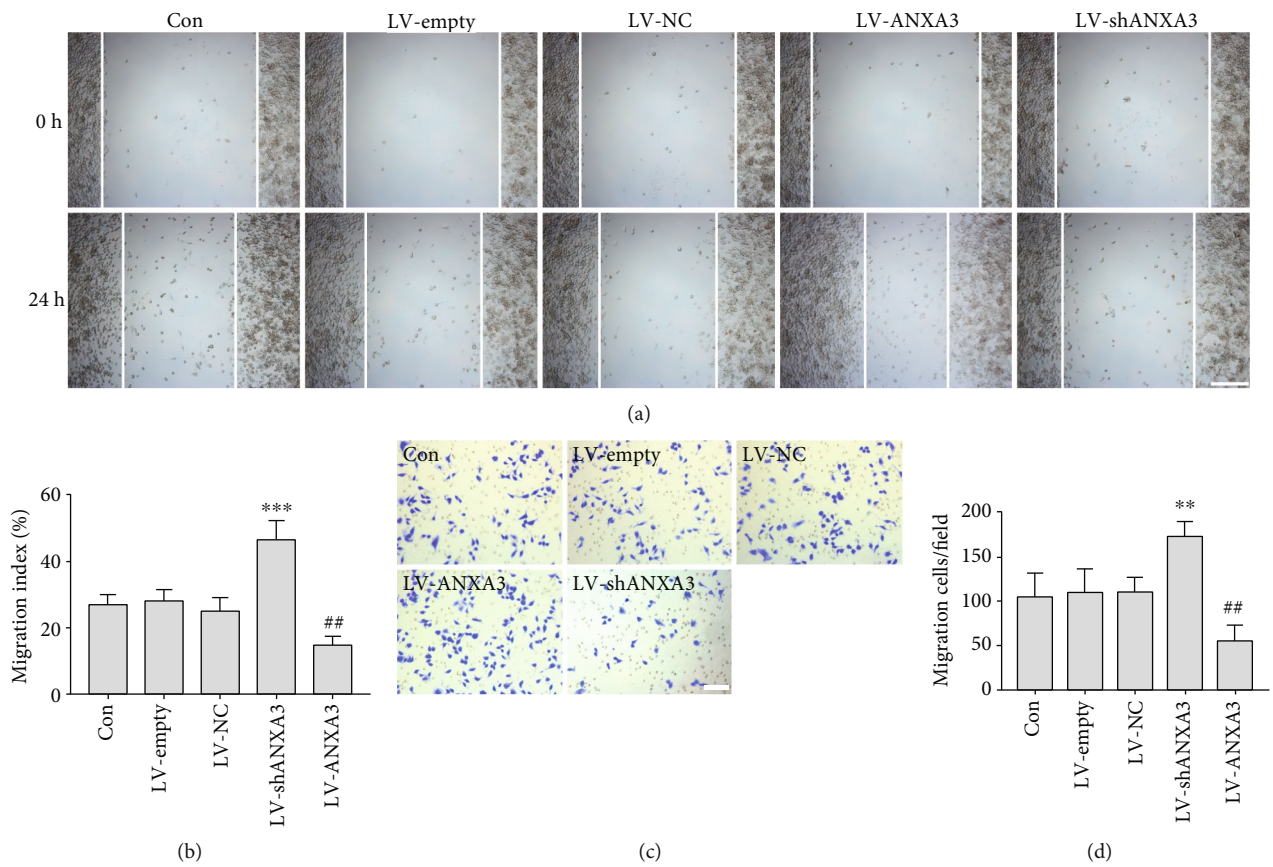

Figure 9: The migration of microglial N9 cells. (a, b) Evaluation of cell migration using a wound healing assay; monolayers were viewed on an inverted microscope. The histogram shows the quantitative analysis of the cell migration index. The data are expressed as the means ± SD and were analyzed by one-way ANOVA with Tukey's post hoc test. $^{***}p < 0.001$ compared with the LV-empty group. $^{\#\#}p < 0.01$ compared with the LV-NC group. The data were pooled from five independent experiments. (c, d) Evaluation of cell migration using the Transwell assay; migratory cells were viewed under an inverted microscope. The histogram shows the quantitative analysis of migrating cells. The data are expressed as the means ± SD and were analyzed by one-way ANOVA with Tukey's post hoc test. $^{**}p < 0.01$ compared with the LV-empty group. $^{\#\#}p < 0.01$ compared with the LV-NC group. The data were pooled from five independent experiments.

plays a crucial role in neuropathic pain. In addition, studies have shown that overexpression of ANXA3 promotes tumor proliferation in lung, liver, and ovarian carcinomas [23, 39]. ANXA3 plays pivotal roles in promoting cancer and stem cell-like features in $CD133^+$ liver cancer stem cells (CSCs) through a dysregulated JNK pathway [40], and overexpression of ANXA3 suppresses apoptosis and promotes autophagic responses via PKCd/p38 MAPK signaling in sorafenib-resistant hepatocellular carcinoma cells (HCCs) [41]. Moreover, downregulation of ANXA3 promotes the repair and healing of myocardial tissues by activating the PI3K/Akt signaling pathway [42]. Consistent with these results, we showed that knockdown of ANXA3 inhibited the proliferation and migration of microglia, while overexpression of ANXA3 resulted in opposing effects. ANXA3 is a key molecule in membrane ruffling and binds to F-actin in a Ca^{2+}-dependent manner [11], suggesting a novel function of ANXA3 in the morphological changes of microglia, which are essential for microglial migration. However, the other functions of ANXA3 in microglia remain to be elucidated.

Our study has some limitations. We only investigated the roles of ANXA3 with regard to the proliferative capacity and migration ability of microglia in vitro; the other functions of microglial ANXA3 in the CNS require further study.

5. Conclusions

This study indicates that ANXA3 may be a novel marker for the microglia of adult rats and enriches our understanding of ANXA3 in the CNS from expression patterns to physiological functions, which is vital in the field of microglial ANXA3 research.

Abbreviations

ANXA3: Annexin A3
CD11b: Cluster of differentiation 11b
Iba1: Ionized calcium-binding adaptor molecule 1
CNS: Central nervous system
CAMs: CNS-associated macrophages.

Data Availability

All data generated or analyzed during this study are included in this published article.

Ethical Approval

The Ethics Committee of the Xiangya Hospital of Central South University approved all animal experiments described in this study.

Conflicts of Interest

The authors declare that they have no competing interests.

Authors' Contributions

ZZ performed the experiments, collected and analyzed the data, and drafted the manuscript. ZZ, LZ, ZM, MD, MX, JW, and SJ performed the experiments. WZ designed the study, analyzed the data, and drafted the manuscript. WZ, QW, and QG revised the manuscript. All authors read and approved the final manuscript.

Acknowledgments

This study was supported by grants from the National Natural Science Foundation of China (81974172 and 81771206 to WZ) and the Natural Science Funds for Distinguished Young Scholar of Hunan Province (2017JJ1036 to WZ).

Supplementary Materials

The transfection efficiencies of LV-empty, LV-NC, LV-ANXA3, and LV-shANXA3 are provided in the *Supplementary material. (Supplementary Materials)*

References

[1] A. Stankov, V. Belakaposka-Srpanova, N. Bitoljanu, L. Cakar, Z. Cakar, and G. Rosoklija, "Visualisation of microglia with the use of immunohistochemical double staining method for CD-68 and Iba-1 of cerebral tissue samples in cases of brain contusions," *PRILOZI*, vol. 36, no. 2, pp. 141–145, 2015.

[2] J. Tischer, M. Krueger, W. Mueller et al., "Inhomogeneous distribution of Iba-1 characterizes microglial pathology in Alzheimer's disease," *Glia*, vol. 64, no. 9, pp. 1562–1572, 2016.

[3] G. J. Harry, "Microglia during development and aging," *Pharmacology & Therapeutics*, vol. 139, no. 3, pp. 313–326, 2013.

[4] D. Ito, Y. Imai, K. Ohsawa, K. Nakajima, Y. Fukuuchi, and S. Kohsaka, "Microglia-specific localisation of a novel calcium binding protein, Iba1," *Brain Research. Molecular Brain Research*, vol. 57, no. 1, pp. 1–9, 1998.

[5] D. G. Walker and L. F. Lue, "Immune phenotypes of microglia in human neurodegenerative disease: challenges to detecting microglial polarization in human brains," *Alzheimer's Research & Therapy*, vol. 7, no. 1, p. 56, 2015.

[6] K. E. Hopperton, D. Mohammad, M. O. Trépanier, V. Giuliano, and R. P. Bazinet, "Markers of microglia in post-mortem brain samples from patients with Alzheimer's disease: a systematic review," *Molecular Psychiatry*, vol. 23, no. 2, pp. 177–198, 2018.

[7] S. Sarkar, E. Malovic, B. Plante et al., "Rapid and refined CD11b magnetic isolation of primary microglia with enhanced purity and versatility," *Journal of Visualized Experiments*, no. 122, 2017.

[8] H. Junker, Y. Suofu, S. Venz et al., "Proteomic identification of an upregulated isoform of annexin A3 in the rat brain following reversible cerebral ischemia," *Glia*, vol. 55, no. 16, pp. 1630–1637, 2007.

[9] W. Zou, W. Xu, Z. Song et al., "Proteomic identification of an upregulated isoform of annexin A3 in the spinal cords of rats in a neuropathic pain model," *Frontiers in Neuroscience*, vol. 11, p. 484, 2017.

[10] V. Gerke and S. E. Moss, "Annexins: from structure to function," *Physiological Reviews*, vol. 82, no. 2, pp. 331–371, 2002.

[11] H. Konishi, K. Namikawa, and H. Kiyama, "Annexin III implicated in the microglial response to motor nerve injury," *Glia*, vol. 53, no. 7, pp. 723–732, 2006.

[12] Z. Zhang, M. Deng, J. Huang et al., "Microglial annexin A3 downregulation alleviates bone cancer-induced pain through inhibiting the Hif-1α/vascular endothelial growth factor signaling pathway," *Pain*, vol. 161, no. 12, pp. 2750–2762, 2020.

[13] Z. Ma, Z. Zhang, F. Bai, T. Jiang, C. Yan, and Q. Wang, "Electroacupuncture pretreatment alleviates cerebral ischemic injury through α7 nicotinic acetylcholine receptor-mediated phenotypic conversion of microglia," *Frontiers in Cellular Neuroscience*, vol. 13, p. 537, 2019.

[14] Z. Zhang, Z. Ma, W. Zou et al., "N-myc downstream-regulated gene 2 controls astrocyte morphology via rho-GTPase signaling," *Journal of Cellular Physiology*, vol. 234, no. 11, pp. 20847–20858, 2019.

[15] J. Yu, X. Li, C. Zhong et al., "High-throughput proteomics integrated with gene microarray for discovery of colorectal cancer potential biomarkers," *Oncotarget*, vol. 7, no. 46, pp. 75279–75292, 2016.

[16] T. Zhou, Y. Li, L. Yang, L. Liu, Y. Ju, and C. Li, "Silencing of ANXA3 expression by RNA interference inhibits the proliferation and invasion of breast cancer cells," *Oncology Reports*, vol. 37, no. 1, pp. 388–398, 2017.

[17] J. Huang, X. Liang, J. Wang et al., "miR-873a-5p targets A20 to facilitate morphine tolerance in mice," *Frontiers in Neuroscience*, vol. 13, p. 347, 2019.

[18] Z. Zhang, P. Qin, Y. Deng et al., "The novel estrogenic receptor GPR30 alleviates ischemic injury by inhibiting TLR4-mediated microglial inflammation," *Journal of Neuroinflammation*, vol. 15, no. 1, p. 206, 2018.

[19] Z. Zhang, Z. Ma, W. Zou et al., "The appropriate marker for astrocytes: comparing the distribution and expression of three astrocytic markers in different mouse cerebral regions," *BioMed Research International*, vol. 2019, 2019.

[20] K. Kierdorf, T. Masuda, M. J. C. Jordão, and M. Prinz, "Macrophages at CNS interfaces: ontogeny and function in health and disease," *Nature Reviews. Neuroscience*, vol. 20, no. 9, pp. 547–562, 2019.

[21] M. G. Dilshara, R. G. Jayasooriya, S. Lee, Y. H. Choi, and G. Y. Kim, "Morin downregulates nitric oxide and prostaglandin E_2 production in LPS-stimulated BV2 microglial cells by suppressing NF-κB activity and activating HO-1 induction," *Environmental Toxicology and Pharmacology*, vol. 44, pp. 62–68, 2016.

[22] L. J. Smithson and M. D. Kawaja, "Microglial/macrophage cells in mammalian olfactory nerve fascicles," *Journal of Neuroscience Research*, vol. 88, no. 4, pp. 858–865, 2010.

[23] R. Du, B. Liu, L. Zhou et al., "Downregulation of annexin A3 inhibits tumor metastasis and decreases drug resistance in breast cancer," *Cell Death & Disease*, vol. 9, no. 2, p. 126, 2018.

[24] J. L. Frost and D. P. Schafer, "Microglia: architects of the developing nervous system," *Trends in Cell Biology*, vol. 26, no. 8, pp. 587–597, 2016.

[25] I. Dalmau, J. M. Vela, B. González, B. Finsen, and B. Castellano, "Dynamics of microglia in the developing rat brain," *The Journal of Comparative Neurology*, vol. 458, no. 2, pp. 144–157, 2003.

[26] C. J. Bohlen, B. A. Friedman, B. Dejanovic, and M. Sheng, "Microglia in brain development, homeostasis, and neurodegeneration," *Annual Review of Genetics*, vol. 53, no. 1, pp. 263–288, 2019.

[27] D. W. Vaughan and A. Peters, "Neuroglial cells in the cerebral cortex of rats from young adulthood to old age: an electron microscope study," *Journal of Neurocytology*, vol. 3, no. 4, pp. 405–429, 1974.

[28] T. Samorajski, "How the human brain responds to aging," *Journal of the American Geriatrics Society*, vol. 24, no. 1, pp. 4–11, 1976.

[29] A. Schuitemaker, T. F. van der Doef, R. Boellaard et al., "Microglial activation in healthy aging," *Neurobiology of Aging*, vol. 33, no. 6, pp. 1067–1072, 2012.

[30] S. L. Valles, A. Iradi, M. Aldasoro et al., "Function of glia in aging and the brain diseases," *International Journal of Medical Sciences*, vol. 16, no. 11, pp. 1473–1479, 2019.

[31] M. G. Frank, R. M. Barrientos, J. C. Biedenkapp, J. W. Rudy, L. R. Watkins, and S. F. Maier, "mRNA up-regulation of MHC II and pivotal pro-inflammatory genes in normal brain aging," *Neurobiology of Aging*, vol. 27, no. 5, pp. 717–722, 2006.

[32] M. Letiembre, W. Hao, Y. Liu et al., "Innate immune receptor expression in normal brain aging," *Neuroscience*, vol. 146, no. 1, pp. 248–254, 2007.

[33] K. Ogura, M. Ogawa, and M. Yoshida, "Effects of ageing on microglia in the normal rat brain: immunohistochemical observations," *Neuroreport*, vol. 5, no. 10, pp. 1224–1226, 1994.

[34] V. H. Perry, M. K. Matyszak, and S. Fearn, "Altered antigen expression of microglia in the aged rodent CNS," *Glia*, vol. 7, no. 1, pp. 60–67, 1993.

[35] M. Olah, K. Biber, J. Vinet, and H. WGM Boddeke, "Microglia phenotype diversity," *CNS & Neurological Disorders Drug Targets*, vol. 10, no. 1, pp. 108–118, 2011.

[36] C. Kaur and E. A. Ling, "Study of the transformation of amoeboid microglial cells into microglia labelled with the isolectin Griffonia simplicifolia in postnatal rats," *Acta Anatomica (Basel)*, vol. 142, no. 2, pp. 118–125, 1991.

[37] R. Weitzdorfer, H. Hoger, K. S. Shim, L. Cekici, A. Pollak, and G. Lubec, "Changes of hippocampal signaling protein levels during postnatal brain development in the rat," *Hippocampus*, vol. 18, no. 8, pp. 807–813, 2008.

[38] T. L. Tay, J. C. Savage, C. W. Hui, K. Bisht, and M. Tremblay, "Microglia across the lifespan: from origin to function in brain development, plasticity and cognition," *The Journal of Physiology*, vol. 595, no. 6, pp. 1929–1945, 2017.

[39] N. Wu, S. Liu, C. Guo, Z. Hou, and M. Z. Sun, "The role of annexin A3 playing in cancers," *Clinical & Translational Oncology*, vol. 15, no. 2, pp. 106–110, 2013.

[40] M. Tong, T. M. Fung, S. T. Luk et al., "ANXA3/JNK signaling promotes self-renewal and tumor growth, and its blockade provides a therapeutic target for hepatocellular carcinoma," *Stem Cell Reports*, vol. 5, no. 1, pp. 45–59, 2015.

[41] M. Tong, N. Che, L. Zhou et al., "Efficacy of annexin A3 blockade in sensitizing hepatocellular carcinoma to sorafenib and regorafenib," *Journal of Hepatology*, vol. 69, no. 4, pp. 826–839, 2018.

[42] H. Meng, Y. Zhang, S. T. An, and Y. Chen, "Annexin A3 gene silencing promotes myocardial cell repair through activation of the PI3K/Akt signaling pathway in rats with acute myocardial infarction," *Journal of Cellular Physiology*, vol. 234, no. 7, pp. 10535–10546, 2019.

Hindawi
Neural Plasticity
Volume 2021, Article ID 9924639, 12 pages
https://doi.org/10.1155/2021/9924639

Review Article

The Efficacy and Predictors of Using GPi-DBS to Treat Early-Onset Dystonia: An Individual Patient Analysis

Wenxiu Chen,[1,2] **Houyou Fan**,[1,2] **and Guohui Lu**[1]

[1]*Department of Neurosurgery, The First Affiliated Hospital of Nanchang University, Nanchang, Jiangxi, China*
[2]*The First Clinical Medical College of Nanchang University, Nanchang, Jiangxi, China*

Correspondence should be addressed to Guohui Lu; guohui-lu@163.com

Received 13 March 2021; Accepted 21 April 2021; Published 7 May 2021

Academic Editor: Fushun Wang

Objective. To compare the efficacy in patients with different genotypes, identify the potential predictive factors, and summarize the complications of globus pallidus deep brain stimulation (GPi-DBS) treating early-onset dystonia. *Methods*. Three electronic databases (PubMed, Embase, and Cochrane databases) were searched with no publication data restriction. The primary outcomes were the improvements in Burke–Fahn–Marsden Dystonia Rating Scale motor (BFMDRS-M) and disability (BFMDRS-D) score. Pearson's correlation coefficients and a metaregression analysis were used to identify the potential predictive factors. This article was registered in Prospero (CRD42020188527). *Results*. Fifty-four studies (231 patients) were included. Patients showed significant improvement rate in BFMDRS-M (60.6%, $p < 0.001$) and BFMDRS-D (57.5%, $p < 0.001$) scores after treatment with GPi-DBS. BFMDRS-M score improved greater in the DYT-1-positive ($p = 0.001$) and DYT-11-positive ($p = 0.008$) patients compared to DYT-6-positive patients. BFMDRS-D score improved greater in the DYT-11 (+) compared to DYT-6 (+) patients ($p = 0.010$). The relative change of BFMDRS-M ($p = 0.002$) and BFMDRS-D ($p = 0.010$) scores was negatively correlated with preoperative BFMDRS-M score. In the metaregression analysis, the best predictive model showed that preoperative BFMDRS-M, disease duration ($p = 0.047$), and the age at symptom onset ($p = 0.027$) were important. *Conclusion*. Patients with early-onset dystonia have a significant effect after GPi-DBS treatment, and DYT-1 (+) and DYT-11 (+) patients are better candidates for GPi-DBS. Lower preoperative score, later age of onset, and an earlier age at surgery probably predict better clinical outcomes.

1. Background

Early-onset dystonia is one type of dystonia, characterized by onset age ≤ 26, often presents with the onset of lower or upper limb symptoms, and progresses to other parts of the body [1]. According to the existing literature, early-onset dystonia is highly correlated with genetic mutations, mainly including DYT-1, DYT-6, DYT-11, and DYT-28 [2].

DYT-1 (+) patients present onset symptoms in childhood or adolescence, typically with dystonia of a single limb that often spreads within 1-3 years to involve all four limbs [3, 4]. The onset age of DYT-6 (+) patients is also during childhood and adolescence, but more than half of patients started onset symptoms earlier than adolescence. Approximately 25% of DYT-6 (+) patients present with cervical dystonia [5]. Patients with DYT-11 genotype present with myoclonus, dystonia, or both, but most patients present with myoclonus in childhood or adolescence [6, 7]. The patients with DYT-28 (+) are registered as an early-onset generalized dystonia with age at onset of symptoms generally between 4 and 6 years old [8].

Clinically, many methods are used to treat dystonia, such as drug therapy, endotoxin injection, and thalamotomy [9, 10]. But for chronic and refractory dystonia, deep brain stimulation (DBS) is the most effective and safe method [11, 12]. Many researches have shown that the globus pallidus DBS (GPi-DBS) is effective for DYT-1 (+) [13] and DYT-11 (+) early-onset dystonia [14]. But for DYT-6 (+) and DYT-28 (+), further research is still needed to identify the efficacy of GPi-DBS [15, 16]. What is more, no literature has reported on whether there are differences in the efficacy of GPi-DBS treating different genotypes of early-

onset dystonia as well as the rate of response and complications. The surgery indications and predictive factors of GPi-DBS treating early-onset dystonia are also not clearly stated in the clinical guidelines.

Therefore, we conducted an individual patient data meta-analysis of all published studies to explore the efficacy, predictors, and complications of GPi-DBS treating early-onset dystonia.

2. Methods

2.1. Search Strategy. The Preferred Reporting Items for Systematic Reviews and Meta-Analysis (PRISMA) guidelines were followed when we were searching literatures. The keywords "early-onset dystonia," "child-onset dystonia," "childhood onset dystonia," "DYT-TOR1A," "DYT-1," "DYT-THAP1," "DYT-6," "DYT-SGCE," "DYT-11," "DYT-KMT2B," "DYT-28," and "deep brain stimulation" were searched in the PubMed, Embase, and Cochrane Central Register of Controlled Trials and Cochrane Movement Disorders Group Trials Register. Two reviewers (CWX and FHY) independently scanned the titles and abstracts and then reviewed the full texts.

2.2. Inclusion and Exclusion Criteria. The inclusion criteria for publications were as follows: (1) baseline characteristics of patients (gender, age at symptom onset, operating age, basic dystonia movement score, and disability); (2) surgical operation (DBS target, stimulation settings, and microelectrode recording (MER)); and (3) outcomes (motor and disability scores of the Burke–Fahn–Marsden Dystonia Rating Scale (BFMDRS-M, BFMDRS-D), follow-up time, and complications mentioned in the article). The collated data are listed in Supplementary Table S1. The published evidence was evaluated following the Oxford Centre for Evidence-based Medicine (OCEBM) Levels of Evidence [17].

Studies were excluded for the following reasons: (1) other surgeries, like thalamotomy, were conducted; (2) other nuclei were targeted; (3) patients have been reported elsewhere; (4) studies were conference articles, letters, or editions.

2.3. Data Extraction. Available data of all patients were extracted. All randomized clinical trials, case series, case reports, and case-control studies that reported demographics, surgery, and outcome data of patients with early-onset dystonia who underwent GPi-DBS surgery were taken into consideration. There were no restrictions on the release date, release status, and language. We searched Medline and browsed reference lists of articles and assessed the research based on these articles. The year of publication, author's name, demographics, and result data were juxtaposed to exclude duplicate patients. Therefore, the data extraction table was gradually developed, piloted, and improved.

2.4. Genotyping. Early-onset dystonia is generally associated with one single genetic mutation, including DYT-1, DYT-6, DYT-11, and DYT-28. DYT-11 (+) and DYT-28 (+) dystonias are both syndromes, which are considered combining dystonia with additional symptoms. DYT-11 (+) is accompanied by myoclonus, while DYT-28 (+) is accompanied by intellectual disability and infantile deformity. Due to insufficient data, DYT-28 (+) was excluded in the comparisons. When the patient's genetic confirmation was not mentioned, only patients with specific diagnosis of dystonia and whose age of onset meets the criteria were included in the early onset of unknown dystonia.

2.5. Analysis Strategy. In order to perform a statistical analysis of the results of the severity of dystonia, the effective changes in the BFMDRS-M and BFMDRS-D were included. Values were extracted using Get Data Graph Digitizer when data were displayed only by graph. The data of demographic characteristics and basic dystonia score are all sorted out and got two characteristic statistical indicators: mean and median. In the BFMDRS scoring system, higher scores indicate more severe diseases, and the relative change rates are calculated with the following algorithm: preoperative scores are divided by the difference between preoperative and postoperative scores [18].

2.6. Statistical Analysis. A paired Student t test was performed to compare baseline (0 months) with the score in different time categories after surgery (0 to ≤6, >6 to ≤12, >12 to ≤24, >24 to ≤36, and >36 months). The relative changes in postoperative BFMDRS-M and BFMDRS-D versus baseline data represented the primary results. We compared the relative change rates between different genotypes of early-onset dystonia using two independent-samples t test [19]. To determine potential predictive factors, Pearson's correlation coefficients and a stepwise multivariate regression analysis were performed between the relative change rates of BFMDRS-M or BFMDRS-D and different predictive factors, including symptom onset (years), course of disease (years), age of surgery (years), MER, follow-up period (months), and preoperative BFMDRS score. Secondary outcomes were the complication rate. Furthermore, since most of the patients were followed up under 3 years, a restriction on the follow-up time of 3 years was set up. Then, we reperformed the same statistical analyses. The statistically significant definition standard is $p \leq 0.05$ [20]. We used SPSS 25.0 (IBM, Armonk, NY) to calculate statistics. When no obvious abnormality was found, Student's t test was used after the comprehensive normality test of D'Agostino and Pearson [21].

3. Results

3.1. Search Results. Among the 366 studies, 54 studies were screened out from the inclusion and exclusion criteria, and the data were extracted (Figure 1). A sample size of 231 patients was distributed into DYT-1 ($n = 101$), DYT-6 ($n = 27$), and DYT-11 ($n = 32$) mutations. Specific documents and data are placed in Supplementary Table S1. All the 54 studies were qualified as level 4 evidence based on the OCEBM.

3.2. Demographics. DYT-1 (+) patients ($n = 101$) largely outnumbered DYT-6 (+) ($n = 27$) and DYT-11 (+) ($n = 32$) patients. The dystonia genotype could not be determined for 71 patients. Table 1 summarizes the demographic

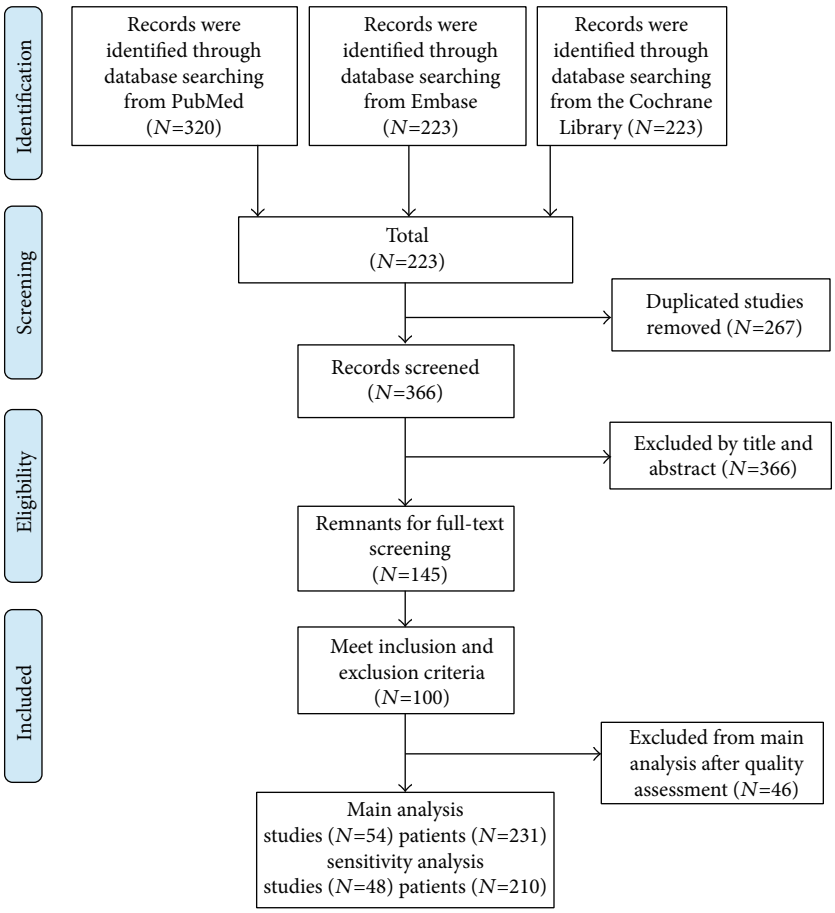

Figure 1: Flow diagram based on PRISMA statement (https://www.prisma-statement.org).

characteristics and basic dystonia score. The mean (range) age at onset of all the 231 patients (110 males, 98 females, and 26 unknown) was 8.9 (0–25) years. Their age at surgery was 24.3 (5.3–72) years, with a disease duration of 15.4 (0.5–66) years. There were no significant differences in the composition of gender, age at symptom onset, age at surgery, and disease duration between DYT-1 (+) and DYT-6 (+). The results of this statistical analysis were the same between DYT-11 (+) and DYT-6 (+), while there existed differences in the duration of the disease. As for DYT-11 (+) and DYT-1 (+), there were no significant differences in the composition of gender and age at symptom onset, but the age at surgery and disease duration between them were of obvious difference.

Baseline data for the three-year follow-up period are shown in Table 2. The disease duration among DYT-6 (+) and DYT-11 (+) was of no significant difference in the three-year follow-up. All the other results of baseline during the three-year follow-up were the same as those at the unrestricted time.

3.3. Surgery Programming and Microelectrode Recordings. All patients underwent bilateral surgery, and all the DBS targets of the extracted article data were GPi. 120 patients used MER. In general, the GPi-DBS amplitudes on the right ranged from 0.5 to 5.6 V (mean of 2.8 V), and the GPi-DBS amplitudes on the left ranged from 0.5 to 4.5 V (mean of 2.7 V) with a frequency bilaterally ranging between 60 and 451 Hz (median of 124.5 Hz). The mean programmed pulse width for the right and left was 155.4 microseconds and 152.4 microseconds, respectively. The bilateral stimulus parameters of DYT-6 (+) were consistent, and all the bilateral frequency stimuli parameters of the early-onset muscle tension disorder were consistent. Half of the patients used microelectrodes.

3.4. The BFMDRS-M and BFMDRS-D Changes at the Five Follow-Up Times. The median follow-up time reported after GPi-DBS was 12 months (1-196 months), and the length of follow-up for patients in the DYT-6 (+) group was longer than that for patients in the DYT-11 (+) group (2-196 months vs. 1-20 months, respectively; $p = 0.003$). The length of follow-up for the patients in the DYT-6 (+) group was longer than that for the patients in DYT-1 (+) group (2-196 months vs. 1-102 months, respectively; $p = 0.01$). Considering the follow-up times showed obvious heterogeneity, the BFMDRS-M and BFMDRS-D were divided into five follow-up time groups as follows: 0 to ≤6, >6 to ≤12, >12 to ≤24, >24 to ≤36, and >36 months. Table 3 shows that, during the 0- to ≤6-, >6- to ≤12-, >12- to ≤24-, >24- to ≤36-, and >36-month time categories, the BFMDRS-M scores were 23.6 ± 24.9 (0–94.5, $n = 97$), 17.1 ± 17.9 (0–72.0, $n = 91$), 23.4 ± 23.0 (0–83.0, $n = 61$), 21.6 ± 16.7 (0–51.0, $n = 25$),

Table 1: Demographic characteristic, baseline dystonia severity, and programming parameters.

	All patients ($n = 231$)	DYT-6 ($n = 27$)	DYT-11 ($n = 32$)	DYT-1 ($n = 101$)	Unknown ($n = 71$)	DYT-6 and DYT-11	DYT-6 and DYT-1	DYT-11 and DYT-1
Male/female/unknown	110/98/26	16/11/0	15/15/2	43/50/8	36/22/13	0.263	0.075	0.640
Age at symptom onset (years), mean/median (range)	8.9/8 (0-25)	9.4/8 (3-25)	7.7/5.5 (0.5-25)	9.1/8 (1-24)	8.9/8 (0-25)	0.277	0.752	0.254
Age at surgery (years), mean/median (range)	24.3/19 (5.3-72)	22.8/20 (8-48)	29.5/27.5 (8-72)	21.5/17 (5.3-65.5)	26.4/22 (7-64)	0.065	0.626	**0.005**
Disease duration before surgery (years), mean/median (range)	15.4/11 (0.5-66)	13.4/11 (2-39)	21.7/18.3 (2-66)	12.4/7 (1-56.5)	17.5/12 (0.5-58)	**0.015**	0.670	**≤0.001**
Intraoperative microelectrode recording used (yes/no/not reported)	120/21/93	10/4/13	13/3/16	59/7/35	38/7/29	0.960	0.079	0.084
Baseline BFMDRS-M (/120), mean/median (range)	49.3/47.5 (4-130)	49.5/44 (16-89)	23.9/18.8 (4-75)	49.8/50 (16.5-107)	58.9/58 (11-130)	**≤0.001**	0.941	**≤0.001**
Postoperative BFMDRS-M (/120), mean/median (range)	20.9/14 (0-94.5)	24.7/18 (3-69.6)	7.0/5 (0-21.5)	15.4/9 (0-94.5)	33.5/33 (0-87)	**≤0.001**	**0.027**	**≤0.001**
Mean change rate (%) of BFMDRS-M (range)	60.6 (-33.8-100)	52.0 (-2.5-92.7)	68.7 (13.2-100)	71.8 (4.1-100)	44.4 (-33.8-100)	**0.008**	**0.001**	0.545
Baseline BFMDRS-D (/30), mean/median (range)	14.7/14 (3-30)	11.2/9.5 (3-21)	8.7/7.5 (5-18)	15.7/14.5 (6-29)	17.8/18 (7-30)	0.458	0.199	**≤0.001**
Postoperative BFMDRS-D (/30), mean/median (range)	6.9/4 (0-29)	6.2/4.5 (1-18)	1.8/2 (0-6)	6.1/4 (0-25)	11.3/10 (2-29)	0.150	0.976	**0.001**
Mean change rate (%) of BFMDRS-D (range)	57.5 (0-100)	46.7 (14.3-88.9)	78.3 (25-100)	63.1 (0-100)	38.9 (0-86.7)	**0.010**	0.230	0.086
Length of follow-up (months), median (range)	12 (1-196)	13 (2-196)	9 (1-20)	12 (1-102)	12 (5-50)	**0.003**	**0.010**	0.061
Mean DBS programming parameters±SD	$N = 98$	$N = 9$	$N = 12$	$N = 42$	$N = 35$			
Voltage(V) Rt	2.8 ± 1.1	2.9 ± 0.7	3.2 ± 0.9	2.8 ± 1.2	2.6 ± 1.3	0.498	0.700	0.326
Voltage(V) Lt	2.7 ± 1.1	2.9 ± 0.7	3.0 ± 0.9	2.8 ± 1.2	2.5 ± 1.1	0.819	0.659	0.493
PW (μs) Rt	155.4 ± 128.6	143.3 ± 118.8	126.9 ± 116.2	212.1 ± 159.4	100.3 ± 37.8	0.755	0.161	0.052
PW (μs) Lt	152.4 ± 128.8	143.3 ± 118.8	126.9 ± 116.2	207.9 ± 162.1	96.9 ± 27.3	0.755	0.188	0.065
Frequency (Hz) Rt	124.5 ± 27.9	128.6 ± 33.3	121.7 ± 32.4	118.2 ± 30.2	132 ± 20.1	0.639	0.363	0.732
Frequency (Hz) Lt	124.5 ± 27.9	128.6 ± 33.3	121.7 ± 32.4	118.2 ± 30.2	132 ± 20.1	0.639	0.363	0.732

BFMDRS-M: Burke–Fahn–Marsden Dystonia Rating Scale-movement component; BFMDRS-D: Burke–Fahn–Marsden Dystonia Rating Scale-disability component.

Table 2: Demographic characteristic and baseline dystonia severity in 3 y follow-up.

	All patients ($n = 210$)	DYT-6 ($n = 20$)	DYT-11 ($n = 32$)	DYT-1 ($n = 91$)	Unknown ($n = 67$)	DYT-6 and DYT-11	DYT-6 and DYT-1	DYT-11 and DYT-1
Male/female/unknown	105/79/26	13/7/0	15/15/2	42/41/8	35/16/16	0.163	0.086	0.850
Age at symptom onset (years), mean/median (range)	8.9/8 (0-25)	10.1/9 (3-25)	7.7/5.5 (0.5-25)	9.1/8 (1-24)	8.7/8 (0-25)	0.187	0.365	0.259
Age at surgery (years), mean/median (range)	23.8/18.8 (5.3-72)	25.2/23 (8-48)	29.5/27.5 (8-72)	20.8/17 (5.3-65.5)	24.8/18.4 (7-63)	0.284	0.159	**0.002**
Disease duration before surgery (years), mean/median (range)	14.9/10 (0.5-66)	15.1/12.5 (2-39)	21.7/18.3 (2-66)	11.6/7 (1-56.5)	16/9 (0.5-58)	0.087	0.220	**≤0.001**
Intraoperative microelectrode recording used (yes/no/not reported)	118/21/71	10/4/6	13/3/16	57/7/27	38/7/22	0.634	0.468	0.892
Baseline BFMDRS-M (/120), mean/median (range)	49.4/48 (4-130)	48/42.5 (16-89)	23.9/18.75 (4-75)	49.8/50 (16.5-107)	59.5/58 (11-130)	**≤0.001**	0.582	**≤0.001**
Postoperative BFMDRS-M (/120), mean/median (range)	21.1/13 (0-94.5)	22.1/16.25 (1-69.6)	6.8/4 (0-21.5)	16.3/10 (0-94.5)	34.2/33.5 (0-87)	**0.002**	0.235	**≤0.001**
Mean change rate (%) of BFMDRS-M (range)	60.9 (-33.8-100)	55.6 (19.5-97.6)	69.8 (13.2-100)	71.2 (4.1-100)	44.2 (-33.8-100)	**0.032**	**0.017**	0.790
Baseline BFMDRS-D (/30), mean/median (range)	14.8/14 (3-30)	11.4/9 (3-21)	8.7/7.5 (5-18)	15.7/14.5 (6-29)	17.9/18 (7-30)	0.507	0.202	**≤0.001**
Postoperative BFMDRS-D (/30), mean/median (range)	7.0/4 (0-29)	6.2/3 (1-18)	1.8/2 (0-6)	6.4/4.5 (0-25)	11.5/10 (2-29)	0.234	0.961	**≤0.001**
Mean change rate (%) of BFMDRS-D (range)	57.1 (0-100)	47.9 (14.3-88.9)	78.3 (25-100)	61.9 (0-100)	37.9 (0-86.7)	**0.023**	0.343	0.061
Length of follow-up (months), median (range)	12 (1-36)	6.5 (2-36)	9 (1-20)	12 (1-36)	9 (5-36)	0.557	0.363	0.056

BFMDRS-M: Burke–Fahn–Marsden Dystonia Rating Scale-movement component; BFMDRS-D: Burke–Fahn–Marsden Dystonia Rating Scale-disability component.

Table 3: Clinical outcomes in different time categories.

Time category (months)	Mean BFMDRS-M score	Improvement (%) in BFMDRS-M score	p value	Mean BFMDRS-D score	Improvement (%) in BFMDRS-D score	p value
>0 and ≤6	23.6 ± 24.9 (0-94.5)	57	**≤0.001**	8.9 ± 8.5 (0-29)	52.5	**≤0.001**
>6 and ≤12	17.1 ± 17.9 (0-72)	67	**≤0.001**	5.7 ± 6.4 (0-29)	62.6	**≤0.001**
>12 and ≤24	23.4 ± 23 (0-83)	57.8	**≤0.001**	8.8 ± 8.2 (0-29)	48.2	**≤0.001**
>24 and ≤36	21.6 ± 16.7 (0-51)	50.1	**≤0.001**	5.8 ± 5.4 (0-17)	61.2	**0.001**
>36	24.5 ± 19.7 (0-75)	50.8	**≤0.001**	7.4 ± 5.9 (0-20)	55.2	**≤0.001**

The improvement of BFMDRS-M(D) = (Preoperative scores − Postoperative scores)/Preoperative scores.

and 24.5 ± 19.7 (0–75.0, $n = 37$), respectively, and the mean relative change rates of BFMDRS-M were 57%, 67%, 57.8%, 50.15%, and 50.8% compared to the preoperative score, respectively ($p \leq 0.001$ for all follow-up time categories). In conclusion, the BFMDRS motor scores were significantly improved by GPi-DBS compared to the preoperative scores at the last follow-up (49.3 ± 24.5 vs. 20.9 ± 21.4, $p < 0.001$).

Regarding the BFMDRS-D score ($n = 84$), GPi-DBS showed a significant improvement over baseline at the last follow-up (14.8 ± 7.0 vs. 7.0 ± 7.0, $p < 0.001$). The average BFMDRS-D scores for 0- to ≤6-, >6- to ≤12-, >12- to ≤24-, >24- to ≤36-, and >36-month time periods were 8.9 ± 8.5 (0–29, $n = 33$), 5.7 ± 6.4 (0–29, $n = 51$), 8.8 ± 8.2 (0–29, $n = 24$), 5.8 ± 5.4 (0–17, $n = 12$), and 7.4 ± 5.9 (0–20, $n = 21$), respectively, and the corresponding mean relative change rates of BFMDRS-D were 52.5%, 62.6%, 48.2%, 61.2%, and 55.2% compared to the preoperative scores, respectively ($p \leq 0.001$ for all follow-up time categories).

3.5. Subgroup Analysis between Different Genotypes of Early-Onset Dystonia. The results showed that there were significant differences in the BFMDRS-M preoperative and postoperative scores between the DYT-6 (+) and DYT-11 (+) groups (49.5 vs. 23.9, $p < 0.001$, for preoperative scores and 24.7 vs. 7.0, $p < 0.001$, for postoperative scores, respectively), with significant differences in the mean improvement (52% vs. 68.7%, $p = 0.008$). The improvement rates in the BFMDRS-M score for the DYT-6 (+) and DYT-1 (+) groups were 52.0% and 71.8% ($p = 0.001$), respectively, and the postoperative BFMDRS-M scores were significantly different between the DYT-6 (+) and DYT-1 (+) groups (49.5 vs. 15.4, $p = 0.027$). However, there was no significant difference in the improvement rate of BFMDRS-M score between the DYT-1 (+) and DYT-11 (+) groups (68.7% vs. 71.8%, $p = 0.545$). With regard to the BFMDRS-D score, there was difference in the improvement rate between the DYT-6 (+) and DYT-11 (+) groups (46.7% vs. 78.3%, $p = 0.010$). Although no significant difference was found after comparison, the improvement rates of BFMDRS-D scores in the DYT-11 (+) and DYT-1 (+) groups were 78.3% and 63.1% ($p = 0.086$), respectively, and 78.3% and 46.7% ($p = 0.230$) in the DYT-1 (+) and DYT-6 (+) groups, respectively.

3.6. Follow-Up and Result with a Limited Follow-Up Time of 3 Years. A longer length of follow-up was considered ≥36 months. However, due to the different follow-up times for each genotype, we extracted data for a three-year follow-up period to remove significant heterogeneity among follow-up lengths. The average follow-up time after surgery was 12 months (range of 1–36 months). There was no difference in the results regarding the improvement rate. The postoperative BFMDRS-M scores of the DYT-6 (+) and DYT-1 (+) groups were not significantly different (22.1 vs. 16.3, $p = 0.235$), which was different from the undefined follow-up time.

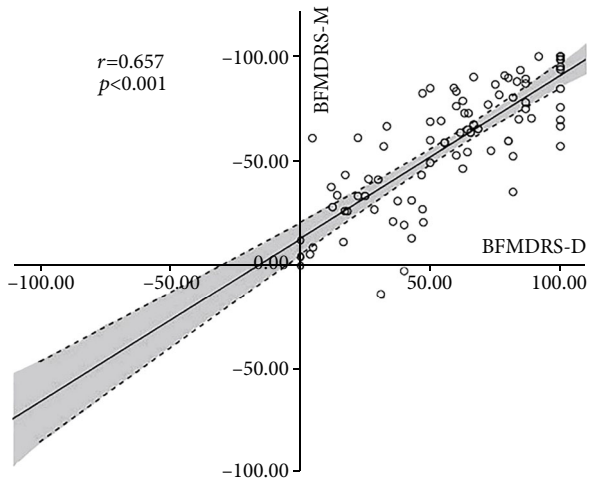

Figure 2: Correlation between relative improvement (%) in BFMDRS-M and BFMDRS-D at the last follow-up visit. There is a positive linear correlation between the relative improvement of BFMDRS-M and BFMDRS-D (Pearson $r = 0.657$, $p < 0.001$). Dots: individual patient values; black solid line: linear regression line; area between the dotted lines: 95% confidence interval; BFMDRS: Burke–Fahn–Marsden Dystonia Rating Scale; BFMDRS-D: BFMDRS disability subscale; BFMDRS-M: BFMDRS movement subscale.

3.7. Correlation and Metaregression Analysis. The relative changes of BFMDRS-D and BFMDRS-M after surgery had a good correlation (Pearson $r = 0.657$, $p < 0.001$; Figure 2). In general, the decrease in BFMDRS-M score was accompanied by a decrease in BFMDRS-D score. In addition, to determine outcome predictors, the relationship between various preoperative variables and the decrease of BFMDRS-M at 3 years after surgery was tested, or there was no follow-up restriction. Each demographical and clinical factor was tested separately. A summarized scatter plot showing the results of each factor is provided in Figure 3. The relative change rates in BFMDRS-M were negatively correlated with preoperative

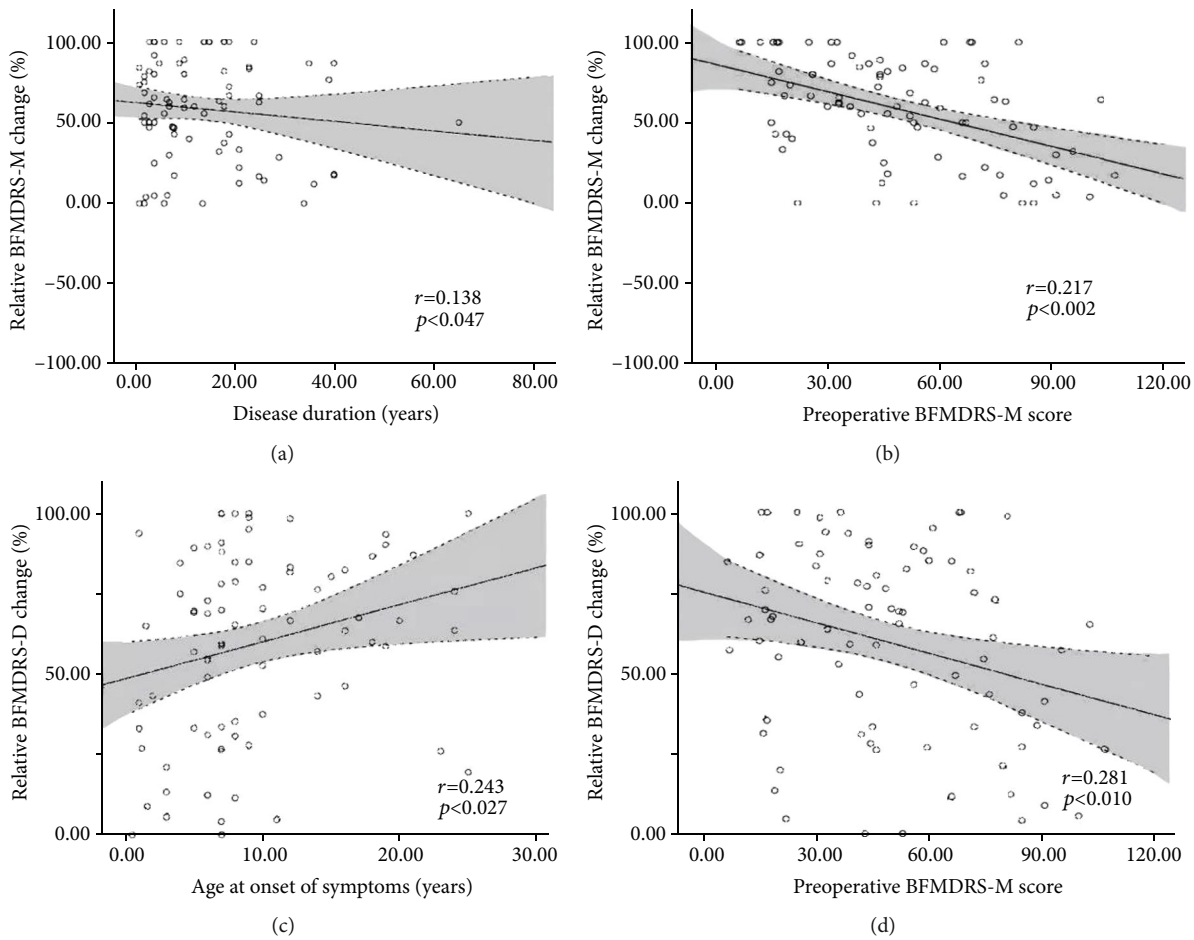

Figure 3: Potential predictive factors for relative improvement (%) in BFMDRS-M and BFMDRS-D under 3 years of follow-up visit. There were significant positive correlations between (a) disease duration and the relative improvement (%) in BFMDRS-M (Pearson $r = -0.138$, $p = 0.047$), (b) preoperative BFMDRS-M score ($r = -0.217$, $p = 0.002$) and the relative improvement (%) in BFMDRS-M, (c) age at onset ($r = 0.243$, $p = 0.027$) and the relative improvement (%) in BFMDRS-D, and (d) preoperative BFMDRS-M score ($r = -0.281$, $p = 0.010$) and the relative improvement (%) in BFMDRS-D. Dots: individual patient values; black solid line: linear regression line; area between the dotted lines: 95% confidence interval; BFMDRS: Burke–Fahn–Marsden Dystonia Rating Scale; BFMDRS-D: BFMDRS disability subscale; BFMDRS-M: BFMDRS movement subscale.

BFMDRS-M score ($r = -0.217$, $p = 0.002$) and disease duration (years) ($r = -0.138$, $p = 0.047$) during the 3-year follow-up period. In addition, the relative change rates in BFMDRS-D were positively correlated with preoperative BFMDRS-M score ($r = -0.281$, $p = 0.010$) and age at symptom onset ($r = 0.243$, $p = 0.027$) during the 3-year follow-up period. When no follow-up restrictions were set up, the relative change rates of BFMDRS-M were negatively correlated with the preoperative BFMDRS-M score ($r = -0.205$, $p = 0.002$). The relative change rates in BFMDRS-D were only positively correlated with age at symptom onset ($r = 0.232$, $p = 0.027$), whereas the association with age at surgery, course of disease, and follow-up period did not reach significance (Table 4).

Furthermore, stepwise multivariable regression analysis was performed to verify the possible predictors, and percent improvement (%) of BFMDRS-M was defined as dependent variable; age at onset, duration of surgery, duration of follow-up, and BFMDRS-M at baseline were included as independent variables. The best predictive model contained preoperative scores of BFMDRS-M ($\beta = -0.280$, $p \leq 0.001$) and disease duration ($\beta = -0.359$, $p = 0.014$). As for BFMDRS-D score, independent variables were the same as BFMDRS-M and percent improvement (%) of BFMDRS-D was defined as dependent variable. The best predictive model contained only the preoperative scores of BFMDRS-M ($\beta = -0.318$, $p = 0.010$).

3.8. Complications. The adverse events are summarized in Table 5. Complications were described in 34 of 231 patients according to the published follow-up reports (4 DYT-6 (+) patients, 9 DYT-11 (+) patients, 11 DYT-1 (+) patients, and 10 unknown-genotype early-onset dystonia patients). During the follow-up period of the 34 patients who had complications, one died from suicide but had no depression, three had depression but had no suicidal tendency, seven had microinfection, 14 had a hardware infection, six had persistent dystonia or showed an improvement, and two had electrode displacement. With regard to the left mesa lateral cranium (by 4.5 cm) 11 months after surgery, two cases

Table 4: Relationship between several factors and relative improvement (%) in BFMDRS.

Patient number	Follow-up period in 3 years		At the last follow-up	
	Improvement (%) in BMFDRS-M ($n = 209$)	Improvement (%) in BMFDRS-D ($n = 83$)	Improvement (%) in BMFDRS-M ($n = 231$)	Improvement (%) in BMFDRS-D ($n = 91$)
Age at onset of symptoms (years)	$r = 0.068$ $p = 0.327$	**$r = 0.243$** **$p = 0.027$**	$r = 0.083$ $p = 0.208$	**$r = 0.232$** **$p = 0.027$**
Age at surgery (years)	$r = -0.102$ $p = 0.143$	$r = 0.088$ $p = 0.427$	$r = -0.082$ $p = 0.212$	$r = 0.118$ $p = 0.264$
Disease duration (years)	**$r = -0.138$** **$p = 0.047$**	$r = -0.021$ $p = 0.851$	$r = -0.123$ $p = 0.063$	$r = 0.020$ $p = 0.854$
Follow-up period (months)	$r = -0.059$ $p = 0.396$	$r = -0.048$ $p = 0.668$	$r = -0.026$ $p = 0.697$	$r = -0.075$ $p = 0.478$
Preoperative BFMDRS-M score	**$r = -0.217$** **$p = 0.002$**	**$r = -0.281$** **$p = 0.010$**	**$r = -0.205$** **$p = 0.002$**	$r = -0.192$ $p = 0.068$

Disease duration refers to the time from the onset to the operative treatment.

Table 5: Frequency of complications following DBS for early-onset dystonia.

At the last follow-up	
Death	1
Surgical infection (electrode infection ($n = 2$), battery infection ($n = 1$), and device infection ($n = 4$))	7
Hardware failure (electrode ($n = 1$), electrode misplacement ($n = 2$), lead fracture ($n = 2$), and internal pulse generators switched off ($n = 9$))	14
Continued worsening of dystonia	6
Unimproved	2
Depression	3
Having complex partial seizures	1

showed a lead fracture, and one case showed complex partial fractures. In the case of hardware failures, IPG switched off occurred in 9 patients. These complications generally occurred after one year. Most of the complications due to hardware failure occurred in the DYT-1 (+) group.

4. Discussion

We extracted all available data from various publications on patients with early-onset dystonia treated with DBS based on individual patient-level data and meta-analysis. We confirmed that GPi-DBS not only has a beneficial effect on motor and disability results in the treatment of early-onset dystonia but also has obtained a remarkable effect. Shorter disease course and lower BFMDRS-M score are related to a better outcome. Differential improvement was observed in DYT-1, DYT-6, DYT-11, and unknown genotype, and it was positively affected by a lower BFMDRS-M score (DYT-6 (+) effect was lower than DYT-1 (+)) and older age at symptom onset (DYT-11 (+), which was opposite of DYT-6 (+)). Our results suggested that the different genotypes of dystonia may contribute to the effect of disease duration on the outcome of GPi-DBS. For example, DYT-1 and DYT-11 carriers obtained more effective results compared to the other genotypes.

4.1. Target of DBS. The thalamic ventralis intermedius nucleus (Vim) is the initial described target of DBS, which is a valid treatment for refractory dystonia, but the GPi takes the place of it quickly [22]. Afterwards, the subthalamic nucleus (STN) was also proved to be a target structure for the treatment of dystonia [23]. As for early-onset dystonia, the STN DBS target was proved to be well tolerated with minor and transient adverse effects [24]. At the same time, in refractory generalized and segmental dystonia, GPi-DBS is a safe and reliable treatment option [25] and it is often applied to hereditary dystonia. Besides, the target of most of the published literature on the remedy of early-onset dystonia is GPi. Therefore, our study discussed the bilateral GPi-DBS treating early-onset dystonia.

4.2. Comparison of BFMDRS-M among Different Genotypes of Early-Onset Dystonia. For movement symptom severity, GPi-DBS was more effective in DYT-1 (+) and DYT-11 (+) patients compared to DYT-6 (+) patients. Moreover, the change rate of BFMDRS-M between DYT-1 (+) and DYT-11 (+) patients was not significantly different on account of many studies have confirmed that GPi-DBS has significant improvement and certain safety for DYT-1 (+) patients and on DYT-11 (+) syndrome [7, 13, 26–30]. Considering the treatment effect is affected by the time after surgery, we set a restriction of 3 years for follow-up time. After reanalysis, the data reprocessing showed the same results that strengthens our trust in the analysis results. The lack of significant difference in the postoperative BFMDRS-M scores may be due to the unpredictable effect of GPi-DBS on DYT-6 (+) patients compared to DYT-1 (+) and DYT-11 (+) patients [31]. Direct comparisons between DYT-11 (+) and DYT-1 (+) patients were hard to perform on account

of some significant between-group differences in their demographic, baseline severity, and clinical factors found. However, no significant difference was found in outcomes among DYT-11 (+) and DYT-1 (+) patients, which was in accordance with previous study [13].

In addition, patients with 6 are more unpredictable. GPi-DBS makes significant outcomes one year for patients of all genotypes [26, 32]. The different degrees of exercise benefits observed in DYT-6 (+) and DYT-1 (+) patients may be due to the different patterns of metabolic abnormalities reported in these two monogenotypes in the dystonia connectivity study [13, 33, 34]. The effect was even more pronounced 12 months after surgery. As time goes on, there may be consequences of failure or need for intervention after a long period of operation, and even serious complications may occur. Carriers of DYT-6 mutation are more likely to undergo additional neurosurgery after surgery, suggesting that eligible patients with severe dystonia should be screened for the mutation before treatment with GPi-DBS. Patients diagnosed as DYT-6 mutation carriers who receive GPi-DBS should be informed of the failure of primary treatment and the possible risk of secondary intervention [31]. Therefore, some authorities recommend for testing DYT-1 and DYT-11, which has a favorable result, and others suggest testing for DYT-6 to inform patients that their surgical success rate may not be high. This may be a reference for patients and can be used as one of the factors influencing the effect of GPi-DBS treatment.

Our results suggested that different genotypes of dystonia may contribute to the effect of disease duration on the outcome of GPi-DBS treatment. Moreover, the outcome of GPi-DBS treatment for early-onset dystonia is related to genes as DYT-1 carriers obtained more effective results compared to other genotypes which is consistent with previous literature [13]. DYT-11 carriers also showed significant improvement in dystonia severity and disability outcomes. Therefore, genetic testing can improve the accuracy of diagnosis and enable patients to have a more accurate and detailed understanding of the expected results.

4.3. Comparison between Outcomes of BFMDRS-D among Different Genotypes of Early-Onset Dystonia. For disability symptom severity, outcomes of BFMDRS-D were the same regardless of follow-up time restriction for the limited data of BFMDRS-D. Some studies suggested that myoclonus is related to globus pallidus, but there is no strong evidence for the specific mechanism [35]. In view of the fact that GPi-DBS treatment of patients in DYT-11 (+) is capable of improving symptoms and treating myoclonus at the same time to achieve a good effect [30], the change rate of DYT-11 (+) patients was higher than that of DYT-6 (+) patients, which was consistent with the previous literature [2]. Further, considering many trials have shown that the GPi-DBS treatment is effective for DYT-1 (+) patients [36] and more patients in DYT-1 (+) patients, there was no significant difference in the GPi-DBS treatment effect between DYT-1 (+) and DYT-11 (+) patients. Mutated DYT-1 may cause abnormal neurotransmission and interfere with neuronal firing in brain motor pathways [37], and GPi-DBS may block the abnormal discharge pattern of GPi, thereby reducing the excessive activation of the cortex [38]. Moreover, there was no significant effect between DYT-1 (+) and DYT-6 (+) patients, which may be due to the different patterns of metabolic abnormalities reported in these two monogenotypes in the dystonia connectivity study as described before. Our study showed that there was a correlation between preoperative BFMDRS-M score and the relative improvement rate of BFMDRS-D, and the preoperative BFMDRS-M score between DYT-1 (+) and DYT-6 (+) patients had no significant difference. Thus, change rate in these comparisons had no significant difference.

4.4. Predictors. The present study demonstrated that BFMDRS-M and BFMDRS-D were positively correlated, indicating that GPi-DBS does not only improve symptoms but also reduce disability [17]. Many studies have investigated the potential predictive factors of DBS for early-onset dystonia. All data were included and analyzed in the present meta-analysis, revealing that patients with lower preoperative BFMDRS-M scores obtained higher improvement rates of the BFMDRS-M score. Furthermore, in an article studying DBS in patients with Meige syndrome, Wang et al. found higher efficacy was related to lower preoperative BFMDRS-M scores and provided a possible explanation in that patients with higher BFMDRS scores or multiple onset sites have a greater overall disease burden and more likely to have unsatisfactory clinical outcomes [39]. Further research is needed to confirm this finding. Later age of onset was a beneficial factor for BFMDRS-D because DYT-11 (+) patients with later age of onset benefit the most from GPi-DBS [13].

Regarding the impact of the follow-up period, we performed a second analysis after data were limited to a 3-year follow-up period. Our results were consistent with a recent metaregression analysis that reported an association between shorter duration of dystonia and greater improvement in motor score after GPi-DBS treatment of patients with isolated dystonia [18, 40]. One possible explanation is that longer disease duration may lead to a greater burden of bone deformities secondary to the disease dystonia [28]. However, people with skeletal deformities are least likely to get symptom relief from DBS [41]. Moreover, patients with lower score of preoperative BFMDRS-M obtained higher improvement rates of BFMDRS-M and BFMDRS-D. To explain the different results after a limited time, the effect may not be as good when the time is prolonged. One study has shown that operation at a younger age is related to the favorable improvement of symptoms in isolated dystonia [27] since younger patients have better tolerance. However, our results showed that patients with older age of onset achieve more beneficial results. In early-onset dystonia, the age of onset often indirectly leads to the shortening of the course of disease. In addition, the course of the disease was positively correlated with the BFMDRS-M score.

In general, shorter disease course and lower BFMDRS-M score are associated with a better outcome. Furthermore, univariate metaregression indicated a remarkable negative correlation between greater baseline damage and a greater effect of DBS (i.e., higher BFMDRS-M and BFMDRS-D).

Therefore, when a disability does not respond to medicine and the quality of life declines, GPi-DBS surgery should be performed [29].

4.5. Complications. Compared to pallidotomy, the complications of DBS surgery involve the hardware [42]. Most of the complications occurred after a long follow-up period. In bilateral GPi-DBS, device infection remained the most significant adverse event with more hardware failures, less symptom aggravation, and only one patient died. The treatment of complications mentioned in the literature was also less. Because most of the complications were hardware-related complications, reoperation or electrode replacement was undergone to relieve symptoms caused by complications.

4.6. Mechanism of DBS for Early-Onset Dystonia. Deep brain stimulation (DBS) is a commonly used intervention to treat dystonia by neuromodulation, and DBS has a significant benefit in up to 90% of children with primary or hereditary dystonias [43]. Specific brain regions can be targeted to significantly improve motor performance. Studies suggested that DBS is well matched with the functional consequences of brain injury, and its impact is most likely due to the scale of downstream target input and the lack of information transmission, rather than the lack of information in a specific pattern [44].

Through direct comparison, it is concluded that the response of DYT-6 mutation patients is more difficult to predict than the response of DYT-1 mutation patients. Excluding genetic influence, some of this variability may be related to stimulus settings and/or lead position [45, 46]. GPi-DBS supports the concept of cortical regulation during high-frequency stimulation by improving the local effects of relative motion locations and inhibiting the consistency of electroencephalographic [47].

Thus, GPi-DBS can affect neuronal activity in local and other functional connections, and components of the cortices-basal ganglia neural network can cause long-term plasticity changes at the cortical level, which can then reestablish normal movement. This cortical modulation may be the explanation why improvements in tetanic motion may delay DBS by weeks and months [29].

Combined with local and distant modulation in neuronal networks, DBS may play an important role in the neurochemical system [48]. Under the premise of microdialysis or voltammetric analysis based on animal models, imaging studies or direct evaluation has involved DBS in the process of modulation of neurotransmitter release such as dopamine, glutamate, and gamma-aminobutyric acid; however, there is currently no specific research on dystonia [29].

4.7. Study Limitations. Several limitations of our study merit mention. First, the insufficiency of our meta-analysis is that the number of patients with DYT-1 (+) was more than twice that of patients with DYT-6 (+) and combined dystonia. Combined dystonia includes DYT-11 (+) and DYT-28 (+) patients, and DYT-28 is a new single-gene inherited early-onset dystonia discovered only in recent years. Thus, there are few relevant studies for combined dystonia.

Second, improvement on a dystonia motor scale does not automatically imply an improvement of quality of life as was previously shown in stimulated patients with generalized dystonia [49]. However, patients evaluated in specialized scales such as SF-36 were few due to the inclusion and exclusion criteria that we strictly followed, and the outcome in our study was only based on BFMDRS-M and BFMDRS-D. Thus, more scoring scales are needed in future studies to more comprehensively and quantitatively evaluate the health-related quality of life and mental status of patients.

Third, the study is based on an unblinded evaluation of published cases. Hence, our conclusions tend to deviate from the expectations of patients and physicians, as well as publication bias that tend to favor better outcomes. However, because we used a conservative approach, the results described may underestimate the actual DBS benefits.

To date, there is limited evidence for short-term benefits, and data for long-term results after treatment of early-onset dystonia with GPi-DBS are also limited. Based on the fact that DBS is an inherent surgical intervention, it should be evaluated and discussed by an experienced multidisciplinary dyskinesia team.

5. Conclusion

The motor and disability symptoms of early-onset dystonia with DYT-1 (+), DYT-6 (+), DYT-11 (+), and DYT-28 (+) genotypes are effectively improved by GPi-DBS. For movement symptom severity, DYT-1 (+) patients and DYT-11 (+) patients are potential candidates for better results with GPi-DBS clinically. For DYT-11 (+) patients with severe disability, GPi-DBS treatment is a great choice. Patients who have been treated with GPi-DBS need to be reviewed or even undergo another surgery after one year. Lower preoperative BFMDRS-M score and shorter disease course indicate better efficacy of movement symptom. Lower preoperative BFMDRS-M score and later age of onset indicate better efficacy of disability symptom. Consequently, GPi-DBS should be considered in a timely manner once the symptoms cannot be controlled by drugs.

Abbreviations

DBS:	Deep brain stimulation
GPi:	Globus pallidus internus
Vim:	Ventral intermediate internus
STN:	Subthalamic nucleus
BFMDRS:	Burke–Fahn–Marsden Dystonia Rating Scale
BFMDRS-M:	BFMDRS movement subscale
BFMDRS-D:	BFMDRS disability subscale
IPDL:	Individual patient data
MER:	Microelectrode recording
IPG:	Implanted pulse generator
OCEBM:	Oxford Centre for Evidence-based Medicine.

Data Availability

The initial data supporting this meta-analysis are from previously reported studies and datasets, which have been cited.

The processed data are available (in the Supplementary Materials).

Conflicts of Interest

The authors report no conflicts of interest concerning the materials or methods used in this study or the finding specified in this paper.

Authors' Contributions

GL contributed to the concept and design of this manuscript. WC and HF collected data, performed statistical analyses and mapped, and finally completed the manuscript. The article was finally revised by the three people based on the discussion. Wenxiu Chen and Houyou Fan are co-first authors.

Acknowledgments

This work was funded by the National Natural Science Foundation of China (grant number 82060249) and the Key and General Programs of Natural Science Foundation of Jiangxi Province (grant numbers 20202ACBL206005, 20192BAB205042, and 20202BABL206098).

Supplementary Materials

Highlights demonstrate the main content and novelty of this article. Table S1 integrates and summarizes the original data and results of the 54 articles used in this meta-analysis. *(Supplementary Materials)*

References

[1] B. J. Robottom, W. J. Weiner, and C. L. Comella, "Early-onset primary dystonia," *Handbook of Clinical Neurology*, vol. 100, pp. 465–479, 2011.

[2] B. R. Aravamuthan, J. L. Waugh, and S. S. Stone, "Deep brain stimulation for monogenic dystonia," *Current Opinion in Pediatrics*, vol. 29, no. 6, pp. 691–696, 2017.

[3] M. Jahanshahi and M. Torkamani, "The cognitive features of idiopathic and DYT1 dystonia," *Movement Disorders*, vol. 32, no. 10, pp. 1348–1355, 2017.

[4] B. Zirn, K. Grundmann, P. Huppke et al., "Novel TOR1A mutation p.Arg288Gln in early-onset dystonia (DYT1)," *Journal of Neurology, Neurosurgery, and Psychiatry*, vol. 79, no. 12, pp. 1327–1330, 2008.

[5] M. S. LeDoux, J. Xiao, M. Rudzińska et al., "Genotype-phenotype correlations in THAP1 dystonia: molecular foundations and description of new cases," *Parkinsonism & Related Disorders*, vol. 18, no. 5, pp. 414–425, 2012.

[6] Y. Kimura, M. Mihara, T. Kawarai et al., "Efficacy of deep brain stimulation in an adolescent patient with DYT11 myoclonus-dystonia," *Neurology and Clinical Neuroscience*, vol. 2, no. 2, pp. 57–59, 2014.

[7] G. Kriegel and M. I. Stuckey, "Psychiatric and behavioral complications of GPi DBS in an adolescent with myoclonus dystonia," *Case Reports in Psychiatry*, vol. 2019, Article ID 1947962, 3 pages, 2019.

[8] M. Zech, D. D. Lam, and J. Winkelmann, "Update on KMT2B-related dystonia," *Current Neurology and Neuroscience Reports*, vol. 19, no. 11, p. 92, 2019.

[9] J. Jankovic, "Botulinum toxin: state of the art," *Movement Disorders*, vol. 32, no. 8, pp. 1131–1138, 2017.

[10] S. Patel and D. Martino, "Cervical dystonia: from pathophysiology to pharmacotherapy," *Behavioural Neurology*, vol. 26, no. 4, pp. 275–282, 2013.

[11] P. Krause, S. Völzmann, S. Ewert, A. Kupsch, G. H. Schneider, and A. A. Kühn, "Long-term effects of bilateral pallidal deep brain stimulation in dystonia: a follow-up between 8 and 16 years," *Journal of Neurology*, vol. 267, no. 6, pp. 1622–1631, 2020.

[12] T. L. Ellis, "Dystonia and the role of deep brain stimulation," *ISRN Surgery*, vol. 2011, Article ID 193718, 5 pages, 2011.

[13] C. A. Artusi, A. Dwivedi, A. Romagnolo et al., "Differential response to pallidal deep brain stimulation among monogenic dystonias: systematic review and meta-analysis," *Journal of Neurology, Neurosurgery, and Psychiatry*, vol. 91, no. 4, pp. 426–433, 2020.

[14] H. Rocha, P. Linhares, C. Chamadoira, M. J. Rosas, and R. Vaz, "Early deep brain stimulation in patients with myoclonus-dystonia syndrome," *Journal of Clinical Neuroscience*, vol. 27, pp. 17–21, 2016.

[15] X. Y. Li, L. F. Dai, X. H. Wan et al., "Clinical phenotypes, genotypes and treatment in Chinese dystonia patients with KMT2B variants," *Parkinsonism & Related Disorders*, vol. 77, pp. 76–82, 2020.

[16] A. Danielsson, M. Carecchio, L. Cif et al., "Pallidal deep brain stimulation in DYT6 dystonia: clinical outcome and predictive factors for motor improvement," *Journal of Clinical Medicine*, vol. 8, no. 12, p. 2163, 2019.

[17] X. Wang, Z. Zhang, Z. Mao, and X. Yu, "Deep brain stimulation for Meige syndrome: a meta-analysis with individual patient data," *Journal of Neurology*, vol. 266, no. 11, pp. 2646–2656, 2019.

[18] R. E. Burke, S. Fahn, C. D. Marsden, S. B. Bressman, C. Moskowitz, and J. Friedman, "Validity and reliability of a rating scale for the primary torsion dystonias," *Neurology*, vol. 35, no. 1, pp. 73–77, 1985.

[19] M. Yang, W. Sun, L. Xiao et al., "Mesenchymal stromal cells suppress hippocampal neuron autophagy stress induced by hypoxic-ischemic brain damage: the possible role of endogenous IL-6 secretion," *Neural Plasticity*, vol. 2020, Article ID 8822579, 12 pages, 2020.

[20] Q. Wang, W. Yang, J. Zhang, Y. Zhao, and Y. Xu, "TREM2 overexpression attenuates cognitive deficits in experimental models of vascular dementia," *Neural Plasticity*, vol. 2020, Article ID 8834275, 10 pages, 2020.

[21] W.-m. Ren, Z.-b. Weng, X. Li, and L.-B. Zhan, "Neuroprotective effects of ZiBuPiYin recipe on db/db mice via PI3K-Akt signaling pathway by activating Grb2," *Neural Plasticity*, vol. 2021, Article ID 8825698, 10 pages, 2021.

[22] R. G. Cury, V. Fraix, and E. Moro, "Celebrating thirty years of deep brain stimulation in movement disorders patients: a successful marriage between neurologists and neurosurgeons," *Parkinsonism & Related Disorders*, vol. 46, pp. 98-99, 2018.

[23] J. L. Ostrem, M. San Luciano, K. A. Dodenhoff et al., "Subthalamic nucleus deep brain stimulation in isolated dystonia: a 3-year follow-up study," *Neurology*, vol. 88, no. 1, pp. 25–35, 2017.

[24] J. L. Ostrem, L. C. Markun, G. A. Glass et al., "Effect of frequency on subthalamic nucleus deep brain stimulation in primary dystonia," *Parkinsonism & Related Disorders*, vol. 20, no. 4, pp. 432–438, 2014.

[25] A. Kupsch, R. Benecke, J. Müller et al., "Pallidal deep-brain stimulation in primary generalized or segmental dystonia," *The New England Journal of Medicine*, vol. 355, no. 19, pp. 1978–1990, 2006.

[26] I. Beaulieu-Boire, C. C. Aquino, A. Fasano et al., "Deep brain stimulation in rare inherited dystonias," *Brain Stimulation*, vol. 9, no. 6, pp. 905–910, 2016.

[27] E. Moro, C. LeReun, J. K. Krauss et al., "Efficacy of pallidal stimulation in isolated dystonia: a systematic review and meta-analysis," *European Journal of Neurology*, vol. 24, no. 4, pp. 552–560, 2017.

[28] I. U. Isaias, R. L. Alterman, and M. Tagliati, "Outcome predictors of pallidal stimulation in patients with primary dystonia: the role of disease duration," *Brain*, vol. 131, no. 7, pp. 1895–1902, 2008.

[29] R. G. Cury, S. K. Kalia, B. B. Shah, J. Jimenez-Shahed, L. K. Prashanth, and E. Moro, "Surgical treatment of dystonia," *Expert Review of Neurotherapeutics*, vol. 18, no. 6, pp. 477–492, 2018.

[30] A. I. Rughani and A. M. Lozano, "Surgical treatment of myoclonus dystonia syndrome," *Movement Disorders*, vol. 28, no. 3, pp. 282–287, 2013.

[31] N. Bruggemann, A. Kuhn, S. A. Schneider et al., "Short- and long-term outcome of chronic pallidal neurostimulation in monogenic isolated dystonia," *Neurology*, vol. 84, no. 9, pp. 895–903, 2015.

[32] L. C. Markun, P. A. Starr, E. L. Air, W. J. Marks Jr., M. M. Volz, and J. L. Ostrem, "Shorter disease duration correlates with improved long-term deep brain stimulation outcomes in young-onset DYT1 dystonia," *Neurosurgery*, vol. 71, no. 2, pp. 325–330, 2012.

[33] M. Carbon and D. Eidelberg, "Abnormal structure-function relationships in hereditary dystonia," *Neuroscience*, vol. 164, no. 1, pp. 220–229, 2009.

[34] J. H. Ahn, A. R. Kim, N. K. D. Kim et al., "The effect of globus pallidus interna deep brain stimulation on a dystonia patient with the GNAL mutation compared to patients with DYT1 and DYT6," *Journal of Movement Disorders*, vol. 12, no. 2, pp. 120–124, 2019.

[35] E. Menozzi, B. Balint, A. Latorre, E. M. Valente, J. C. Rothwell, and K. P. Bhatia, "Twenty years on: myoclonus-dystonia and ε-sarcoglycan - neurodevelopment, channel, and signaling dysfunction," *Movement Disorders*, vol. 34, no. 11, pp. 1588–1601, 2019.

[36] F. Panov, Y. Gologorsky, G. Connors, M. Tagliati, J. Miravite, and R. L. Alterman, "Deep brain stimulation in DYT1 dystonia: a 10-year experience," *Neurosurgery*, vol. 73, no. 1, pp. 86–93, 2013, discussion 93.

[37] J. W. Wang, J. P. Li, Y. P. Wang, X. H. Zhang, and Y. Q. Zhang, "Deep brain stimulation for myoclonus-dystonia syndrome with double mutations in DYT1 and DYT11," *Scientific Reports*, vol. 7, no. 1, article 41042, 2017.

[38] J. Jankovic, "Treatment of dystonia," *The Lancet Neurology*, vol. 5, no. 10, pp. 864–872, 2006.

[39] X. Wang, Z. Mao, Z. Cui et al., "Predictive factors for long-term clinical outcomes of deep brain stimulation in the treatment of primary Meige syndrome," *Journal of Neurosurgery*, vol. 132, no. 5, pp. 1367–1375, 2019.

[40] Y. S. Wu, L. H. Ni, R. M. Fan, and M. Y. Yao, "Meta-regression analysis of the long-term effects of pallidal and subthalamic deep brain stimulation for the treatment of isolated dystonia," *World Neurosurgery*, vol. 129, pp. e409–e416, 2019.

[41] I. U. Isaias, R. L. Alterman, and M. Tagliati, "Deep brain stimulation for primary generalized dystonia: long-term outcomes," *Archives of Neurology*, vol. 66, no. 4, pp. 465–470, 2009.

[42] V. Levi, G. Zorzi, G. Messina et al., "Deep brain stimulation versus pallidotomy for status dystonicus: a single-center case series," *Journal of Neurosurgery*, vol. 134, no. 1, pp. 197–207, 2021.

[43] M. Vidailhet, L. Vercueil, J. L. Houeto et al., "Bilateral deep-brain stimulation of the globus pallidus in primary generalized dystonia," *The New England Journal of Medicine*, vol. 352, no. 5, pp. 459–467, 2005.

[44] T. D. Sanger, "A computational model of deep-brain stimulation for acquired dystonia in children," *Frontiers in Computational Neuroscience*, vol. 12, p. 77, 2018.

[45] B. D. Berman, P. A. Starr, W. J. Marks, Jr, and J. L. Ostrem, "Induction of bradykinesia with pallidal deep brain stimulation in patients with cranial-cervical dystonia," *Stereotactic and Functional Neurosurgery*, vol. 87, no. 1, pp. 37–44, 2009.

[46] H. A. Jinnah, R. Alterman, C. Klein et al., "Deep brain stimulation for dystonia: a novel perspective on the value of genetic testing," *Journal of Neural Transmission (Vienna)*, vol. 124, no. 4, pp. 417–430, 2017.

[47] E. Barow, W. J. Neumann, C. Brücke et al., "Deep brain stimulation suppresses pallidal low frequency activity in patients with phasic dystonic movements," *Brain*, vol. 137, no. 11, pp. 3012–3024, 2014.

[48] K. Udupa and R. Chen, "The mechanisms of action of deep brain stimulation and ideas for the future development," *Progress in Neurobiology*, vol. 133, pp. 27–49, 2015.

[49] M. Jahanshahi, M. Torkamani, M. Beigi et al., "Pallidal stimulation for primary generalised dystonia: effect on cognition, mood and quality of life," *Journal of Neurology*, vol. 261, no. 1, pp. 164–173, 2014.

Hindawi
Neural Plasticity
Volume 2024, Article ID 9780493, 1 page
https://doi.org/10.1155/2024/9780493

Retraction

Retracted: Molecular Basis of GABA Hypofunction in Adolescent Schizophrenia-Like Animals

Neural Plasticity

Received 23 January 2024; Accepted 23 January 2024; Published 24 January 2024

This article has been retracted by Hindawi following an investigation undertaken by the publisher [1]. This investigation has uncovered evidence of one or more of the following indicators of systematic manipulation of the publication process:

(1) Discrepancies in scope
(2) Discrepancies in the description of the research reported
(3) Discrepancies between the availability of data and the research described
(4) Inappropriate citations
(5) Incoherent, meaningless and/or irrelevant content included in the article
(6) Manipulated or compromised peer review

The presence of these indicators undermines our confidence in the integrity of the article's content and we cannot, therefore, vouch for its reliability. Please note that this notice is intended solely to alert readers that the content of this article is unreliable. We have not investigated whether authors were aware of or involved in the systematic manipulation of the publication process.

Wiley and Hindawi regrets that the usual quality checks did not identify these issues before publication and have since put additional measures in place to safeguard research integrity.

We wish to credit our own Research Integrity and Research Publishing teams and anonymous and named external researchers and research integrity experts for contributing to this investigation.

The corresponding author, as the representative of all authors, has been given the opportunity to register their agreement or disagreement to this retraction. We have kept a record of any response received.

References

[1] X. Wang, Y. Hu, W. Liu et al., "Molecular Basis of GABA Hypofunction in Adolescent Schizophrenia-Like Animals," *Neural Plasticity*, vol. 2021, Article ID 9983438, 15 pages, 2021.

Hindawi
Neural Plasticity
Volume 2021, Article ID 9983438, 15 pages
https://doi.org/10.1155/2021/9983438

Research Article

Molecular Basis of GABA Hypofunction in Adolescent Schizophrenia-Like Animals

Xiaodan Wang,[1,2,3] **Ying Hu**,[4] **Wenxin Liu**,[5] **Yuanyuan Ma**,[4] **Xi Chen**,[1,2] **Ting Xue**,[1,2] **and Donghong Cui**[1,2,6]

[1]*Shanghai Mental Health Center, Shanghai Jiao Tong University School of Medicine, Shanghai, China*
[2]*Shanghai Key Laboratory of Psychotic Disorders, Shanghai, China*
[3]*Department of Neurology & Institute of Neurology, Rui Jin Hospital, Shanghai Jiao Tong University School of Medicine, Shanghai, China*
[4]*Shenzhi Department of the Fourth Affiliated Hospital of Xinjiang Medical University, Urumqi, China*
[5]*College of Life Sciences, Shanghai Normal University, Shanghai, China*
[6]*Brain Science and Technology Research Center, Shanghai Jiao Tong University, Shanghai, China*

Correspondence should be addressed to Ting Xue; xueting221314@126.com and Donghong Cui; manyucc@126.com

Received 5 March 2021; Revised 22 March 2021; Accepted 30 March 2021; Published 15 April 2021

Academic Editor: Fushun Wang

Schizophrenia is a neurodevelopmental disorder that NMDA receptor (NMDAR) hypofunction appears centrally involved. Schizophrenia typically emerges in adolescence or early adulthood. Electrophysiological and several neurochemical changes have linked the GABA deficits to abnormal behaviors induced by NMDAR hypofunction. However, few studies have systematically investigated the molecular basis of GABA deficits, especially during adolescence. To address this issue, we transiently administrated MK-801 to mice on PND 10, which exhibited schizophrenia-relevant deficits in adolescence. Slice recording showed reduced GABA transmission and PVI^+ hypofunction, indicating GABAergic hypofunction. Cortical proteomic evaluation combined with analysis of single cell data from the Allen Brain showed that various metabolic processes were enriched in top ranks and differentially altered in excitatory neurons, GABAergic interneurons, and glial cells. Notably, the GABA-related amino acid metabolic process was disturbed in both astrocytes and interneurons, in which we found a downregulated set of GABA-related proteins (GAD65, SYNPR, DBI, GAT3, SN1, and CPT1A). They synergistically regulate GABA synthesis, release, reuptake, and replenishment. Their downregulation indicates impaired GABA cycle and homeostasis regulated by interneuron-astrocyte communication in adolescence. Our findings on molecular basis of GABA deficits could provide potential drug targets of GABAergic rescue for early prevention and intervention.

1. Introduction

Schizophrenia is a devastating disorder that disrupts multiple brain systems, ending in decade-long psychosis and social and cognition impairment [1]. Although considered as a neurodevelopmental disorder [2], the onset of psychotic symptoms typically emerge in adolescence or early adulthood [1]. Recent findings suggest that therapeutic interventions during adolescence, typically before the onset of symptoms, might prevent or ameliorate the development of illness [3]. As the prefrontal cortex (PFC) continues to mature through adolescence and it is closely related to schizophrenia [4], understanding how PFC disruption occurs during adolescence will reveal key pathological mechanisms of illness and help early prevention and intervention.

NMDA receptor (NMDAR) hypofunction plays a key role in the pathophysiology of schizophrenia [5, 6]. This hypothesis is supported by the observations that NMDAR antagonists such phencyclidine, MK-801, and ketamine can produce schizophrenia-like symptoms in healthy humans and exacerbate preexisting symptoms in schizophrenic patients [7]. Rodents, repeatedly treated with NMDAR antagonists [6], during neonatal periods, also recapitulate schizophrenia-related behaviors, including locomotor

hyperactivity, impairment of spatial learning and memory, and decreased sensory gating [8].

NMDAR hypofunction-related abnormal behaviors have been linked to excitation-inhibition (E/I) imbalance regulated by GABA deficits [9]. GABA (Y-aminobutyric acid) is the principal inhibitory neurotransmitter in CNS released by GABAergic interneurons [10]. Electrophysiological recordings of NMDAR antagonists reveal reduced presynaptic GABAergic transmission and disinhibition of pyramidal neurons [9, 11]. Rescue with $GABA_A$ receptor could restore behavioral deficits [9]. In animals, repeated injection of NMDAR antagonists reduces the expression of parvalbumin [12]. Bidirectional manipulation of parvalbumin and GAD67 (regulating GABA synthesis) levels in the mice hippocampus could regulate their learning ability [13]. In addition, postmortem studies of schizophrenia have persistently documented lower levels of parvalbumin [14, 15] and GAD67 [16, 17] in parvalbumin-positive GABAergic interneurons ($PVIs^+$), indicating deficits in GABAergic circuits. Although electrophysiological and several neurochemical changes implicate the GABAergic deficits by NMDAR hypofunction, in addition, current data indicate the importance of astrocytes in regulating the dynamic GABAergic-astrocyte communication [18], and few studies provide a panoramic view of the molecular basis of GABAergic deficits, especially during the adolescence.

To address this issue, we transiently administrated MK-801 to mice on PND 10. They exhibited schizophrenia-relevant behaviors in adolescence. Accordingly, electrophysiological recording of PFC revealed reduced GABA transmission and $PVIs^+$ hypofunction. We performed cortical proteomic studies and combined analysis of single-cell sequencing data from the Allen Brain. Integrative analysis of omics revealed that metabolic processes were differentially altered in excitatory neurons, interneurons, and glial cells. Notably, a set of GABA-related proteins regulating GABA cycle, consisted of synthesis, release, reuptake and replenishment, were downregulated. Particularly, these proteins were exclusively dysregulated in interneurons and astrocytes, indicating the impaired GABAergic-astrocyte communication. We revealed the molecular basis of GABA deficits, providing a global view of how GABA dysfunction occurred during adolescence. Our results may provide insight into the pathophysiological mechanisms of schizophrenia.

2. Materials and Methods

2.1. Mice and MK-801 Administration. For all experiments, we used wild-type C57BL/6 J male mice. All animal experiments were approved by the Experimental Animal Committee of Shanghai Jiao Tong University. Housing conditions include a 12 h light/dark cycle, a humidity of 50 ± 5%, and a controlled temperature of 22–25°C in the Individual Ventilated Caging System (IVC, TECNIPLAST S.P.A.). Food and water were provided ad libitum. The day of birth was defined as PND 1. On PND 10, pups were received two intraperitoneal injections of saline or MK-801 (Sigma-Aldrich) at a dose of 0.5 mg/kg (i.e., 10 ml/kg) at 9 : 00 AM and 17 : 00 AM, respectively. Mice were weaned on PND 21 and housed in single-sex groups (four to five per cage).

2.2. Behavioral Tests. A battery of behavioral tests related to schizophrenia, including open field test, elevated plus maze test, nesting building, Barnes maze, and prepulse inhibition test, were conducted in adolescent mice (~PND 35). Before behavioral tests, mice were acclimatized in the testing room for 1 h, and tests were conducted during 9 : 00 AM and 4 : 00 PM. The details of behavioral methods are provided in the supplementary methods. Electrophysiological recording, proteomic analysis, western blot, and immunohistochemistry were also performed in adolescent mice.

2.3. Electrophysiological Recording. Coronal slices were prepared from the PFC in an ice-cold and oxygenated sucrose solution containing (in mM) 212 sucrose, 3 KCl, 26 $NaHCO_3$, 1.25 NaH_2PO_4, 0.5 $CaCl_2$, 7 $MgSO_4$, and 10 D (+) glucose. Following an incubation period of 30 min, recordings were performed in the oxygenated artificial CSF (ACSF). Micropipettes (4-6 MΩ) were filled with an intracellular solution containing the following (in mM): 130 K^+ gluconate, 10 HEPES, 5 KCl, 0.5 EGTA, 10 phosphocreatine, 4 ATP-Na, 0.3 GTP-Na and 2.5 $MgCl_2$, pH 7.23, and osmolality 313 mOsm/kg. Whole-cell patch-clamp recordings were obtained from $PVIs^+$ or pyramidal neurons in the II/III layer of the prelimbic region (PrL). To measure intrinsic excitability, current was injected in 25 pA steps from 0 pA to 800 pA. Action potential (AP) threshold and frequency were recorded. sIPSC and sEPSC recordings (holding potentials of −70 mV) were monitored in pyramidal neurons. For sIPSC recordings, ACSF containing 10 μM NBQX and 50 μM APV and a high Cl intracellular solution were used. For sEPSC recordings, ACSF containing 100 μM Picrotoxin and K^+ gluconate intracellular solution was used. Data were acquired with a PatchMaster (HEKA, Germany) instrument and analyzed using MiniAnalysis (Synaptosoft, NJ). Data were normalized to the average baseline response. Cells whose access resistance exceeded 25 MΩ and had an unstable resting membrane potential or aberrant spiking pattern were excluded from the analysis.

2.4. Sample Preparation for MS Analysis. The PFC was mechanically homogenized (Dremel, USA) in the strong RIPA lysis buffer. 100 μg of proteins was denatured in UA buffer (8 M Urea in 50 mM NH_4HCO_3, pH 7.8), reduced with 5 mM TCEP (Tris(2-carboxyethyl)phosphine), and alkylated with 15 mM IAA (iodoacetamide) for 30 min in the dark. Proteins were precipitated with precooled acetone and digested at 37°C for 18 h with trypsin (Promega) at a concentration of 1 : 50 (w/w) in 50 mM NH_4HCO_3. After digestion, peptides were desalted using a Mono spin column (GL Science, Tokyo).

2.5. Nano-LC-MS/MS. 300 ng of peptides was reconstituted in 0.1% formic acid (FA) and separated by nanoscale reversed-phase UPLC on a nanoAcquity UPLC system (Waters Corporation), equipped with a Symmetry C18 5 mm, 180 μm × 20 mm trap column and an HSS T3 C18 1.8 mm, 75 μm × 250 μm analytical column (Waters

Corporation). Injected peptides were separated over a 120 min gradient from 3-35% B at a flow rate of 300 nL/min. Solvent A consisted of 0.1% FA in H_2O, and solvent B was 0.1% FA in acetonitrile. The mass spectrometric analysis was performed on a Synapt G2-Si quadrupole time-of-flight mass spectrometer (Waters Corporation) in $UDMS^E$ (ultra-definition MS^E) mode. Positive ions in a mass range of 50 to 2000 m/z were acquired at a resolution mode of 20000 FWHM (full width at half maximum). A frequency of 30 s lock mass correction of [Glu1]-fibrinopeptide B was delivered.

MS raw spectra processing was performed in Waters Progenesis QI (QIP, version 3.0.2) as described previously [19], searched against the UniProt mouse proteomic database (version 2020/06). Default parameters for peak picking and alignment algorithm were applied. Carbamidomethylation of cysteine and oxidation of methionine were specified as fixed and variable modifications, respectively. A single missed trypsin cleavage was allowed. FDR for protein identification was set at a 4% threshold. Only peptides with a minimum length of seven amino acids identified with a confidence score ≥ 4 and<20 ppm mass error were considered.

2.6. Proteomic Data Analysis. Data normalization on peptide levels was performed automatically in the QIP software. Proteins were quantified using the Top 3 method [20, 21]. Only proteins with at least one unique peptide were considered. Duplicated technical replicates were performed. Proteins whose intensities were outside the range of the mean ± 2 sigma of each group were defined as outliers and removed. *K*-nearest neighbor (k-NN) imputation was applied to impute the missing values. The samr *R* package [22] was used to identify differentially expressed proteins using the paired two class of samr with 1,000 permutations and an FDR threshold of 0.05 [23]. Proteins identified with at least two unique peptides and a fold change of ≥ |1.3| were defined as differentially expressed proteins. Biological function analysis and protein-protein interaction were performed in STRING (http://string-db.org/), and the latter was visualized with Cytoscape 3.6.1 [24]. The protein expression in each cortical cell type was downloaded from the mouse brain single-cell sequencing database (http://mousebrain.org) [25].

2.7. Western Blot. Proteins were separated by 10% SDS-PAGE gel and blotted with primary antibodies as follows: mouse anti-PV (1 : 1000, Sigma), mouse anti-GAD65 (1 : 500, Abcam), rabbit anti-GAD67 (1 : 1000, Cell Signaling Technology), and rabbit anti-β-actin (1 : 2000, Cell Signaling Technology). The secondary antibodies used included goat anti-rabbit IgG (1 : 10000, Sigma) and goat anti-mouse IgG (1 : 10000, Sigma).

2.8. Immunohistochemistry. Brains were dissected and fixed overnight in 4% PFA at 4°C before cryoprotection in 30% sucrose. Brains were sectioned coronally in 20 μm slices using a freezing microtome (Leica). Sections between bregma 1.54 mm to 2.46 mm were collected for cell counting. The primary antibody was anti-PV antibody (1 : 500; Sigma).The secondary antibody was Alexa Fluor 488 donkey anti-mouse antibody (1 : 000; Jackson lab). $PVIs^+$ in the PrL region, consistent with electrophysiological recording, were counted every sixth of sections.

2.9. Statistical Analysis. Student's *t*-test was used when comparing two groups. Two-way analysis of variance (ANOVA) followed by post hoc Tukey's multiple comparison was used to analyze two factors and multiple group comparisons. A repeated measures ANOVA determined statistical differences of cumulative distribution. Statistical significance was defined as $p < 0.05$.

3. Results

3.1. Transient Blockade of NMDARs on PND 10 Induces Schizophrenia-Like Behaviors in Adolescent Mice. $PVIs^+$ have been documented with the most sensitivity to NMDAR inhibition, especially during development [26]. PND 10 is when (1) mice brain growth reaches its peak [27], (2) maturation of mice cortical parvalbumin immunoreactivity of $PVIs^+$ appears [28], and (3) excitatory synapses and fast-spiking properties of $PVIs^+$ present in two days [29]. Hence, we targeted PND 10 as the critical point to induce NMDAR hypofunction. Male pups received two consecutive injections of MK-801 at 8 h intervals on PND 10. Considering the short half-life of MK801 (~2 h) in the brain [30], to effectively induce abnormal behaviors by the transient blockade strategy, a high dosage of MK801 (0.5 mg/kg) was chosen [31–33]. In contrast, a low (0.05-0.1 mg/kg) or moderate (0.2-0.25 mg/kg) dosage is generally used in the chronic treatment of rodents [8]. A battery of behavioral tests related to schizophrenia were performed during their adolescent stages (from PND 35) [34] when schizophrenia typically emerges in humans [1] (Figure 1(a)).

MK-801 injection on PND 10 did not affect mice weight in adolescence (Figure S1a). The open field test showed that mice locomotion activity was not disturbed (Figure S1b-c). Schizophrenia may increase comorbidity with anxiety disorders. We found that MK-801-injected mice spent less time in open arms while had a higher closed arm duration (Figure 1(b)), suggesting elevated anxiety-related activity. Next, we performed a PPI test to measure sensorimotor gating, which is frequently reduced in schizophrenic patients [35]. We observed no significant difference in baseline amplitude for the startle response (Figure 1(c)). However, MK-801-treated mice showed a significantly decreased prepulse inhibition at 85 dB (Figure 1(d)), indicating impaired sensory gating. Nest building is a measure of cooperative or social activity for rodents [36], whose decrease could correspond to negative symptoms in schizophrenic patients [37]. We found MK-801-treated mice exhibited a significantly lower ability of nest building (Figure 1(e)), who failed to build fluffy nests and tended to scatter pieces of cotton across the cage floor (Figure 1(f)). Impaired long-term explicit or declarative memory [38, 39] is one of the cognitive impairments in schizophrenia, which could be measured by the Barnes maze in rodents [40]. MK-801-treated mice showed significantly longer latency in

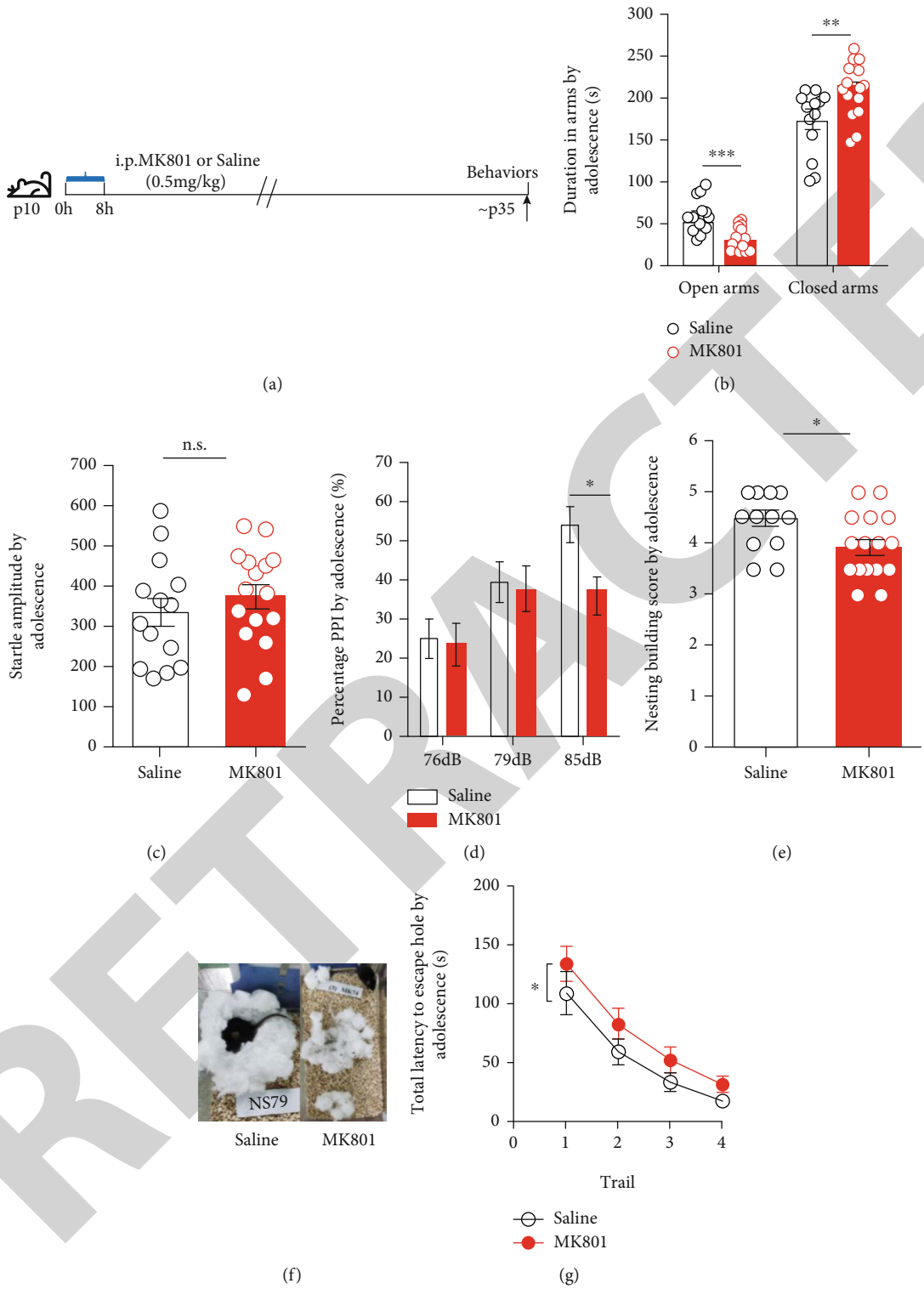

Figure 1: Mice administrated with MK-801 on PND 10 showed schizophrenia-like behaviors in adolescence. (a) C57BL/6 male mice intraperitoneally received two consecutive injections of MK-801 (0.5 mg/kg) or saline on PND 10 with an interval of 8 h. Behavioral tests were performed from PND 35. (b) Time spends in the open ($p < 0.001$) and closed arms, $p = 0.0069$. (c) There was no significant difference in the baseline startle response amplitude between MK-801-treated and control groups, $p = 0.4083$. (d) Prepulse inhibition was significantly inhibited at 85 dB in MK-801-injected mice ($p = 0.0334$). (e) Nesting building score was significantly lower in MK-801-treated mice, $p = 0.0154$. (f) The nesting building image between MK-801-treated and control mice. (g) MK-801-treated mice showed longer latency in entering the escape chamber ($F_{(1,112)} = 6.109$, $p = 0.015$, two-way ANOVA). Data were represented as mean ± SEM. $n = 14$ of saline and $n = 16$ of MK801. $^{*}p < 0.05$, $^{**}p < 0.01$, $^{***}p < 0.001$. Student's t-test for two groups' comparison. Two-way ANOVA by post hoc Tukey's multiple comparison for two factors and two group analysis.

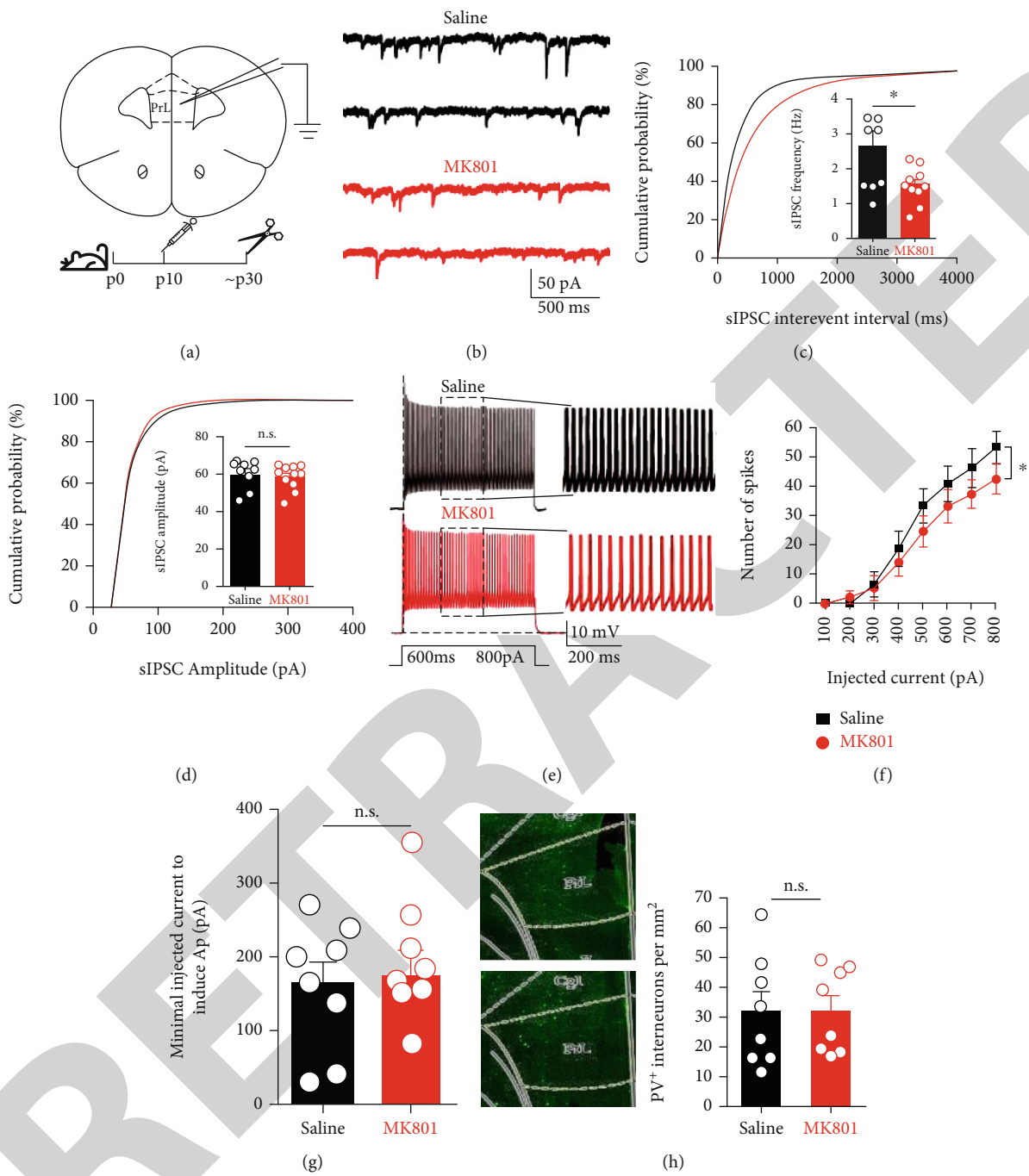

Figure 2: Continued.

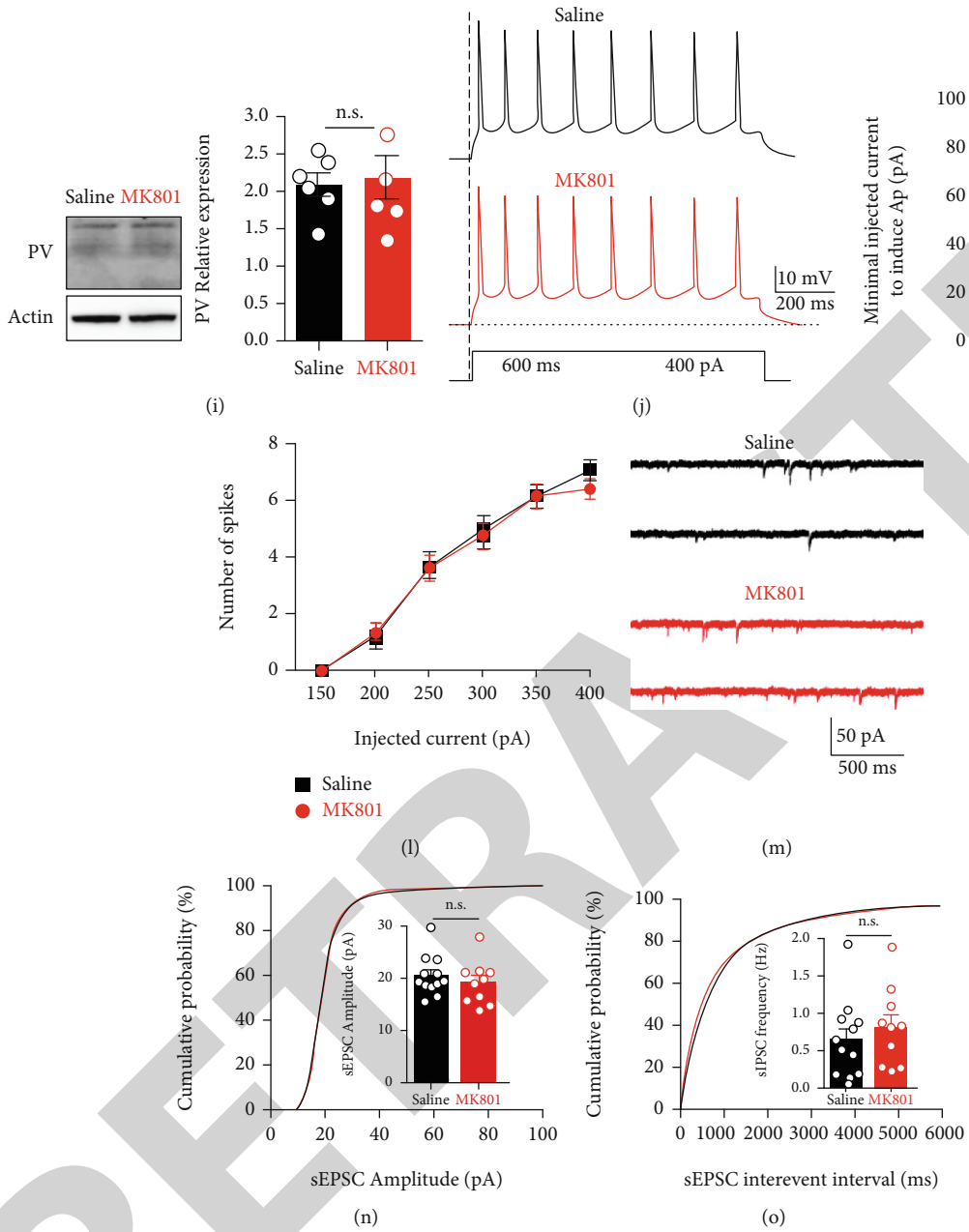

Figure 2: Electrophysiological recording of pyramidal neurons and PVIs$^+$ in the mPFC in adolescence. (a) Schematic diagram of whole-cell patch-clamp of sIPSC obtained from pyramidal neurons in the PrL region of mPFC. Saline or MK-801-treated mice were sacrificed on ~PND 30 and subjected for electrophysiological recording. (b) Example traces of sIPSC in pyramidal neurons. (c) Cumulative probability and the average frequency of sIPSC (saline/MK801: $n = 10/9$ cells from 3/3 mice per group, $^*p = 0.0224$). (d) Cumulative probability and average amplitude of sIPSC (saline/MK-801: $n = 10/9$ cells from 3/3 mice per group, $p = 0.5741$). (e) Example traces of PVIs$^+$ response to depolarizing current steps. (f) Input-output curve showing the average firing rate of PVIs$^+$ in response to a series of increasing current steps. PVIs$^+$ in the MK-801 group fired at an overall higher rate (two-way repeated-measures ANOVA, saline/MK-801: $n = 8/9$ cells from 4/3 mice per group, $^*p = 0.0365$). (g) Average action potential threshold of PVIs$^+$ (Student's t-test: saline/MK-801: $n = 8/9$ cells from 4/3 mice per group, $p = 0.7731$). (h) Density of cells with PVIs$^+$ immunoreactivity in the PrL region. Student's t-test: $n = 8$ for each group, $p = 0.9477$. (i) Western blot analysis of PV immunoreactivity: $n = 6/5$ for the saline/MK-801 group. Student's t-test, $p = 0.7783$. (j) Example traces of pyramidal neurons in response to depolarizing current steps. (k) Average action potential threshold of pyramidal neurons (saline/MK-801: $n = 13/15$ cells from 3/4 mice per group, $p = 0.2118$). (l) Input-output curve showing the average firing rate of pyramidal neurons in response to a series of increasing current steps (two-way repeated-measures ANOVA, saline/MK-801: $n = 13/15$ cells from 3/4 mice per group, $p = 0.5589$). (m) Example traces of sEPSC in pyramidal neurons. (n) Cumulative probability and the average amplitude of sEPSC (saline/MK801: $n = 12/10$ cells from 4/3 mice per group, $p = 0.4242$). (o) Cumulative probability and the average frequency of sEPSC (saline/MK-801: n = 12/10 cells from 4/3 mice per group, $p = 0.4544$). Data were represented as mean ± SEM, $^*p < 0.05$. Student's t-test for two groups' comparison.

entering the escape chamber than control mice across the four blocks of daily training (Figure 1(g)). However, the time spent in exploring the target hole in the probe test was not different between the two groups (Figure S1e). These data suggest learning but not memory ability was impaired in adolescent mice. Collectively, these observations demonstrate that transient blockade of NMDARs on PND 10 could induce schizophrenia-like behaviors in mice's adolescence.

3.2. Schizophrenia-Relevant Reduced GABA Transmission and PVIs$^+$ Hypofunction Induced in Adolescent Mice. GABA deficits, especially PVI$^+$ dysfunction, have been linked to the illness pathology of schizophrenia [14, 15]. Electrophysiological recording of reduced GABA transmission has been observed in NMDAR antagonist animals. Accordingly, we observed a significantly decreased interevent interval distribution and mean frequency of sIPSCs in the pyramidal neurons of MK-801-treated mice in adolescence (Figures 2(a)–2(c)). However, we found no significant changes in the cumulative amplitude distribution and mean amplitude (Figure 2(d)) in these neurons. These observations suggest a decreased GABAergic inhibitory input to pyramidal neurons. We next investigated the physiological function of PVIs$^+$ in the PrL region. Fast-spiking features were used to identify PVIs$^+$. The firing frequency of PVIs$^+$ in MK-801-treated mice experienced a significant decline with increasing current injections (Figures 2(e) and 2(f)). However, we found no difference in action potential (AP) threshold (Figure 2(g)). These data suggest decreased excitability of PVIs$^+$. We found no decrease in the density of PVIs$^+$ (Figure 2(h)) or parvalbumin expressing (Figure 2(i)) in the PrL region, suggesting that the decreased excitability is likely due to a functional deficit of the PVIs$^+$ and not a reduction in their numbers.

PVI$^+$ control the E-I balance of neural circuits, and their inhibition is likely to disinhibit the activity of pyramidal neurons. However, we found no difference in AP threshold or firing frequency of pyramidal neurons when comparing mice from both groups (Figures 2(j)–2(l)). Mean amplitude, frequency, and both cumulative distribution of sEPSC in pyramidal neurons were also not different between groups (Figures 2(m)–2(o)), indicating that the excitability of pyramidal neurons was unaffected in adolescence.

3.3. Altered Global Proteome of PFC in Adolescent Mice. Treatment with MK-801 on PND 10 results in abnormal behaviors and GABAergic hypofunction in adolescence, reminiscent of schizophrenia. We next investigated the molecular basis of GABAergic deficit by proteomic analysis of PFC (Figure 3(a)). We generated high-quality proteomic data with high technical (median coefficient of variance (CV) < 10% and $R^2 > 0.9$, Figure S2a-c) and intersample reproducibility (median CV < 15%, Figure S2d). Of the 4833 proteins identified, 3222 had a CV of technical reproducibility < 20% across all samples, and they were used for subsequent analysis (Figure 3(b)). 119 of cortical proteins were differentially expressed (DEPs) (fold change > |1.3 |, adjusted $p < 0.05$) in MK-801-treated mice (Figures 3(c) and 3(d)). Notably, 77% of the DEPs were downregulated (92 down vs. 27 up, Figure 3(c)). Their top Gene Ontology (GO) functions involved in different aspects of metabolic processes (Figure 3(e)). In contrast, we did not find significantly enriched biological function (data not shown) for the upregulated proteins. These data indicated impaired metabolic processes in adolescence of MK-801-treated mice. Hence, we hypothesized the observed reduction of GABA transmission in our electrophysiological recording that might be associated with the impaired GABA-related metabolic processes.

3.4. Integrative Analysis of Proteomics and Single-Cell Sequencing Revealed that Metabolic Processes Were Differentially Affected Depending on Cell Types. GABA-related metabolic processes could be coregulated by different cell types. Hence, we mapped the DEPs with the mouse single-cell sequencing data (http://mousebrain.org) to examine the cell-type specific functional alteration. We downloaded the expressed value of DEPs in their cortical cell types. We used hierarchical clustering to classify the cell types that DEPs have their most expression. We found DEPs were mainly clustered into three cell types: excitatory neurons, interneurons, and glial cells (Figure 4(a)). These cells were involved in different aspects of metabolic and developmental processes (Figures 4(b) and 4(c), Figure S3a-b). Reduced level of GABA is the core feature of GABA hypofunction. GABA is the naturally occurred amino acid working as the inhibitory neurotransmitter in the brain. What is interesting is that we found proteins enriched in interneurons and astrocytes which were both significantly enriched in the amino acid metabolic process (Figures 4(b) and 4(c)). In addition, astrocytes were also involved in the ion transport, which could be associated with neurotransmission (Figure 4(c)). Therefore, we further analyzed the proteins involved in the metabolic processes of the two cells. Notably, we found six of them were associated with GABA signaling, including GAD65 (encoding glutamate decarboxylase 65), SYNPR (encoding synaptoporin), GAT3 (encoding sodium and chloride dependent GABA transporter 3), SN1 (encoding sodium coupled neutral amino acid transporter 3), DBI (encoding acyl-CoA binding protein), and CPT1A (encoding carnitine O-palmitoyltransferase 1) (Figure 4(d)). These proteins were either from astrocytes or interneurons and were all downregulated in MK-801-treated mice. These data suggest impaired GABA signaling regulated by astrocytes and interneurons in adolescence.

3.5. Downregulated GABAergic Networks Coregulated by Interneurons and Astrocytes. We further analyzed how these GABA signaling-related proteins could affect GABAergic hypofunction. We found that the expression of GAD65, SYNPR, GAT3, SN1, DBI, and CPT1A showed a significant correlation with each other (Figure 5(a)), indicating their interaction in the network. Hence, we explored all the GABA-related proteins in our proteomic data. We found GAD65, SYNPR, GAT3, SN1, DBI, and CPT1A interacted with other GABAergic network components, like GAD67, GAT1, VGAT, PVALB, and GLU (Figure 5(b)). However,

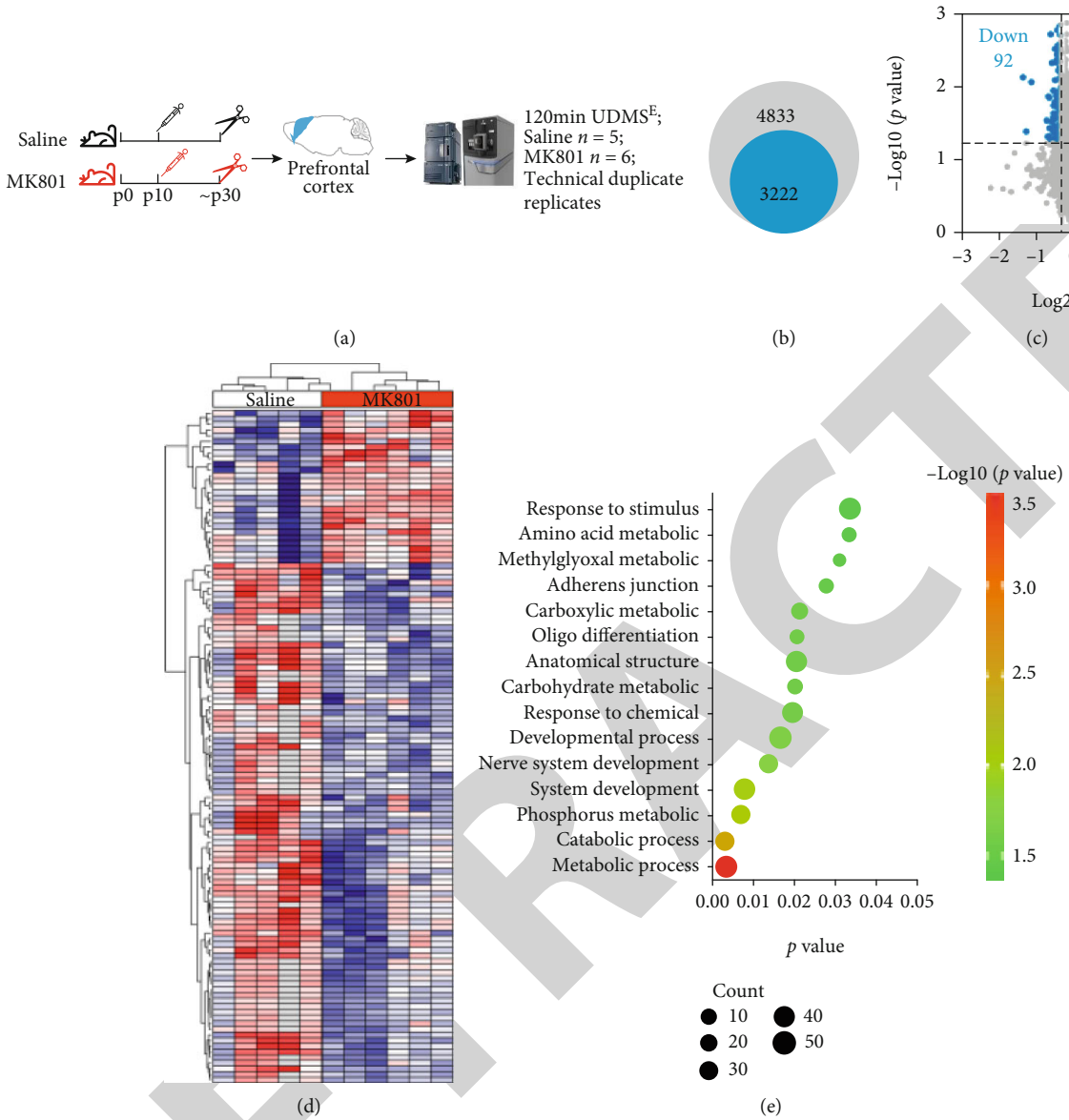

Figure 3: Overview of the altered proteome of PFC in adolescent mice by data-independent UDMS^E approach. (a) Schematic diagram of data-independent proteomic acquisition. Saline or MK-801-treated mice were sacrificed on ~PND 30. The PFC was dissected for trypsin digestion and a 120 min gradient LC-MS acquisition. Duplicate technical replicates were performed for each sample. $n = 5$ of the saline group and $n = 6$ of the MK801 group. (b) 4833 proteins were identified, and only 3222 of them that the CV value of technical replicates ≤ 20% across all samples were used for subsequent analysis. (c) Volcano plot of significantly expressed proteins, Fold change ≥ |1.3|, adjusted $p < 0.05$. (d) Hierarchical clustering of significant proteins. Each square represents one sample. Red: upregulated. Blue: downregulated. Protein's intensity was scaled across all samples and displayed as Z score. (e) The top GO enrichment of biological function of all significant proteins. Circle size represents the protein numbers in each item. p value was adjusted by FDR correction.

these interacted components were not changed in the MK-801-treated mice (Figure 5(b)). GABA is synthesized from glutamate by glutamate decarboxylase (GAD), which exists in two isoforms, that is, GAD65 and GAD67. Both GAD 65 and 67 are expressed in GABAergic neurons. We validated the downregulated expression of GAD65 by western blot, consisted with our proteomics result. However, the expression of GAD67 was not changed in MK-801-treated mice (Figures 5(c) and 5(d)). SYNPR is also expressed in GABAergic neurons. SYNPR interacts with the SNARE core complex and is responsible for synaptic vesicle fusion to regulate GABA release [41]. In addition, DBI can act on astrocytes' mitochondria to stimulate neurosteroid biosynthesis, which may regulate $GABA_AR$ [42] activity. GAT3 is a GABA transporter found on astrocytes to reuptake GABA and inactive GABAergic signaling [43]. Interestingly, SN1 is also exclusively expressed in astrocytes. It is required to release glutamine from astrocytes and furnish GABAergic neurons with the primary neurotransmitter precursor for GABA synthesis [44]. In addition, GABA release is known to be decreased through CPT1A reduction [45]. Thus, downregulation of these proteins suggest an inhibited GABA cycling (synthesis,

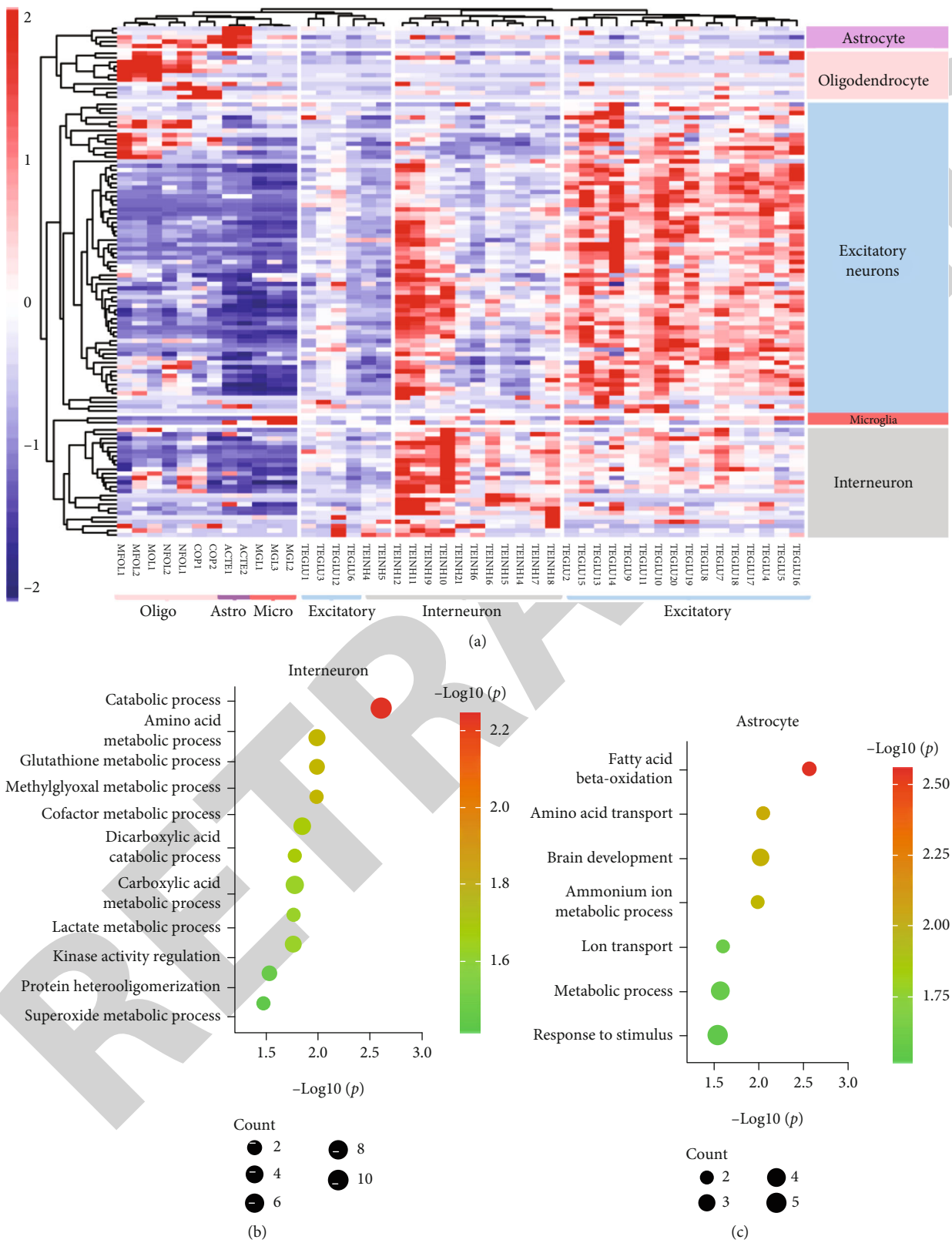

Figure 4: Continued.

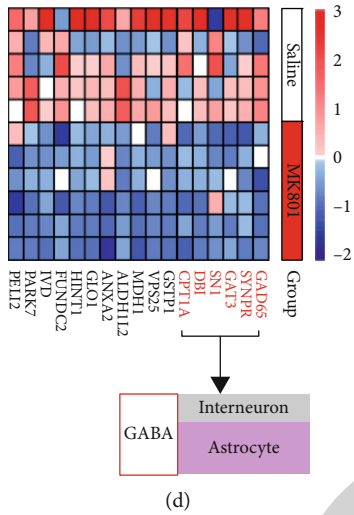

(d)

Figure 4: Integrative analysis of proteomics and single-cell sequencing data of differentially expressed proteins in adolescent mice. (a) All of the differentially expressed proteins in PFC identified in proteomics analysis were mapped to the mouse brain single-cell sequencing database (http://mousebrain.org). We downloaded the expression value of each differentially expressed protein within its clustered cell types in the cortex. A total of 45 cellular subtypes were showed, consisted of five major cell types of excitatory neurons, inhibitory neurons, astrocytes, oligodendrocytes, and microglia. Hierarchical clustering of the expression of significant proteins in all cell types showed their prominent cellular location. Red: higher protein expression. Blue: lower protein expression. Protein's expression was scaled in a row and represented as Z score. Pie graphs on the right panel showed the number and percentage of downregulated proteins in each cell type. (b, c) Top GO enrichment of biological function of differentially expressed proteins in interneurons and astrocytes. Circle size represents the protein numbers in each item. (d) Heatmap of differentially expressed proteins involved in the metabolic processes in astrocytes and interneurons. Proteins associated with GABA signaling were from astrocytes and interneurons and downregulated after postnatal MK-801 injection. Each square represents one sample. Red: upregulated. Blue: downregulated. Protein's expression was scaled in a row and represented as Z score.

release, termination, and replenishment) coregulated by GABAergic neurons and astrocytes in adolescence, which could explain the molecular mechanism of GABAergic hypofunction (Figure 5(e)).

4. Discussion

Here, we established a transient blockade of NMDARs on PND 10, which was sufficient to induce schizophrenia-relevant deficits in adolescent mice, such as deficits in sensory gating and impaired social and learning ability. Mice in adolescence exhibited reduced GABA transmission and PVI$^+$ hypofunction by electrophysiological recording, indicating GABAergic deficits, which is the pathological feature of schizophrenia and consistent with previous studies by NMDAR antagonists [9, 11]. We then presented a cortical proteomic evaluation and combined analysis of single-cell sequencing data. We globally identified the molecular basis of GABAergic deficits induced by NMDAR hypofunction in adolescence, which is few investigated previously. Such fundamental overview could provide potential drug targets of GABAergic rescue for prevention and intervention.

Comparing the chronic blockade of NDMARs by antagonists during the neonatal period of rodents, the strategy of transient blockade on PND 10 showed a comparable effect on inducing schizophrenia-relevant behaviors. PND 10 is a critical time for the physiological maturation of PVIs$^+$ [29]. PVIs$^+$ are the major population of cortical GABAergic neurons and delicately control the excitation/inhibition balance [46]. Functional and molecular impairment of PVIs$^+$ is frequently observed in schizophrenia. PVIs$^+$ are more sensitive to NMDAR hypofunction compared to the pyramidal neurons [47], especially during development [48], due in part to its more highly expressed NMDARs in this period than in adulthood [49]. Genetic NMDAR ablation in PVIs$^+$ during neonatal period, instead of the adulthood of mice, confers schizophrenia-like phenotypes [48], supporting the sensitive window of PVIs$^+$ to NMDAR hypofunction. Hence, it is possible that the transient blockade of NMDARs on PND 10 alters the orchestrated process of PVI$^+$ maturation, contributing to subsequent abnormal behaviors. Our results suggest that NMDAR hypofunction, even a subtle one during the critical stage of neonatal development, could have adverse effects amplified in later life, emphasizing the importance of neonatal health care.

Our study found impaired excitability of PVIs$^+$ in adolescence, but not their amount or their PV immunoreactivity. We suggest that the observed reduced GABA transmission could be associated with the reduced excitability of PVIs$^+$. The inhibition of PVIs$^+$ is likely to decrease the strength of inhibitory inputs onto pyramidal neurons [9, 11]; however, in our study, we found that the excitability of pyramidal neurons was not affected. It could be a compensatory strategy to prevent excessive excitation and cell injury. Yet, additional studies will be required to confirm these findings.

We found that 77% of alternated proteins were downregulated in adolescence by postnatal MK-801 treatment. Some of them (e.g., GLOT1, PLXAN2, and TUBB5) have previously been associated with schizophrenia [50–52]. We found downregulated proteins were mostly enriched in a series of

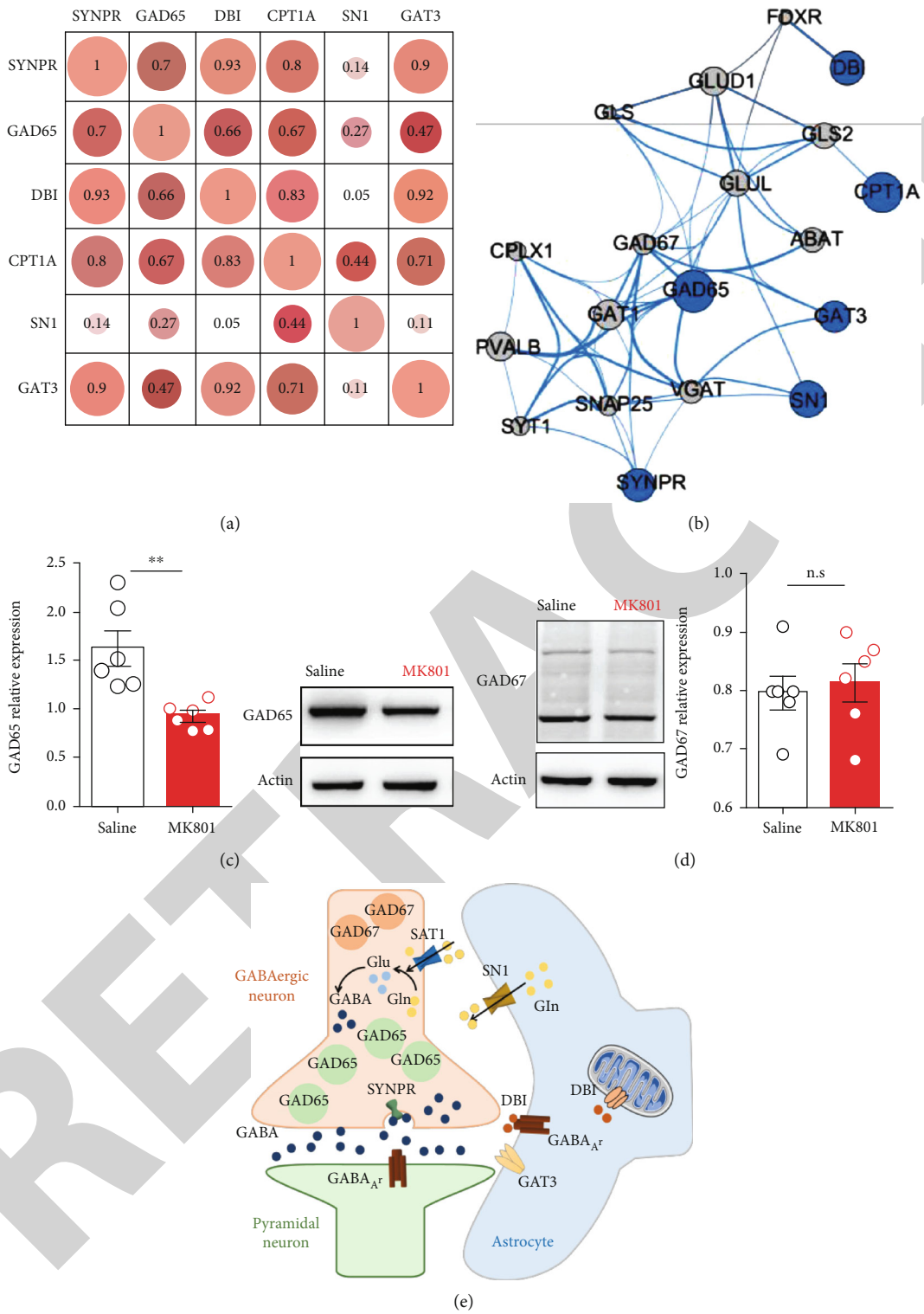

Figure 5: Protein network analysis of GABA neurotransmission. (a) Pearson correlation analysis of the expression of significant proteins involved in GABA neurotransmission. The number inside the circle represents the R value. (b) Network of proteins involved in GABA neurotransmission. Blue: downregulated proteins. Grey: proteins whose expression were not changed in this study by MS analysis. Circle size represents the value of the adjusted p value. The larger size indicated the smaller p value. The p value of blue circles was below 0.05; otherwise, they were above 0.05. The thickness of lines represents the combined score of edges. (c) Western blot validation of the GAD65 expression, $n = 6$ of each group, $p = 0.0043$. (d) Western blot validation of the GAD67 expression. $n = 6$ of each group, $p = 0.7108$. Data were represented as mean ± SEM. $^{**}p < 0.01$. Student's t-test. (e) Schema depicting the contribution of downregulated proteins in GABA dysfunction. GAD65 and SYNPR are responsible for GABA synthesis and release, respectively. GAT3 reuptakes GABA in the synaptic cleft. DBI is the GAGB$_A$ receptor. SN1 transports GABA-derived glutamine to GABAergic neurons for GABA replenishment.

metabolic processes, in which excitatory neurons, interneurons, astrocytes, and oligodendrocytes were differentially affected. Energy-related and amino acid processes were preferentially disturbed in interneurons and astrocytes. Organic substance and nitrogen metabolic process was affected in excitatory neurons and oligodendrocytes. These differences might be associated with the different functions of NMDARs on these cell types. Studies have shown that MK-801 could affect glycolysis-related proteins in oligodendrocytes, but much less in neurons and astrocytes [53].

Notably, we identified that multiple GABA-related proteins were significantly downregulated in adolescence, including GAD65, SYNPR, DBI, GAT3, SN1, and CPT1A. These molecular participate in the GABA cycle, consisted of GABA synthesis, release, reuptake, and replenishment, to maintain the proper GABA homeostasis. Our finding indicates the molecular basis of GABAergic deficit observed in our electrophysiological recording, which could be resulted from the impaired GABA homeostasis.

GABAergic neurotransmission is comprised of phasic and tonic inhibition. The former is regulated by the classical vesicular release of GABA confined to the synapses, while the tonic inhibition involves the GABA spillover from the synapses and activates extrasynaptic receptors. GAD65 is located explicitly in axon terminals and specially regulates the vesicular release of GABA for synaptic transmission [54]. Although the evenly distributed cytosol GAD67 produces ~90% of GABA in the brain for cell metabolism and neurotransmission, it has been revealed that GAD65 is crucial to maintain the synaptic GABA by conversion of astrocytic glutamine via glutamate [55], especially when extensive synaptic GABA is required during peak demand [56, 57], so as to fine tune the GABAergic synaptic function. In addition, GAD65 is important in maintenance of the tonic inhibition [58], which has been estimated to constitute a prominent part of GABAergic transmission [59]. Evidence has suggested the key roles of tonic inhibition in memory, cognition, and schizophrenia [60]. $GAD65^{-/-}$ mice exhibited pronounced deficits in pre-pulse inhibition [61]. Although postmortem studies have consistently shown lower expression GAD67 in the dorsolateral prefrontal cortex of subjects with schizophrenia, in our study, we did not find its alternation as previously reported. We suggested that the deficits in GAD65, rather than GAD67, could be the developmental feature of schizophrenia.

Astrocytes wrap around the pre and postsynaptic elements of neurons and exert profound effect on neuronal networks [18]. Current data support astrocytes' significance in regulating the dynamic GABAergic-astrocyte communication. Astrocytes regulate GABAergic synapses' activity by modulating the synaptic GABA content via its high-affinity transporters for GABA clearance and providing the neurotransmitter precursor for synthesis. Our study found that these two processes could be diminished in adolescence by downregulation of GAT3 and SN1. In addition to astrocytic clearance, GABA could be cleared from the synapses by uptake into the presynaptic neurons via GABA transporter 1 (GAT1). However, we did not find the alternated expression of GAT1, indicating that the process of neuronal clearance was not disturbed in adolescence. What is more, we suggest $GABA_AR$ signaling in astrocytes could also be inhibited by downregulation of DBI. DBI selectively knockout mice has shown certain forms of impaired spatial learning and memory [62]. NMDARs express in a low abundance on astrocytes. Activation of NMDARs on astrocytes could generate intracellular calcium signaling. However, their roles in astrocyticneuronal interaction in neurotransmission are unclear. Only one study reported that ablation or blockade of NMDARs on the hippocampus promoted the presynaptic inhibitory tone on excitatory neurons [63]. Collectively, we suggest that the inhibitory network mutually regulated by GABAergic neurons and astrocytes is impaired in adolescence, which could be astrocytic NMDAR-dependent or independent.

5. Conclusion

This study showed that a transient blockade of NMDARs postnatally had chronic behavioral and GABA deficits in adolescence. Our results revealed a downregulated set of GABA-related molecular, which synergistically regulate the whole process of GABA cycle, including GABA synthesis, release, reuptake, and replenishment. Although there have been studies targeting on GABA or other targets in new drug developments, our findings provided a comprehensive view of GABA deficits during adolescence, which is few studied. In addition, molecular like SYNPR, SN1, and CPTA1 has not been well investigated as drug targets. Hence, our study provided more clues and could benefit drug development.

Data Availability

The data used to support the findings of this study are available from the corresponding author upon request.

Conflicts of Interest

The authors declare no conflict of interest.

Authors' Contributions

X.D.W. established the mice model and performed the behavior, in vitro slice electrophysiology, and image. Y.H. established the mice model and performed the behavior. W.X.L. performed the western blot. Y.Y.M performed the image counting. X.C. drew the schematic diagram. T.X. designed the study, performed the proteomic experiment and data analysis, and wrote and edited the paper. D.H.C. conceived the study and review and editing.

Acknowledgments

The authors would like to thank Dr. Tifei Yuan and Yanjia Luo for the paper discussion and Lanting Huang, Shiyu Peng, and Xinyou Lv for the guidance of electrophysiology. This work was funded by the Youth Program of National Natural Science Foundation of China (81801324), Shanghai Sailing Program (17YF141630), and the National Natural Science Foundation of China (81671336).

Supplementary Materials

Fig. S1 Mice administrated with MK-801 on PND 10 showed schizophrenia-like behaviors in adolescence. Figure S2: quality control of proteomic data. Figure S3: integrative analysis of proteomics and single-cell sequencing data of differentially expressed proteins in early-adolescent mice. Supplementary Methods Information: open field test, elevated plus maze test, prepulse inhibition test, nesting behavior test, and Barnes maze. *(Supplementary Materials)*

References

[1] M. J. Owen, A. Sawa, and P. B. Mortensen, "Schizophrenia," *Lancet*, vol. 388, no. 10039, pp. 86–97, 2016.

[2] D. R. Weinberger, "Implications of normal brain development for the pathogenesis of schizophrenia," *Archives of General Psychiatry*, vol. 44, no. 7, pp. 660–669, 1987.

[3] O. Marin, "Developmental timing and critical windows for the treatment of psychiatric disorders," *Nature Medicine*, vol. 22, no. 11, pp. 1229–1238, 2016.

[4] G. D. Hoftman and D. A. Lewis, "Postnatal developmental trajectories of neural circuits in the primate prefrontal cortex: identifying sensitive periods for vulnerability to schizophrenia," *Schizophrenia Bulletin*, vol. 37, no. 3, pp. 493–503, 2011.

[5] B. Moghaddam and D. Javitt, "From revolution to evolution: the glutamate hypothesis of schizophrenia and its implication for treatment," *Neuropsychopharmacology*, vol. 37, no. 1, pp. 4–15, 2012.

[6] C. H. Lin, Y. M. Chen, and H. Y. Lane, "Novel treatment for the most resistant schizophrenia: dual activation of NMDA receptor and antioxidant," *Current Drug Targets*, vol. 21, no. 6, pp. 610–615, 2020.

[7] H. Gunduz-Bruce, "The acute effects of NMDA antagonism: from the rodent to the human brain," *Brain Research Reviews*, vol. 60, no. 2, pp. 279–286, 2009.

[8] A. L. Lim, D. A. Taylor, and D. T. Malone, "Consequences of early life MK-801 administration: long-term behavioural effects and relevance to schizophrenia research," *Behavioural Brain Research*, vol. 227, no. 1, pp. 276–286, 2012.

[9] E. Flores-Barrera, D. R. Thomases, and K. Y. Tseng, "MK-801 exposure during adolescence elicits enduring disruption of prefrontal E-I balance and its control of fear extinction behavior," *The Journal of Neuroscience*, vol. 40, no. 25, pp. 4881–4887, 2020.

[10] C. Le Magueresse and H. Monyer, "GABAergic interneurons shape the functional maturation of the cortex," *Neuron*, vol. 77, no. 3, pp. 388–405, 2013.

[11] Y. Huang, H. Jiang, Q. Zheng et al., "Environmental enrichment or selective activation of parvalbumin-expressing interneurons ameliorates synaptic and behavioral deficits in animal models with schizophrenia-like behaviors during adolescence," *Molecular Psychiatry*, 2021.

[12] D. Xi, W. Zhang, H. X. Wang, G. G. Stradtman, and W. J. Gao, "Dizocilpine (MK-801) induces distinct changes of N-methyl-D-aspartic acid receptor subunits in parvalbumin-containing interneurons in young adult rat prefrontal cortex," *The International Journal of Neuropsychopharmacology*, vol. 12, no. 10, pp. 1395–1408, 2009.

[13] F. Donato, S. B. Rompani, and P. Caroni, "Parvalbumin-expressing basket-cell network plasticity induced by experience regulates adult learning," *Nature*, vol. 504, no. 7479, pp. 272–276, 2013.

[14] J. R. Glausier, K. N. Fish, and D. A. Lewis, "Altered parvalbumin basket cell inputs in the dorsolateral prefrontal cortex of schizophrenia subjects," *Molecular Psychiatry*, vol. 19, no. 1, pp. 30–36, 2014.

[15] T. Hashimoto, D. W. Volk, S. M. Eggan et al., "Gene expression deficits in a subclass of GABA neurons in the prefrontal cortex of subjects with schizophrenia," *The Journal of Neuroscience*, vol. 23, no. 15, pp. 6315–6326, 2003.

[16] M. P. Vawter, J. M. Crook, T. M. Hyde et al., "Microarray analysis of gene expression in the prefrontal cortex in schizophrenia: a preliminary study," *Schizophrenia Research*, vol. 58, no. 1, pp. 11–20, 2002.

[17] A. A. Curley, D. Arion, D. W. Volk et al., "Cortical deficits of glutamic acid decarboxylase 67 expression in schizophrenia: clinical, protein, and cell type-specific features," *The American Journal of Psychiatry*, vol. 168, no. 9, pp. 921–929, 2011.

[18] M. Ishibashi, K. Egawa, and A. Fukuda, "Diverse actions of astrocytes in GABAergic signaling," *International Journal of Molecular Sciences*, vol. 20, no. 12, p. 2964, 2019.

[19] S. B. Siems, O. Jahn, M. A. Eichel et al., "Proteome profile of peripheral myelin in healthy mice and in a neuropathy model," *eLife*, vol. 9, 2020.

[20] E. Ahrne, L. Molzahn, T. Glatter, and A. Schmidt, "Critical assessment of proteome-wide label-free absolute abundance estimation strategies," *Proteomics*, vol. 13, no. 17, pp. 2567–2578, 2013.

[21] J. C. Silva, M. V. Gorenstein, G. Z. Li, J. P. C. Vissers, and S. J. Geromanos, "Absolute quantification of proteins by LCMS^{E}:," *Molecular & Cellular Proteomics*, vol. 5, no. 1, pp. 144–156, 2006.

[22] J. Li and R. Tibshirani, "Finding consistent patterns: a nonparametric approach for identifying differential expression in RNA-Seq data," *Statistical Methods in Medical Research*, vol. 22, no. 5, pp. 519–536, 2013.

[23] Q. Gao, H. W. Zhu, L. Q. Dong et al., "Integrated Proteogenomic Characterization of HBV-Related Hepatocellular Carcinoma," *Cell*, vol. 179, no. 2, pp. 561–577.e22, 2019.

[24] P. Shannon, A. Markiel, O. Ozier et al., "Cytoscape: a software environment for integrated models of biomolecular interaction networks," *Genome Research*, vol. 13, no. 11, pp. 2498–2504, 2003.

[25] A. Zeisel, H. Hochgerner, P. Lönnerberg et al., "Molecular architecture of the mouse nervous system," *Cell*, vol. 174, no. 4, pp. 999–1014.e22, 2018, e1022.

[26] K. Nakazawa and K. Sapkota, "The origin of NMDA receptor hypofunction in schizophrenia," *Pharmacology & Therapeutics*, vol. 205, p. 107426, 2020.

[27] H. Viberg, "Exposure to polybrominated diphenyl ethers 203 and 206 during the neonatal brain growth spurt affects proteins important for normal neurodevelopment in mice," *Toxicological Sciences*, vol. 109, no. 2, pp. 306–311, 2009.

[28] J. A. del Rio, L. de Lecea, I. Ferrer, and E. Soriano, "The development of parvalbumin-immunoreactivity in the neocortex of the mouse," *Brain Research. Developmental Brain Research*, vol. 81, no. 2, pp. 247–259, 1994.

[29] T. Miyamae, K. Chen, D. A. Lewis, and G. Gonzalez-Burgos, "Distinct physiological maturation of parvalbumin-positive neuron subtypes in mouse prefrontal cortex," *The Journal of Neuroscience*, vol. 37, no. 19, pp. 4883–4902, 2017.

[30] A. Vezzani, R. Serafini, M. A. Stasi et al., "Kinetics of MK-801 and its effect on quinolinic acid-induced seizures and neurotoxicity in rats," *The Journal of Pharmacology and Experimental Therapeutics*, vol. 249, no. 1, pp. 278–283, 1989.

[31] B. Dyck, K. Guest, C. Sookram, D. Basu, R. Johnson, and R. K. Mishra, "PAOPA, a potent analogue of pro-Leu-glycinamide and allosteric modulator of the dopamine D_2 receptor, prevents NMDA receptor antagonist (MK-801)-induced deficits in social interaction in the rat: implications for the treatment of negative symptoms in schizophrenia," *Schizophrenia Research*, vol. 125, no. 1, pp. 88–92, 2011.

[32] A. Fredriksson and T. Archer, "Neurobehavioural deficits associated with apoptotic neurodegeneration and vulnerability for ADHD," *Neurotoxicity Research*, vol. 6, no. 6, pp. 435–456, 2004.

[33] R. J. Beninger, A. Jhamandas, H. Aujla et al., "Neonatal exposure to the glutamate receptor antagonist MK-801: effects on locomotor activity and pre-pulse inhibition before and after sexual maturity in rats," *Neurotoxicity Research*, vol. 4, no. 5-6, pp. 477–488, 2002.

[34] A. R. Burke and K. A. Miczek, "Stress in adolescence and drugs of abuse in rodent models: role of dopamine, CRF, and HPA axis," *Psychopharmacology*, vol. 231, no. 8, pp. 1557–1580, 2014.

[35] R. San-Martin, L. A. Castro, P. R. Menezes, F. J. Fraga, P. W. Simoes, and C. Salum, "Meta-analysis of sensorimotor gating deficits in patients with schizophrenia evaluated by prepulse inhibition test," *Schizophrenia Bulletin*, vol. 46, no. 6, pp. 1482–1497, 2020.

[36] J. N. Crawley, "Designing mouse behavioral tasks relevant to autistic-like behaviors," *Mental Retardation and Developmental Disabilities Research Reviews*, vol. 10, no. 4, pp. 248–258, 2004.

[37] C. M. Powell and T. Miyakawa, "Schizophrenia-relevant behavioral testing in rodent models: a uniquely human disorder?," *Biological Psychiatry*, vol. 59, no. 12, pp. 1198–1207, 2006.

[38] R. W. Heinrichs and K. K. Zakzanis, "Neurocognitive deficit in schizophrenia: a quantitative review of the evidence," *Neuropsychology*, vol. 12, no. 3, pp. 426–445, 1998.

[39] A. J. Saykin, D. L. Shtasel, R. E. Gur et al., "Neuropsychological deficits in neuroleptic naive patients with first-episode schizophrenia," *Archives of General Psychiatry*, vol. 51, no. 2, pp. 124–131, 1994.

[40] C. A. Barnes, "Memory deficits associated with senescence: a neurophysiological and behavioral study in the rat," *Journal of Comparative and Physiological Psychology*, vol. 93, no. 1, pp. 74–104, 1979.

[41] I. Singec, R. Knoth, M. Ditter et al., "Synaptic vesicle protein synaptoporin is differently expressed by subpopulations of mouse hippocampal neurons," *Journal of Comparative Neurology*, vol. 452, no. 2, pp. 139–153, 2002.

[42] A. Guidotti, "Role of DBI in brain and its posttranslational processing products in normal and abnormal behavior," *Neuropharmacology*, vol. 30, no. 12, pp. 1425–1433, 1991.

[43] Y. Zhou and N. C. Danbolt, "GABA and glutamate transporters in brain," *Frontiers in Endocrinology*, vol. 4, 2013.

[44] L. S. H. Nissen-Meyer and F. A. Chaudhry, "Protein kinase C phosphorylates the system N glutamine transporter SN1 (Slc38a3) and regulates its membrane trafficking and degradation," *Frontiers in Endocrinology*, vol. 4, 2013.

[45] J. F. Mir, S. Zagmutt, M. P. Lichtenstein et al., "Ghrelin causes a decline in GABA release by reducing fatty acid oxidation in cortex," *Molecular Neurobiology*, vol. 55, no. 9, pp. 7216–7228, 2018.

[46] H. Hu, J. Gan, and P. Jonas, "Fast-spiking, parvalbumin$^+$ GABAergic interneurons: from cellular design to microcircuit function," *Science*, vol. 345, no. 6196, p. 1255263, 2014.

[47] N. Picard, A. E. Takesian, M. Fagiolini, and T. K. Hensch, "NMDA 2A receptors in parvalbumin cells mediate sex-specific rapid ketamine response on cortical activity," *Molecular Psychiatry*, vol. 24, no. 6, pp. 828–838, 2019.

[48] J. E. Belforte, V. Zsiros, E. R. Sklar et al., "Postnatal NMDA receptor ablation in corticolimbic interneurons confers schizophrenia-like phenotypes," *Nature Neuroscience*, vol. 13, no. 1, pp. 76–83, 2010.

[49] H. X. Wang and W. J. Gao, "Cell type-specific development of NMDA receptors in the interneurons of rat prefrontal cortex," *Neuropsychopharmacology*, vol. 34, no. 8, pp. 2028–2040, 2009.

[50] R. Mizutani, R. Saiga, A. Takeuchi et al., "Three-dimensional alteration of neurites in schizophrenia," *Translational Psychiatry*, vol. 9, no. 1, p. 85, 2019.

[51] M. W. Breuss, A. H. Hansen, L. Landler, and D. A. Keays, "Brain-specific knockin of the pathogenic _Tubb5_ E401K allele causes defects in motor coordination and prepulse inhibition," *Behavioural Brain Research*, vol. 323, pp. 47–55, 2017.

[52] X. F. Zhao, R. Kohen, R. Parent et al., "PlexinA2 forward signaling through Rap1 GTPases regulates dentate Gyrus development and schizophrenia-like behaviors," *Cell Reports*, vol. 22, no. 2, pp. 456–470, 2018.

[53] P. C. Guest, K. Iwata, T. A. Kato et al., "MK-801 treatment affects glycolysis in oligodendrocytes more than in astrocytes and neuronal cells: insights for schizophrenia," *Frontiers in Cellular Neuroscience*, vol. 9, 2015.

[54] J. J. Soghomonian and D. L. Martin, "Two isoforms of glutamate decarboxylase: why?," *Trends in Pharmacological Sciences*, vol. 19, no. 12, pp. 500–505, 1998.

[55] A. B. Walls, E. M. Eyjolfsson, O. B. Smeland et al., "Knockout of GAD65 has major impact on synaptic GABA synthesized from astrocyte-derived glutamine," *Journal of Cerebral Blood Flow and Metabolism*, vol. 31, no. 2, pp. 494–503, 2011.

[56] N. Tian, C. Petersen, S. Kash, S. Baekkeskov, D. Copenhagen, and R. Nicoll, "The role of the synthetic enzyme GAD65 in the control of neuronal gamma-aminobutyric acid release," *Proceedings of the National Academy of Sciences of the United States of America*, vol. 96, no. 22, pp. 12911–12916, 1999.

[57] S. Y. Choi, B. Morales, H. K. Lee, and A. Kirkwood, "Absence of long-term depression in the visual cortex of glutamic acid decarboxylase-65 knock-out mice," *The Journal of Neuroscience*, vol. 22, no. 13, pp. 5271–5276, 2002.

[58] A. B. Walls, L. H. Nilsen, E. M. Eyjolfsson et al., "GAD65 is essential for synthesis of GABA destined for tonic inhibition regulating epileptiform activity," *Journal of Neurochemistry*, vol. 115, no. 6, pp. 1398–1408, 2010.

[59] M. C. Walker and A. Semyanov, "Regulation of excitability by extrasynaptic GABAA receptors," *Results and Problems in Cell Differentiation*, vol. 44, pp. 29–48, 2008.

[60] R. M. Hines, P. A. Davies, S. J. Moss, and J. Maguire, "Functional regulation of $GABA_A$ receptors in nervous system pathologies," *Current Opinion in Neurobiology*, vol. 22, no. 3, pp. 552–558, 2012.